UNIVERSITAT ROVIRA i VIRGILI

COPPE
Instituto Alberto Luiz Coimbra de Pós-Graduação e Pesquisa de Engenharia
UFRJ

# Integrating Computational Tools to Address the Thermophysical Behavior of Deep Eutectic Solvents in Gas Separation Applications

Luan Vittor Tavares Duarte de Alencar

## DOCTORAL THESIS

2024

Luan Vittor Tavares Duarte de Alencar

# Integrating Computational Tools to Address the Thermophysical Behavior of Deep Eutectic Solvents in Gas Separation Applications

Cotutelle PhD Thesis

**Universitat Rovira i Virgili**

*Doctoral Programme in Nanoscience, Materials, and Chemical Engineering*

and

**Universidade Federal do Rio de Janeiro**

*Programa de Pós-Graduação em Engenharia Química, COPPE*

Supervised by: Prof. Fèlix Llovell Ferret

Prof. Frederico Wanderley Tavares

2024

*Aos meus pais.*

# Acknowledgements

A conclusão desta tese de doutorado marca o fim de um ciclo repleto de desafios e aprendizados. Este trabalho não teria sido possível sem o apoio e a colaboração de várias pessoas e instituições às quais sou profundamente grato.

Primeiramente, gostaria de expressar minha imensa gratidão aos meus orientadores, cuja orientação e apoio constante foram fundamentais para o desenvolvimento deste trabalho.

A Félix, muchas gracias por toda la confianza que has puesto en mí desde el primer momento que nos conocimos. Tengo mucho orgullo del trabajo que hemos hecho juntos y, además de ser mi supervisor, me alegra profundamente tenerte como un gran amigo. Tu orientación ha sido increíblemente valiosa para mí.

Ao Fred, gostaria de expressar o quanto me sinto privilegiado por ter sido seu aluno e orientando. Muito obrigado pela sua orientação sempre sábia; você é uma inspiração não só como profissional, mas também como ser humano.

Me gustaría agradecer también a mi amiga Belén, que prácticamente fue mi supervisora. Eres una profesional muy dedicada y todos los que te tienen cerca son muy afortunados. Muchas gracias por todo! No puedo dejar de mencionar a mis amigos del grupo de investigación en España, Carlos y Merve. Extraño mucho nuestros cafés en la universidad y nuestras inolvidables cenas internacionales.

Gostaria de agradecer às universidades UFRJ e URV pela incrível oportunidade de realizar um doutorado em cotutela, assim como aos órgãos de fomento Capes e CNPq pelo apoio financeiro crucial. Também gostaria de expressar meu profundo agradecimento ao grupo de pesquisa ATOMS, do qual tenho muito orgulho de fazer parte.

Agradeço também a tantos amigos que me acompanharam nessa jornada. Em especial, gostaria de expressar minha gratidão à minha amiga Carol, que me ajudou em todo o processo de cotutela e, ao final, desenvolvemos uma linda amizade. Agradeço também aos meus amigos Iago e Larissa, que foram essenciais na minha inscrição no doutorado. Em especial, Larissa, com quem compartilhei tantos momentos durante esse período. Estou muito feliz de ver onde chegamos juntos. También quiero agradecer a mi amigo Bastián, con quien realizamos un excelente trabajo en colaboración.

No coração deste agradecimento, mesmo sabendo que eles não leem, estão meus queridos companheiros de quatro patas: Luna e Loke. Durante o período de home office da pandemia, vocês foram muito mais do que apenas gatos; foram minha companhia constante e meu refúgio.

Claro que eu não poderia deixar de agradecer ao meu Tai pelo amor e por todo o seu apoio, compreensão e paciência durante todas as fases deste doutorado. Sua presença foi essencial para mim neste período.

Por fim, mas não menos importante, a base da minha vida: minha família. Agradeço aos meus pais amados, Marise e Geraldo, ao meu irmão Geraldo Junior, à minha sobrinha mais linda do mundo, Maria Isis, e à minha companheira de vida, minha irmã Maysa. Tudo é por vocês, e esta conquista é nossa!

Finalizo essa trajetória com o coração cheio de orgulho e gratidão. Que venham os próximos desafios!

Luan Alencar

# Abstract

Global warming stands as one of the most critical issues in modern science, profoundly impacting society and prompting legislative actions, regulations, and scientific studies. The primary cause is the anthropogenic emission of greenhouse gases (GHGs), which have increased significantly in recent years. Effective capture and separation techniques for GHGs reduction, such as solvent-based absorption, are pivotal for sustainability efforts. In this sense, Deep Eutectic Solvents (DESs) have emerged as a promising eco-friendly solution for gas capture due to their high absorption capacity, cost-effectiveness, non-toxicity nature, and biodegradability, presenting a sustainable alternative to conventional solvents. Understanding the thermophysical properties of DESs is crucial for their industrial application. Given the diversity of DESs combinations and varying industrial conditions, relying solely on experimental measurements is impractical. Therefore, developing computational models to predict these properties and guide experiments is crucial. When constructing predictive models, it is important to consider the influence of cosolvents like water on DESs properties, particularly viscosity. Thus, this thesis aims to incorporate diverse theoretical frameworks to elucidate the thermophysical characteristics of DESs and their mixtures with cosolvents. Moreover, it seeks to explore their application in GHGs capture, including within commercial high global warming potential refrigerant gas blends, as well as their role in capturing carbon dioxide ($CO_2$) and separating it from ammonia ($NH_3$). The proposed framework employs the soft-SAFT equation of state for developing an accurate and transferable model, alongside machine learning techniques artificial neural networks trained with molecular descriptors derived from atomic-level analyzes using COSMO-SAC. This comprehensive approach facilitates the screening of DESs thermophysical properties, providing insights into their potential as alternative absorbents for GHGs separation and capture.

# Resumo

O aquecimento global é uma das questões mais críticas na ciência moderna, impactando profundamente a sociedade e levando a ações legislativas, regulamentações e estudos científicos. A sua principal causa é a emissão antropogênica de gases de efeito estufa, o qual aumentou significativamente nos últimos anos. Técnicas eficazes de captura e separação para a redução desses gases, como a absorção baseada em solventes, são fundamentais para os esforços de sustentabilidade. Nesse sentido, os Solventes Eutéticos Profundos (SEPs) surgiram como uma solução ecologicamente promissora para a captura de gases devido à sua alta capacidade de absorção, custo-benefício, natureza não tóxica e biodegradabilidade, apresentando uma alternativa sustentável aos solventes convencionais. Compreender as propriedades termo físicas dos SEPs é crucial para sua aplicação industrial. Desse modo, dado o vasto número de possíveis combinações de SEPs e as variadas condições industriais, confiar apenas em medições experimentais é impraticável. Portanto, o desenvolvimento de modelos computacionais para prever essas propriedades e orientar os experimentos é essencial. No desenvolvimento de modelos computacionais preditivos, é importante considerar a influência de cosolventes, como a água, nas propriedades dos SEPs, especialmente na viscosidade. Assim, esta tese visa incorporar diversos métodos teóricos para elucidar as características termofísicas dos SEPs e suas misturas com cosolventes. Além disso, esse trabalho busca explorar sua aplicação na captura de gases do efeito estufa, incluindo misturas de gases refrigerantes comerciais de alto potencial de aquecimento global, bem como misturas de de dióxido de carbono ($CO_2$) com amônia ($NH_3$). A abordagem proposta emprega a equação de estado soft-SAFT para desenvolver um modelo preciso e transferível, juntamente com técnicas de aprendizado de máquina, como redes neurais artificiais treinadas com descritores moleculares derivados de análises em nível atômico utilizando COSMO-SAC. Esta abordagem abrangente facilita a triagem das propriedades termofísicas dos SEPs, fornecendo informações valiosas sobre seu potencial como absorventes alternativos para a separação e captura de gases do efeito estufa.

# Resum

L'escalfament global ha esdevingut un dels problemes més crítics de la ciència moderna, afectant profundament la societat i provocant accions legislatives, regulacions i estudis científics. La causa principal és l'emissió antropogènica de gasos d'efecte hivernacle (GEH), els quals han augmentat significativament en els darrers anys. Les tècniques efectives de captura i separació per a la reducció de GEH, com l'absorció basada en solvents, són essencials per a contribuir en els esforços de sostenibilitat. En aquest sentit, els Solvents Eutèctics Profunds (SEPs) han sorgit com una solució prometedora i ecològica per a la captura de gasos a causa de la seva alta capacitat d'absorció, la seva rendibilitat, la seva naturalesa no tòxica i la seva biodegradabilitat, presentant-se com una alternativa sostenible als solvents convencionals. Comprendre les propietats termofísiques dels SEPs és crucial per a la seva aplicació industrial. Donada la diversitat de combinacions de compostos que formen SEPs i les condicions industrials variables, el nombre de mesures experimentals necessàries per a la seva caracterització resulta enorme. Per tant, desenvolupar models computacionals per predir aquestes propietats és crucial. Quan es construeixen models predictius, és important considerar la influència dels cosolvents com l'aigua sobre les propietats dels SEPs, especialment la viscositat. Així doncs, aquesta tesi pretén incorporar diversos marcs teòrics per dilucidar les característiques termofísiques dels SEPs i les seves mescles amb cosolvents. A més, busca explorar la seva aplicació en la captura de GEH, incloent-hi la separación de mescles de gasos refrigerants comercials d'alt potencial d'escalfament global, així com el seu paper en la captura de diòxid de carboni ($CO_2$) i separación de l'amoníac ($NH_3$). El marc proposat empra l'equació d'estat soft-SAFT per desenvolupar un model precís i transferible, juntament amb tècniques d'aprenentatge automàtic com les xarxes neuronals artificials entrenades amb descriptors moleculars derivats d'anàlisis a nivell atòmic utilitzant COSMO-SAC. Aquest enfocament integral facilita la selecció de les propietats termofísiques dels SEPs, proporcionant informació sobre el seu potencial com a absorbents alternatius per a la separació i captura de GEH.

# Contents

# List of Figures

# List of Tables

# List of Abbreviations

| | |
|---|---|
| **AAD** | Absolute Averaged Deviations |
| **AD** | Applicability Domain |
| **AARD** | Average Absolute Relative Deviation |
| **ANN** | Artificial Neural Network |
| **1,4-BT** | 1,4-Butanediol |
| **2,3-BT** | 2,3-Butanediol |
| **[Ch]Cl** | Choline Chloride |
| **$R^2$** | Coefficient of determination |
| **COSMO** | Conductor like Screening Model |
| **COSMO-RS** | COSMO – for Real Solvents |
| **COSMO-SAC** | COSMO - Segment Activity Coefficient |
| **DES** | Deep Eutectic Solvent |
| **DBN** | 1,5-diazabicyclo[4.3.0]-non-5-ene |
| **DBU** | 1,8-diazabicyclo[5.4.0]undec-7-ene |
| **DEA** | Diethanolamine |
| **DETA** | Diethylenetriamine |
| **R-32** | Difluoromethane |
| **D-FT** | D-Fructose |
| **D-GLU** | D-Glucose |
| **DH** | Diethylamine Hydrochloride |
| **DMSO** | Dimethyl Sulfoxide |
| **EoS** | Equation of State |
| **EaCl** | Ethylamine hydrochloride |
| **EtOH** | Ethanol |
| **EG** | Ethylene Glycol |
| **F-gas** | Fluorinated Gas |
| **FIL** | Fluorinated Ionic Liquid |
| **FVT** | Free-Volume Theory |
| **GHG** | Greenhouse Gas |
| **GWP** | Global Warming Potential |
| **GA** | Glycolic Acid |
| **GLA** | Glutaric Acid |
| **GL** | Glycerol |
| **GC** | Guaiacol |
| **HFC** | Hydrofluorocarbon |
| **HBA** | Hydrogen Bond Acceptor |
| **HBD** | Hydrogen Bond Donor |
| **EU** | 2-imidazolidone |
| **[ImH]Cl** | Imidazolium hydrochloride |
| **IL** | Ionic Liquids |

| | |
|---|---|
| **IPA** | Isopropanol |
| **LA** | Lactic Acid |
| **LJ** | Lennard-Jones |
| **LevA** | Levulinic Acid |
| **LiCl** | Lithium chloride |
| **ML** | Machine Learning |
| **MA** | Malonic Acid |
| **MDA** | Methyldiethanolamine |
| **MEA** | Monoethanolamine |
| **MeOH** | Methanol |
| **NADES** | Natual Deep Eutectic Solvents |
| **OPLS-DES** | Nonpolarizable force-field |
| **NRTL** | Nonrandom two-liquid model |
| **OA** | Oxalic Acid |
| **PaD** | Partial Derivatives |
| **ppm** | Parts per million |
| **PR** | Peng-Robinson |
| **R-125** | Pentafluoroethane |
| **PA** | Propionic Acid |
| **PH** | Phenol |
| **SDR** | Standardized residual |
| **SLE** | Solid/liquid Equilibria |
| **R-134a** | 1,1,1,2-tetrafluoroethane |
| **R-143a** | 1,1,1-trifluoroethane |
| **SAFT** | Statistical Association Fluid Theory |
| **TMAC** | Tetramethylammonium Chloride |
| **TBD** | 1,5,7-triazabicyclo[4.4.0]-dec-5-ene |
| **TGE** | Triethylene Glycol |
| **UR** | Urea |
| **VLE** | Valor-Liquid Equilibria |
| **RMSE** | Root-mean-square error |

# List of Symbols

| | | |
|---|---|---|
| α | Helmholtz free energy | $J.mol^{-1}$ |
| $C_p$ | isobaric heat capacity | $J.mol^{-1}.K^{-1}$ |
| $C_v$ | isobaric heat capacity | $J.mol^{-1}.K^{-1}$ |
| $g_R$ | radial distribution function | |
| $\Delta H_{dis}$ | enthalpy of dissolution | $kJ.mol^{-1}$ |
| $\Delta S_{dis}$ | entropy of dissolution | $J.mol^{-1}.K^{-1}$ |
| $k_B$ | Boltzmann constant | $J.K^{-1}$ |
| $\xi_{ij}$ | energy binary interaction parameter | |
| $\eta_{ij}$ | size binary interaction parameter | |
| $K_T$ | isothermal compressibility | $Pa^{-1}$ |
| $K_S$ | isentropic compressibility | $Pa^{-1}$ |
| $M_w$ | molecular weight | $kg.mol^{-1}$ |
| $P$ | pressure | $Pa$ |
| $T$ | temperature | $K$ |
| $Q$ | quadrupolar moment | $C.m^{-2}$ |
| $x_i$ | molar fraction in the liquid phase | |
| $y_i$ | molar fraction in the vapor phase | |
| $m$ | chain length parameter | |
| $B$ | Free-volume overlap | |
| $\gamma$ | activity coefficient | |
| ε | dispersive energy | $J$ |
| $\sigma$ | segment diameter | $m$ |

| | | |
|---|---|---|
| $\varepsilon^{HB}$ | energy of association | $J$ |
| $k^{HB}$ | volume of association | $m^3$ |
| $\rho$ | molar density | $mol.L^{-1}$ |
| $k_{H,eff}$ | effective Henry's constants | $Pa$ |
| α | ideal selectivity | |
| Ƞ | dynamic viscosity | $mPa.s$ |
| $W$ | synaptic weights | |
| b | bias | |
| $\alpha$ | proportionality parameter of the FVT | $J.m^3.mol^{-1}.kg^{-1}$ |
| $u$ | speed of sound | $m.s^{-1}$ |

# 1

# Introduction

*In this chapter, a general introduction to the subject of this doctoral thesis is provided. The motivation behind this research is discussed, along with the main objectives and structure of the document.*

## 1.1 Motivation

The phenomenon of global warming represents a significant challenge in contemporary science, exerting profound societal impacts and driving the implementation of new legislation, regulatory frameworks, and extensive scientific research. Its far-reaching consequences extend beyond environmental degradation, influencing economic stability, public health, and global ecosystems. Global surface temperatures have reached 1.1°C above 1850-1900 levels during the period of 2011-2023 (See Figure 1.1) (*Climate Change 2023 Synthesis Report: Summary for Policymakers*, 2024).

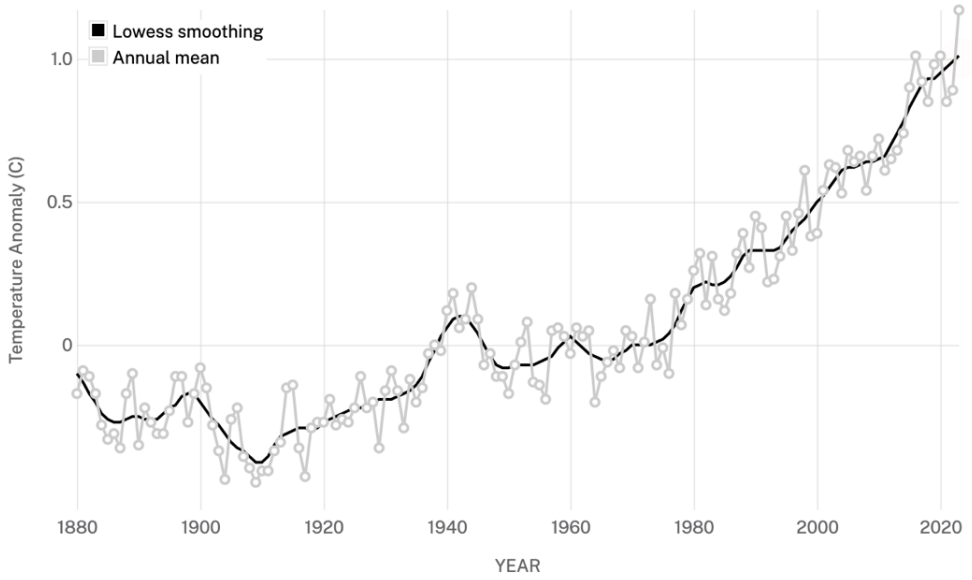


***Figure 1.1*** *Global Surface Temperature Change (1880-2023) Relative to 1951-1980 Average (NASA, 2024).*

Research indicates that the primary reason for this increase is the emission of greenhouse gases (GHGs). Historically, the most common GHGs have been carbon dioxide ($CO_2$), nitrous oxide, methane, and fluorinated gases (F-gases). Human activities have raised the atmosphere's $CO_2$ content by 50% in less than 200 years, meaning the

amount of $CO_2$ is now 150% of its value in 1750 since the onset of industrial times in the 18th century, rising from 365 parts per million (ppm) in 2002 to over 420 ppm currently (NASA, 2024). Regarding F-gases, predominantly used in refrigeration, despite their relatively low emission rates, they have extremely high global warming potentials (GWPs), often exceeding thousands of times that of $CO_2$ (Velders et al., 2022).

As temperatures rise and weather patterns become increasingly erratic, the urgency to address this phenomenon intensifies, driving innovations and collaborations across scientific disciplines. The multifaceted nature of global warming demands comprehensive strategies to mitigate its effects and ensure a sustainable future.

Among the various strategies to mitigate GHG emissions, solvent-based absorption techniques have gained significant attention due to their effectiveness in capturing and separating these harmful gases. However, traditional volatile organic solvents, particularly amine-based ones, commonly used in $CO_2$ capture, present inherent issues including toxicity, thermal instability, and degradation (Aissaoui et al., 2017; Harifi-Mood & Sarafrazi, 2023). Therefore, it seems necessary to explore and develop cost-effective, efficient, and environmentally sustainable solvents based on green chemistry principles for GHG capture.

Deep Eutectic Solvents (DESs) have emerged as a novel class of solvents mixtures that offer several advantages over traditional solvents in gas capture applications. DESs are known for their high absorption capacities, cost-effectiveness, ease of preparation and potential for non-toxicity and biodegradability. Choline chloride stands out as the most commonly used hydrogen bond acceptor in DESs, owing to its alignment with green chemistry principles, favorable properties, and affordability. The unique characteristics of DESs arise from a robust network of hydrogen bonds between their components, in a way that the strength of these bonds directly affects the transition temperature, stability

and physicochemical properties of the eutectic mixture (Hansen et al., 2021; Smith et al., 2014). Their attributes make them a sustainable alternative to conventional solvents, aligning with the global drive towards greener and more eco-friendly technologies.

For large-scale industrial application of DESs, reliable and accurate knowledge of their thermophysical properties and behavior under diverse industrial conditions is crucial. In addition, an important challenge to address is the impact of cosolvents on DESs properties. This is crucial because most DESs exhibit high viscosity at room temperature, limiting their industrial usability, and the addition of controlled amounts of cosolvents, particularly water, offers a practical solution to reduce viscosity, improving their applicability in industrial processes (Gabriele et al., 2019; Vilková et al., 2020).

Given the numerous combinations of DESs and operational environments, depending solely on experimental measurements for such analyses becomes time-consuming. Therefore, developing computational models for reliably predicting the properties of these systems and analyzing their potential applicability in capturing and separating GHGs plays a key role to quickly screen diverse options, guiding the experimental work towards the most promising systems.

Among the computational tools available, statistical mechanics-based equations of state (EoSs) offer a balanced approach, combining a simplified physical model with fast computation, making them highly attractive. The soft-SAFT EoS (as any other SAFT-based equation) is particularly favored for modelling DESs due to its explicit treatment of hydrogen bonding and short-range physical interactions, which are essential for DESs formation. Similarly, machine learning methods like Artificial Neural Networks (ANN), in conjunction with molecular-level approaches, present promising solutions for predicting the complex dynamics within DES systems, particularly when they are combined with cosolvents (Alkhatib, I. et al., 2020; Velez & Acevedo, 2022).

This thesis addresses the thermophysical modelling of different DESs systems, including their mixtures with cosolvents, and explores their application in GHGs capture and separation. By integrating advanced techniques such as the soft-SAFT EoS and molecular-based ANNs, this study introduces novel modelling approaches and parameterization methodologies aimed at enhancing the predictive and extrapolative capabilities of current models, while maintaining or improving overall accuracy.

## 1.2 General and Specific Objectives

This Ph.D. thesis' overall purpose is to ***comprehensively investigate the physicochemical behavior of Deep Eutectic Solvents (DESs), mostly focused on Choline Chloride-based systems, using different computational tools, with a particular interest on analyzing their potential applications in greenhouse gases (GHGs) capture and separation processes***. This includes addressing its main thermophysical properties of pure and aqueous DESs, and studying particular industrial challenges, related to the recovery of commercial refrigerant high global warming potential (GWP) hydrofluorocarbon (HFC) mixtures, as well as the carbon dioxide ($CO_2$) capture and separation from ammonia ($NH_3$), originated during the melamine production. This research framework encompasses atomic-level analysis using COSMO-SAC combined with machine learning techniques, and mesoscale investigation utilizing the soft-SAFT Equation of State (EoS). Specific objectives include:

- Developing two types of soft-SAFT models for Choline-Chloride based DESs: one treating the DESs as a single compound, and another one modeling each entity independently.
- Modelling the density of pure and aqueous DESs as a function of temperature and pressure, considering both previous approaches.
- Modelling the derivative properties for pure DESs, including speed of sound and the isentropic compressibility coefficient, using the individual component approach.
- Describing the vapor-liquid equilibria and water activity coefficients of aqueous DES, treating them as ternary mixtures.
- Modeling the viscosity of pure DES and their mixtures with cosolvents using the Free Volume Theory coupled in soft-SAFT.
- Developing an Artificial Neural Network (ANN) using the charge distribution profiles of DESs compounds, generated with COSMO-SAC, as molecular descriptors to predict the viscosity of DESs and their mixtures with cosolvents.
- Investigating the impact of molecular descriptors as ANN inputs on the viscosity of DESs
- Validating the reliability of the developed ANN model by analyzing statistical parameters, assessing its applicability domain, and evaluating its predictive capability.
- Developing a transferable soft-SAFT model to calculate the solubility of HFCs, $CO_2$ and $NH_3$ in DESs, encompassing the determination of enthalpy and entropy of dissolution, Henry's constants, and the ideal selectivity of the DES in specific GHG blends.

- Predicting the competitive selectivity between gases in multi-component mixtures based on GHG blends and DESs, proposing a list of best candidates for practical operation.

## 1.3 Thesis Outline

Following this general introduction chapter, which presents the motivation behind this work and establishes the basis of this Ph.D. thesis, *Chapter 2* guides the reader through recent advancements and research in deep eutectic solvents (DESs) and their applications, particularly in separation and gas capture processes. This chapter begins with the fundamentals of DESs, highlighting their unique properties, with a focus on choline chloride ([Ch]Cl)-based DESs and the impact of cosolvents on their performance. Since this doctoral thesis is centered on the application of DESs in gas capture, this chapter also presents various applications of DESs in this field, emphasizing their use in absorbing gases such as $CO_2$, fluorinated gases (F-gases), and ammonia ($NH_3$). Additionally, the chapter discusses the modeling tools used to study DESs, with particular attention on the soft-SAFT equation of state and artificial neural networks.

*Chapter 3* is devoted to describe the details of the different computations tools used along the thesis, ordered by the degree of scale approximation (quantum-molecular, coarse-grained or macroscale). First, a general overview of the COSMO-SAC theoretical background is provided, along with its practical implementation used in this thesis. Next, the physical background for the SAFT Equation of State (EoS) is explained, including the specific variant used in this thesis, the soft-SAFT EoS, which is derived from the original SAFT. Additionally, the chapter explores the theoretical background of the Free Volume

Theory, providing insights into its conceptual framework and applications. The final section includes a comprehensive overview of artificial neural networks, detailing their structure and the processes involved in their learning algorithms.

*Chapter 4* is the first chapter of the results, where the impact of cosolvents in the key thermophysical properties of the [Ch]Cl-based DESs is analyzed. Using the soft-SAFT Equation of State, a robust coarse-grained molecular model is developed through accurate and transferable parametrization. The Free-Volume Theory (FVT), coupled into soft-SAFT, is employed to address the viscosity of these systems through the Spider-Web optimization approach. Furthermore, to enhance the study of DESs and overcome some of the limitations of FVT, an Artificial Neural Network framework is introduced to predict the viscosity in DESs and their mixtures, leveraging molecular parameters derived from COSMO-SAC.

The second chapter of the results, *Chapter 5*, investigates the selective recovery of Greenhouse Gases (GHGs) using DESs. The investigation encompasses two primary areas: the separation of commercial refrigerant blends and the recovery of ammonia from a mixture containing carbon dioxide from melamine streams. Here, using the soft-SAFT EoS, the solubility of a range of GHGs in DESs is examined, which includes determining enthalpy and entropy of dissolution, Henry's constants, as well as ideal selectivity of the DES in GHG blends. Additionally, the chapter explores the prediction of the competitive selectivity among gases in multi-component mixtures involving GHG blends and DESs, providing a selection of the most suitable DESs to carry out the recovery/separation process.

The concluding chapter summarizes the most significant conclusions discussed in the preceding chapters and explores potential future directions for this research.

# 2

# State of the Art

*The purpose of this chapter is to guide the reader through recent advancements and research in DESs and their applications, particularly in separation and gas capture processes. It begins with the fundamentals of DESs, highlighting their unique properties, with a focus on [Ch]Cl-based DESs and the impact of cosolvents. The chapter then explores the applications of DESs in gas separation and capture, particularly $CO_2$, F-gases, and $NH_3$ absorption. Finally, it discusses modelling tools used to study DESs, emphasizing the use of SAFT-based equations of state and Machine Learning approach.*

## 2.1 Deep Eutectic Solvents (DESs)

### 2.1.1 Fundamentals of DESs

First reported in 2003 by Abbott et al. (2003), Deep Eutectic Solvents (DESs) are considered an emerging class of promising solvents (Chen & Mu, 2021; Hansen et al., 2021; Paiva et al., 2014; Santana-Mayor et al., 2021). They are eutectic mixtures composed of two or more components, which have significant depressions in melting points compared to those of the neat constituent components (Smith et al., 2014; Zhang et al., 2012). In the solid/liquid equilibria (SLE) diagram of those systems, the eutectic point represents the minimum melting temperature along the two intersecting melting curves (Gamsjäger et al., 2008). A schematic representation of the resulting SLE diagram for a eutectic mixture is shown in Figure 2.1.

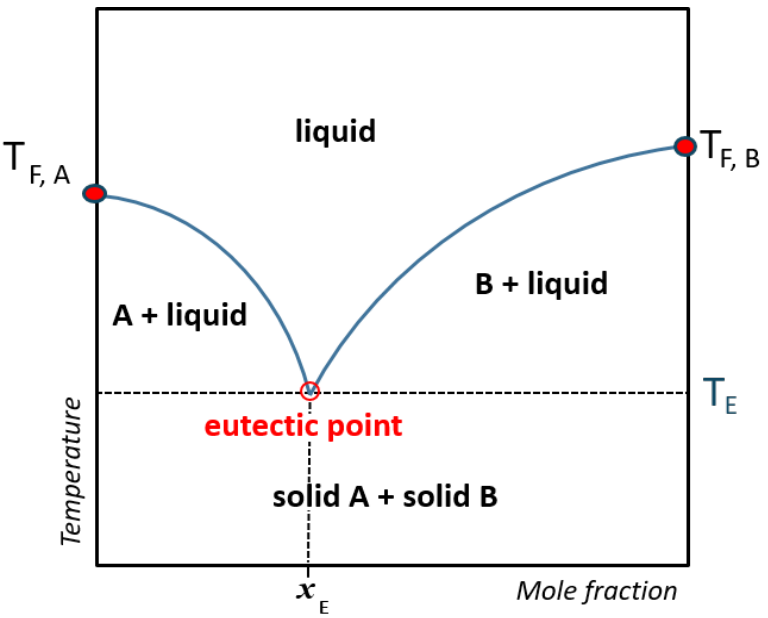


***Figure 2.1.*** *Schematic phase diagram of the melting temperatures for a eutectic mixture formed by two components (A and B). Notation: T for temperature and x for mole fraction; sub-index E means equilibrium and F means freezing.*

However, the existence of a eutectic point on a mixture is not enough to define a DES, since all mixtures of compounds that are completely or partly immiscible in the solid phase present a eutectic point (Martins et al., 2019). Thus, to be characterized as a DES, the mixture of pure compounds must have a eutectic point temperature below of an ideal liquid mixture (Florindo et al., 2019; Martins et al., 2019). This can be observed by analyzing Eq. 1.1, which was proposed by Rowlinson (1970), to describe melting curves (assuming pure solid phase and neglecting the temperature influence on the heat capacities):

$$\ln(x_i\gamma_i) = \frac{\Delta_{\mathrm{m}}H}{R}\left(\frac{1}{T_{\mathrm{m}}} - \frac{1}{T}\right) + \frac{\Delta_{\mathrm{m}}C_{\mathrm{p}}}{R}\left(\frac{T_{\mathrm{m}}}{T} - ln\frac{T_{\mathrm{m}}}{T} - 1\right) \quad , \qquad (1.1)$$

where $x_i$ is a liquid mole fraction composition and $\gamma_i$ is the activity coefficient of compound $i$, $\Delta_{\mathrm{m}}H$ is the melting enthalpy of the pure compound, $\Delta_{\mathrm{m}}C_{\mathrm{p}}$ is the difference between the molar heat capacity of compound $i$ in the liquid and solid phases, $T_{\mathrm{m}}$ is the melting temperature, T is the absolute temperature and R is the universal gas constant. Particularly, when the equilibrium temperature is not far from the melting temperature of the pure compound, the last term of the Eq. 1.1 has an insignificant value when compared to melting enthalpy term and so, can be neglected (Alhadid et al., 2019; Coutinho et al., 1995; Martins et al., 2019):

$$\ln(x_i\gamma_i) = \frac{\Delta_{\mathrm{m}}H}{R}\left(\frac{1}{T_{\mathrm{m}}} - \frac{1}{T}\right) \qquad (1.2)$$

In this case, when considering an ideal mixture ($\gamma_i = 1$), the SLE is dominated by the melting enthalpy and melting temperature of each compound, as can be seen in Eq. 1.2. Thus, the freezing point depression for an ideal eutectic mixture is the result of the intersection of two melting curves that are governed by the fusion properties of the pure components (Martins et al., 2019). In the case of a real mixture, the DESs present significant negative deviations from ideality ($\Delta T > 0$), whose freezing point depression is mainly ruled by the forces of interactions between the components of the mixture (Florindo et al., 2019; Martins et al., 2019). Consequently, strong interactions between DESs components lead to a lower freezing point (Harris, 2009). This phenomenon is illustrated in the SLE diagram of a deep eutectic mixture shown in Figure 2.2, where the composition range considered a DES lies between $x_1$ and $x_2$.

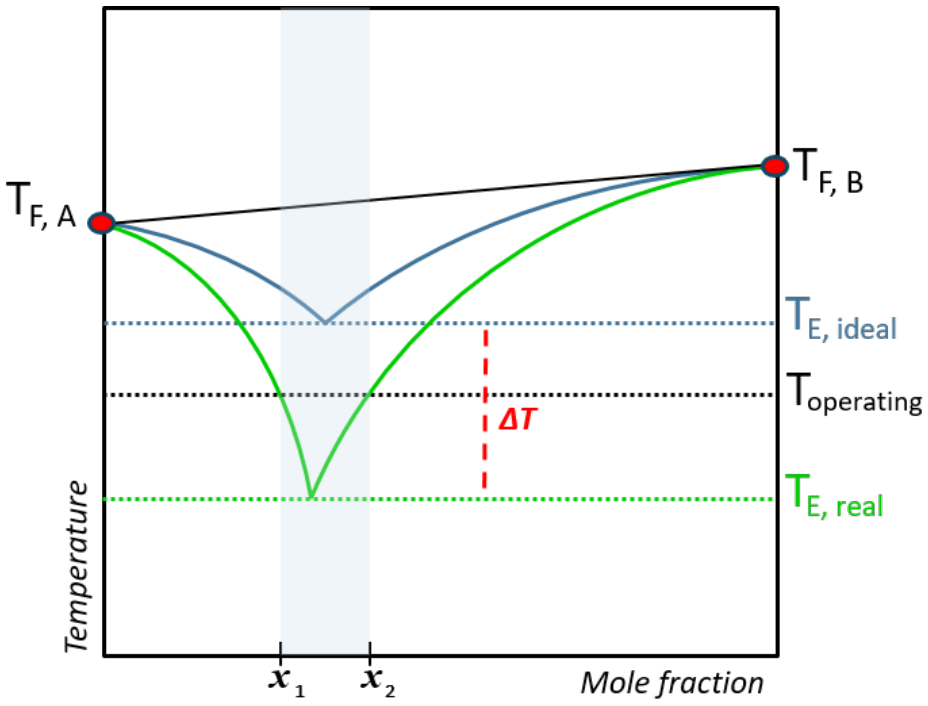


***Figure 2.2.*** *Schematic representation of the comparison of the SLE of an ideal eutectic mixture (blue line) and a deep eutectic mixture (green line) by two components (A and B). Notation: T for temperature and x for mole fraction; sub-index E means equilibrium, f means freezing and ΔT is the difference between the $T_{E,\,real}$ and the $T_{E,\,ideal}$ of the eutectic point.*

The driving force behind the formation of DESs is the origin of a strong and complex network of hydrogen bonds between the compounds, where one acts as a hydrogen bond donor (HBD) and the other as a hydrogen bond acceptor (HBA) at certain defined stoichiometric proportions, as illustrated in Figure 2.2 (Smith et al., 2014; Yu et al., 2022; Zhang et al., 2012). In addition, van der Waals interactions or even occasional electrostatic forces are also present in these mixtures (Mbous et al., 2017; Santana-Mayor et al., 2021). The molar ratios where the system is considered a DES are those where the mixture is in the liquid state at the operating temperature of the system or process (Martins et al., 2019).

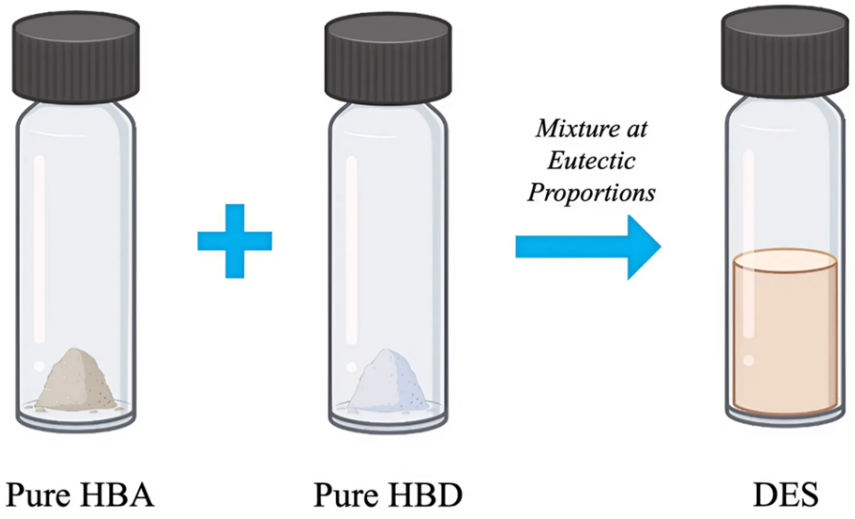


***Figure 2.3**. Illustration of deep eutectic system preparation, adapted from Sarmento et al. (2024).*

DESs can be generally described by the general formula (Smith et al., 2014):

$$Cat^{+}X^{-}zY. \quad , \qquad (1.3)$$

where $Cat^{+}$ is any cation, and X is a Lewis base, generally a halide anion. The complex anionic species are formed between $X^{-}$ and either a Lewis or Brønsted acid Y (z refers to

the number of Y molecules that interact with the anion). DESs are classified based on the nature of the complexing agent used, as shown in Table 2.1.

***Table 2.1****.Classification and general formula for DESs, from* Smith et al. (2014).

| Type | General Formula | Terms |
|---|---|---|
| Type I | $Cat^+X^-zMCl_x$ | M = Zn, Sn, Fe, Al, Ga, In |
| Type II | $Cat^+X^-zMCl_x.yH_2O$ | M = Cr, Co, Cu, Ni, Fe |
| Type III | $Cat^+X^-zRZ$ | Z = $CONH_2$, COOH, OH |
| Type IV | $MCl_x + RZ = MCl_{x-1}^+.RZ + MCl_{x+1}^-$ | M = Al, Zn and Z = $CONH_2$, OH |

From these four groups, the most studied correspond to Type III DESs due to their ability to solvate a wide range of components. In general, various components can acts HBD or HBA in the formation of DESs. Typically, HBAs include quaternary ammonium salts and metal salts; and HBDs include polyalcohols, polyacids, and polyamines (de Andrade et al., 2022; Smith et al., 2014; Wang, Jiake et al., 2021). Figure 2.4 summarizes typical combinations of HBAs and HBDs used in the formation of DESs commonly reported in the literature (Florindo et al., 2019; Hansen et al., 2021; Smith et al., 2014).

The physical and chemical properties of DESs depend on their individual constituents and HBD:HBA ratio, since the vast hydrogen bond network directly affects the characteristics of these mixtures (Mbous et al., 2017; Rodríguez et al., 2015; Santana-Mayor et al., 2021). However, in general, these eutectic mixtures are characterized by simple preparation, low volatilization at high temperature, low flammability, selectivity, strong and dissolving ability (Mbous et al., 2017; Santana-Mayor et al., 2021; Tomé et al., 2018; Zhao et al., 2020). Additionally, DESs offer chemical tunability, enabling tailored designs for specific applications through adjustments in the molar ratio and types of HBAs and HBDs. This versatility makes them an attractive alternative for a wide range of applications, including material synthesis (Carriazo et al., 2012; Hu et al., 2018; Pavlić

et al., 2022; Pereira & Andrade, 2017; Valente et al., 2023; Vladić et al., 2023b; Vladić et al., 2023c), separation processes (Marcus, 2018; Sarmad et al., 2017; Zhang et al., 2020; Zhang et al., 2018), nanotechnology (Abo-Hamad et al., 2015; Xu et al., 2016), biotechnology (Gotor-Fernández & Paul, 2019; Li et al., 2016), and pharmaceutical processing (Emami & Shayanfar, 2020; Sarmento et al., 2024; Vladić et al., 2023a; Vladić et al., 2024), food industry (Gavarić et al., 2023), among others.

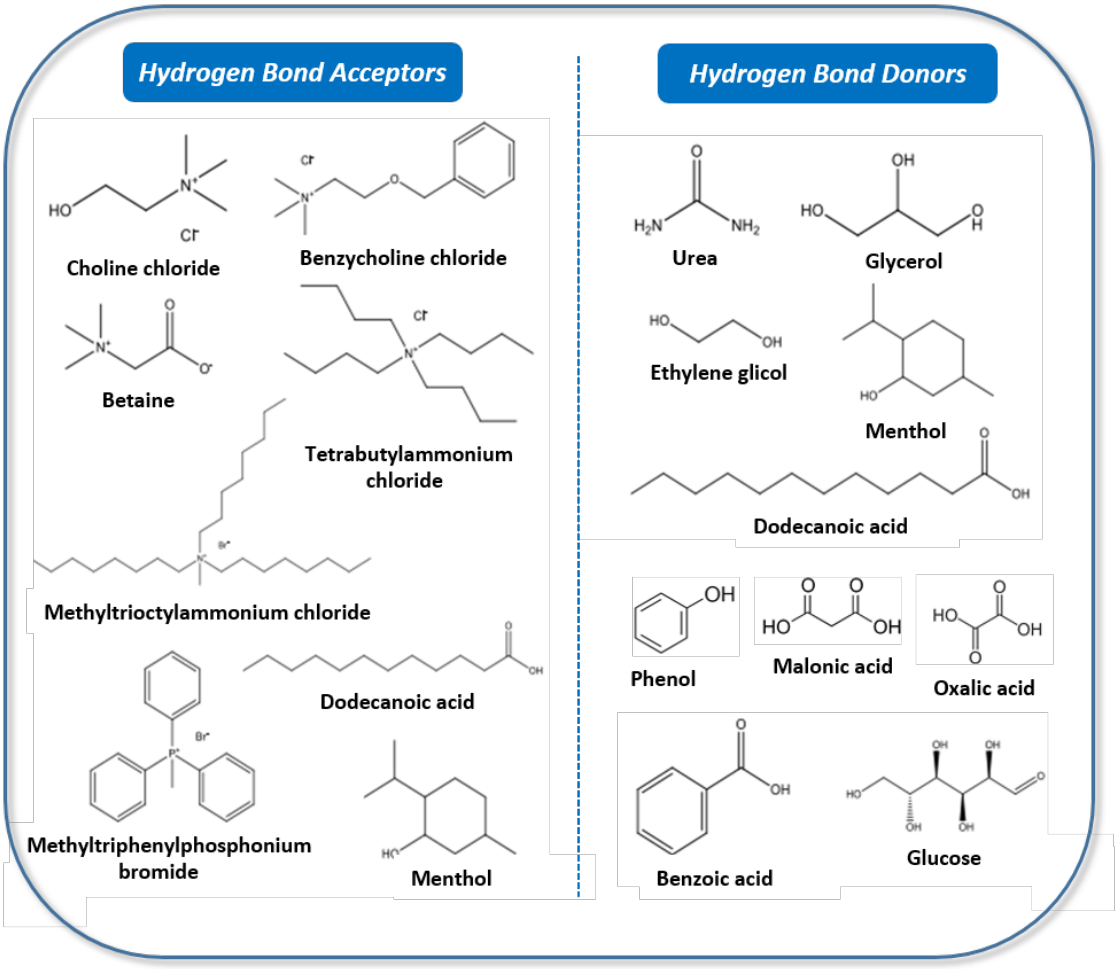


***Figure 2.4.*** *Chemical structures of HBDs and HBAs often used in DES preparation.*

### 2.1.2 Choline Chloride-Based DESs

The quaternary ammonium salt choline chloride ([Ch]Cl) is the most widely used HBA to prepare DESs, due to its low cost, non-toxicity, biodegradability, biocompatibility and economic synthesis (Martins et al., 2019; Smith et al., 2014; Yadav et al., 2014). Originating as an essential nutrient, choline chloride can be derived from biomass sources and is recognized within the B-complex vitamin group (Yates et al., 1998), or alternatively synthesized from fossil reserves (Ferreira & Sarraguça, 2024).

The [Ch]Cl-urea mixture was one of the first studied DES and has become one of the prototypical examples of this class of solvents. While both components have high melting points ([Ch]Cl = 302 ºC and Urea = 133 ºC), the eutectic mixture of [Ch]Cl:urea at a 1:2 molar ratio has reported 12 ºC of melting point and has unusual solvent properties (Abbott et al., 2003). Since then, DESs based on [Ch]Cl have been proposed as green solvents for a wide range of applications, such as metal extraction (Abbott et al., 2004), phenolic compound extraction from bio-based sources (Alam et al., 2021; Pavlić et al., 2022), polymer synthesis (Carriazo et al., 2012) and the formation of metal-organic frameworks (MOFs) (Hu et al., 2018). Additionally, these DESs hold promise for greenhouse gas capture, as discussed further in subsequent sections.

One of the reasons [Ch]Cl is a preferred component in DESs is due to its well-known non-toxic properties. Research has shown that DESs containing [Ch]Cl are significantly less toxic than many conventional solvents. For example, studies have demonstrated that microorganisms such as Escherichia coli can grow in [Ch]Cl-based DESs, while they do not survive n more aggressive chemical environments (Alam et al., 2023). Moreover, [Ch]Cl-based DESs have been tested on aquatic invertebrates like Hydra sinensis and found to be non-toxic (Juneidi et al., 2016). These DESs also exhibit

high biodegradability, with various formulations, including those with urea, showing efficient breakdown in environmental conditions (Juneidi et al., 2015; Radošević et al., 2015; Wen et al., 2015; Xu et al., 2017). Additionally, [Ch]Cl-based DESs exhibit high long-term thermal stability and lower toxicity to bacteria (Marchel et al., 2022). This combination of low toxicity and high biodegradability positions [Ch]Cl-based DESs as environmentally friendly alternatives for a wide range of applications.

Another reason behind [Ch]Cl being such a useful quaternary ammonium salt is related to the fact it is an asymmetric quaternary ammonium salt with a polar functional group, where the asymmetric nature of this molecule reduces the freezing point of the ionic molecular liquid, as does the polar functional group (Harris, 2009).

Thus, when mixing [Ch]Cl with most hydrogen bond donors (see Figure 2.5), the self-association between the HBD and HBA significantly modifies the physical properties of the formed DES (by respect of the independent single compounds) becoming more attractive for industrial applications. In particular, DESs based in [Ch]Cl have been of interest due to their ability to solvate a wide range of transition metal species, including chlorides and oxides (Smith et al., 2014). Furthermore, compared to other quaternary ammonium salts, DES formed by [Ch]Cl and hydrogen bond donors showed lower viscosities and higher conductivities (Harris, 2009).

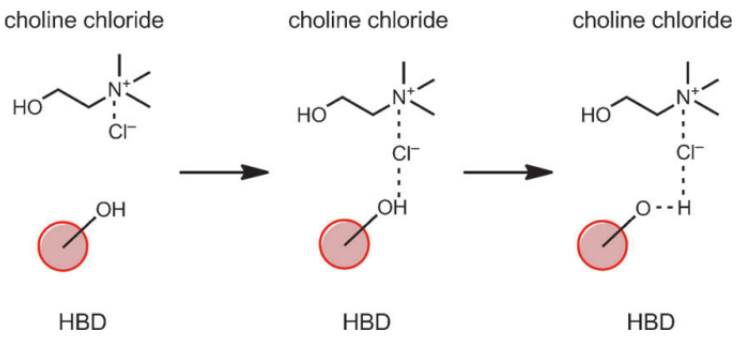


***Figure 2.5.*** *Mechanism of interaction of a HBD with the quaternary ammonium salt choline chloride. Image taken from Francisco et al. (2013a).*

### 2.1.3 Effect of Cosolvents on DESs

Cosolvents play a crucial role in modifying the properties of DESs, offering a versatile approach to tailor their characteristics for specific applications. By incorporating cosolvents like water and alcohols into DES formulations, their physicochemical attributes can be adjusted, enhancing their utility across various industries (El Achkar et al., 2019; Gabriele et al., 2019; Li et al., 2022; Ma, C. et al., 2018; Shah & Mjalli, 2014).

Water, in particular, manifests robust interactions with the hygroscopic constituents of DESs, as it can act both as HBA and HBD due to its high polarity (El Achkar et al., 2019; Hammond et al., 2017; Ma, C. et al., 2018; Vilková et al., 2020). When a small amount of water is added to a DES, the molecules of water mix with DES with evidence of a strong interaction without forming water clusters. Further addition of water provides the ion dissociation of the DES components, which are gradually hydrated. When the water content becomes very high, the DES structures are completely dissociated in ions. In this case, depending on the size of the ions of the DES, some of them are fully hydrated, while some are partially hydrated. Moreover, a high excess of water can lead to the complete disruption of the DES supramolecular structure (Gabriele et al., 2019; Ma, C. et al., 2018; Shah & Mjalli, 2014). Despite the common belief that high dilution disrupts the hydrogen bond network completely, some studies indicate that DES systems can retain certain properties even with significant water dilution (>50% water). Furthermore, in some systems, solvated DESs clusters may exist instead of discrete water molecules. Thus, water can either strengthen hydrogen bonds or facilitate the formation of solvated DESs clusters (Altamash et al., 2017; Aroso et al., 2017; Sarmento et al., 2024). The general schematic mechanism of the effect of increasing water content for a typical DES/water mixture is shown in Figure 2.6.

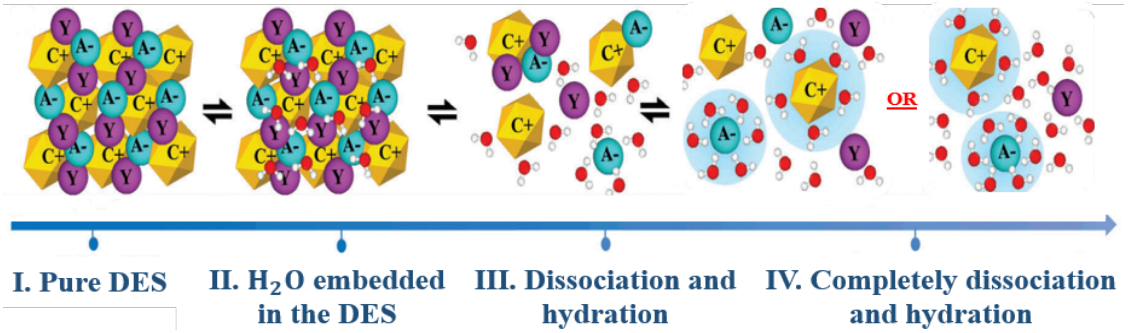


***Figure 2.6.*** *The general schematic mechanism for a typical DES/water system with increasing water content. Note: the yellow (C+), blue (A-), purple (Y), and red ones represent cation, anion, HBD, and water, respectively. Image adapted from Ma, C. et al. (2018).*

The physicochemical properties of a DES/cosolvent system are a macroscopic manifestation of the microscopic interactions between them (Ma, C. et al., 2018). Thereby, the gradual changes of the DES supramolecular structure during dilution probably affect the thermodynamic properties of these eutectic mixtures, which can then be tailored by controlling the amount of added cosolvent (Gabriele et al., 2019; Ma, C. et al., 2018; Shah & Mjalli, 2014; Vilková et al., 2020; Yadav et al., 2014). For example, the addition of water (or any other cosolvent) to the DES can tailor its polarity to favor the extraction of polar over weakly polar compounds in specific applications (Dai et al., 2014; Dai et al., 2015; Farooq et al., 2020; Vilková et al., 2020) or modify the polarity of reaction media (Harifi-Mood & Sadrzadeh, 2018)

The effect of cosolvents on the thermodynamic properties such as density and viscosity of DESs has been reported in the literature, including DESs based in [Ch]Cl (Florindo et al., 2014; Wang et al., 2020; Yadav et al., 2015; Yadav & Pandey, 2014; Yadav et al., 2014). The presence of cosolvents weakens the hydrogen bonding network between DESs molecules, resulting in the decrease of the density and viscosity of these eutectic mixtures (Gabriele et al., 2019; Ma, C. et al., 2018; Shah & Mjalli, 2014; Vilková et al., 2020).

In general, the impact of the addition of a cosolvent in density is not very severe, as most DESs exhibit densities only slightly higher than water (El Achkar et al., 2019; Li et al., 2022). However, in terms of viscosity, most pure DESs have high viscosities at room temperature, mainly due to the hydrogen bond network between their molecules (El Achkar et al., 2019). These high viscosities may hinder their practical applications for different industrial processes (Gabriele et al., 2019; Li et al., 2022). Consequently, the use of water or alcohols, for example, with DESs as a cosolvent, may lead to a good alternative to overcome this obstacle, since the viscosity decreases significantly when a cosolvent is added to the system (El Achkar et al., 2019; Gabriele et al., 2019; Li et al., 2022; Ma, C. et al., 2018; Shah & Mjalli, 2014).

To mention some examples of interest, Yadav and Pandey (2014) showed that a mere 2.25% weight of water added to [Ch]Cl: Urea (1:2) DES induced a significant 33.27% viscosity reduction (from 1003.94 to 669.90 mPa·s at 293.15K and 0.1MPa). Additionally, Aravena et al. (2022) showed that the addition of 20% weight of water on the [Ch]Cl + Urea DES produces a significant increase of the surface tension and decrease of density and viscosity, resulting in a $CO_2$ absorption improvement and converting this DES in a potential alternative to conventional alkanolamine absorbents for use in carbon capture. Similarly, Xie et al. (2014) demonstrated that the addition of water to [Ch]Cl + Urea diminishes its viscosity, once again facilitating its application in $CO_2$ separation processes (Ma, Chunyan et al., 2018).

Moreover, Zhang et al. (2022) observed that adding 70 wt% water to [Ch]Cl:Monoethanolamine(MEA) DES (1:6) decreased viscosity to 6% of pure DES, significantly improving $CO_2$ absorption. Zhang et al. (2023) improved $CO_2$ solubility in [Ch]Cl: Diethylenetriamine (1:5) DES with 25 wt% water, which also reduced the

viscosity of the DES. Dai et al. (2015) and Vilková et al. (2020) also noted viscosity reductions with water addition in DESs, enhancing extraction efficiency.

Beyond water, methanol and ethanol have been effective cosolvents in reducing DES viscosity. Wang et al. (2020) explored the impact of methanol addition to [Ch]Cl-based DESs containing glycerol and ethylene glycol, while Haghbakhsh et al. (2021a) investigated the effects of ethanol on viscosity in [Ch]Cl : Ethylene glycol (1:2) DES. Both studies demonstrate that increasing alcohol concentrations can dramatically change the viscosities of the DESs mixture. For instance, adding just 3.18% weight of methanol in [Ch]Cl: Glycerol (1:2) DES can induce a significant 41.42% viscosity reduction (from 516.05 to 302.30 mPa·s at 292.15K and 0.1MPa) (Wang et al., 2020).

Thus, it is evident that cosolvents like water or alcohols can significantly influence the properties of DESs, primarily by reducing their viscosity. This reduction is highly beneficial for enhancing its suitability, while preserving the structure of DESs. Therefore, incorporating an environmentally friendly and adequate cosolvent in controlled amounts can be a simple and practical way to modify and improve the properties of DESs for specific applications (El Achkar et al., 2019; Gabriele et al., 2019; Li et al., 2022; Ma, C. et al., 2018; Shah & Mjalli, 2014).

## 2.2 Applications of DESs in Separation and Gas Capture

The exploration and application of DESs in various fields have garnered significant attention due to their unique properties. Among the most promising areas of DESs utilization are separation processes and gas capture technologies. These solvents enable the selective extraction and separation of diverse compounds, offering a sustainable and efficient alternative to traditional solvents. Moreover, the ability of DESs

to facilitate gas capture, particularly $CO_2$ and other greenhouse gases, highlights their potential in addressing environmental challenges and contributing to cleaner industrial processes. This section investigates the innovative applications of DESs, including [Ch]Cl-based DESs and other variants, in capture of $CO_2$, F-gases and $NH_3$, showing their effectiveness and versatility in this important field. The DESs discussed in the subsequent subsections are summarized in Table 2.2, detailing the gases they have been applied to capture and the references of the work, with further details provided in the sections below.

***Table 2.2.*** *Summary of the DESs applied as gas absorbents detailed in this section.*

| DES | Gas absorbed | References |
|---|---|---|
| [Ch]Cl : UR (1:2) | $CO_2$ | (García et al., 2015; Li et al., 2008) |
| [Ch]Cl : LA (1:2) | $CO_2$ | (Francisco et al., 2013b) |
| [Ch]Cl: MEA (1:8) | $CO_2$ | (Adeyemi et al., 2017b) |
| [Ch]Cl : GC (1:3, 1:4, 1:5) | $CO_2$ | (Liu et al., 2017) |
| [Ch]Cl : MEA (1:6, 1:8, 1:10) | $CO_2$ | (Adeyemi et al., 2017a) |
| [Ch]Cl : MEA (1:5) | $CO_2$ | (Li et al., 2019) |
| [Ch]Cl : LevA (1:2, 1:3) | $CO_2$ | (Aboshatta & Magueijo, 2021) |
| [Ch]Cl : DETA:$H_20$ (1:5:2) | $CO_2$ | (Zhang et al., 2023) |
| TMAC : MEA (1:5) | $CO_2$ | (Li et al., 2019) |
| DH : GC (1:3, 1:4, 1:5) | $CO_2$ | (Liu et al., 2017) |
| TBD : EG (1:1, 1:4) | $CO_2$ | (García-Argüelles et al., 2017) |
| DBU : EG (1:1, 1:4) | $CO_2$ | (García-Argüelles et al., 2017) |
| DBN : EU (1:2) | $CO_2$ | (Jiang, B. et al., 2019) |
| [Ch]Cl : EG (1:3) | F-gases (R-32, R-125, R-143a, R-134a) | (Codera et al., 2023) |
| [Ch]Cl : GL (1:3) + 10wt% $H_2O$ | F-gases (R-32, R-125, R-143a, R-134a) | (Codera et al., 2023) |
| $[N_{4444}][C_4F_9SO_3]$ : $C_4F_9CO_2H$ | F-gases (R-32, R-125, R-134a) | (Castro et al., 2020) |
| [Ch]Cl : Xylose (1:1, 1.5:1, 2:1) | $NH_3$ | (Li et al., 2020) |
| [Ch]Cl : Ribose (1.5:1) | $NH_3$ | (Li et al., 2020) |
| [Ch]Cl : Frutose (1.5:1) | $NH_3$ | (Li et al., 2020) |
| EaCl : GL (1:2) | $NH_3$ | (Jiang, W.-J. et al., 2019) |
| [ImH]Cl : GL (1:2) | $NH_3$ | (Ma et al., 2021) |
| LiCl : EG (1:3) | $NH_3$ | (Li et al., 2021) |

### 2.2.1 $CO_2$ Capture using DESs

Managing $CO_2$ emissions is crucial for environmental sustainability. Chemical absorption, primarily using amine-based methods, has been a leading technology for $CO_2$ capture for over 70 years (García et al., 2015). Despite its widespread use, this technology faces significant challenges, including solvent degradation, high costs, and substantial corrosion rates. Addressing these limitations, DESs have been seen as a promising alternative for $CO_2$ capture, with extensive focus on their $CO_2$ solubility in the literature (García et al., 2015; Oke, 2024; Warrag et al., 2017; Zhang et al., 2018; Zhang, Y. et al., 2024).

Beginning with [Ch]Cl-based DESs, Li et al. (2008) investigated the solubility of $CO_2$ in these DESs, formed with urea at various proportions, pressures, and temperatures, revealing a significant influence of the [Ch]Cl : urea (UR) molar ratio on $CO_2$ solubility. Notably, the DES composed of [Ch]Cl : UR (1:2) displayed outstanding performance, with a measured $CO_2$ uptake of 3.559 mol $kg^{-1}$ at 303.15 K and 60 bar (García et al., 2015). Francisco et al. (2013b) also employed [Ch]Cl-based DESs, coupled with lactic acid (LA) in a 1:2 ratio, which revealed similar trends in phase behavior compared with other choline-based solvents. Adeyemi et al. (2017b) demonstrated that [Ch]Cl : Monoethanolamine (MEA) DES (1:8) has 265% higher $CO_2$ solubility than 30 wt% MEA solution.

Investigations by Liu et al. (2017) and Adeyemi et al. (2017a) highlighted the impact of molar ratios on $CO_2$ solubility in various amine-based DESs, showing that higher ratios, such as 1:3 to 1:5 for [Ch]Cl : Guaiacol (GC) DES and diethylamine hydrochloride (DH) : GC DES, or 1:6 to 1:10 for [Ch]Cl : MEA DES, enhanced $CO_2$ absorption. Li et al. (2019) also explored different amine-based DESs for $CO_2$ absorption,

using ammonium-based salts as HBAs and a variety of amines as HBDs. They observed that the molar ratio of [Ch]Cl-based DESs significantly affected $CO_2$ solubility, with [Ch]Cl and tetramethylammonium chloride (TMAC) showing similar performance due to their similar chemical structures. Further investigations noticed that the addition of inorganic salts altered $CO_2$ absorption capacity of the DESs, with $NiCl_2$, $FeCl_3$, $CoCl_2$ showing minimal impact and $ZnCl_2$, LiCl, or $NH_4Cl$ enhancing absorption.

Aboshatta and Magueijo (2021) explored [Ch]Cl : levulinic acid (LevA) DESs for $CO_2$ absorption, highlighting their temperature and pressure-dependent absorption capacities. They demonstrated excellent recyclability, maintaining stable performance over five consecutive cycles of $CO_2$ absorption at 298 K and desorption at 353 K, with a moderate selectivity favoring $CO_2$ over $N_2$. Zhang et al. (2023) employed a novel DES based on [Ch]Cl : diethylenetriamine (DETA) : $H_20$ (1:5:2) with high $CO_2$ absorption capacity, up to 0.250 $gCO_2/gDES$, employing a rotor-stator reactor for enhanced $CO_2$ absorption efficiency and mass transfer.

Using other variants of DESs, additional contributions by García-Argüelles et al. (2017) and Jiang, B. et al. (2019) explored DESs based on superbases (compounds with a high protonic affinity) for $CO_2$ absorption. García-Argüelles et al. (2017) found that DESs composed of 1,5,7-triazabicyclo[4.4.0]-dec-5-ene (TBD) and ethylene glycol (EG) exhibited superior performance compared to those based on 1,8-diazabicyclo[5.4.0]undec-7-ene (DBU). Jiang, B. et al. (2019) discovered that 1,5-diazabicyclo[4.3.0]-non-5-ene (DBN) : 2-imidazolidone (EU) (1:2) DES showed improved $CO_2$ absorption with decreased DBN ratios, highlighting the significance of choosing a right proportion.

Fu et al. (2021) proposed a novel $CO_2$ absorption mechanism, emphasizing the role of superbases based-DES ionicity and viscosity, where system was further refined to

enhance $CO_2$ absorption by increasing the HBA to HBD ratio, improving ionicity and reducing DESs viscosity. For instance, a recent finding by Qin et al. (2024) revealed a strong correlation between DESs basicity/acidity and $CO_2$ capture efficiency, suggesting that as the basicity/acidity of DESs increases, so does its efficiency in $CO_2$ solubility, providing valuable insights into enhancing $CO_2$ capture processes.

### 2.2.2 Fluorinated Refrigerants Gas Absorption in DESs

Fluorinated gases (F-gases), predominantly used in refrigeration, have extremely high global warming potentials (GWPs), often exceeding thousands of times that of $CO_2$, despite their relatively low emission rates (Velders et al., 2022). These gases are present in mixtures within refrigeration equipment, and they need to be recovered separately to enable the reuse of those with lower GWP (Castro et al., 2021; Sheldon & Crimmin, 2022) . Among techniques involved in the recovery of F-gases, absorption into ionic liquids (ILs) and deep eutectic solvents (DESs) has raised as a promising alternative. The application of ILs to the absorption process is widely spread on literature (Asensio-Delgado et al., 2021; Han & Row, 2010; Lei et al., 2014; Vega et al., 2010), while DESs have been studied in a more limited way, with an important increase over the past years (Castro et al., 2020; Codera et al., 2023; Demirbek et al., 2024; Jovell et al., 2020).

For the case of F-gases, the addition of fluorine atoms to either the HBA or HBD is believed to significantly enhance the solubility capacity of DESs. This inference is based on previous research on fluorinated ionic liquids (FILs), which have shown to present three nano-segregated domains (fluorinated, nonpolar, and polar), providing unique properties and increasing solubility power, with promising results for F-gas solubility (Lepre et al., 2019a; Lepre et al., 2019b; Shiflett & Yokozeki, 2008). In that

direction, Castro et al. (2020) employed DESs derived from FILs and combined with perfluorinated acids, such as $[N_{4444}][C_4F_9SO_3]$ : $C_4F_9CO_2H$. These fluorinated DESs were used to study the absorption of three common F-gases used in refrigeration (R-32, R-125, and R-134a) at temperatures between 303.15 and 323.15 K and pressures up to 1 MPa. The results indicated that R-134a exhibited the highest solubility across all tested DES combinations, with R-134a and R-125 in fluorinated DESs showing similar solubility to that observed in FILs. The results showed that it was possible to achieve elevated solubility at low-pressure conditions. However, the choice of cation-anion pairing in the salt and fluorinated acid, as well as their relative proportions, exerted a considerable influence on the final capacity of each solvent. This factor played a pivotal role in determining the most appropriate DESs for specific separation scenarios. Additionally, Demirbek et al. (2024) employed a soft-SAFT Equation of State to model these compounds and estimate selectivity. Their predictions affirmed that while these DESs show high solubility for F-gases, they do not effectively differentiate between gases.

Concerning the use of [Ch]Cl non-fluorinated DESs, Codera et al. (2023) studied the solubility of refrigerants 1,1,1,2-tetrafluoroethane (R-134a), difluoromethane (R-32), pentafluoroethane (R-125), and 1,1,1-trifluoroethane (R-143a) in various [Ch]Cl-based DESs, with ethylene glycol (EG) and glycerol (GL) as HBDs. The results found that R-32 exhibited the highest solubility among all tested DES combinations. However, overall solubility in these DES was low. However, remarkable differences between the F-gases were found, providing a promising ideal selectivity for the separation of binary mixtures containing the studied gases.

### 2.2.3 $NH_3$ Absorption in DESs

Ammonia ($NH_3$) is an alkaline gas with pungent odor, primarily emitted from ammonia and urea synthesis processes. Its emission has led to serious environmental problems. However, this gas is also an important chemical material in the fields of fertilizers and refrigeration (Shao et al., 2024; Zhong et al., 2019). Therefore, efficient capture and recycling of $NH_3$ from industrial exhaust gas are crucial for environmental and economic benefits.

Over the past few years, DESs have been recognized as a promising $NH_3$ absorbent (Chen et al., 2020; Shao et al., 2024; Zhang, J. et al., 2024; Zhong et al., 2019). Regarding [Ch]Cl-based DESs, Li et al. (2020) prepared sugar-based DESs by combining [Ch]Cl with natural sugars like fructose, ribose, and xylose. Their $NH_3$ absorption experiments at 333.2 K and 18.0 kPa showed that [Ch]Cl + fructose DESs had the highest $NH_3$ capacity (1.86 mol/kg) due to the numerous hydroxyl sites in fructose, despite their high viscosities limit mass and heat transfer.

Jiang, W.-J. et al. (2019) tested $NH_3$ absorption in DESs based on weakly acidic ethylamine hydrochloride (EaCl) with glycerol (GL). These DESs showed $NH_3$ capacities of 9.63 mol/kg at 298.2 K and 106.7 kPa, indicating strong interactions between the DES and $NH_3$. Ma et al. (2021) prepared DESs using imidazolium hydrochloride ([ImH]Cl) with GL, achieving $NH_3$ capacities of 12.934 mol/kg at 298.2 K and 101.3 kPa, and exhibiting good recycling performance. Li et al. (2021) combined lithium chloride (LiCl) with ethylene glycol (EG), which demonstrated $NH_3$ capacities of 12.82 mol/kg at 303.2 K and 101.3 kPa. The high $NH_3$ capacities in this DES are due to Lewis acid-base ($Li^+$ and $NH_3$) and hydrogen-bond donor-acceptor (OH and $NH_3$) interactions.

In general, the hydroxyl and amide groups exhibit significant $NH_3$ trapping capabilities (Duan et al., 2019). At present, quaternary ammonium salts, amines, azoles, and halides are commonly employed as HBAs to synthesize DESs for $NH_3$ absorption (Wang et al., 2024).

## 2.3 Modelling Tools for DESs

For the large-scale industrial application of DESs, it is crucial to have reliable knowledge of their thermophysical properties. This information is necessary for accurately simulating and designing new processes, optimizing existing ones, and conducting reliable economic evaluations under various working conditions and configurations (Alkhatib, I. et al., 2020; Crespo et al., 2019). However, the vast number of possible DESs, created from numerous combinations of HBAs and HBDs, along with the diverse conditions like temperature, pressure, and potential cosolvent addition, makes the experimental determination of these properties a cumbersome task (Dietz et al., 2019; Haghbakhsh et al., 2021c; Zuo et al., 2021).

This challenge can be addressed through the development of modelling approaches capable of capturing properties of DESs at the molecular level and their formation, in addition to predicting their properties, even under industrially relevant conditions (Alkhatib, I. et al., 2020; Haghbakhsh et al., 2021c). This would facilitate a pre-screen of properties for many DESs combinations, reducing the amount of experimental work, which will be always necessary to get accurate values.

Nonetheless, modelling DESs is quite difficult owing to their highly non-ideal behavior due to the asymmetry of their components and the complexity of the formed hydrogen bond networks (Florindo et al., 2019; Zuo et al., 2021). Towards the

development of such a modelling approach, several techniques have emerged as valuable tools for modelling DESs over the past few years (see Figure 2.7). These modelling techniques can be classified into four broad categories namely, empirical models, classical thermodynamics, statistical thermodynamics, and quantum chemistry-based models.

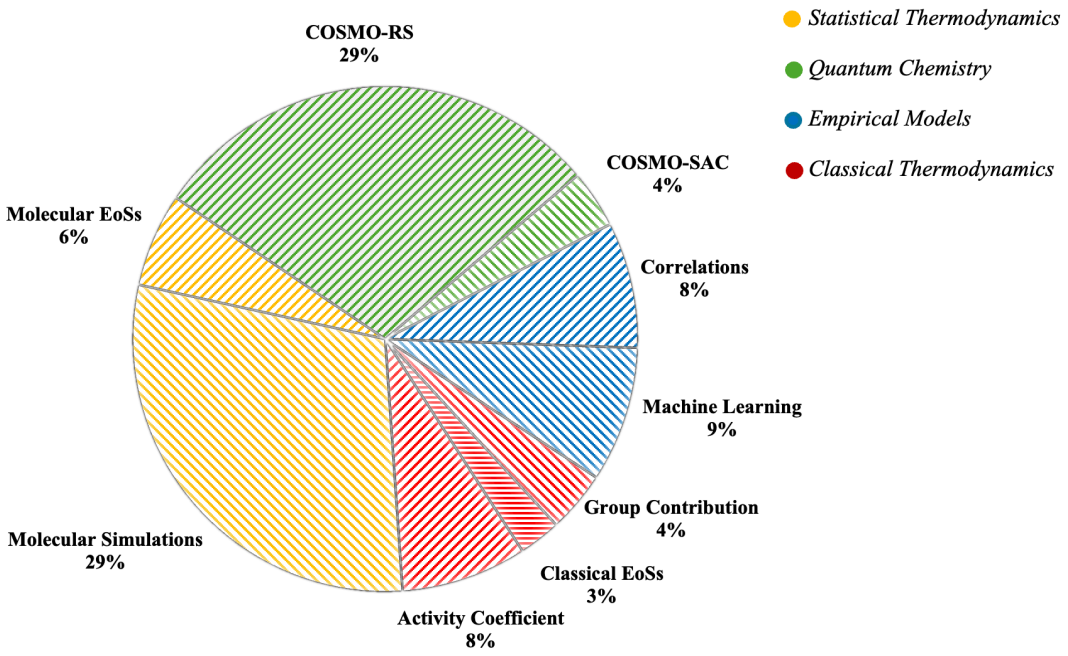


***Figure 2.7.*** *Schematic breakdown of categories and types of theoretical models towards modelling DESs, according to SCOPUS (May 29th, 2024). These values represent a total of 484 contributions since 2011.*

These computational techniques vary in their complexity, robustness, prediction capabilities, accuracy, and transferability of parameters for modelling DESs, depending on the degree of rigor in their theoretical formulation (Alkhatib, I. et al., 2020). The advantages and disadvantages of each computational technique for modelling DESs are listed in Table 2.3.

***Table 2.3.*** *Advantages and disadvantages of some modelling techniques usually used for the thermodynamic characterization of pure DESs and their multicomponent mixtures, adapted from Alkhatib, I. et al. (2020).*

| **Thermodynamic models** Class | Type | **Advantages** | **Disadvantages** |
|---|---|---|---|
| Empirical models | Correlations | ➢ Easy and simplicity of implementation | ➢ Large experimental database for fitting<br>➢ No physical meaning of parameters |
| | Machine Learning | ➢ High prediction accuracy and efficient as an *ad-hoc* model | ➢ Large experimental database for fitting needed for high accuracy<br>➢ Remains a sophisticated correlation |
| Classical thermodynamic | Group contribution | ➢ Purely predictive | ➢ Large experimental database for fitting the group parameters<br>➢ Used in conjunction with other models |
| | Classical equation of state | ➢ Simple and available in all engineering simulators | ➢ Need of critical points information<br>➢ Only applicable to phase equilibria calculations |
| | Activity coefficient | ➢ Accurate for phase equilibria calculations | ➢ Large number of fitted parameters<br>➢ Only applicable to phase equilibria calculations |
| Statistical thermodynamics | Molecular equation of state | ➢ Explicit representation of complex molecular interactions<br>➢ Transferability of molecular parameters | ➢ Moderate number of fitted parameters<br>➢ Moderate transferability of binary parameters using individual-component approach |
| | Molecular simulations | ➢ Predictive and molecular insight | ➢ High computational time<br>➢ Need accurate force fields |
| Quantum chemistry | COSMO models | ➢ Purely predictive and molecular insight | ➢ Qualitative agreement<br>➢ High computational time |

Regarding correlations, various empirical linear and non-linear regression models have been used to correlate a wide range of physicochemical properties of pure DESs and their mixtures. For instance, Lapeña et al. (2019) found a linear dependence on temperature for thermophysical properties of [Ch]Cl : EG and its mixtures with water, including density, speed of sound, refractive index, heat capacity, and surface tension. Moghimi and Roosta (2019) developed non-linear regression models to capture the

temperature and mixture composition effects on density, refractive index, and viscosity of an aqueous DESs ([Ch]Cl + glucose). However, despite their simplicity, these models face limitations in terms of accuracy, robustness, and parameter transferability for process design and simulation applications.

Concerning modelling techniques using concepts drawn from classical thermodynamics, group contribution methods have been used for predicting physicochemical properties of DESs based on their chemical composition, estimating, for example, critical properties and acentric factors by evaluating components and mixtures using appropriate mixing rules (Mirza et al., 2015). The obtained properties can be used in other modelling techniques, for example, Roosta et al. (2023) combined a group contribution method with machine learning (ML) techniques to predict the viscosities of 305 DESs using 2533 data points. Despite their utility, verifying predictive accuracy is challenging due to limited experimental data like critical properties and acentric factors.

Classical Equations of State (EoS), such as cubic equations like the Peng-Robinson (PR) EoS (1976), offer a straightforward and comprehensive approach to characterize the thermodynamic properties of pure DESs and their mixtures, including phase equilibria. For instance, Ainai et al. (2024) utilized the PR EoS to model $CO_2$ solubility in various DESs based on phosphonium and ammonium with EG, adjusting binary interaction parameters for each DES + $CO_2$ mixture at different temperatures to match experimental data accurately. However, EoS modelling techniques are limited because of the absence of any explicit consideration of the formation of hydrogen bond networks found in DESs.

Among other classical thermodynamic models, activity coefficient models such as excess Gibbs energy models are highly representative of complex mixtures like those found in DESs (Kontogeorgis & Folas, 2010). The nonrandom two-liquid model (NRTL)

(1968), a popular formulation of excess Gibbs energy models, is commonly used to predict phase equilibria and solubility in DESs. For example, Crespo et al. (2017) used NRTL to model the SLE phase behaviour governing the formation of various [Ch]Cl-based DESs with fatty acids and alcohols, accurately obtaining the composition and temperature at the eutectic point. However, these models have limited predictive capabilities, relying on numerous adjustable parameters and extensive thermodynamic data for accurate correlations. They are primarily used for phase equilibria calculations and lack demonstrated applications in predicting physicochemical properties essential for process simulation and design.

Regarding molecular simulations, these techniques based on statistical mechanics consider molecular structure and interactions, enabling the prediction of phase equilibria and physicochemical, dynamic, and structural properties of pure DESs and their mixtures (Frenkel & Smit, 2002; Wagle et al., 2017). For example, Doherty and Acevedo (2018) developed a comprehensive, transferable set of parameters for [Ch]Cl-based DESs using a nonpolarizable force-field (OPLS-DES), accurately predicting various physical properties. Salehi et al. (2019) also used OPLS-DES to predict vapor phase composition, enthalpy of vaporization, and solubility parameters of several [Ch]Cl-based DESs. Although computationally intensive, simulation methods provide valuable molecular-level insights into structural, energetic, and dynamic properties, aiding in the rational design of novel materials and the enhancement of thermodynamic models.

In addition to these methods, The Conductor like Screening Model (COSMO), introduced by Klamt and Schüürmann (1993), integrate quantum chemistry and electrostatics with statistical thermodynamics, linking molecular-level quantum chemistry to chemical engineering thermodynamics. This approach has been applied as a predictive tool to design and characterize DESs. For instance, the SLE behaviour and

eutectic point governing the formation of several [Ch]Cl-based DESs have been predicted to determine the adequacy of several HBAs for the formation of potential DESs (Abranches et al., 2019; Fernandez et al., 2017). Despite its advantages, the approach COSMO only provides qualitative agreement with experimental data and is computationally expensive. However, it remains valuable for understanding system behavior and developing screening tools for characterizing un-synthesized DESs and evaluating their industrial potential.

After evaluating various computational techniques for modelling DESs, this thesis now centers on two specific methods employed in this study. The following sections delve into the application of a Molecular EoS (soft-SAFT) and a Machine Learning Technique (Artificial Neural Network) for modelling DESs, each offering unique advantages and challenges that contribute to an enhanced understanding and prediction of DES behavior across diverse conditions.

### 2.3.1 Soft-SAFT Equation of State

Molecular-based EoSs are highly suitable for robust and efficient process simulation and design of DESs, due to their accurate prediction of complex fluid behavior under extreme conditions using a set of transferable molecular parameters (Alkhatib, I. et al., 2020; Pedrosa et al., 2005). In this regard, the soft-SAFT EoS (Blas & Vega, 1997) is an attractive framework for reliable estimates of the physicochemical behavior of complex mixtures, like DESs, due the hydrogen bonding and other association effects that can be explicitly considered in the model. Indeed, this equation has been successfully employed to describe the thermophysical properties of IL (Alkhatib, I. I. I. et al., 2020a;

Andreu & Vega, 2007; Llovell et al., 2015; Oliveira et al., 2016; Vega & Llovell, 2016) and DESs (Alkhatib, I. I. I. et al., 2020a; Crespo et al., 2019; Lloret et al., 2017; Ojeda & Llovell, 2018), among many other systems.

Lloret et al. (2017) were the first to apply the soft-SAFT EoS for modelling DESs, describing the density, surface tension, viscosity and $CO_2$ solubility of several tetraalkylammonium chloride based DESs. In their work, DESs were modeled using two approaches: one treated the DESs as a pseudo-pure compound and the other described them as a mixture of two independent constituents. In general, a very good description of the investigated properties were found using both approaches, although the individual-component modelling approach provided a more realistic and physically consistent methodology towards modelling DESs.

Ojeda and Llovell (2018) used the individual-component approach via soft-SAFT to model various eutectic ammonium chloride and bromide salt-based DESs, accurately describing their densities and $CO_2$ and $SO_2$ solubility. COSMO-RS (COSMO - for Realistic Solvents) software was used to estimate the number of association sites for each molecule by determining the charge density of the DESs components.

Similarly, DESs based in [Ch]Cl and tetra-alkyl ammonium chlorides/bromides were modeled by Alkhatib, I. I. I. et al. (2020a), as a mixture of two independent constituents. They examined the potentiality of DESs for $CO_2$ capture using soft-SAFT as a modelling tool for the screening of these solvents based on key process indicators, such as cyclic working capacity, enthalpy of desorption, and $CO_2$ diffusion coefficients. Once the models were assessed versus experimental data, the soft-SAFT EoS was used as an accurate predictive tool to calculate the thermophysical properties needed for evaluating their performance.

Crespo et al. (2019) employed soft-SAFT, relying on molecular simulations and ab initio calculations to develop a more accurate and robust coarse-grain model for [Ch]Cl with five association sites, being representative of the tendencies of this salt to form highly-complex hydrogen bonds. The developed model was robust and accurate in modelling SLE behaviour of mixtures of [Ch]Cl and other substances such as water, glycols, phenols and glycerol, and their densities, with the use of binary energy interaction parameters fitted to the available SLE data.

Jovell et al. (2020) used soft-SAFT for a thermodynamic characterization of R134a solubility in various FILs and DESs. Similarly, as mentioned before, Demirbek et al. (2024) applied soft-SAFT to model the solubility of three F-gases (R-134a, R-32, and R-125) in five DESs derived from fluorinated salts and perfluorinated acids at different temperatures. Both studies developed accurate molecular models using the individual-component approach, showing good agreement with experimental data.

Overall, these works demonstrate that applying soft-SAFT EoSs for modelling DESs provides extensive chemical information in an accurate and transferable manner, especially using the individual-component modelling approach. This method offers high predictive capabilities, making it suitable for process design and simulation. The theoretical fundamentals of the soft-SAFT EoS are explained in Chapter 3.

### 2.3.2 Artificial Neural Network Approach

Machine learning (ML) techniques are increasingly suitable for the robust and efficient prediction of thermophysical properties of complex mixtures, as they can model non-linear relationships and handle large datasets with high accuracy. Among these

techniques, Artificial Neural Networks (ANNs) emerge as a powerful tool for modelling complex procedures, because they can capture intricate patterns in a provided database, utilizing experimental information during the learning process to accurately predict system outcomes (Khandelwal & Singh, 2009).

The accuracy of ANNs hinges not only on optimizing the network architecture but also on selecting precise input descriptors that effectively represent the molecular characteristics involved. In this context, several contributions in the literature have demonstrated the elevated accuracy achieved by molecular-based ANNs models in predicting the physicochemical properties of DESs (Adeyemi et al., 2018; Bagh et al., 2013; Benguerba et al., 2019; Boublia et al., 2022; Lemaoui et al., 2022). For instance, Bagh et al. (2013) and Adeyemi et al. (2018) utilized of DES components as input variables, while Benguerba et al. (2019), Boublia et al. (2022) and Lemaoui et al. (2022) employed information from the charge density distributions ($\sigma$-profile) obtained from COSMO-RS as input parameters to ANN. The σ-profile descriptors are derived from the integral area under their curve, which quantifies the total charge of the molecule, serving as a robust molecular descriptor. This approach have been used as input parameters in machine learning models to obtain highly accurate predictions of various properties of DESs, such as density (Lemaoui et al., 2020b), thermal conductivity (Lemaoui et al., 2023), pH (Lemaoui et al., 2021), surface tension (Lemaoui et al., 2022), $CO_2$ solubility (Wang, Jingwen et al., 2021), electrical conductivity (Boublia et al., 2022; Lemaoui et al., 2020a) viscosity (Benguerba et al., 2019) and extraction efficiency of contaminants from aqueous media (Awaja et al., 2023).

For example, Benguerba et al. (2019) developed an ANN model using COSMO-RS-based $\sigma$-profiles as molecular parameter inputs to predict the viscosity of five amine-based DESs. They employed a dataset containing 108 experimental data, achieving $R^2$

values of 0.9975 and 0.9863 for the training and validation steps, respectively. Similarly, Lemaoui et al. (2022) applied this methodology to predict the surface tension of 133 different DESs mixtures, utilizing a dataset comprising 1571 data points. The resulting ANN model demonstrated excellent performance, achieving $R^2$ values of 0.986 and 0.977 for training and testing, respectively, with an overall average absolute relative deviation of 2.20%.

In summary, ANNs can effectively model intricate patterns and correlations that may be challenging for traditional techniques to capture, even though they may lack a formal theoretical connection. Therefore, utilizing molecular-based descriptors as inputs in ANN development is crucial, as these descriptors provide essential molecular characteristics, ensuring accurate predictions of specific physicochemical properties. Further elaboration on the theoretical basis of ANNs is provided in the next Chapter.

# 3

# Theoretical Background

*This chapter outlines the various approaches employed throughout this thesis. The different scalar approaches presented in this work include quantum-based scales (such as COSMO-SAC) and mesoscale methods (such as soft-SAFT EoS). Furthermore, an empirical model based on Machine Learning techniques, specifically Artificial Neural Networks, is introduced. Together, this information can describe the main thermophysical properties of the DES and guide the application and design of industrial processes under a wide range of operating conditions.*

## 3.1 Chemical and Structural Modelling Methods

The analysis of the different chemical and structural characteristics of a fluid can be studied at different scales (see Figure 3.1), depending on the degree of detail required. These approaches have varying levels of resolution and complexity to study a system. They can be used together in multiscale simulations, where one might be able to strike a balance between accuracy (which favors using more detailed and microscopic models) and feasibility (which favors using less detailed, more macroscopic models). The combination of these perspectives aims to find a good balance between precision and efficiency. In this section, we will outline the approaches used in this thesis at two different scales: quantum and mesoscopic.

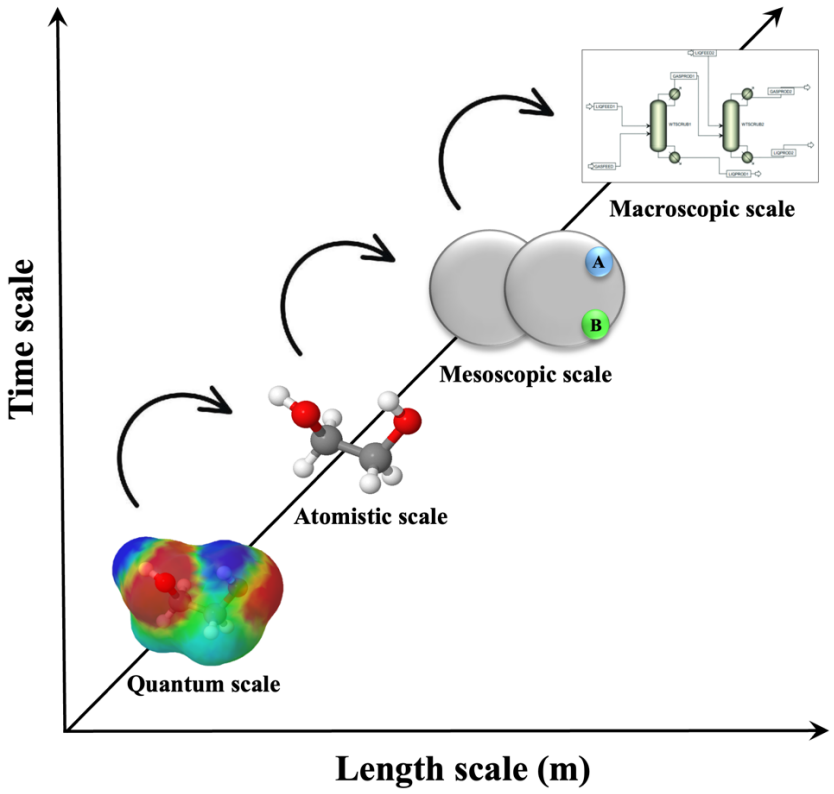


***Figure 3.1.*** *Schematic diagram of multiscale simulation.*

### 3.1.1 Quantum-Based Methods: COSMO-SAC

The Conductor like Screening Model (COSMO), introduced by Klamt and Schüürmann (1993), is a dielectric solvation model that can predict the activity coefficients ($\gamma_i$) and other thermophysical properties of chemical species in a multicomponent mixture, by using reults from computational chemistry. The essential requirement for determining $\gamma_i$ involves understanding the shielding effect experienced by a molecule within a conductor. When a molecule is situated inside a cavity within a perfect conductor, the electric field must equate to zero. To achieve this, an induced charge appears on the surface of the cavity, canceling out the charge induced by the molecule in that region. The COSMO-SAC (COSMO - Segment Activity Coefficient) model, developed by Lin and Sandler (2002), discretizes molecules into charge segments and computes interactions between these segments using statistical thermodynamics and quantum mechanics theories, which gives the model its strong predictive capability. A three-dimensional visualization of the shielding phenomenon can be generated following COSMO technique calculations, as depicted in Figure 3.2 for the ethylene glycol molecule, where the reddish regions represent induced positive charges (because the highly electronegative oxygen attracts positive charges on the surface of its cavity). The bluish regions represent induced negative charges, and the greenish regions represent neutral charges.

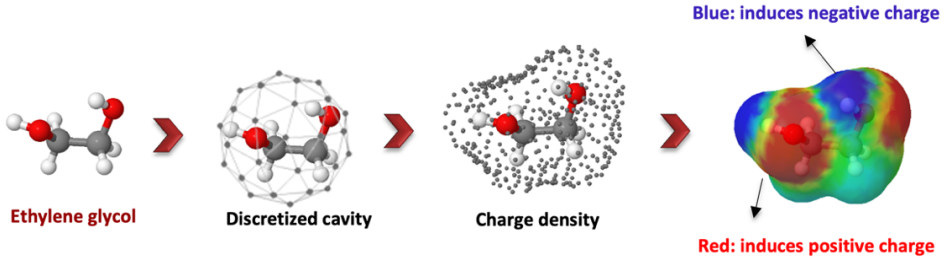


***Figure 3.2.*** *Generation of a three-dimensional surface charge densities around ethylene glycol obtained after COSMO-SAC calculations.*

In COSMO-based models, the activity coefficient ($\gamma_i$) is viewed as the sum of combinatorial ($\gamma_i^{comb}$) and residual ($\gamma_i^{res}$) contributions:

$$\ln \gamma_i = \ln \gamma_i^{comb} + \ln \gamma_i^{res} \tag{3.1}$$

In the COSMO-SAC model, the $\gamma_i^{comb}$ term, which takes into account the molecular size and shape effects, is given by the Staverman-Guggenheim formula, as described by Lin and Sandler (2002). The second term, $\gamma_i^{res}$, accounting for electrostatic interactions between molecules in solute/solvent mixtures, is calculated as the difference between the free energy required to restore the charge around the solute molecule in the solution (denoted as $s$) and the free energy required to restore the charge in a pure liquid (denoted as $i$):

$$\ln \gamma_i^{res} = \sum_{m \in i} \frac{Q_m^i}{a_{eff}} \left( \ln \Gamma_m^s - \ln \Gamma_m^i \right) \quad , \tag{3.2}$$

where $Q_m^i$ is the area of the segment $m$ in a molecule $i$; $a_{eff}$ is the standard segment surface area, which is the same for all molecules and is one of the universal parameters in this model; and $\ln \Gamma_m^s$ and $\ln \Gamma_m^i$ are the logarithms of the activity coefficient of a segment $m$ of the molecule's surface in solution and in pure liquid, respectively, as given by the *self-consistency* equations:

$$\ln \Gamma_m^s = -\ln \left[ \sum_{n \in i} p_n^s \Gamma_n^s \exp\left( \frac{-\Delta W_{n,n}}{RT} \right) \right] \tag{3.3}$$

$$\ln \Gamma_m^i = -\ln\left[\sum_{n\in i} p_n^i \Gamma_n^i \exp\left(\frac{-\Delta W_{n,n}}{RT}\right)\right] \quad , \tag{3.4}$$

where the probability of finding a segment $m$ in a mixture $s$ ($p_m^s$) and in a pure liquid $i$ ($p_m^i$) are given by Eq. 3.5 and 3.6, respectively.

$$p_m^s = \frac{x_i Q_m^i}{\sum_j x_j Q^j} \tag{3.5}$$

$$p_m^i = \frac{Q_m^i}{Q^i} \quad , \tag{3.6}$$

where $Q^i = \sum_{m\in i} Q_m^i$ is the total cavity surface area of molecule $i$. Finally, the interaction energy $\Delta W_{m,n}$ for each contact between segments $m$ and $n$ can be computed under different assumptions. Using the formulation of Lin and Sandler (2002), it is computed as a function of the segment charge densities $\sigma_m$ and $\sigma_n$:

$$\Delta Wm,n = \left(\frac{\alpha'}{2}\right)(\sigma_m + \sigma_n)^2 + c_{\mathrm{hb}} \max[0, \sigma_{\mathrm{acc}} - \sigma_{\mathrm{hb}}] \times \min[0, \sigma_{\mathrm{don}} + \sigma_{\mathrm{hb}}] \tag{3.7}$$

where $\alpha'$ is the constant for the misfit energy; $c_{\mathrm{hb}}$ is a constant for hydrogen bonding; $\sigma_{\mathrm{hb}}$ is the sigma-value cutoff for hydrogen bonding; and $\sigma_{\mathrm{acc}}$ and $\sigma_{\mathrm{don}}$ are the larger and smaller values of $\sigma_m$ and $\sigma_n$.

The probability $p_m^i$ can be represented through graphs called $\sigma$-profiles. The $\sigma$-profile of a molecule is a two-dimensional representation of the distribution of induced charges on its surface and is unique for every molecule. Figure 3.3 shows the $\sigma$-profile of the ethanol molecule, where the horizontal axis shows the charge densities of the

molecules, typically ranging from -0.03 to 0.03 (e/Å), while the vertical axis shows the area of the molecule corresponding to each charge density.

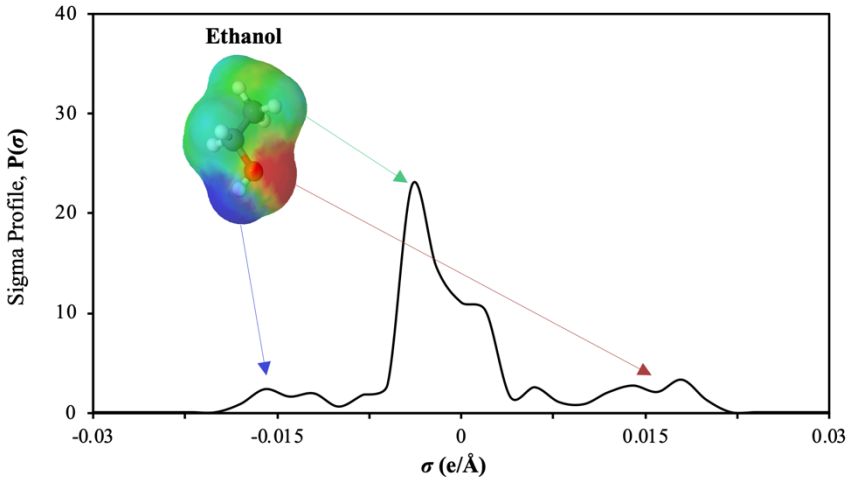


***Figure 3.3.*** *Three-dimensional apparent surface charge density of ethanol and its σ-profile.*

The integral of the area under the sigma profile curve provides the total charge of the molecule, serving as a molecular descriptor. These descriptors capture essential characteristics of the molecule, enabling accurate determination of specific physicochemical properties. Various studies have used molecular descriptors from the area under the $\sigma$-profile as input parameters in machine learning models to achieve highly accurate predictions of different attributes across various systems (Alkhatib et al., 2022; Boublia et al., 2023; Li et al., 2024). This includes properties of DESs, as shown in Section 2.3.2.

### 3.1.2 Mesoscopic Scale Modelling: SAFT EoS

Equations of state (EoS) are essential tools for describing the thermodynamic properties of complex fluids such as DESs. Traditional cubic EoS provide a

straightforward framework for a versatile thermodynamic properties description of pure DESs and their multicomponent mixtures, but they are limited by their inability to explicitly account for the intricate hydrogen bond networks that govern DES formation and their unique structural features. In contrast, the Statistical Association Fluid Theory (SAFT) EoS, built under Wertheim's first order thermodynamic perturbation theory (Wertheim, 1984a, b, 1986a, b), addresses this limitation.

Originally proposed by Chapman et al. (1989; 1990), the SAFT EoS explicitly consider strong directional interactions and the formation of molecular chains as perturbations within the system. In this EoS framework, molecules are generally represented as a number of monomers of the same size, which are covalently bonded to each other forming chains that interact with each other through a certain intermolecular potential, being able to associate at specific association sites, as depicted in Figure 3.4.

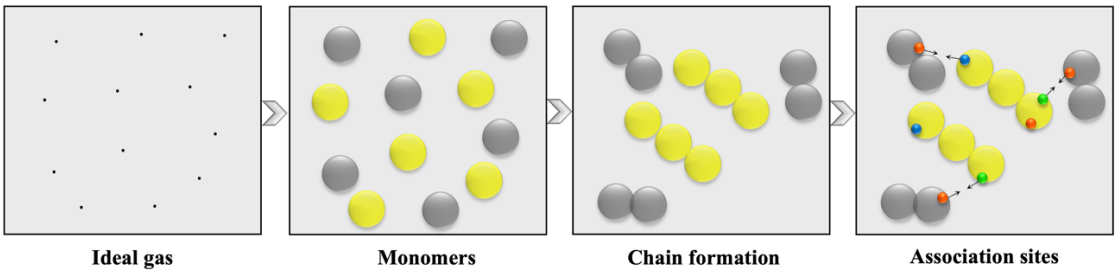


***Figure 3.4.*** *Schematic representation of the physical foundation of SAFT. Yellow and gray colors are used to represent two different monomers; while green, blue and orange are used to distinguish three different association site types.*

The SAFT EoS is expressed in terms of residual Helmholtz energy ($\alpha^{res}$), defined as the difference between the molar Helmholtz energy of the fluid ($\alpha$) and that of an ideal gas ($\alpha^{id}$), at the same temperature and density. This residual energy ($\alpha^{res}$) can be assumed as the sum of different microscopic contributions to a given molecule, according to the Eq. 3.8:

$$\alpha^{res} = \alpha - \alpha^{id} = \alpha^{ref} + \alpha^{chain} + \alpha^{assoc} \quad (3.8)$$

In this equation, $\alpha^{ref}$ denotes to the residual Helmholtz free energy of nonassociated spherical segments. The original SAFT of Chapman et al. (1989; 1990) uses a perturbation expansion using a hard-sphere as a reference term and a dispersion term as a perturbation. Moreover, $\alpha^{chain}$ refers to a chain term, accounting the contribution resulting from the formation of chains that connect individual monomers, while $\alpha^{assoc}$ represents the association term, that corresponds to the contribution of strong and short-range directional interactions, as resulting from the formation of hydrogen bonds. These last two terms come from Wertheim's first-order thermodynamic perturbation theory (Wertheim, 1984a, b, 1986a, b).

In the original SAFT equation, a total of five molecular parameters are required for fluid characterization, as illustrated in Figure 3.5. These parameters represent the main structural and energetic characteristics of the fluid. Among them, three parameters are required for non-associated species: the segment diameter (σ), chain length ($m$), and dispersive energy between segments (ε), while for associated species, two additional parameters are included, related to volume ($k^{HB}$) and energy ($\varepsilon^{HB}$).

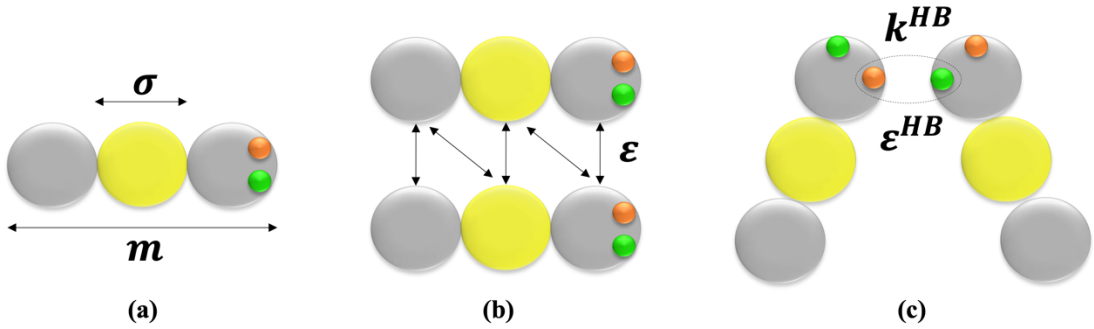


***Figure 3.5.*** *Schematic representation of molecular parameters used in the SAFT EoS; (a) segment diameter (σ) and chain length (m); (b) dispersive energy between segments (ε) and (c) volume association ($k^{HB}$) and energy association ($\varepsilon^{HB}$).*

In the last decade, this equation has become an accurate tool for describing the thermodynamic behavior of complex mixtures, especially in systems where strong short-range directional forces such as hydrogen bonds play an important role (Lloret et al., 2017). Due to its success, many versions of the original SAFT equation were developed, for example, soft-SAFT (Blas & Vega, 1997), SAFT-VR (Gil-Villegas et al., 1997), SAFT-BACK (Pfohl & Brunner, 1998) and PC-SAFT (Gross & Sadowski, 2001). Moreover, heteronuclear versions employing a group contribution approach have been developed, including SAFT-γ (Lymperiadis et al., 2007), GC-SAFT-VR (Peng et al., 2009), and SAFT-γ-Mie (Papaioannou et al., 2014). In this thesis, the soft-SAFT version is used as a modelling tool.

*Soft-SAFT EoS*

The original SAFT model employs in the reference term ($\alpha^{ref}$) from Eq. 3.8 a perturbation approach in which a hard sphere fluid is taken as a reference for the repulsive interactions and the attractive interactions are added as a perturbation term. Instead, soft-SAFT, developed by Blas and Vega (1997), considers the Lennard-Jones (LJ) potential for the reference fluid, accounting for both the repulsive and attractive interactions between the monomers in a single term, calculated from the equation of Johnson et al. EoS (1993), fitted to simulations of a LJ segment in a wide range of temperature and pressure.

Regarding $\alpha^{chain}$, which pertains to the formation of chains from $m_i$ spherical monomers, the equation reads:

$$\alpha^{chain} = RT \sum_i x_i (1 - m_i) \ln g_R(\sigma) \quad , \qquad (3.9)$$

where $g_R$ is the pair correlation function of the reference fluid for the interaction of two segments in a mixture of segments, evaluated at the segment contact $\sigma$. Again, the original SAFT uses the radial distribution function (or pair correlation function) of hard spheres, while soft-SAFT uses a radial distribution function of a LJ fluid. This term is computed through the equation of Johnson et al. for LJ chains (1994).

The association term ($\alpha^{assoc}$) for the different SAFT variants, including soft-SAFT is expressed by:

$$\alpha^{assoc} = RT \sum_i x_i \sum_\alpha \left( ln\, X_{\alpha_i} - \frac{X_{\alpha_i}}{2} + \frac{M_i}{2} \right) \quad , \qquad (3.10)$$

where $M_i$ is the number of association sites of each component $i$, and $X_\alpha$ is the fraction of molecules not bonded to the site $\alpha$. To calculate $X_{\alpha_i}$ , one needs to adjust two parameters for each hydrogen bonding: the site-site bonding volume of association $k^{HB}_{\alpha\beta_{ii}}$, and the site-site association energy $\varepsilon^{HB}_{\alpha\beta_{jj}}$, which are related to $X_{\alpha_i}$ through a mass action balance (Eq. 3.11 and 3.12).

$$X_{\alpha_i} = \frac{1}{1 + N_\alpha \rho \sum_j x_j \sum_\beta x_j^\beta \, \Delta i^{\alpha_i \beta_j}} \quad , \qquad (3.11)$$

where $\Delta i^{\alpha_i \beta_j}$ is the association strenght between site $\alpha$ on molecule $i$ and site $\beta$ on molecule $j$, and is defined as:

$$\Delta^{\alpha_i\beta_j} = k^{HB}_{\alpha\beta_{ij}}[\exp(\varepsilon^{HB}_{\alpha\beta_{ij}}/k_BT) - 1]g_{ij} \quad (3.12)$$

Soft-SAFT considers an additional $\alpha^{polar}$ term to Eq. 3.8 for the explicit consideration and accurate modelling of polar forces such as dipolar forces. The polar contribution to the residual Helmholtz energy is based on the multipolar expression of Twu and Gubbin (1978; 1978) for spherical molecules written as the Padé approximation of Stell et al. (1972):

$$\alpha^{polar} \approx \frac{a_2}{1-\frac{a_3}{a_2}} \quad , \quad (3.13)$$

where $a_2$ and $a_3$ re the second and third-order terms in the perturbation expansion terms, respectively, and are related to two and three-body interactions.

$$a_2^{polar} = a_2^{\mathrm{D}} + 2a_2^{\mathrm{cross}} + a_2^{\mathrm{Q}} \quad (3.14)$$

$$a_3^{polar} = a_{3\mathrm{A}}^{polar} + a_{3\mathrm{B}}^{polar} \quad (3.15)$$

$$a_{3\mathrm{A}}^{polar} = 3a_{3\mathrm{A}}^{\mathrm{cross}_1} + 6a_{3\mathrm{A}}^{\mathrm{cross}_2} + 6a_{3\mathrm{A}}^{\mathrm{cross}_3} + 3a_{3\mathrm{A}}^{\mathrm{Q}} \quad (3.16)$$

$$a_{3\mathrm{B}}^{polar} = 3a_{3\mathrm{B}}^{\mathrm{D}} + 3a_{3\mathrm{B}}^{\mathrm{cross}_2} + 3a_{3\mathrm{B}}^{\mathrm{cross}_3} + a_{3\mathrm{B}}^{\mathrm{Q}} \quad , \quad (3.17)$$

where $a_2^{\mathrm{D}}$ and $a_{3\mathrm{B}}^{\mathrm{D}}$ refer to the second and third-order perturbation terms for dipole-dipole interactions, $a_2^{\mathrm{Q}}$, $a_{3\mathrm{A}}^{\mathrm{Q}}$ and $a_{3\mathrm{B}}^{\mathrm{Q}}$ refer to the perturbation terms for quadrupolar–quadrupolar interactions, while the rest of the terms are those for all possible cross-polar interactions such as dipolar–quadrupolar interactions (Alkhatib, I. I. I. et al., 2020b). The reader is referred to the original contribution for further details about the expressions. In this work,

$a_2$ and $a_3$ are taken from the interpolation equations over pair- and triplet-correlation functions of a LJ fluid proposed by Luckas et al. (1986). The application of the polar term to chain molecules is made using the segment approach of Jog et al. (2001), which assumes that polar moments are located on certain segments of the chain molecules and oriented perpendicular to the moment axis. In turn, each polar moment is associated with two additional molecular parameters: the fraction of polar segments $x_p$ and dipole moment $\mu$.

In general, the soft-SAFT EoS provides a physically grounded theoretical approach to describe with accuracy the thermophysical properties and phase behavior of mixtures of complex compounds, like ionic liquids (IL) (Alkhatib, I. I. I. et al., 2020a; Andreu & Vega, 2007; Llovell et al., 2015; Oliveira et al., 2016; Vega & Llovell, 2016) and DESs (Alkhatib, I. I. I. et al., 2020a; Crespo et al., 2019; Lloret et al., 2017; Ojeda & Llovell, 2018).

At this point, it is important to note that each term contribution to the total residual Helmholtz free energy in the Eq. 3.8 must be expressed in terms of composition for studies involving mixtures. Unlike the rest of the contributions, the reference term ($\alpha^{ref}$) is formulated for a pure compound. To handle multicomponent mixtures, where each compound may consist of varying numbers of segments with different sizes or dispersive energies, it is necessary to consider "averaged" values to construct a pseudo-binary system that mimics the thermodynamic properties of the mixture. This process involves applying mixing rules, with the van der Waals fluid theory being the most commonly used approach. The corresponding expressions for the size and energy parameters of the conformal fluid are as follows:

$$m = \sum_{i=1}^{n} x_i m_i \tag{3.18}$$

$$\sigma^3 = \frac{\sum_i \sum_j x_i x_j m_i m_j \sigma_{ij}^3}{(\sum_i x_i m_i)^2} \tag{3.19}$$

$$\varepsilon\sigma^3 = \frac{\sum_i \sum_j x_i x_j m_i m_j \varepsilon_{ij} \sigma_{ij}^3}{(\sum_i x_i m_i)^2} \quad , \tag{3.20}$$

where $x_i$ is the mole fraction and $m_i$ is the chain length of each of the components of the mixture, denoted by the indexes *i* and *j*. $\sigma_{ij}$ and $\varepsilon_{ij}$ are the crossed interaction parameters and are calculated using the Lorentz-Berthelot combination rules:

$$\sigma_{ij} = \eta_{ij} \frac{(\sigma_{ii} + \sigma_{jj})}{2} \tag{3.21}$$

$$\varepsilon_{ij} = \xi_{ij} \sqrt{\varepsilon_{ii} \varepsilon_{jj}} \quad , \tag{3.22}$$

where $\eta_{ij}$ and $\xi_{ij}$ are the size and energy binary adjustable parameters that modify the arithmetic and geometric averages, respectively. These parameters account for asymmetry and non-idealities between the different nature of the mixture compounds. They can be fitted to binary experimental data if predictions from the pure components ($\eta_{ij} = \xi_{ij} = 1$) are not satisfactory.

For mixtures of compounds with hydrogen-bonding interactions, cross-association between different molecules or different functional groups within the same molecules are calculated using combination rules, analogously to Eq. 3.21 and 3.22. When energies and volumes between a site type $\alpha$ in component *i* and a site type $\beta$ in component *j* are required, the following combining rules are applied, according to the Eq. 3.23 and 3.24:

$$\varepsilon_{\alpha\beta_{ij}}^{HB} = \sqrt{\varepsilon_{\alpha\beta_{ii}}^{HB}\varepsilon_{\alpha\beta_{jj}}^{HB}} \tag{3.23}$$

$$k_{\alpha\beta_{ij}}^{HB} = \left(\frac{\sqrt[3]{k_{\alpha\beta_{ii}}^{HB}} + \sqrt[3]{k_{\alpha\beta_{jj}}^{HB}}}{2}\right)^3 \tag{3.24}$$

*Free-Volume Theory Coupled into soft-SAFT*

The SAFT EoSs are powerful tools for predicting thermodynamic properties of complex fluids, such as density and phase behavior. However, these equations are not inherently designed to predict transport properties like viscosity. To address this limitation, specific methodologies can be employed to calculate transport properties and can be coupled with EoS for more comprehensive modelling. Among these methodologies are friction theory (Quiñones-Cisneros et al., 2000), entropy scaling (Dyre, 2018; Rosenfeld, 1977), and free volume theory, which will be explained in detail below.

The Free Volume Theory (FVT) approach, developed by, Allal et al. (2001a) is a methodology that allows the calculation of this property from the use of thermodynamic variables. In this method, the viscosity ($\eta$) of a system is expressed as the sum of dense state correction term ($\Delta_\eta$), related to the density and microstructure of the fluid, and a dilute gas term ($\eta_o$), where intermolecular effects are neglected.

$$\eta = \eta_o + \Delta_\eta \tag{3.25}$$

The dilute gas term ($\eta_o$) can by described by (Chung et al., 1988):

$$\eta_o = 40.785 \times 10^{-2} \frac{\sqrt{M_w T}}{V_c^{3/4} \Omega^*(T^*)} F_c \quad , \tag{3.26}$$

where $M_w$ is molecular weight (g/mol), $M_w$ is the critical volume (cm$^3$/mol) and $T^* = 1.2593 \times T_r$, being $T_r$ the reduced temperature with respect to the critical temperature of the compound (K). $F_c$ is the corrected factor introduced by Chung et al. (1988), to encompass the effects of chain bonding, hydrogen bonding, and polarity to the original kinetic theory of Chapman-Eskong, as shown in Eq. 3.27, where ω is the acentric factor. $\Omega^*$ is he reduced collision integral, which depends on the intermolecular potential chosen and is a complex function of the temperature. Neufeld et al. (1972) determined the collision integral for the LJ potential, used in the soft-SAFT framework, and came up with an empirical correlated expression (Eq. 3.28).

$$F_c = 1 - 02756\omega - 0.059035 \tag{3.27}$$

$$\Omega(2;2) = \frac{1.16145}{T^{*0.14874}} + \frac{0.52487}{\exp(0.77320 \times T^*)} + \frac{2.16178}{\exp(2.43787 \times T^*)} - 6.435 \times 10^{-4} \times T^{*0.14874} \times \sin\left(18.0323 \times T^{*-0.76830} - 7.27371\right) \tag{3.28}$$

Nonetheless, it has been shown that the influence of $\eta_o$ on molecules is less than the uncertainty associated with its calculation (Lloret et al., 2017; Llovell & Vega, 2014) for medium and high molecular weight molecules. As a result, this term is omitted to evaluate the viscosity of DESs, reducing the Eq. 3.25 to $\eta = \Delta_\eta$. The dense state term ($\Delta_\eta$) comes from linking two concepts. The first one is based on a generalized Dumbbell model (Allal et al., 2001a; Allal et al., 2001b), which assumes that the dense fluid term connects viscosity with the microstructure of the fluid, according to Eq. 3.29.

$$\Delta_\eta = 10^{-14}\rho N_a \zeta L^2 \quad , \tag{3.29}$$

where $\rho$ is the density (mol/L), $N_a$ is the Avogadro's number ($mol^{-1}$), $\zeta$ is a friction coefficient related to the diffusion process and the mobility of the molecule (kg/s), and $L^2$ is an average quadratic length related to the size of the molecule ($Å^2$). The second idea is based on Doolittle model (Doolittle, 1951), which is grounded in viscosity as dependent on the empty space between molecules. In this concept, the viscosity is related to the free-volume fraction ($f_v$) through an exponential relation, according to the Eq. 3.30.

$$\Delta_\eta = A\, exp\left(\frac{B}{f_v}\right) \tag{3.30}$$

By combining Eq. 3.29 and 3.30, the friction coefficient can be written as:

$$\zeta = \zeta_0\ exp\left(\frac{B}{f_v}\right) \tag{3.31}$$

Then,

$$\Delta_\eta = 10^{-14}\rho N_a L^2 \zeta_0\ exp\left(\frac{B}{f_v}\right) \tag{3.32}$$

In Eqs. 3.30–3.32, $B$ is characteristic of the free-volume overlap among the molecules. The free-volume fraction is defined as the ratio between the free molecular volume available ($v_f$) and the total molecular volume ($v$). This ratio can also be related to the potential energy of interaction, $E$ (J), according to the Eq. 3.33:

$$f_v = \left(\frac{RT}{E}\right)^{3/2} \tag{3.33}$$

In Eq. 3.33, $R$ is the universal constant for gases (J/mol·K). It is then considered that the potential energy of interaction $E$ is a sum of two terms, according to Eq. 3.34.

$$E = \frac{10^3 P}{\rho} + \alpha \rho M_w \tag{3.34}$$

In Eq. 3.34, the first term is related to the energy necessary to form the vacant vacuums available for the diffusion of the molecules as an ideal gas, where $P$ is the pressure of the system (MPa). Regarding the second term, it is directly related to the density, which is connected to the energy barrier that the molecule has to cross to diffuse, which depends on the density and on an activation energy parameter $\alpha$ (J.m$^3$/mol.kg). Then, from the expression of the friction coefficient (Eq. 3.31), $\zeta_0$ (kg/s) can be related to the force of dissipation, $F$ (N), according to Eq. 3.35.

$$F = \zeta_0 \, \bar{v} \quad , \tag{3.35}$$

where $\bar{v}$ is the speed of dissipation (m/s). The force of dissipation is related to the energy of dissipation $E$ given in a certain length of dissipation $b_f$ (Å). An additional assumption is made in the treatment by considering that all the thermal energy of activation is transformed into kinetic energy. By combining these considerations, $\zeta_0$ can be rewritten as:

$$\zeta_0 = 10^{10} \frac{E}{N_a b_f} \left( \frac{10^{-3} M_w}{3RT} \right)^{1/2} \quad (3.36)$$

When combining Eqs. 3.32 - 3.34 and 3.36, a final expression for the dense fluid term in (mPa·s) can be written as Eq. 3.37.

$$\Delta_\eta = L_v (0.1P + 10^{-4} \alpha \rho^2 M_w) \sqrt{\frac{10^{-3} M_w}{3RT}} exp \left[ B \left( \frac{10^3 P + \alpha \rho^2 M_w}{\rho RT} \right)^{\frac{3}{2}} \right] \quad (3.37)$$

The final equation includes three adjustable parameters related to the structural and energetic properties of the fluid: $L_v$ (Å) is a length parameter related to the structure of the molecules and the characteristic relaxation time, which is $L^2 / b_f$; $\alpha$ (J.m$^3$/mol.kg) describe the proportionality between the energy barrier and the density and $B$ corresponds to the free-volume overlap. These parameters are fitted to available experimental viscosity data.

The viscosity calculations to multicomponent mixtures is done using linear mixing rule of the on-fluid theory for each FVT adjustable parameter (Llovell et al., 2013c) , such as:

$$\alpha_{mixt} = \sum_{i=1}^{n} \alpha_i x_i \quad (3.38)$$

$$B_{mixt} = \sum_{i=1}^{n} B_i x_i \quad (3.39)$$

$$L_{v,mixt} = \sum_{i=1}^{n} L_{v,i} x_i \quad (3.40)$$

Hence, Eq. 3.37 is readily applicable to mixtures using the mixture viscosity parameters from Eqs. 3.38 – 3.40. The description of the viscosity requires the previous calculation of some thermodynamic properties, mainly the density and the pressure and temperature of the system. The accuracy of the calculated viscosity heavily relies on the accurate calculation of those properties. This approach has been coupled into soft-SAFT for the description of the viscosity of *n*-alkanes (Llovell et al., 2013a, b), ionic liquids (Pereiro et al., 2017) and DESs (Lloret et al., 2017) with excellent agreement between the calculated viscosity and the reported experimental data.

The Spider-Web methodology, proposed by Vega et al. (2017) optimizes the parameters of the FVT for robust viscosity calculations. This methodology consists of connecting the parameters of the compounds of interest through mixtures between them. Thus, experimental viscosity data for mixtures is used in this procedure to obtain the parameters of the pure compounds. The use of the methodology requires the previous evaluation of the density, which is calculated from the soft-SAFT EoS before the FVT is used.

In the Spider-Web methodology, the FVT parameters are fitted simultaneously to mixtures, assuming the parameters of one compound in a mixture influence the values of the parameters of the other compounds in the mixture. Ideally, having a considerable number of mixtures with common compounds allows the connection of the parameters of all the studied molecules, which can be imagined as a structure similar to a spider web. This minimizes the possible combinations of the three viscosity parameters that achieve good accuracy on the calculated viscosities, searching for the optimum set values.

In order to be able to fit the parameters with this approach, the density ($\rho$) is calculated with soft-SAFT for all the experimental points where viscosity data are available. Then, the viscosity ($\eta$) of each point is calculated with the FVT and, changing

simultaneously the values for $\alpha$, $B$, and $L_v$ of the pure compounds, the summation of absolute averaged deviations (%AAD – Eq. 3.41) of the pure compounds and mixtures is minimized.

$$\text{AAD}\ (\%) = 100 \times \frac{1}{N} \sum_{1}^{N} \frac{|\eta^{calc} - \eta^{exp}|}{\eta^{exp}} \tag{3.41}$$

In Eq. 3.41, $N$ is the number of data points and $\eta^{exp}$ is the experimental data of viscosity and $\eta^{calc}$ is the viscosity calculated using soft-SAFT.

## 3.2 Empirical Methods

Empirical models are widely used in various scientific and engineering fields, mainly due to their simplicity and ease of implementation, as they can provide accurate predictions based on observed data without requiring a deep understanding of the underlying physical processes. These models, built from experimental data, are particularly useful in situations where theoretical modelling is complex or computationally intensive. In this section, we will delve into a more sophisticated empirical modelling techniques based on Machine Learning (ML), specifically focusing on Artificial Neural Network (ANN).

### 3.2.1 Machine Learning Technique: Artificial Neural Network

Machine Learning (ML) is a rapidly evolving field that leverages data to create predictive models capable of making informed decisions. These models operate by

identifying patterns and relationships within the data, often without explicitly understanding the underlying causal mechanisms. Because of their lack of interpretability, these models are usually known as black boxes. Among the various ML techniques, methods such as linear regression, support vector machines, multivariate adaptive regression splines, and latent variable methods are widely used in many fields, including chemical engineering (Carranza-Abaid et al., 2020). However, this thesis will focus specifically on Artificial Neural Networks (ANNs), a powerful and versatile class of computational modelling tool that mimic the structure and function of the human brain to solve intricate problems.

The human nervous system can be seen as a three-stage system, as shown in the block diagram in Figure 3.6. At the core of this system is the brain, represented by the neural net, which continuously receives, processes, and responds to information. The diagram shows two sets of arrows, left-to-right (black) that indicate the forward flow of information-bearing signals, while the blue arrows pointing right to the left represent feedback within the system. Receptors convert stimuli into electrical impulses sent to the brain, and effectors transform these impulses into responses as outputs of the system (Haykin, 2009).

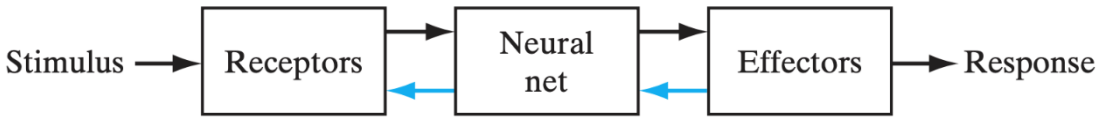


***Figure 3.6.*** *Block diagram representation of nervous system. Imagen taken from Haykin (2009).*

Similar to the three-stage structure of the human nervous system involving receptors, the neural net, and effectors, an ANN comprises a basic structure consisting of

an input layer, one or multiple hidden layers, and an output layer, each composed of artificial neurons, as depicted in Figure 3.7. The input layer works similarly to receptors, receiving external stimuli and converting them into signals that propagate through the network. Within the hidden layers, complex neural processing occurs, extracting and refining patterns and feature. Finally, the output layer acts like effectors, transforming the processed information from the network into responses as outputs of the system. This structure allows ANNs to handle intricate tasks by learning from data, similar to how the human nervous system learns and adapts through experience and feedback mechanism. The number of hidden layers and the number of neurons in each of these layers depend on the complexity of the considered system (Basheer & Hajmeer, 2000; Haykin, 2009).

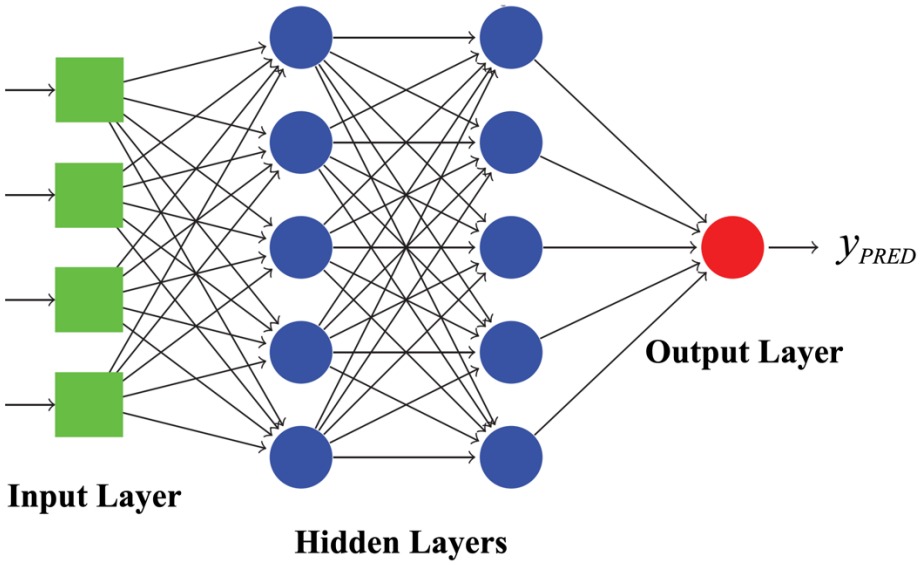


***Figure 3.7.*** *General Structure of an Artificial Neural Network.*

Artificial neurons form the basis for designing a wide variety of neural networks. These neurons, whether in the input, hidden, or output layers, are interconnected and work together to process information. Figure 3.8 illustrates the structure of this artificial neuron

model in the first hidden layer, which receives external input sources and can be understood through three primary stages. The first stage is composed of a set of synapses (connecting links), each of which is characterized by a weight. Specifically, a signal $u_j$ at the input of synapse $j$ connected to neuron $n$ is multiplied by the synaptic weight $W_{n,j}$. The second stage sums all the multiplications of the input signals ($u_j$) and their respective synaptic weights ($W_{n,j}$) from all synapses connected to the neuron. Additionally, this stage includes an externally applied bias, denoted by $b_n$, which is added to the summation result. The final stage involves an activation function $f$, which processes the summed input $v_n$ to produce the output of the neuron ($y_n$). The activation function limits the amplitude of the output, often introducing non-linearity into the model. Typically, the normalized amplitude range of the output of a neuron is written as the closed unit interval [0,1], or, alternatively, [-1,1], enabling neural networks to effectively identify patterns and trends in data.

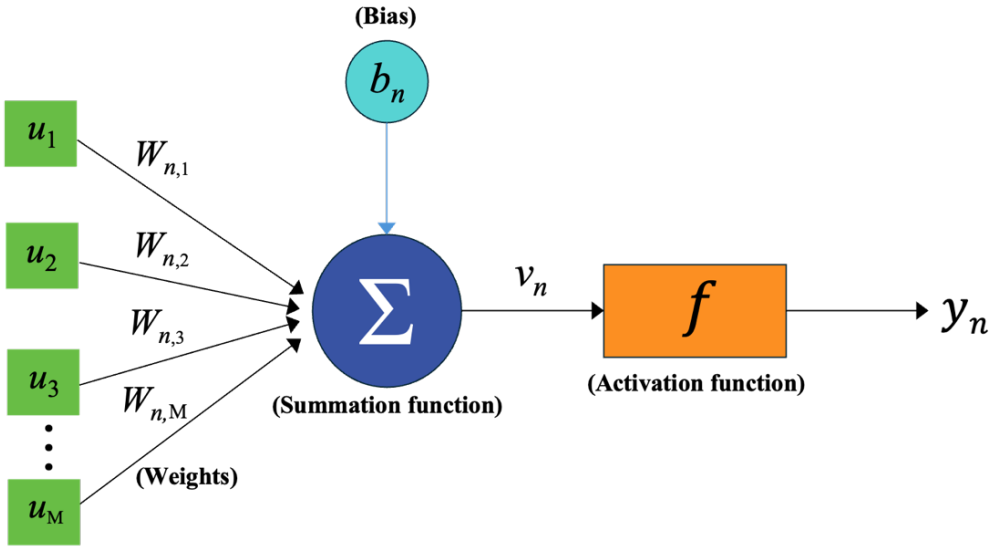


***Figure 3.8.****Block of a single artificial neuron, with M input features.*

The same structural components and operations described (synaptic weights, bias, and activation function) are applicable to neurons throughout subsequent layers, including the output layer. The output of a neuron ($y_n$) in one layer serves as input for neurons in the adjacent layer, allowing the flow of information through the neural network. In mathematical terms, the output of the neuron ($y_n$) depicted in Figure 3.8 can be described by the following pair of equations:

$$x_n = \sum_{j=1}^{M} W_{n,j}.u_j \quad , \tag{3.42}$$

where, $u_1$, $u_2$, …, $u_M$ are the input signals, $W_{n,1}$, $W_{n,2}$, …, $W_{n,M}$, are the respective synaptic weights of the neuron $n$. The linear combiner output, denoted as $x_n$, results from the weighted sum of these input signals. Subsequently, $x_n$ is summed with the bias $b_n$ of the neuron $n$, effectively applying an affine transformation to the output $x_n$, as shown by:

$$v_n = x_n + b_n \tag{3.43}$$

Next, an activation function $f$ processes the summed input $v_n$, referred to as the activation potential, to produce the output of the neuron ($y_n$):

$$y_n = f(v_n) \tag{3.44}$$

There are various activation functions used in neural networks, such as hard-limit, linear, logarithmic sigmoid, hyperbolic tangent sigmoid, and Gaussian, to mention the most common ones. Among these, the hyperbolic tangent sigmoid function (tanh),

defined by Eq. 3.45, is particularly prominent for hidden layers due to its ability to introduce non-linearity and normalize outputs to the range [-1, 1] (Hamidian et al., 2019; Kalman & Kwasny, 1992). This property enhances the network's capability to model complex patterns.

$$f(v) = \tanh(v) \tag{3.45}$$

For the output layer, a linear transfer function (purelin), expressed by Eq. 3.46, is typically employed (Reyes-Téllez et al., 2020). This choice is due to its simplicity and effectiveness in producing a continuous output range, which is essential for tasks requiring regression or precise numerical outputs.

$$f(v) = v \tag{3.46}$$

Figure 3.9 illustrates these activation functions: (a) Hyperbolic Tangent Sigmoid (tanh) and (b) linear transfer function (purelin).

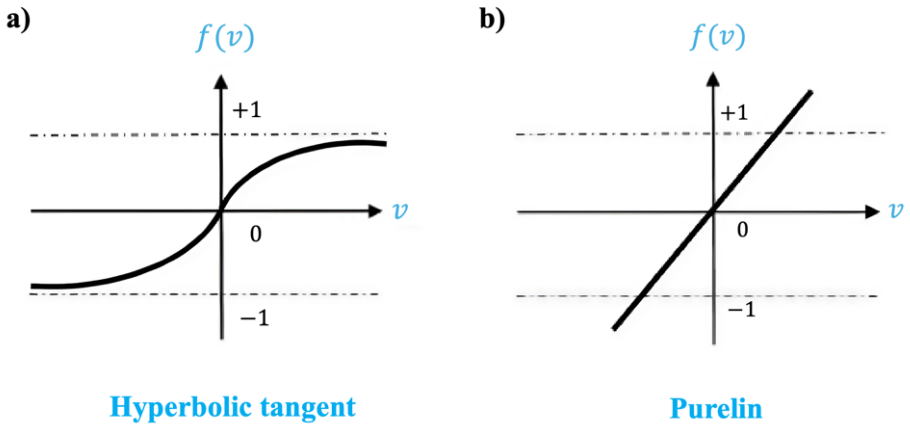


***Figure 3.9.*** *Activation functions plots.*

The learning process of an ANN involves optimizing the weights and biases of the network to minimize the error between the predicted outputs and the actual target values. This optimization is achieved through an iterative process of forward propagation, error calculation, and backward propagation of the error to update the weights, as illustrated in Figure 3.10.

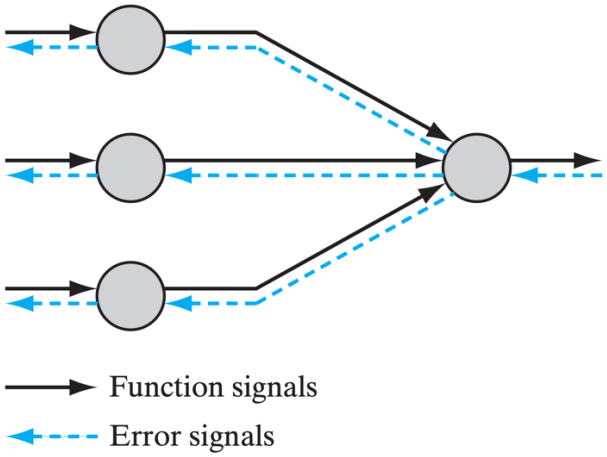


***Figure 3.10.*** *Illustration of the directions of two basic signal flows in an ANN: the forward propagation of activation signals and the backward propagation of error signals.Image taken from Haykin (2009).*

During the forward propagation, the input data ($u$) is passed through the network, where each layer performs a linear transformation followed by an activation function, as described by Equation 3.44. After calculating the output prediction ($y_{PRED}$), the error is calculated by comparing this prediction with the actual target values ($y$). A common error function is calculated as follows:

$$E_D = \frac{1}{N}\sum_{i=1}^{N}(y_{PRED}^{i} - y^{i})^2 \quad , \tag{3.47}$$

where $E_D$ is the mean sum of squares of the network error and $N$ is the number of samples in the training set. This error function evaluates the performance of an ANN by computing the distance between real and predicted data. Based on this evaluation, a backpropagation signal adjusts weights and biases to minimize the error function.

In this manner, neural networks can learn very complicated relationships between inputs and their outputs. However, when datasets contain a large number of attributes, the model may become overly specific to the training data. This can result in poor performance when applied to new, unseen data, a problem known as overfitting (Lawrence et al., 1997). To address this, regularization techniques modify the error function by introducing penalty terms on weights. One such technique is Bayesian regularization algorithm (Foresee & Hagan, 1997) , chosen for its superior generalization capabilities compared to other methods like Levenberg-Marquardt (Abaid, 2022). Bayesian regularization adds an additional term to the objective function to penalize large weights, promoting smoother mapping. The objective function used in Bayesian Regularization algorithm is (Foresee & Hagan, 1997):

$$F = \beta E_D + \alpha E_W \quad , \tag{3.48}$$

where, $E_D$ is the mean sum of squares of the network error (Eq. 3.47), and $E_W$ is the sum of squared weights $\left(\frac{1}{M}\sum_{j=1}^{M} W_j^2\right)$, with $M$ being the total number of weights, and $\alpha$ and $\beta$ are regularization parameters. The process during training adjusts $\alpha$ and $\beta$ to balance the compromise between minimizing the error and the complexity of the model (measured

by the sum of squared weights). This approach helps in improving the ability of the ANN to generalize well to unseen data, thereby reducing the risk of overfitting.

# 4

# Characterizing the Thermophysical Properties of Choline Chloride-Based DESs and Their Mixtures with Cosolvents

*This first chapter of results aims to develop a consistent framework to describe the impact of cosolvents in the key thermophysical properties of the [Ch]Cl-based DESs. To do so, the soft-SAFT EoS is employed to establish a straightforward yet robust coarse-grained molecular model by developing an accurate and transferable parametrization. To complement the DESs modelling studies, an Artificial Neural Network framework is introduced to address the viscosity of the DESs and their mixtures, leveraging molecular parameters derived from COSMO-SAC.*

For large-scale industrial applications of DESs, reliable and accurate knowledge of their thermophysical properties and phase behavior is required. However, given the extensive range of potential DES combinations, including mixtures with cosolvents under various industrial conditions (e.g., different molar ratio, temperature, and pressure), relying solely on experimental measurements becomes time-consuming. Hence, the development of computational models for predicting thermophysical properties of these systems is crucial for expediting their industrial integration. In constructing predictive models, it is pivotal to account for the influence of cosolvents like water on DESs, given their significant impact on DES properties, particularly viscosity, as highlighted in Section 2.1.3. Nonetheless, the development of more general theoretical models remains limited, and the description of the thermodynamic properties over the entire compositional range from pure DESs to a solution of DESs infinitely diluted in a cosolvent is scarce. To overcome this gap, the molecular-based soft-SAFT equation of state and a machine learning technique have been employed to describe physicochemical properties of DESs and their cosolvents mixtures in a quick, efficient, and easy-to-extend manner.

## 4.1 Thermophysical Behavior of DESs from Classical Molecular-Based EoS

As extensively discussed in Section 2.3.1, the soft-SAFT EoS is an attractive framework for reliable estimates of the physicochemical behavior of DESs, as it provides a physically grounded theoretical approach to describing the thermophysical properties of complex molecules and their mixtures. However, one of the most challenging tasks of using this equation for modelling DESs is determining a unique set of parameters for each

compound in the mixture, which must be fully transferable when these compounds form a new DES (Florindo et al., 2019; Zuo et al., 2021). Additionally, the complexity of these solvent mixtures increases when another associating component, such as an alcohol or water, is added as a cosolvent, modifying the network of interactions.

Thus, to address this challenge, the soft-SAFT EoS is used to provide an adequate description of the effect of water, methanol, and ethanol in the thermodynamic properties of several [Ch]Cl-based DESs with up to seven different HBDs. These donors include phenol (PH), ethylene glycol (EG), malonic acid (MA), glycerol (GL), oxalic acid (OA), urea (UR) and glycolic acid (GA) (see Figure 4.1), chosen based on its practical applications as sustainable solvents. The accuracy of the models is evaluated by comparing their performance with available experimental data on the density and viscosity of pure DESs and their mixtures with cosolvents. Additionally, other properties of interest are considered, such as the isentropic compressibility coefficient and speed of sound for pure DES, as well as saturated properties like vapor-liquid equilibrium and water activity coefficients for aqueous DES mixtures.

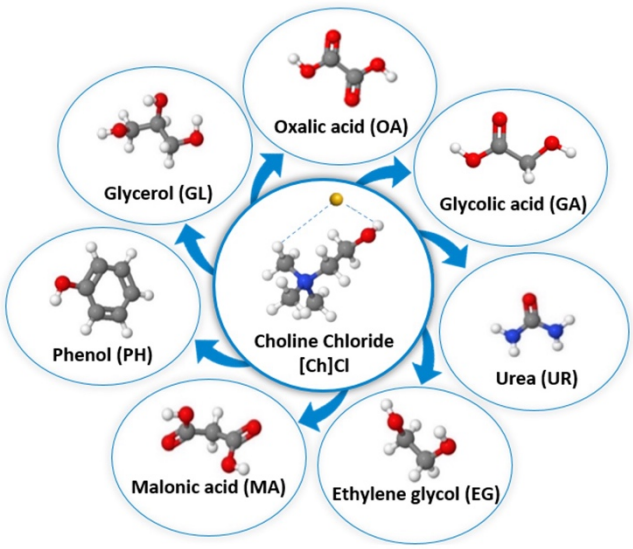


***Figure 4.1.*** *Chemical structures and respective acronyms of the DESs studied in this section.*

### 4.1.1 Molecular Modelling of DESs

The molecular models used with soft-SAFT to describe DESs are a key aspect during the parameterization of molecular parameters and their future transferability. In this regard, it is interesting to present different strategies and compare its performance in addressing this challenge. Consequently, two different approaches are checked in this work to model DESs: the so-called pseudo-pure compound model treats the whole DESs as a single entity, while the individual compound approach considers them as a mixture of two (or more) independent constituents. Both models are schematically shown in Figure 4.2.

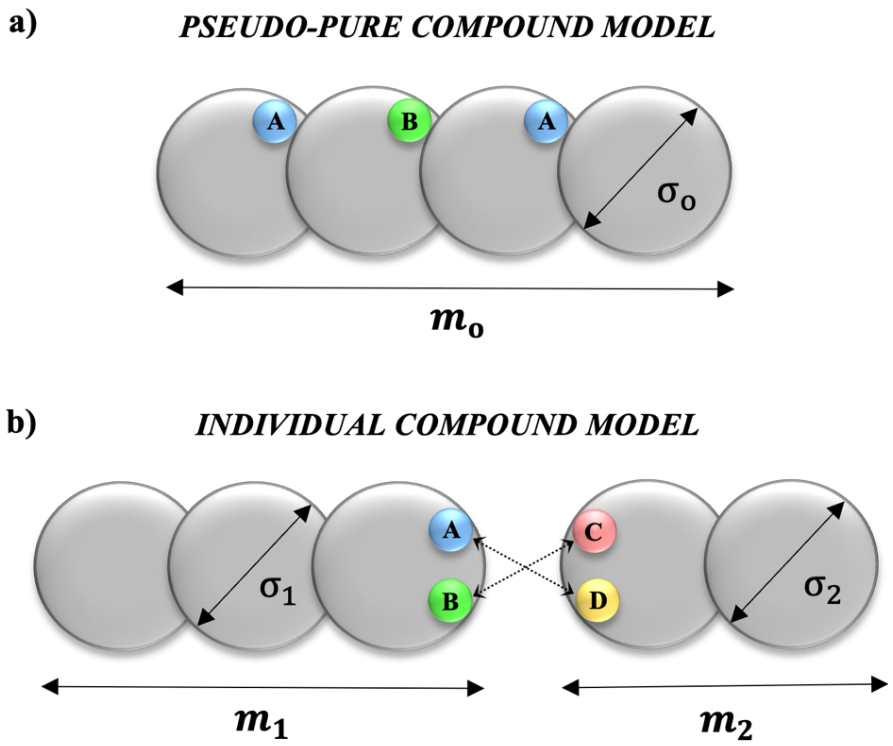


***Figure 4.2.*** *Sketch of the two molecular approaches proposed in this work to model DESs using soft-SAFT: a) Pseudo-pure compound molecular model, b) Individual compound molecular model.*

*Pseudo-Pure Compound Approach*

In this approach, the DESs are considered a pseudo-pure component, with an average molecular mass based on the proportion between their constituents. Implicitly, this means that the compounds forming the DES can never be separated and, consequently, are treated as a whole. Following the classical 3B scheme by Huang and Radosz (1990) three association sites (two type A and one type B associative sites) were included in all cases in order to consider the self-association between the HBA and HBD of the DESs to form a hydrogen bond. In this oversimplified approach, several assumptions and constraints are given: not only the number of sites is fixed, but association interactions are also assumed to be approximately constant, considering that the contribution of association of the hydrogen bonding is the same in all cases (i.e. same volume and energy of association). In addition, the dispersive energy term between the segments also remains fixed. These constraints were successfully applied in modelling DESs of similar nature using soft-SAFT, as reported by Lloret et al. (2017) and Ojeda and Llovell (2018).

The parameters optimization procedure follows two steps, focusing on transferability and repeatability. The values of the three previously mentioned parameters (i.e., $\varepsilon^{HB}/k_B$, $k^{HB}$, $\varepsilon/k_B$) are transferred from previous contributions (Crespo et al., 2019) for all the studied DESs. Then, the parameters referring to the segment diameter ($\sigma$) and chain length ($m$) are optimized in the DES constituted by [Ch]Cl:EG in the proportion 1:2 (see the values in Table 4.1). The optimized $\sigma$ value for this DES (i.e., [Ch]Cl:EG 1:2) is then transferred to other studied DESs, remaining fixed. Finally, the chain length ($m$) is optimized for the remaining investigated DESs, being the only changing parameter. In fact, these assumptions are based on the fact that all [Ch]Cl-based DES share the same

HBA and the size differences can be effectively accounted with the chain length ($m$), reducing the number of parameters to be fitted. Single-phase density data at atmospheric pressure is used for the fitting. The final list of soft-SAFT molecular parameters for each DES using the pseudo-pure component approach are included in Table 4.1.

The highest degree of transferability was sought to obtain consistent sets of molecular parameters among the compounds. As a result of the procedure, four (i.e. σ, $\varepsilon/k_B$, $\varepsilon^{HB}/k_B$, $k^{HB}$) out of five molecular parameters were kept constant in all DESs investigated in this work. Additionally, the remaining chain length parameter ($m$) follows clear linear tendency with the molecular weight ($M_w$) of the respective DES. This may indicate that the volume change of DES, related to different ratios of the involved species, is properly captured by the $m$ parameter (Lloret et al., 2017; Zubeir et al., 2016).

***Table 4.1.*** *soft-SAFT EoS molecular parameters optimized for [Ch]Cl-based DESs with the pseudo-pure compound approach*

| DES | $M_w$ (g/mol) | $m$ | σ (Å) | $\varepsilon/k_B$ (K) | $\varepsilon^{HB}/k_B$ (K) | $k^{HB}$ (Å$^3$) |
|---|---|---|---|---|---|---|
| [Ch]Cl:EG (1:2.5) | 83.790 | 2.30897 | 3.71343 | 387.308 | 3450 | 2250 |
| [Ch]Cl: EG (1:2) | 88.030 | 2.43006 | 3.71343* | 387.308 | 3450 | 2250 |
| [Ch]Cl:EG (1:1.77) | 89.990 | 2.47464 | 3.71343 | 387.308 | 3450 | 2250 |
| [Ch]Cl:UR (1:2) | 88.690 | 2.22802 | 3.71343 | 387.308 | 3450 | 2250 |
| [Ch]Cl:PH (1:6) | 100.61 | 2.85287 | 3.71343 | 387.308 | 3450 | 2250 |
| [Ch]Cl:PH (1:5) | 101.70 | 2.87887 | 3.71343 | 387.308 | 3450 | 2250 |
| [Ch]Cl:PH (1:4) | 103.21 | 2.91499 | 3.71343 | 387.308 | 3450 | 2250 |
| [Ch]Cl:PH (1:3) | 105.49 | 2.97023 | 3.71343 | 387.308 | 3450 | 2250 |
| [Ch]Cl:PH (1:2) | 109.28 | 3.06379 | 3.71343 | 387.308 | 3450 | 2250 |
| [Ch]Cl:GL (1:3) | 103.97 | 2.64902 | 3.71343 | 387.308 | 3450 | 2250 |
| [Ch]Cl: GL (1:2) | 107.95 | 2.78270 | 3.71343 | 387.308 | 3450 | 2250 |
| [Ch]Cl: GL (1:1) | 115.86 | 3.06842 | 3.71343 | 387.308 | 3450 | 2250 |
| [Ch]Cl:MA (1:2) | 115.80 | 3.00973 | 3.71343 | 387.308 | 3450 | 2250 |
| [Ch]Cl:GA (1:1) | 107.84 | 2.77007 | 3.71343 | 387.308 | 3450 | 2250 |
| [Ch]Cl:OA (1:1) | 114.83 | 2.80538 | 3.71343 | 387.308 | 3450 | 2250 |

$k_B$= 1.380649.10$^{-23}$ J K$^{-1}$, Boltzmann constant,

* σ parameter adjusted for these mixture dataset and transferred to the other DESs in this table.

This identified trend in the *m* parameter can be easily correlated with the linear expressions in Eqs. 4.1- 4.3, for [Ch]Cl:EG, [Ch]Cl:PH and [Ch]Cl:GL, respectively:

$$m = 0.027M_w + 0.0469 \quad (R^2 = 0.9974) \quad (\mathrm{EG}) \quad (4.1)$$

$$m = 0.0243M_w + 0.4042 \quad (R^2 = 0.9999) \quad (PH) \quad (4.2)$$

$$m = 0.0368M_w - 1.1838 \quad (R^2 = 0.9991) \quad (\mathrm{GL}) \quad (4.3)$$

Thus, only one parameter ($m$) was adjusted in all cases, without resulting in any loss of precision. The behavior of parameter *m*, described through the Eqs. 4.1, 4.2 and 4.3, is shown in Figure 4.3.

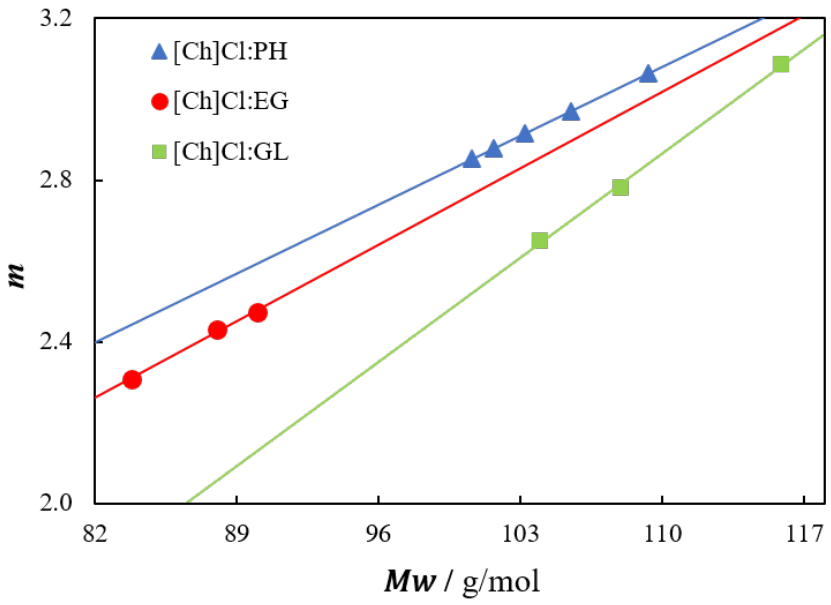


***Figure 4.3.*** *Trend for the chain length (m) molecular parameter of soft-SAFT EoS with the molecular weight ($M_w$) of DESs for [Ch]Cl: PH; [Ch]Cl:EG and [Ch]Cl:GL (pseudo-pure component approach). The symbols are the specific values for each compound and the lines are linear regressions. The remaining soft-SAFT parameters considered are reported in Table 4.1. of this section.*

As it is shown in Fig. 4.3, within the same family of compositions, the chain length parameter exhibits the same pattern, increasing with the molecular weight. The fact that the parameters have a clear pattern facilitates the possibility of describing, in a transferable manner, the thermophysical properties of other DESs from the same family, but different proportions, for which no experimental data are available, seeking a compromise between simplicity and precision.

*Individual Component Approach*

Applying a more rigorous method, this second approach treats DESs as a mixture of independent species. In this case, individual molecular models for [Ch]Cl, phenol (PH), ethylene glycol (EG), malonic acid (MA), glycerol (GL), oxalic acid (OA), urea (UR), and glycolic acid (GA) are proposed. Crespo et al. (2019) identified five associative sites for [Ch]Cl; however, despite yielding promising results, this model complicates the number of cross-associations. To maintain the transferability of soft-SAFT parameters, we simplified these interactions to two association sites for [Ch]Cl, one positive and one negative, simulating the cation-anion interaction, similar to the approach used for tetraalkylammonium salts (Lloret et al., 2017). The MA, OA, and GA are also modeled with two association sites, one positive and one negative, in order to mimic the hydroxyl groups that are present in these molecules, following the same hypothesis done for lactic acid (Lloret et al., 2017) and 1-alkanols (Llovell et al., 2013d). For consideration of hydrogen bonding in UR, two association sites were also used in a similar way when modeled in the literature using PC-SAFT (Held et al., 2010). Seeking the transferability of parameters, the association parameter values of [Ch]Cl, MA, OA, GA, and UR were

the same and were transferred from Lloret et al. (2017) work. The molecular models for the PH, GL, and EG are the same as those published by Crespo et al. (2019) for the first two and by Pedrosa et al. (2005) for the latest one and all their parameters are taken from those respective works. PH, GL, and EG molecules are modeled using 2-site association schemes. Water, which here is considered independently in both, pseudo-pure compound and individual component approaches, is modeled using the 4-site model as proposed by Vega et al. (2009), and their parameters are taken from that work. Finally, methanol and ethanol are modeled using a 2-site association scheme, as proposed by Pàmies (2003) and their parameters are taken from that work.

While in the classical soft-SAFT approach, the molecular parameters of a species are fitted to their vapor pressure and liquid density data (i.e. water, phenol), the approach to compounds exhibiting negligible vapor pressures, such as is the case of Ionic Liquids or DESs, requires an alternative approach. Single-phase densities are commonly used. An additional constraint, particularly important in the case of DESs, is the fact that the individual components are solid when being alone (not forming the eutectic mixture), as is the case of [Ch]Cl at room temperature. In this regard, Lloret et al. (2017) circumvented this issue by estimating the molecular parameters of the salt using the DESs data that this salt forms with another compound, for which the pure component could be well characterized. Therefore, the same approach is followed here: the molecular parameters of [Ch]Cl are estimated using the density data of the DESs that this salt forms with PH (whose molecular parameters where previously obtained using saturated liquid density and vapor pressure data (Crespo et al., 2019). The choice of [Ch]Cl:PH DES is done given the considerable amount of data at many different proportions available in the open literature (Guo et al., 2013), reducing the parameters degeneracy and ensuring a good

realistic parametrization of [Ch]Cl. Once the [Ch]Cl parameters are found, they are used to describe their mixtures with EG and GL in a predictive manner, given the fact that EG and GL can also be fitted using pure component information. Finally, the density data of the [Ch]Cl-based DESs with MA, OA, GA and UR are used to obtain the molecular parameters of these latter molecules, as pure density data for them are unavailable. A scheme depicting the soft-SAFT molecular parametrization procedure for DESs followed in this second approach is shown in Figure 4.4.

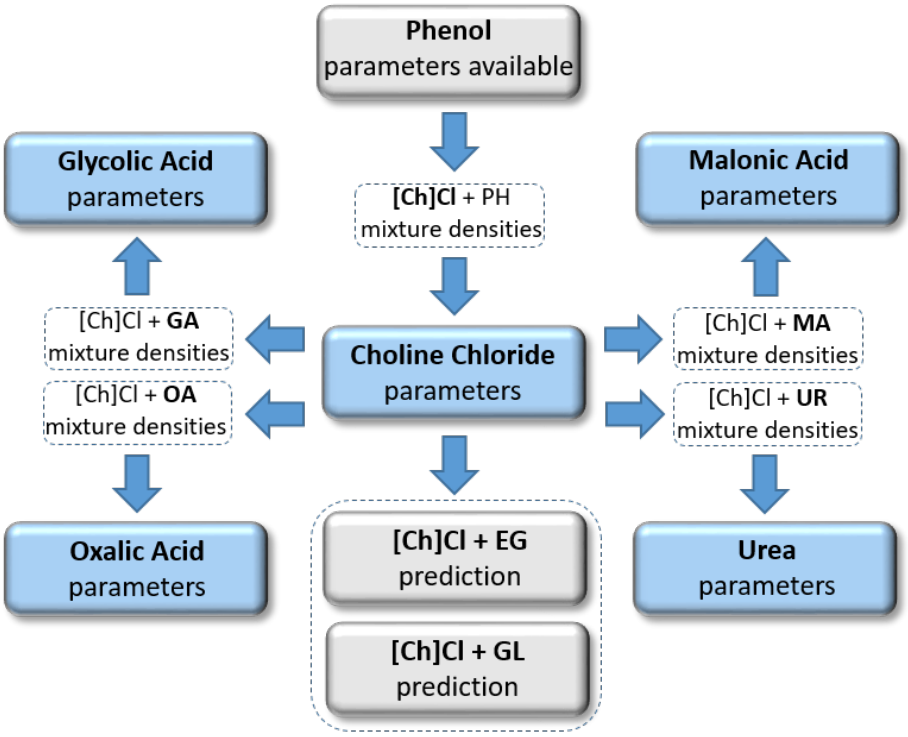


***Figure 4.4.*** *Scheme of the procedure followed to optimize the soft-SAFT molecular parameters of the different DESs forming species considered in section.*

The soft-SAFT molecular parameters using the individual component approach of the compounds involved in the different DESs are summarized in Table 4.2.

***Table 4.2.*** *soft-SAFT molecular parameters optimized for the species that form Deep Eutectic Solvents using the individual component approach, and cosolvents.*

| Compound | $M_w$ (g/mol) | $m$ | $\sigma$ (Å) | $\varepsilon/k_B$ (K) | $\varepsilon^{HB}/k_B$ (K) | $k^{HB}$ (Å$^3$) | Reference |
|---|---|---|---|---|---|---|---|
| Choline chloride | 139.63 | 5.096 | 3.401 | 428.40 | 3384* | 2100* | This work |
| Malonic acid | 104.06 | 4.674 | 3.052 | 403.40 | 3384* | 2100* | This work |
| Oxalic acid | 90.03 | 2.675 | 3.208 | 380.90 | 3384* | 2100* | This work |
| Glycolic acid | 107.84 | 2.526 | 3.241 | 425.20 | 3384* | 2100* | This work |
| Urea | 60.06 | 2.458 | 3.090 | 420.70 | 3384* | 2100* | This work |
| Phenol | 94.11 | 2.155 | 3.995 | 384.65 | 3099 | 2250 | (Crespo et al., 2019) |
| Ethylene glycol | 62.07 | 1.751 | 3.668 | 326.05 | 4384 | 4195 | (Pedrosa et al., 2005) |
| Glycerol | 92.09 | 2.397 | 3.638 | 392.95 | 4945 | 2250 | (Crespo et al., 2019) |
| Water | 18.02 | 1.000 | 3.154 | 365.00 | 2388 | 2932 | (Vega et al., 2009) |
| Methanol | 32.04 | 1.491 | 3.375 | 220.40 | 3213 | 4847 | (Pàmies, 2003) |
| Ethanol | 46.07 | 1.740 | 3.635 | 234.80 | 3387 | 2641 | (Pàmies, 2003) |

In order to maximize the degree of transferability of the parameters and assure consistency among the obtained values, several working hypotheses and constraints are applied. For instance, the energy and volume of association of the compounds calculated in this thesis (the carboxylic acids and urea) are kept constant, and transferred from the molecular parameters obtained for tetraalkylammonium chloride salts by Lloret et al. (2017). Consequently, the energetic differences between these compounds have then been effectively accounted for in the dispersive energy contribution ($\varepsilon/k_B$), finding a higher value for [Ch]Cl due to its stronger hydrogen bonding character compared to the other molecules (Crespo et al., 2019). In terms of size and volume, a comparison of the *m* values of these compounds reveals they follow the same trend with the order of their respective van der Waals volumes (Chemspider, 2022): [Ch]Cl > MA > OA > GA > UR (see Table 4.2). Furthermore, the molecular parameters obtained for [Ch]Cl under this approach are found to be in good agreement with those reported by Lloret et al. (2017) for tetraalkylammonium chloride salts, as the chain length (*m*) is in between that obtained for

tetramethylammonium chloride and tetrabutylammonium chloride, as expected given the size of the different salts.

### 4.1.2 Validation of Pure DESs

*Density*

The performance of soft-SAFT in predicting the density-temperature diagram for pure DESs utilizing the pseudo-pure components approach with optimized parameters for each DES listed in Table 4.1 is illustrated in Figure 4.5.

As it can be observed, soft-SAFT properly reproduces the values and tendencies of densities, since the model quantitatively describes the increase of density when decreasing temperature for a given DES. An excellent agreement between the densities of the experimental data (Florindo et al., 2014; Guo et al., 2013; Shahbaz et al., 2012; Yadav et al., 2015; Yadav & Pandey, 2014; Yadav et al., 2014) and those calculated using soft-SAFT is achieved, with a maximum %AAD of 0.241% among all the studied cases. Moreover, within a DES family with different HBA:HBD ratios, soft-SAFT properly captures the density change with the HBD ratio modification in the mixture. The results corroborate the same conclusions achieved when this approach was successfully applied in modelling tetraalkylammonium-based DESs using soft-SAFT EoS, as reported by Lloret et al. (2017) and Ojeda and Llovell (2018).

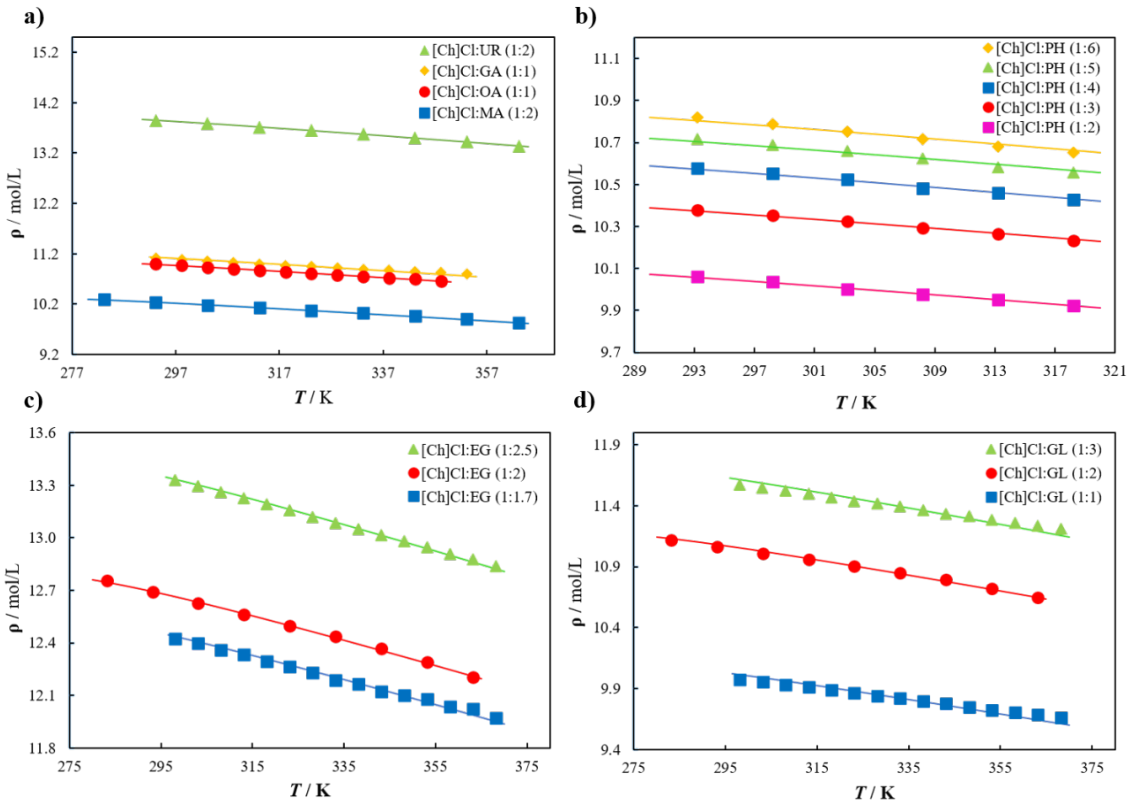


***Figure 4.5.*** *Density (ρ) – temperature (T) diagram, at atmospheric pressure, using the pseudo-pure compound approach for [Ch]Cl:UR (1:2), [Ch]Cl:GA (1:1), [Ch]Cl:OA (1:1) and [Ch]Cl:MA (1:2); b) [Ch]Cl:PH at different ratio; c) [Ch]Cl:EG at different ratio; d) [Ch]Cl:GL at different ratio. In all Figures, symbols are experimental data (Florindo et al., 2014; Guo et al., 2013; Shahbaz et al., 2012; Yadav et al., 2015; Yadav & Pandey, 2014; Yadav et al., 2014), while the lines are the soft-SAFT predictions (with parameters from Table 4.1).*

Although the modelling of the DESs using the pseudo-pure component approach is a quite simple model, it nonetheless provides an excellent description of their densities across all systems investigated in this section. However, one drawback of this methodology is the fact that a different $m$ parameter is required at each different HBA:HBD proportion, even if the same compounds are utilized. In addition, the impossibility to separate both compounds may become unrealistic under the addition of water or other cosolvents.

Following the rigorous individual component approach previously explained, the performance of soft-SAFT in describing the density of the studied pure DESs using optimized parameters for each constituent compound of the DES (refer to Table 4.2) is depicted in Figure 4.6. The results demonstrate that the description of the densities of DESs remains very good, despite treating each system as a binary mixture without binary parameters. The average absolute deviation (%AAD) remains consistently below 0.901% across all cases, underscoring the accuracy of the model. Here, it is important to notice that, while the data of Figures 4.6 (a) and 4.6 (d) were used to fit the single-compound parameters, the description of the DES with EG - Figure 4.6 (b), and GL - Figure 3 (c) is fully predictive. The density changes with DESs compositions and temperatures are properly captured in all cases, with the highest deviations found for the DESs with EG, where the experimental information comes from two different sources: at (1:2) from Yadav et al. (2015), and at (1:1.7) and (1:2.5) from Shahbaz et al. (2012). Still, the description of the system is rather accurate, and the methodology presented here offers a higher degree of transferability compared to the pseudo-pure component approach.

Consequently, from now on, the individual component approach is the model chosen and used in a systematic manner in the rest of the chapter for the characterization of DESs.

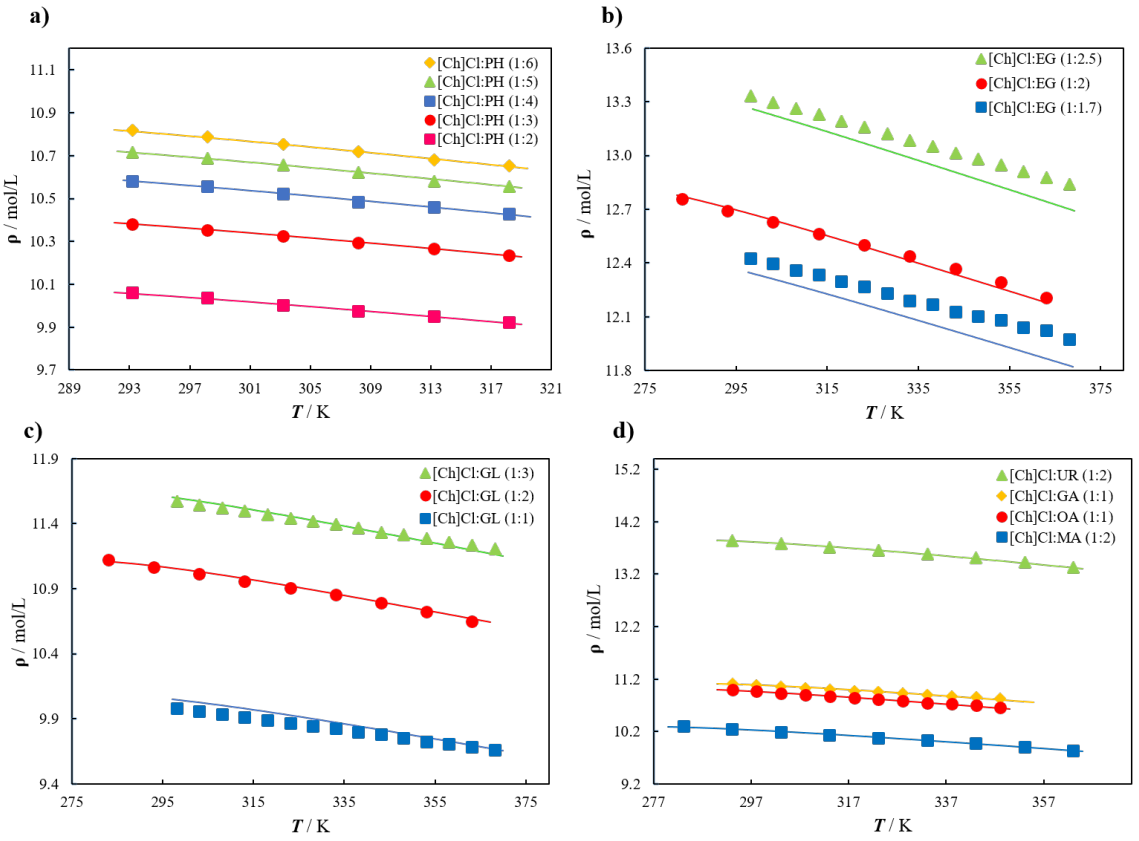


***Figure 4.6.*** *Density (ρ) – temperature (T) diagram, at atmospheric pressure, using the individual-component approach for a) [Ch]Cl:PH at different ratios; b) [Ch]Cl:EG at different ratios; c) [Ch]Cl:GL at different ratios; d) [Ch]Cl:UR (1:2), [Ch]Cl:GA (1:1), [Ch]Cl:OA (1:1) and [Ch]Cl:MA (1:2);. In all figures, symbols correspond to experimental data (Florindo et al., 2014; Guo et al., 2013; Shahbaz et al., 2012; Yadav et al., 2015; Yadav & Pandey, 2014; Yadav et al., 2014), while the lines to soft-SAFT calculations and predictions (with parameters from Table 4.2).*

*Derivative properties*

The molecular nature of the soft-SAFT parameters allows the prediction of derivative thermodynamic properties for the studied DES. Apart from the necessity of this information in industrial applications, these properties constitute an excellent validation test for the model, as they are second-order properties of a primary thermodynamic function and, consequently, are more prone to errors. In this sense,

although the previous parametrization using the individual-component approach allowed an excellent description of the density, further validation of the reliability of these parameters for each constituent compound is performed by predicting some derivative properties of importance for process design. The expressions for the speed of sound and the compressibility, computed in this work, are:

$$u = \sqrt{\frac{C_p}{C_v}\left(\frac{\partial P}{\partial \rho}\right)_T} \tag{4.4}$$

$$K_S = \frac{C_v K_T}{C_p} \quad , \tag{4.5}$$

where $u$ is the speed of sound, $C_v$ and $C_p$ are the isochoric and isobaric heat capacity, and $K_S$ and $K_T$ are the isentropic and isothermal compressibility, respectively. Following Yokozeki and Shiflett (2010), the Harrison-Seaton method (Harrison & Seaton, 1988) has been utilized to calculate the ideal gas heat capacity of DESs, which is added to the residual term evaluated from soft-SAFT. The coefficients determined using the Harrison-Seaton method, which are used to calculate the ideal gas heat capacity, are shown in Table 4.3.

***Table 4.3.*** *Coefficients for calculating the ideal gas heat capacity of DESs.*

| DES | Cp0 ($J\ mol^{-1}$) | Cp1 ($J\ mol^{-1}K^{-1}$) | Cp2 ($10^{-4}J\ mol^{-1}K^{-2}$) | Cp3 ($10^{-8}J\ mol^{-1}K^{-3}$) |
|---|---|---|---|---|
| ChCl:UR (1:2) | 17.8766 | 1.2224 | -0.0007 | 2E-07 |
| ChCl:EG (1:2) | -24.6896 | 1.3673 | -0.0008 | 2E-07 |

* $C_P^0 = Cp0 + Cp1 * T + Cp2 * T^2 + Cp3 * T^3$, *estimated from Harrison-Seaton method (Harrison & Seaton, 1988).*

In particular, the speed of sound and the isentropic compressibility coefficient for [Ch]Cl:UR (1:2) and [Ch]Cl:EG (1:2), were predicted and displayed in Figure 4.7. The results show that the proposed model captures well the influence of temperature on both derivative properties studied here. This is an important fact, given the strong sensitivity of these properties to slight deviations in the density description. The agreement with the available experimental data (Abdel Jabbar & Mjalli, 2019) for the speed of sound (AAD%) was 1.72% for [Ch]Cl:EG (1:2) and 3.01% for [Ch]Cl:UR (1:2), while for the isentropic compressibility coefficient it slightly increased up to 1.93% for [Ch]Cl:EG (1:2) and 4.30% for [Ch]Cl:UR (1:2).

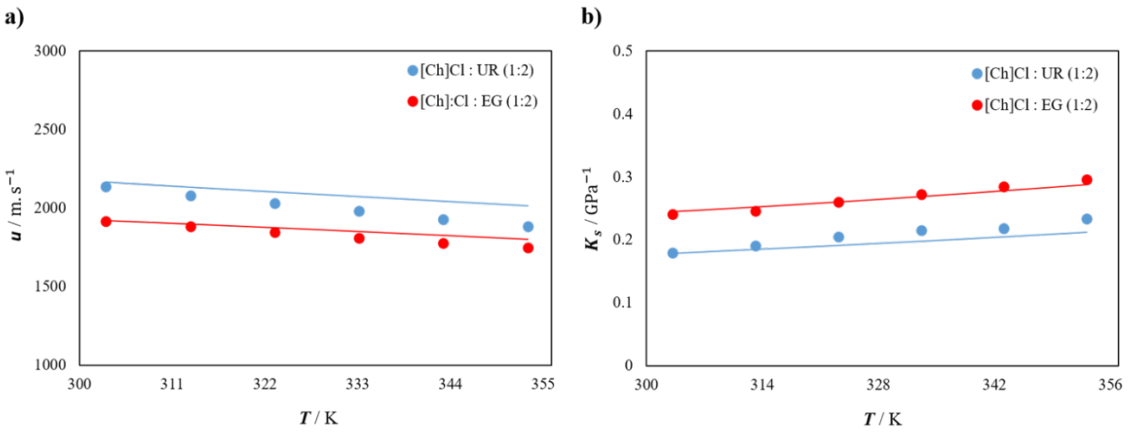


***Figure 4.7.*** *a) Speed of sound (u) – temperature (T) diagram, of [Ch]Cl:UR (1:2) and [Ch]Cl:EG (1:2), and b) Isentropic compressibility coefficient ($K_s$) – temperature (T) diagram. These derivative properties were calculated at atmospheric pressure, using the individual-component approach. In both figures, symbols correspond to experimental data (Abdel Jabbar & Mjalli, 2019), while the lines to soft-SAFT predictions (with parameters from Table 4.2).*

*Viscosity*

Another property that generally governs the use of DESs as a solvent in different fields of application is its viscosity. In this regard, measurements of the viscosity of

[Ch]Cl:EG (1:2) (Wang et al., 2020), [Ch]Cl:GL (1:2) (Yadav et al., 2014), [Ch]Cl:UR (1:2) (Yadav & Pandey, 2014) and [Ch]Cl:OA (1:1) (Florindo et al., 2014), [Ch]Cl:MA (1:2) (Mjalli & Naser, 2015) and [Ch]Cl:PH (Guo et al., 2013) at different molar proportions are available. The viscosities of these DESs were obtained by means of the FVT treatment combined with soft-SAFT, applying the spider-web methodology (Cané et al., 2017) to fit the FVT parameters for the molecules forming the examined DESs using mixture data. The density values required for the use of FVT were calculated through the soft-SAFT EoS considering the proposed individual compounds model approach. The optimized parameters for both the DESs constituents and cosolvents are listed in Table 4.4, and the model's performance in describing pure DES viscosities is shown in Figure 4.8. Overall, there is excellent agreement (ADD% of 4.01) between the experimental viscosities (Florindo et al., 2014; Guo et al., 2013; Mjalli & Naser, 2015; Wang et al., 2020; Yadav & Pandey, 2014; Yadav et al., 2014) and those calculated using soft-SAFT + FVT, with the major deviations observed for [Ch]Cl:UR (1:2) DES at low temperatures. In general, a slight deterioration occurs at the highest viscosity values, where the data also has a higher degree of uncertainty. It should be noted that the calculations of the viscosity of DESs using the FVT parameters indicated in Table 4.4 do not require the use of any binary parameter to reproduce the data shown in Figure 4.8

***Table 4.4.*** *Free-Volume Theory viscosity parameters optimized for Deep Eutectic Solvents forming molecules and cosolvents.*

| Compound | $M_w$ (g/mol) | $\alpha$ (J m$^3$ mol$^{-1}$ kg$^{-1}$) | $B \cdot 10^2$ | $L_v \cdot 10^2$ (Å) |
|---|---|---|---|---|
| Choline chloride | 139.63 | 374.58 | 0.6867 | 0.0170 |
| Phenol | 94.11 | 223.94 | 0.5742 | 3.1873 |
| Glycerol | 92.09 | 335.74 | 0.2794 | 2.9452 |
| Ethylene glycol | 62.07 | 356.55 | 0.0911 | 8.5466 |
| Malonic acid | 104.06 | 835.54 | 0.0001 | 0.0648 |
| Urea | 60.06 | 603.47 | 0.0001 | 1.7156 |
| Oxalic acid | 90.03 | 698.09 | 0.0170 | 0.0292 |
| Water | 18.02 | 485.21 | 0.1001 | 1.4239 |
| Methanol | 32.04 | 408.65 | 0.1358 | 4.7032 |
| Ethanol | 46.07 | 433.36 | 0.1373 | 9.2660 |

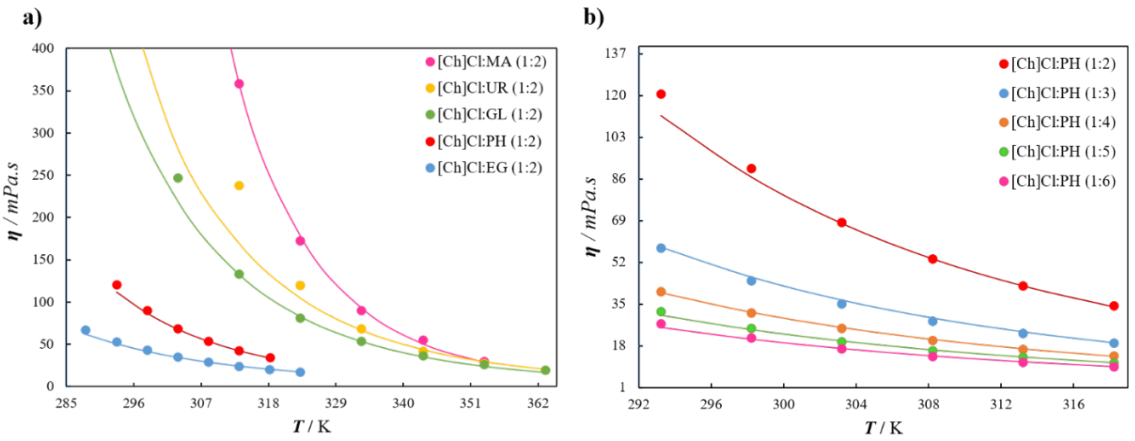


***Figure 4.8.*** *Viscosity (η) – temperature (T) diagram, at atmospheric pressure, modeled using FVT parameters shown in Table 4.4 for a) [Ch]Cl-based DESs with different HBD b) [Ch]Cl: PH at different ratio. In all figures, symbols correspond to experimental data (Florindo et al., 2014; Guo et al., 2013; Mjalli & Naser, 2015; Wang et al., 2020; Yadav & Pandey, 2014; Yadav et al., 2014), while the lines to soft-SAFT + FVT predictions.*

### 4.1.3 Validation of Properties of Aqueous Mixtures of DESs

*Vapor-liquid equilibria and water activity coefficients*

After the validation of the parametrization strategy proposed in previous section, the individual component approach of the DESs is used to calculate the vapor-liquid phase equilibria (VLE) and water activity coefficients ($\gamma_{H20}$) of their aqueous ternary mixtures. The $\gamma_{H20}$ of the aqueous mixtures were calculated using Eq. 4.6, as in Oliveira et al. (2016), which states the isofugacity condition considering the ideal vapor phase:

$$\gamma_{H20} = \frac{P\, y_{H20}}{x_{H20}\, P_{H20}^{sat}} \quad , \tag{4.6}$$

where $P$ the pressure of the system, $P_{H20}^{sat}$ is the saturation pressure of pure water at the working temperature, and $x_{H20}$ and $y_{H20}$ represent the mole fraction of water in the liquid and vapor phases, respectively.

To achieve a good agreement of soft-SAFT predictions with the experimental data (Peng et al., 2017; Sharma et al., 2018; Sharma et al., 2020), the addition of one energy binary parameter is necessary for all mixtures. The cross-dispersive energy parameter for each mixture, $\xi_{ij}$ (see Eq. 3.22, in Section 3.1.2), is obtained by fitting VLE data at atmospheric pressure, minimizing the %AAD. A summary of the binary parameters used for each case is provided in Table 4.5.

***Table 4.5.*** *Fitted soft-SAFT energy binary interaction parameter.*

| Compound *i* | Compound *j* | $\xi_{ij}$ | References* |
|---|---|---|---|
| Choline chloride | Water | 1.045 | (Peng et al., 2017) |
| Urea | Water | 1.280 | (Peng et al., 2017) |
| Glycolic Acid | Water | 1.280 | (Sharma et al., 2020) |
| Malonic Acid | Water | 1.370 | (Sharma et al., 2018) |

* Source of adjusted experimental data.

Note that $\xi_{ij}$ is adjusted to account for interactions between water-HBD and water-HBA. It is possible to observe that the cross-dispersive energy parameter $\xi_{ij}$, is fitted in all cases to values greater than one, which is evidence that the model underestimates the van der Waals interactions between water and the DESs. On the other hand, it is important to notice that the water-Choline Chloride parameter is common in all mixtures and can be transferred to any system where these two compounds are present. An additional strength is the fact that all parameters are temperature-independent. The results of this modelling are displayed in Figure 4.9.

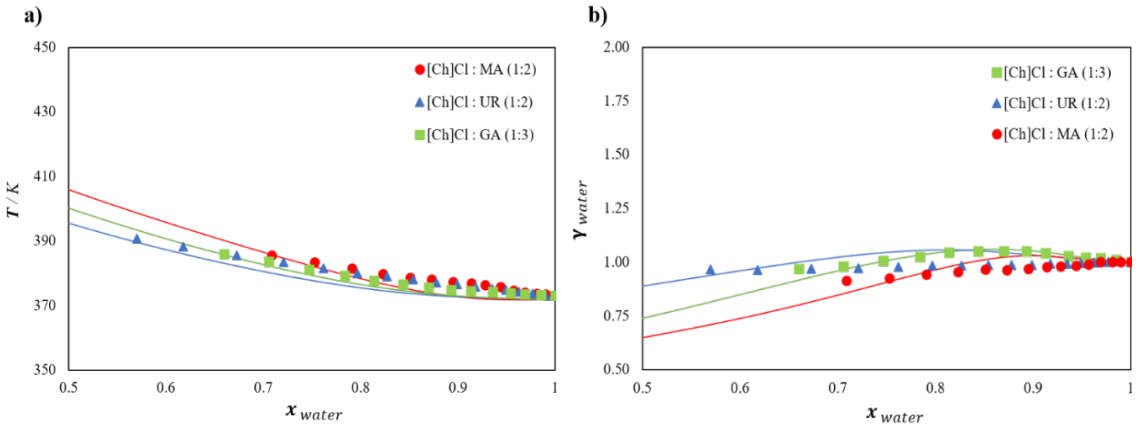


***Figure 4.9.*** *a) Vapor-Liquid Equilibrium and b) Water activity coefficients at 298.15 K, at atmospheric pressure, considering ternary mixture for aqueous DESs: [Ch]Cl:UR (1:2), [Ch]Cl:GA (1:3) and [Ch]:Cl:MA (1:2). In both figures, symbols are experimental data (Peng et al., 2017; Sharma et al., 2018; Sharma et al., 2020) while the lines are the soft-SAFT predictions (with parameters from Tables 4.2 and 4.5).*

In general terms, good agreement with the experimental data (Peng et al., 2017; Sharma et al., 2018; Sharma et al., 2020) is found in most of the cases for the VLE (with an AAD% of 6.05%, 8.11%, and 11.08% for [Ch]:Cl:GA (1:3), [Ch]Cl:MA (1:2) and [Ch]Cl:UR (1:2) respectively); and in all cases for $\gamma_{H20}$ (with an AAD% between 1.76% and 4.6%)

*Density*

Once the energy interaction parameters between water and the compounds forming the eutectic mixture have been established, this information is used to predict the effect of water on other thermophysical properties, such as the density of DESs. Using the pure-component parameters from Table 4.2 and the binary parameters from Table 4.4, excellent predictions of the ternary mixture densities are obtained, as shown in Figure 4.10.

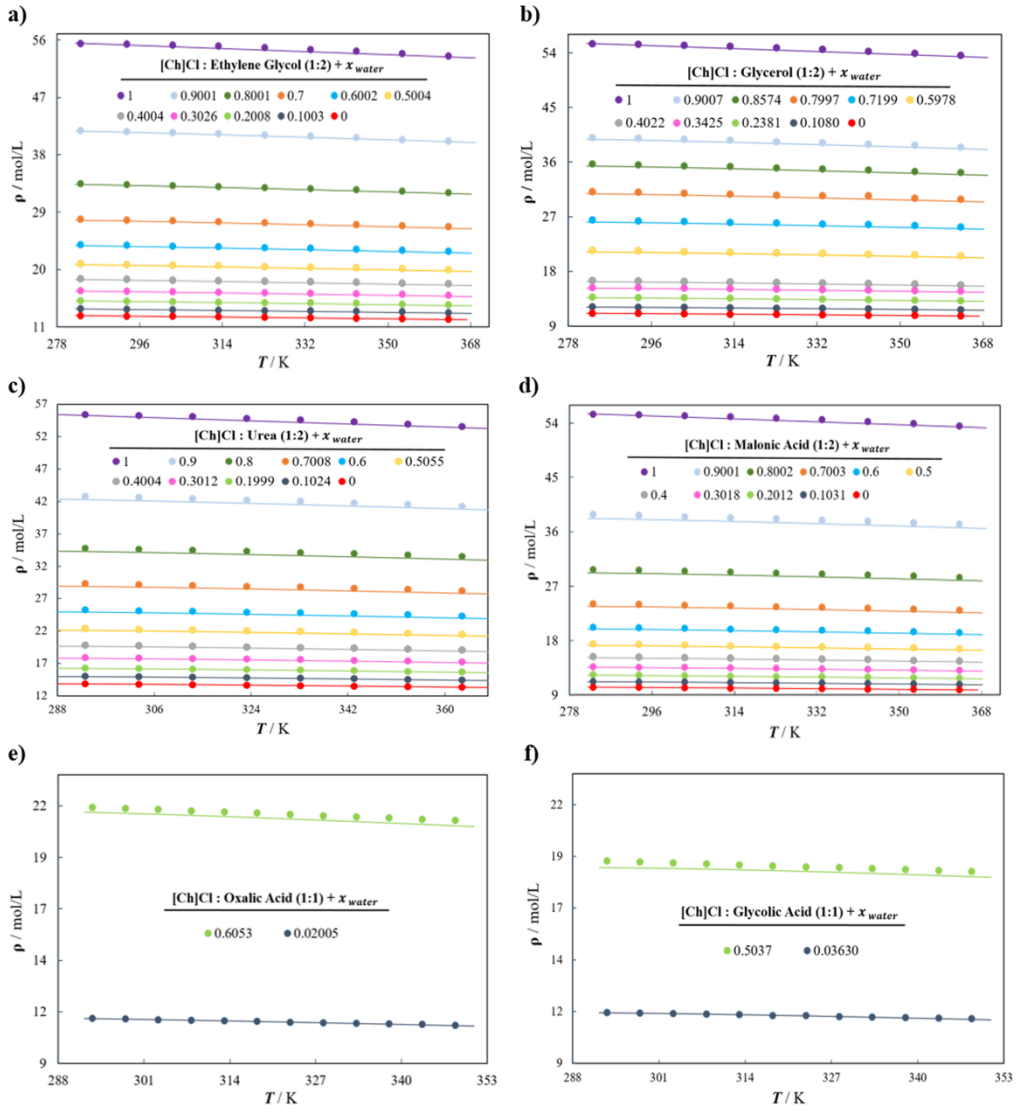


***Figure 4.10.*** *Density (ρ) – temperature (T) diagram, at atmospheric pressure, considering ternary mixture for aqueous mixtures of DESs at different molar fraction of water for a) [Ch]Cl:EG (1:2); b) [Ch]Cl:GL (1:2); c) [Ch]Cl:UR (1:2); d) [Ch]Cl:MA (1:2) , e) [Ch]Cl:OA (1:1) and f) [Ch]Cl:GA (1:1). In all figures, symbols correspond to experimental data (Florindo et al., 2014; Yadav et al., 2015; Yadav & Pandey, 2014; Yadav et al., 2014), while the lines to soft-SAFT predictions (with parameters from Tables 4.2 and 4.5).*

The %AAD values which stand for the deviations of the densities predicted with the soft-SAFT from the experimental data (Florindo et al., 2014; Yadav et al., 2015; Yadav & Pandey, 2014; Yadav et al., 2014) are 0.67%, 0.81%, 0.88%, 1.01%, 0.56%, and 0.79% for the aqueous mixtures of the studied DESs (i.e, [Ch]Cl:EG, [Ch]Cl:GL, [Ch]Cl:UR, [Ch]Cl:MA, [Ch]Cl:OA and [Ch]Cl:GA, respectively). Baz et al. (Baz et al., 2019) predicted the densities of the liquid phase for aqueous [Ch]Cl + GL (1:2) DESs mixtures through PC-SAFT EoS and a similar two-compounds approach. They observed that, while predictions were accurate for pure compounds and mixtures with high water content, the experimental densities were overestimated, up to 2.6% of deviation, for mixtures with low water content (less than 0.5 in molar basis). In this thesis, soft-SAFT predictions are fully accurate in the whole range of compositions, from pure DESs to infinitely dilute solutions, regardless of the DESs being studied.

For the sake of comparison, an additional test with the pseudo-pure compound approach was performed by predicting the density in aqueous solutions of DESs when considering the system as a binary mixture (one compound is a DES as a pseudo-pure compound and the other is water). For this approach, the parameters of Table 4.1 in this section were used for the DESs and the parameters of Table 4.2 were employed for water. The results considering the binary mixtures of aqueous solutions of DESs, treated as pseudo-pure compounds, are displayed in Figure 4.11, and they look almost identical to Figure 4.10 (considering a ternary mixture). Again, excellent agreement between the soft-SAFT predictions and the available experimental data (Florindo et al., 2014; Yadav et al., 2015; Yadav & Pandey, 2014; Yadav et al., 2014) of the density of aqueous solutions of the DESs were obtained for all systems investigated using this approach, with a %AAD of 0.432% with respect to all the points shown in Figure 4.11.

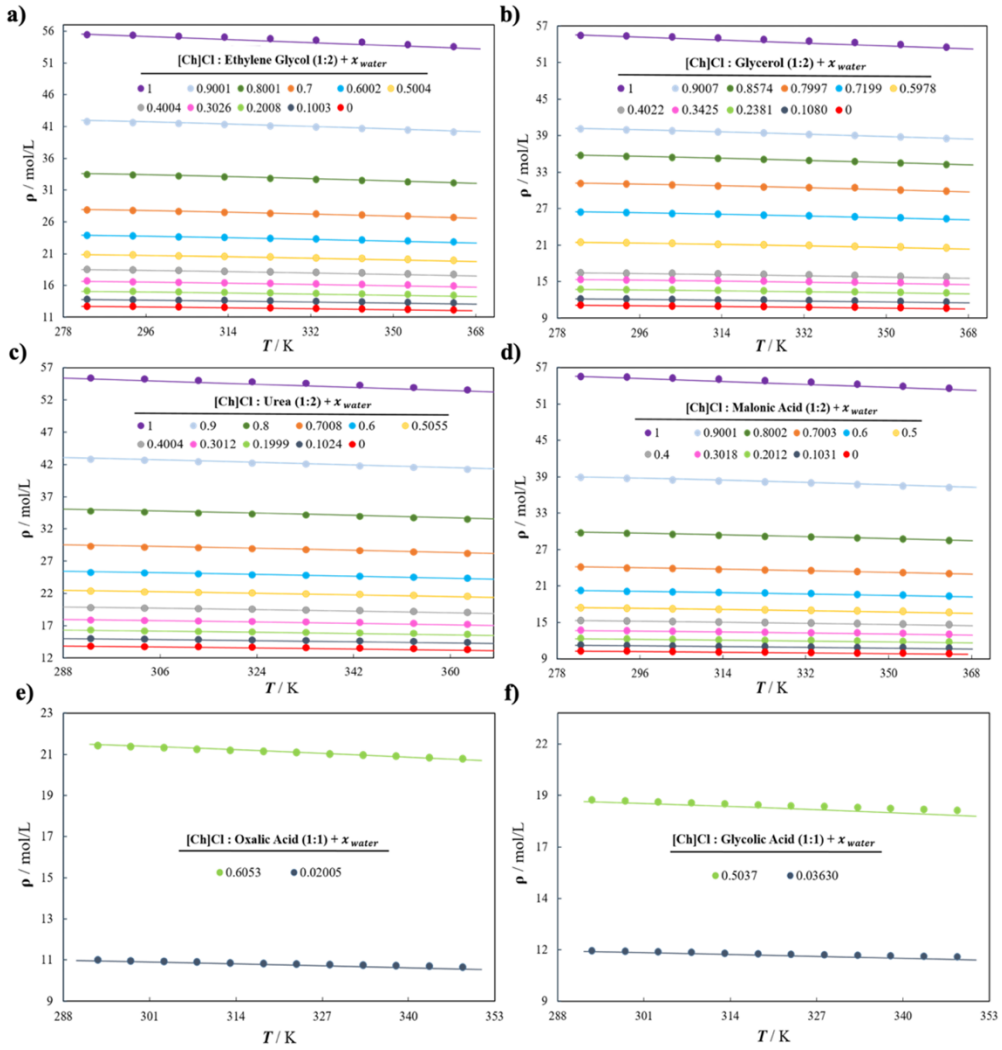


***Figure 4.11.*** *Density (ρ) – temperature (T) diagram, at atmospheric pressure, considering binary mixture for aqueous mixtures of DESs at different molar fraction of water for a) [Ch]Cl:EG (1:2); b) [Ch]Cl:GL (1:2); c) [Ch]Cl:UR (1:2); d) [Ch]Cl:MA (1:2) , e) [Ch]Cl:OA (1:1) and f) [Ch]Cl:GA (1:1). In all figures, symbols correspond to experimental data (Florindo et al., 2014; Yadav et al., 2015; Yadav & Pandey, 2014; Yadav et al., 2014), while the lines to soft-SAFT predictions (with parameters from Tables 4.1 for DES and from Tables 4.2 for water).*

In general, it must be noted that, although the results obtained considering both compounds forming the DESs as a single constituent were also satisfactory for the density, the transferability of the model remains limited. Even so, this simplified hypothesis can still be very useful for describing the behavior of a wide range of DESs with similar sets of available experimental data. However, the individual-component

approach considering them as different entities, offers a more reliable model of the behavior of the DESs and will provide a better description of other properties (solubility, enthalpy, activity coefficients) dominated by energetic interactions.

One final remark is related to the DESs structure, which is not studied in this work and may be affected by the amount of water, breaking the DES and converting the system in a "soup" of solvents. While this analysis is out of the scope of this thesis, the models presented here intend to accurately describe a physical property, such as the density, in a quantitative manner, regardless of the possible structural changes among the compounds.

*Viscosity*

As widely exposed in the Section 2.1.3, the addition of water in the DESs cause a very strong impact on the viscosity of the system. Hence, it is critical for the thermophysical framework presented in this work to know how accurate the description of this property is. Consequently, the performance of the viscosities using the soft-SAFT + FVT of the aqueous mixtures of [Ch]Cl:EG (1:2), [Ch]Cl:GL (1:2), [Ch]Cl:UR (1:2), [Ch]Cl:OA (1:1), are displayed in Figure 4.12.

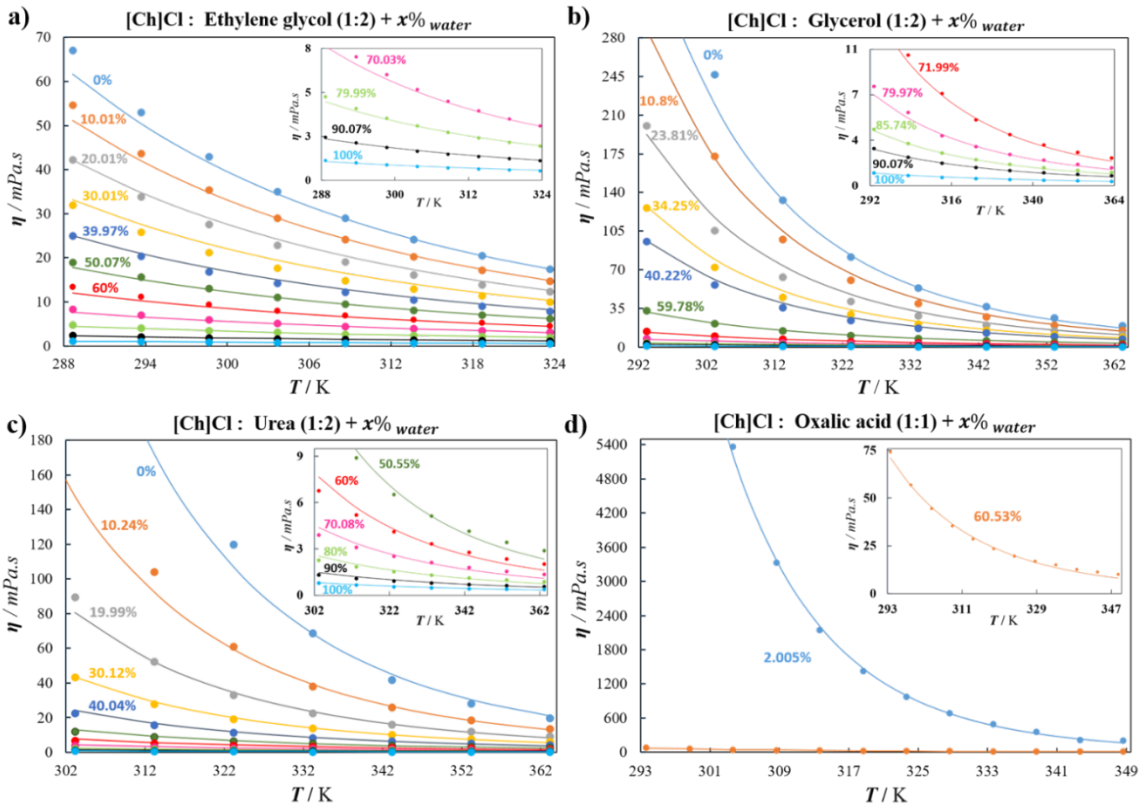


***Figure 4.12.*** *Viscosity (η) – temperature (T) diagram, at atmospheric pressure, modeled using FVT parameters shown in Table 4.3 for aqueous mixtures of [Ch]Cl based DESs in different molar fraction of water for a) [Ch]Cl:EG (1:2), b) [Ch]Cl:GL (1:2), c) [Ch]Cl:UR (1:2) and d) [Ch]Cl:OA (1:1). In all Figures, symbols correspond to experimental data (Florindo et al., 2014; Wang et al., 2020; Yadav & Pandey, 2014; Yadav et al., 2014), while the lines correspond to the soft-SAFT + FVT calculations.*

In general, it must be noted that the soft-SAFT + FVT approach is capable of reproducing the highly non-ideal behavior at all water compositions with remarkable agreement (ADD% of 5.91 with respect to the experimental data displayed in Figure 4.12). A slight deterioration can be observed at the lowest temperatures, which corresponds to the highest viscosity values, where the experimental measurements also have a higher degree of uncertainty. Still with this, it is striking to notice how the viscosity is well captured from pure DESs to infinite diluted solutions, covering a wide range of values. In particular, Figure 4.12 (d) compares the performance of the model to reproduce the viscosity of [Ch]Cl:OA, where the effect of water is decreasing the viscosity two

orders of magnitude. The soft-SAFT + FVT model can perfectly reproduce the trend at very high (2.00% of water) and low (60.53% of water) viscosity values using the same molecular parameters, without further correction.

### 4.1.4 Validation of Properties of DESs with Alcohols

The addition of other cosolvents, such as methanol or ethanol, has also been evaluated to widen the capacity of the current thermophysical framework for different applications. Hence, following the same methodology previously described, the effect of methanol and ethanol on the density of DESs has been predicted and compared to the available experimental data for methanol (Haghbakhsh & Raeissi, 2018a; Wang et al., 2020) and ethanol (Haghbakhsh & Raeissi, 2018b, 2020; Kim & Park, 2018) mixtures with the DESs: [Ch]Cl:EG (1:2), [Ch]Cl:GL (1:2), [Ch]Cl:UR (1:2). As done before, no binary parameters are used. As it occurred with water, excellent predictions of the ternary mixtures are obtained, as can be seen in Figure 4.13. The model is capable to describe this property with an %AAD of 0.875%, 0.709%, 0.955% for the methanol mixtures, and 0.560%, 0.488%, 0.442% for the ethanol mixtures of the studied DESs (i.e, [Ch]Cl:EG, [Ch]Cl:GL and [Ch]Cl:UR respectively). These results are of the same order of accuracy as those of water and allow to validate the robustness of the model when facing alternative solvents in combination with DESs, regardless of the composition.

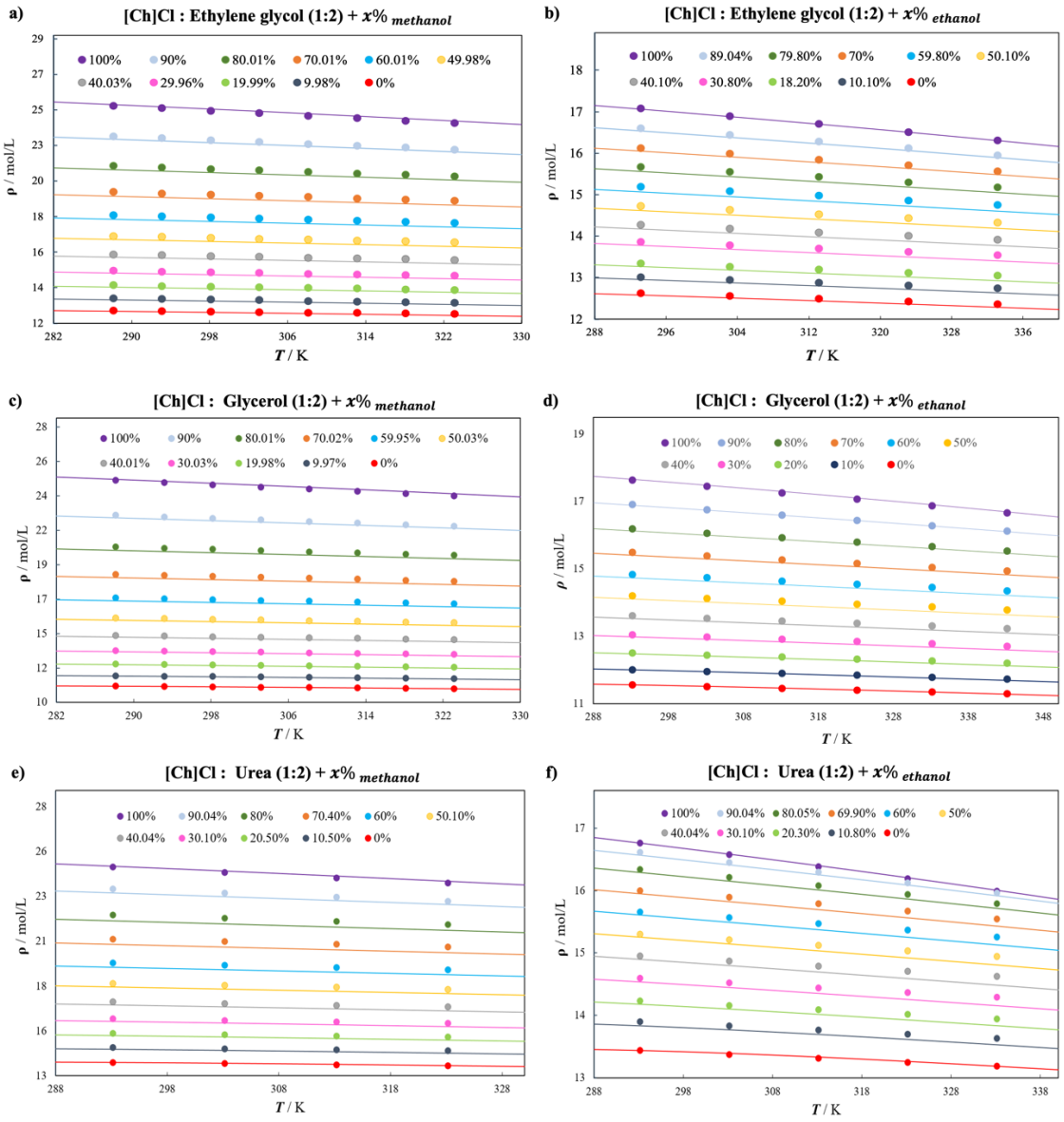


***Figure 4.13.*** *Density (ρ) – temperature (T) diagram at atmospheric pressure for ternary mixtures: [Ch]Cl : EG (1:2) DES with methanol (a) and ethanol (b), [Ch]Cl : GL (1:2) DES with methanol (c) and ethanol (d), [Ch]Cl : UR (1:2) DES with methanol (e) and ethanol (f), all at different molar fractions of the respective cosolvent. In all figures, symbols correspond to experimental data (Haghbakhsh & Raeissi, 2018a, b, 2020; Kim & Park, 2018; Wang et al., 2020), while the lines to soft-SAFT predictions (with parameters from Table 4.2).*

Finally, the viscosities of [Ch]Cl:EG (1:2) in solutions with methanol and ethanol and of [Ch]Cl:GL (1:2) in solutions with methanol were also estimated using soft-SAFT + FVT and displayed in Figure 4.14.

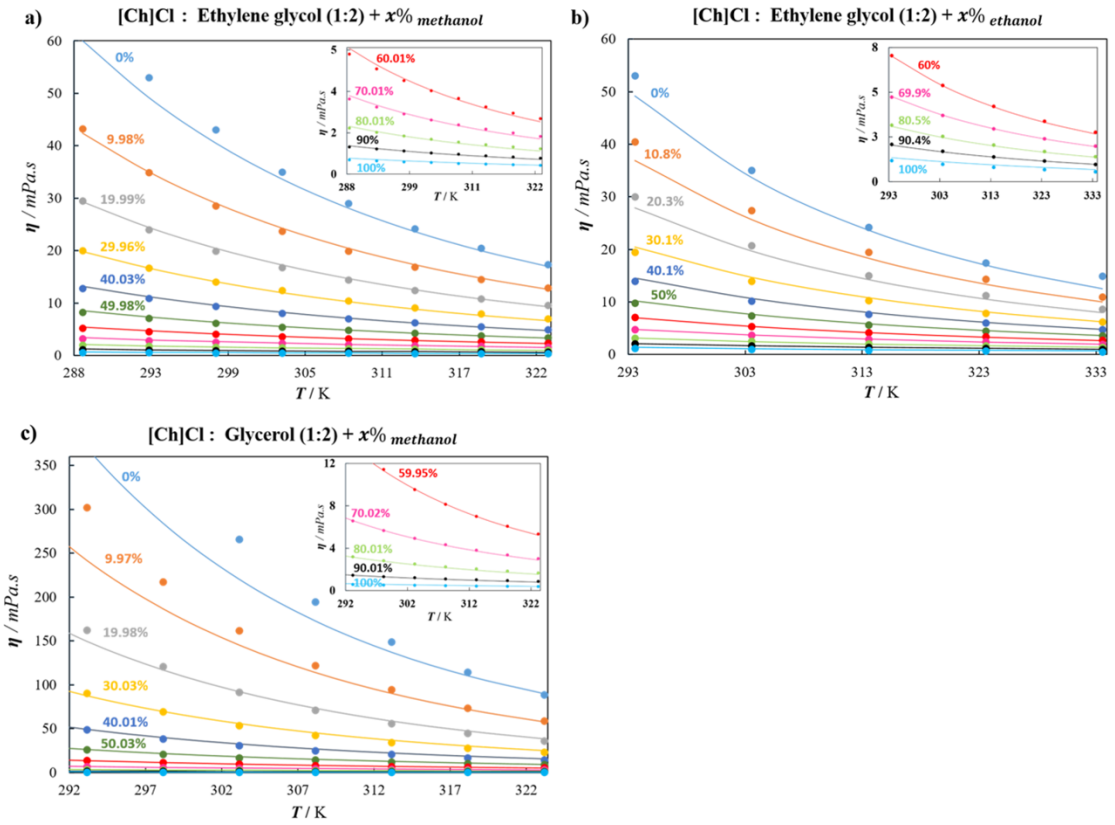


***Figure 4.14.*** *Viscosity (η) – temperature (T) diagram, at atmospheric pressure, modeled using FVT parameters shown in Table 4.3 for the mixtures: [Ch]Cl:EG (1:2) DES with methanol (a) and ethanol (b) and [Ch]Cl:GL (1:2) DES with methanol (c), all at different molar fraction of the respective cosolvent. In all Figures, symbols correspond to experimental data (Haghbakhsh et al., 2021b; Wang et al., 2020), while the lines correspond to the soft-SAFT + FVT calculations.*

Similarly, the model is also capable to reproduce the non-ideal behavior at all methanol and ethanol compositions with remarkable agreement (ADD% of 3.74 for [Ch]Cl:EG (1:2) and ADD% of 4.71 for [Ch]Cl:GL (1:2)). This reconfirms the validity of soft-SAFT + FVT to provide a common framework to describe the viscosity of the [Ch]Cl based DESs studied in this Section, as well as the effect of water, methanol and ethanol on this property.

Despite this success, this approach has limitations, particularly related to the sensitivity of FVT parameters. Llovell et al. (2013a) demonstrated that minor changes in these parameters had a significant impact in the viscosity of the n-alkanes family, particularly at low temperatures. This sensitivity can be extrapolated to other families of compounds, adding a challenge when predicting the viscosity of new DESs or mixtures for which experimental data are not readily available.

In order to overcome this limitation, a complementary approach based on Machine Learning technique for a more flexible and versatile viscosity modelling is presented in the next Section.

## 4.2 Addition of an Artificial Neural Network-Based Molecular Approach for Predicting the Viscosity

Section 2.3.2 highlights that numerous studies in the literature have demonstrated the elevated accuracy achieved by molecular-based ANNs models in predicting the physicochemical properties of DESs. Nonetheless, achieving a good level of accuracy does not only depend on optimizing the ANN effectively, but also on selecting the appropriate input descriptors. These descriptors should be capable of capturing the molecule's essential characteristics and leading to the accurate determination of a specific physicochemical property value. In this context, the conductor-like screening model for real solvents (COSMO-RS) and their molecular charge density distributions ($\sigma$-profile) have been previously used as input parameters in ML models to obtain highly accurate predictions of different properties of DESs, as discussed in Section 2.3.2.

However, the use of ML techniques to quantify viscosities across wide temperature and compositional ranges for mixtures of DESs with cosolvents has received limited attention. Considering the critical role of cosolvents on DES viscosity, the objective of this Section is to construct an ANN model to anticipate this influence precisely, as an alternative and more versatile method than the use of the Free-Volume Theory, whose parameters degeneracy may restrict the parametrization of more mixtures. The ANN model is designed to describe the viscosity of the prevalent sustainable [Ch]Cl-based DESs, whether in their pure form or when combined with water or other cosolvents, by employing the temperature and the compound $\sigma$-profiles as molecular descriptors, acquired through the conductor-like screening model for real solvent segment activity coefficient (COSMO-SAC). The reliability of the developed model is validated using several statistical parameters, and its predictive capability is verified by addressing new hydrogen bond donors and solvents not included in the training, as well as calculating the applicability domain evaluation. Additionally, the influence of the molecular descriptors as input parameters on the viscosity of DESs is reported and rationally discussed. A summarized representation of the methodology used is in this Section shown in Fig. 4.15.

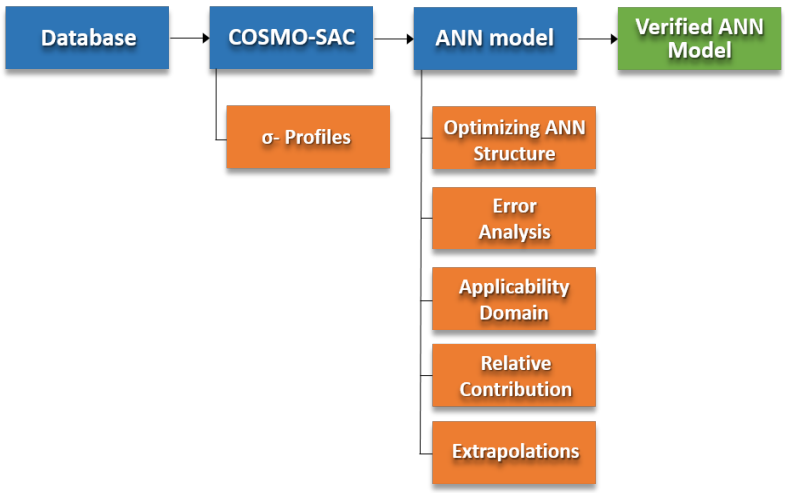


***Figure 4.15.*** *Summary of the methodology scheme used in the development of the ANN.*

### 4.2.1 Experimental Dataset

In this study, a DES viscosity (mPa·s) database containing 1891 experimental data points was used to develop a feed-forward ANN model. The collected experimental data includes 48 different DES mixtures based on [Ch]Cl with 18 different HBDs: phenol (PH), glycerol (GL), ethylene glycol (EG), triethylene glycol (TEG), propionic acid (PA), oxalic acid (OA), levulinic acid (LevA), glutaric acid (GLA), malonic acid (MA), lactic acid (LA), p-cresol, 1,4-butanediol (1,4-BT), monoethanolamine (MEA), diethanolamine (DEA), methyldiethanolamine (MDEA), D-glucose (D-GLU), D-fructose (D-FT) and urea (UR). Additionally, the database also contains mixtures of DESs with four cosolvents: water, methanol (MeOH), isopropanol (IPA) and dimethyl sulfoxide (DMSO). The exact distribution includes 273 data points of pure DESs, and 1618 DESs + cosolvent data points, including Water (894), Methanol (360), Isopropanol (208), and Dimethyl sulfoxide (156).

Table 4.6 presents a comprehensive list of the dataset, with DESs and mixtures considered in this study for the ANN design, along with the composition and temperature ranges for the datasets and the corresponding references. The dataset covers a wide range of viscosity measurements (0.3862 – 4722 mPa·s) and temperature (283.15 – 363.15 K), with data containing 279 systems of different compositions at atmospheric pressure for binary and ternary mixtures.

***Table 4.6.*** *Summary of studied DESs and DES + cosolvents including their experimental temperature and viscosity ranges at atmospheric pressure, number of data points and corresponding references.*

| DES | System | Range of T (K) | Range of η (mPa.s) | Data points | References |
|---|---|---|---|---|---|
| DES1 | [Ch]Cl + PH (1:2) | 293.2 – 333.15 | 19.5 – 120.77 | 9 | (Guo et al., 2013; Zhu et al., 2017) |
| DES2 | [Ch]Cl + PH (1:3) | 293.2 – 333.15 | 13.77 – 57.84 | 8 | (Guo et al., 2013; Haghbakhsh et al., 2022) |
| DES2.1 | [Ch]Cl + PH (1:3) + $H_2O$ | 293.2 – 333.15 | 1.09 – 56.09 | 45 | (Haghbakhsh et al., 2022) |
| DES3 | [Ch]Cl + PH (1:4) | 293.2 – 318.2 | 14 – 40.23 | 6 | (Guo et al., 2013) |
| DES3.1 | [Ch]Cl + PH (1:4) + $H_2O$ | 293.2 – 333.15 | 1.1 – 43.9 | 45 | (Haghbakhsh et al., 2022) |
| DES4 | [Ch]Cl + PH (1:5) | 293.2 – 318.2 | 11.26 – 31.96 | 6 | (Guo et al., 2013) |
| DES5 | [Ch]Cl + PH (1:6) | 293.2 – 318.2 | 9.46 – 27.03 | 6 | (Guo et al., 2013) |
| DES6 | [Ch]Cl + GL (1:2) | 283.15 – 363.15 | 19.59 – 1003.9 | 13 | (Wang et al., 2020; Yadav et al., 2014) |
| DES6.1 | [Ch]Cl + GL (1:2) + $H_2O$ | 283.15 – 363.15 | 0.39 – 669.90 | 204 | (Wang et al., 2020; Yadav et al., 2014) |
| DES6.2 | [Ch]Cl + GL (1:2) + MeOH | 288.15 – 323.15 | 0.43 – 425.75 | 144 | (Wang et al., 2020) |
| DES6.3 | [Ch]Cl + GL (1:2) + DMSO | 288.15 – 323.15 | 1.418 – 497.3 | 104 | (Zuo et al., 2024) |
| DES6.4 | [Ch]Cl + GL (1:2) + IPA | 288.15 – 323.15 | 1.13 – 418.5 | 104 | (Zuo et al., 2024) |
| DES7 | [Ch]Cl + GL (1:3) + $H_2O$ | 298.15 – 343.15 | 10.98 – 62.05 | 10 | (Codera et al., 2023) |
| DES8 | [Ch]Cl + GL (1:4) | 293.15 – 323.15 | 87.96 – 578.2 | 7 | (Rodriguez et al., 2016) |
| DES9 | [Ch]Cl + EG (1:2) | 283.15 – 323.15 | 17.41 – 87.45 | 9 | (Wang et al., 2020) |
| DES9.1 | [Ch]Cl + EG (1:2) + $H_2O$ | 288.15 – 323.15 | 0.6 – 54.67 | 144 | (Wang et al., 2020) |
| DES9.2 | [Ch]Cl + EG (1:2) + MeOH | 283.15 – 323.15 | 0.43 – 60.35 | 153 | (Haghbakhsh et al., 2021a; Wang et al., 2020) |
| DES9.3 | [Ch]Cl + EG (1:2) + DMSO | 308.15 – 323.15 | 1.40 – 24.88 | 52 | (Zuo et al., 2024) |
| DES9.4 | [Ch]Cl + EG (1:2) + IPA | 288.15 – 323.15 | 1.16 – 55.70 | 104 | (Zuo et al., 2024) |
| DES10 | [Ch]Cl + EG (1:3) | 293.15 – 348.15 | 6.79 – 30.17 | 12 | (Codera et al., 2023) |
| DES10.1 | [Ch]Cl + EG (1:3) + $H_2O$ | 293.15 – 333.15 | 10.47 – 37.35 | 9 | (Gajardo-Parra et al., 2020) |
| DES11 | [Ch]Cl + EG (1:4) + $H_2O$ | 293.15 – 333.15 | 9.01 – 31.8 | 9 | (Gajardo-Parra et al., 2020) |
| DES12 | [Ch]Cl + EG (1:5) + $H_2O$ | 293.15 – 333.15 | 7.5 – 28.49 | 9 | (Gajardo-Parra et al., 2020) |
| DES13 | [Ch]Cl + EG (1:6) + $H_2O$ | 293.15 – 333.15 | 6.91 – 25.56 | 9 | (Gajardo-Parra et al., 2020) |
| DES14 | [Ch]Cl + MA (1:0.5) | 303.15 – 353.15 | 46.2 – 1460.3 | 6 | (Mjalli & Naser, 2015) |
| DES15 | [Ch]Cl + MA (1:1) | 303.15 – 353.15 | 15.2 – 417 | 6 | (Mjalli & Naser, 2015) |
| DES15.1 | [Ch]Cl + MA (1:1) + $H_2O$ | 293.15 – 348.15 | 10.14 – 2016 | 24 | (Florindo et al., 2014) |
| DES16 | [Ch]Cl + MA (1:2) | 303.15 – 353.15 | 30 – 800 | 6 | (Mjalli & Naser, 2015) |
| DES17 | [Ch]Cl + TEG (1:3) | 298.15 – 358.15 | 9 – 68 | 7 | (Mjalli & Naser, 2015) |
| DES18 | [Ch]Cl + TEG (1:4) | 298.15 – 358.15 | 8.1 – 61.9 | 7 | (Mjalli & Naser, 2015) |
| DES19 | [Ch]Cl + TEG (1:5) | 298.15 – 358.15 | 7.5 – 53 | 7 | (Mjalli & Naser, 2015) |
| DES20 | [Ch]Cl + TEG (1:6) | 298.15 – 358.15 | 6.5 – 44.9 | 7 | (Mjalli & Naser, 2015) |
| DES21 | [Ch]Cl + UR (1:1.5) | 303.15 – 353.15 | 36.5 – 663 | 6 | (Mjalli & Naser, 2015) |
| DES22 | [Ch]Cl + UR (1:2) | 293.15 – 363.15 | 19.95 – 1371.9 | 8 | (Yadav & Pandey, 2014) |
| DES22.1 | [Ch]Cl + UR (1:2) + $H_2O$ | 293.15 – 363.15 | 0.57 – 436.11 | 72 | (Yadav & Pandey, 2014) |
| DES23 | [Ch]Cl + UR (1:2.5) | 303.15 – 353.15 | 24.8 – 473 | 6 | (Mjalli & Naser, 2015) |
| DES24 | [Ch]Cl + OA (1:1) | 308.15 – 348.15 | 208.3 – 3332 | 9 | (Florindo et al., 2014) |
| DES24.1 | [Ch]Cl + OA (1:1) + $H_2O$ | 293.15 – 348.15 | 10 – 74.18 | 12 | (Florindo et al., 2014) |
| DES25 | [Ch]Cl + LevA (1:2) | 293.15 – 348.15 | 22.23 – 320.6 | 12 | (Florindo et al., 2014) |
| DES25.1 | [Ch]Cl + LevA (1:2) + $H_2O$ | 293.15 – 348.15 | 7.21 – 53.39 | 12 | (Florindo et al., 2014) |
| DES26 | [Ch]Cl + GLA (1:1) | 293.15 – 353.15 | 105.8 – 2968 | 13 | (Florindo et al., 2014) |
| DES26.1 | [Ch]Cl + GLA (1:1) + $H_2O$ | 293.15 – 353.15 | 9.32 – 78.24 | 13 | (Florindo et al., 2014) |
| DES27 | [Ch]Cl + LA (1:1) | 303.15 – 333.15 | 202.4 – 1245.3 | 7 | (Alcalde et al., 2018) |
| DES27.1 | [Ch]Cl + LA (1:1) + $H_2O$ | 288.15 – 353.15 | 5.53 – 1554.5 | 33 | (Alcalde et al., 2019) |
| DES27.2 | [Ch]Cl + LA (1:1) + MeOH | 303.15 – 333.15 | 0.7 – 220.96 | 63 | (Alcalde et al., 2018) |
| DES28 | [Ch]Cl + LA (1:1.5) + $H_2O$ | 288.15 – 353.15 | 4.60 – 4005.06 | 26 | (Alcalde et al., 2019) |
| DES29 | [Ch]Cl + LA (1:2) + $H_2O$ | 288.15 – 353.15 | 5.43 – 3823.11 | 25 | (Alcalde et al., 2019) |
| DES30 | [Ch]Cl + LA (1:2.5) + $H_2O$ | 288.15 – 343.15 | 7.08 – 4722.11 | 23 | (Alcalde et al., 2019) |
| DES31 | [Ch]Cl + p-cresol (1:2) | 293.15 – 333.15 | 19.6 – 133.68 | 9 | (Zhu et al., 2017) |
| DES32 | [Ch]Cl + 1,4-BT (1:3) | 303.15 – 343.15 | 15.7 – 49.3 | 9 | (Deng et al., 2020) |
| DES33 | [Ch]Cl + 1,4-BT (1:4) | 303.15 – 343.15 | 14 – 54.75 | 9 | (Deng et al., 2020) |
| DES34 | [Ch]Cl + 1,4-BT (1:5) | 293.15 – 333.15 | 19.64 – 93.6 | 9 | (Gajardo-Parra et al., 2020) |
| DES35 | [Ch]Cl + 1,4-BT (1:6) | 293.15 – 333.15 | 18.98 – 91.44 | 9 | (Gajardo-Parra et al., 2020) |
| DES36 | [Ch]Cl + MEA (1:5) | 293.15 – 323.15 | 14.98 – 18.98 | 4 | (Li et al., 2022) |
| DES36.1 | [Ch]Cl + MEA (1:5) + $H_2O$ | 293.15 – 323.15 | 1.21 – 58.42 | 36 | (Li et al., 2022) |
| DES37 | [Ch]Cl + MEA (1:6) | 293.15 – 323.15 | 13.62 – 54.07 | 4 | (Li et al., 2022) |
| DES37.1 | [Ch]Cl + MEA (1:6) + $H_2O$ | 293.15 – 323.15 | 1.12 - 50.14 | 36 | (Li et al., 2022) |
| DES38 | [Ch]Cl + MEA (1:8) | 293.15 – 323.15 | 11.42 – 44.9 | 4 | (Li et al., 2022) |
| DES38.1 | [Ch]Cl + MEA (1:8) + $H_2O$ | 293.15 – 323.15 | 1.12 – 42.61 | 36 | (Li et al., 2022) |
| DES39 | [Ch]Cl + MEA (1:10) | 293.15 – 323.15 | 10.29 – 39.49 | 4 | (Li et al., 2022) |
| DES39.1 | [Ch]Cl + MEA (1:10) +$H_2O$ | 293.15 – 323.15 | 1.18 – 37.94 | 36 | (Li et al., 2022) |
| DES40 | [Ch]Cl + DEA (1:6) | 293.15 – 333.15 | 49.91 – 567 | 3 | (Adeyemi et al., 2018) |
| DES41 | [Ch]Cl + DEA (1:8) | 293.15 – 333.15 | 53.36 – 565.3 | 3 | (Adeyemi et al., 2018) |
| DES42 | [Ch]Cl + DEA (1:10) | 293.15 – 333.15 | 54.56 – 611.4 | 3 | (Adeyemi et al., 2018) |
| DES43 | [Ch]Cl + MDEA (1:6) | 293.15 – 333.15 | 22.01 – 139.8 | 3 | (Adeyemi et al., 2018) |
| DES44 | [Ch]Cl + MDEA (1:8) | 293.15 – 333.15 | 20.99 – 126.3 | 3 | (Adeyemi et al., 2018) |
| DES45 | [Ch]Cl + MDEA (1:10) | 293.15 – 333.15 | 9.26 – 54.54 | 3 | (Adeyemi et al., 2018) |
| DES46 | [Ch]Cl + D-GLU(1:1) +$H_2O$ | 293.15 – 353.15 | 52.01 – 2509.5 | 13 | (Florindo et al., 2017) |
| DES47 | [Ch]Cl + D-FT (1:1) + $H_2O$ | 293.15 – 353.15 | 28.99 – 995.34 | 13 | (Florindo et al., 2017) |
| DES48 | [Ch]Cl + PA (1:2) | 288.15 – 338.15 | 13.53 – 91.74 | 11 | (Cui et al., 2017) |

### 4.2.2 Molecular Inputs

In this study, COSMO-SAC is employed to obtain the molecular descriptors, specifically $\sigma$-profiles, which represent the investigated DESs. These $\sigma$-profiles, discussed in Section 3.1.1, are used as inputs for the ANN model. All $\sigma$-profiles obtained in this Section were taken from the open-source LVPP-sigma profile database (Soares et al., 2017), freely available at https://github.com/lvpp/sigma. The 2D molecular structure and the geometrically optimized 3D COSMO-SAC surfaces of the 24 compounds investigated in this study are shown in Fig. 4.16. The molecular polarity is visually represented through a spectrum of colors ranging from blue to red. Shades of blue indicate a higher positive charge (associated with hydrogen-donating areas). In contrast, deeper shades of red denote a greater negative charge (corresponding to hydrogen-accepting areas).

The $\sigma$-profile of a molecule provides valuable information about its structure, such as its polarity and the concentration of specific atoms within it. Consequently, the area under the $\sigma$-profile curves can be utilized to quantitatively represent the molecular surface, denoted as the $S_{\sigma\text{-profiles}}$ (Torrecilla et al., 2010). Therefore, using these molecular descriptors as ANN inputs allows to establish a connection between the molecular structure and a specific property of the DES, such as the viscosity.

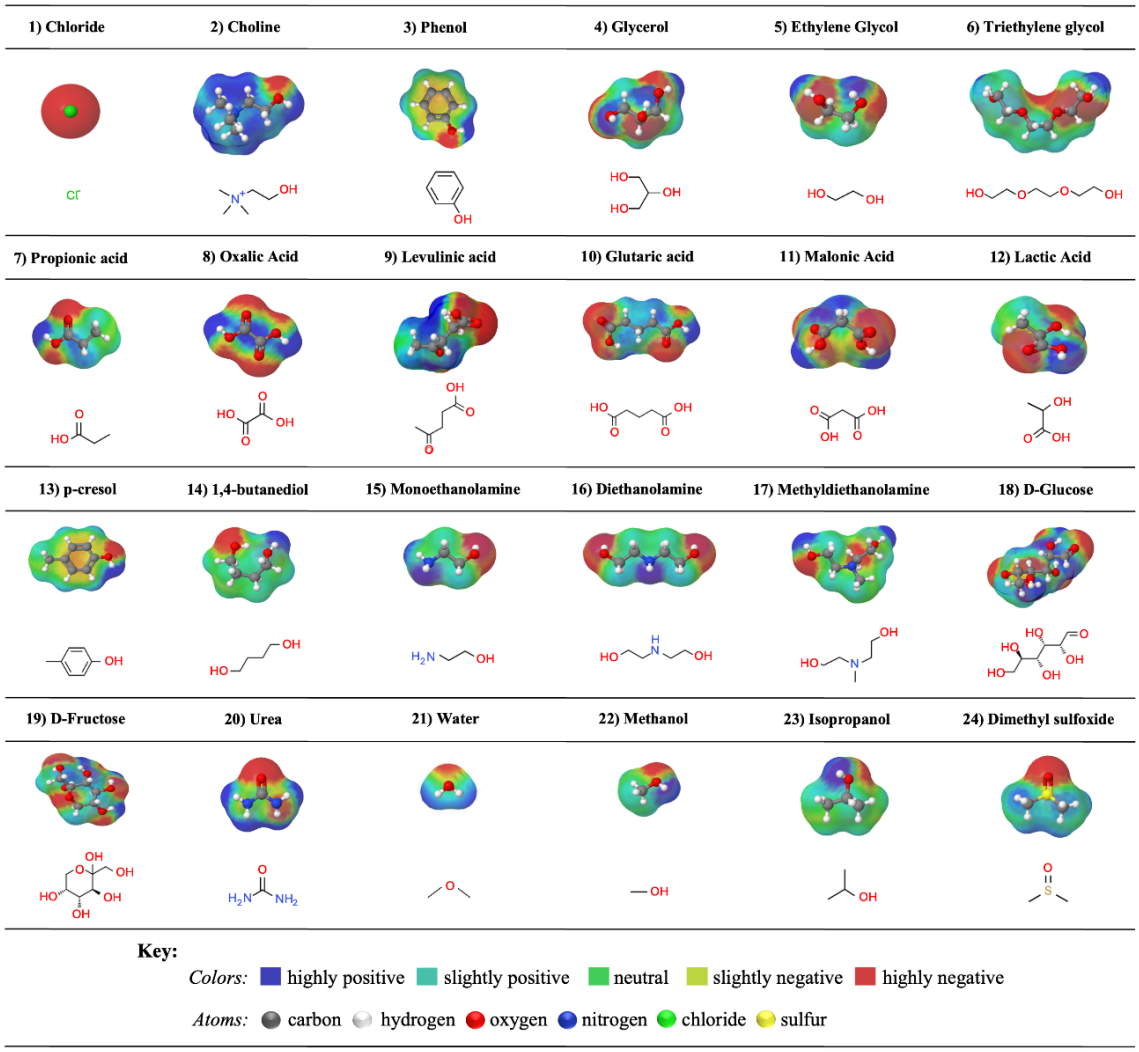


***Figure 4.16.*** *3D geometrically optimized COSMO-SAC surfaces and 2D molecular structures of the compounds used to form the DESs and cosolvents investigated in this thesis.*

The accuracy of the developed models can be significantly improved by dividing the $\sigma$-profiles into multiple regions, which provides a more detailed representation of the molecule. However, this increased detail also introduces greater complexity, as it requires managing a larger number of inputs. Therefore, it is essential to strike a balance between model complexity and accuracy. Previous studies have experimented with σ-profiles divided into 6 (Wang, Jingwen et al., 2021), 8 (Alkhatib et al., 2022; Lemaoui et al., 2022; Sosa et al., 2020), 10 (Palomar et al., 2010), and even 51 regions (Awaja et al., 2023).

In this study, to achieve an optimal balance between precision and computational complexity for the neural network, we chose to partition the $\sigma$-profiles of the compounds into eight distinct regions. The areas under the $\sigma$-profile curves within each of these delineated regions were computed through the trapezoidal rule, and their resulting numerical area values were then employed as $S_{\sigma\text{-profiles}}$ of the 24 compounds investigated. Subsequently, the $S_{\sigma\text{-profiles}}$ of the modeled DESs and their mixtures with cosolvents were computed through the conventional approach employed in the literature (Boublia et al., 2022; Lemaoui et al., 2021; Lemaoui et al., 2022; Lemaoui et al., 2020a), which involves calculating the molar-weighted average of its constituents:

$$S_i^{DES} = \sum_{j=1}^{NC} x_j \times S_i^j = x_{[Ch]Cl} \times \left(S_i^{[Ch]} + S_i^{Cl}\right) + x_{HBD} \times S_i^{HBD} + x_{cosolv} \times S_i^{cosolv}, \qquad (4.7)$$

where NC is the total number of components in the DES mixture, $x_j$ is the mole fraction of component $j$ in the mixture, and $S_i^j$ is the $S_{\sigma\text{-profiles}}$ of component $j$ in region $i$, from 1 to 8 (e/$\dot{A}$). $x_{[Ch]Cl}$, $x_{HBD}$ and $x_{cosolv}$ represent the molar fractions of [Ch]Cl, the HBD and the cosolvent present within the DES, respectively.

*Analysis of the $\sigma$-Profiles*

The discretized $\sigma$-profiles of the 24 compounds investigated were obtained through a COSMO-SAC methodology (Ferrarini et al., 2018) and contain 31 data points in the range of ± 0.03 (e/$\dot{A}$). The results are graphically represented in Fig. 4.17. By analyzing this figure, it is possible to observe different regions of $S_{\sigma\text{-profiles}}$ based on their

polarized charge density: the strong hydrogen-bonding donor (HBD) region [$S_1$ and $S_2$], the weak HBD region [$S_3$], the non-polar region [$S_4$ and $S_5$], the weak hydrogen bond acceptor (HBA) region [$S_6$] and the strong HBA region [$S_7$ and $S_8$]. A detailed outline of the charge density ranges for these regions, accompanied by their corresponding molecular descriptors, is provided in Table 4.7.

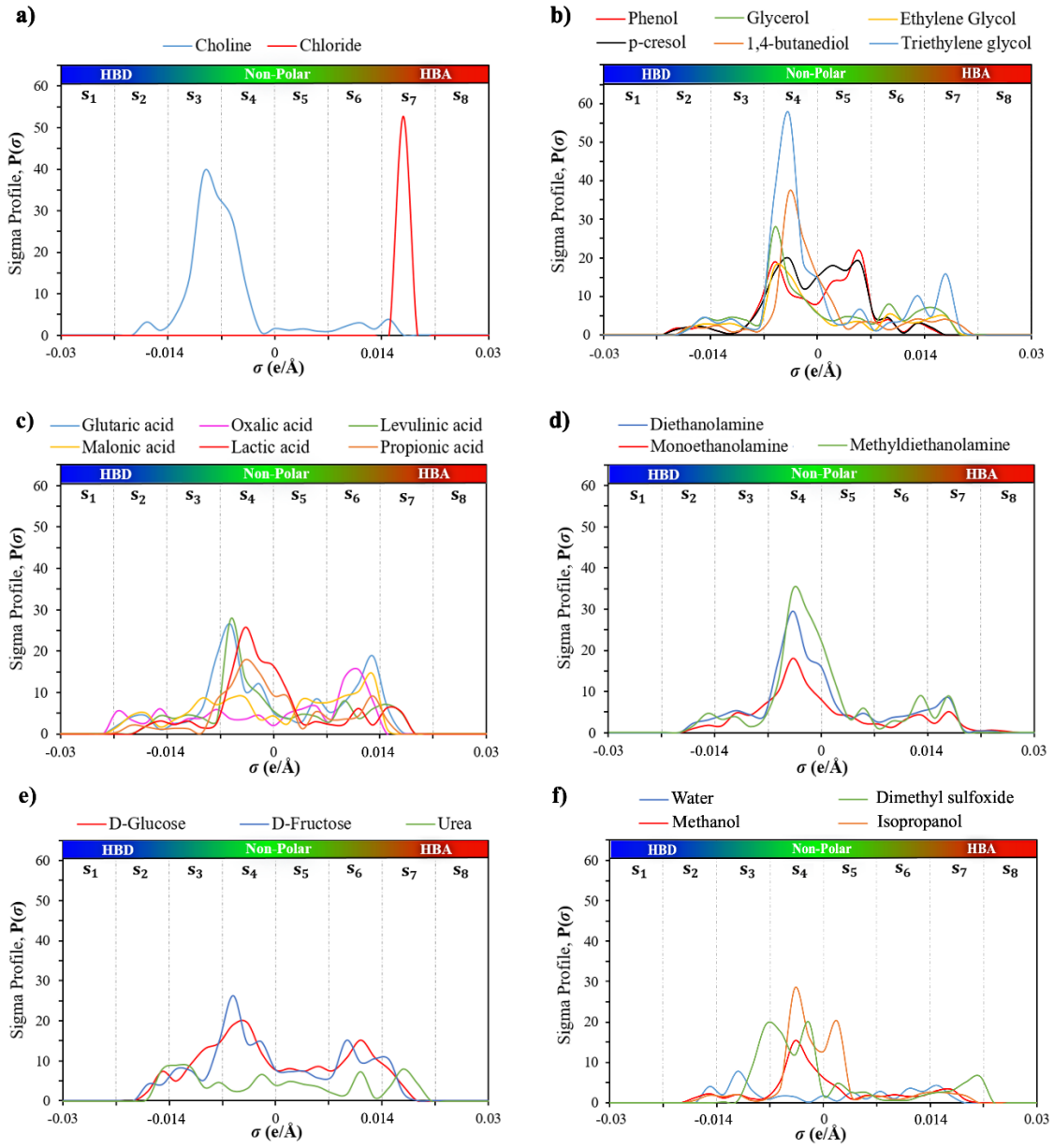


*Figure 4.17. COSMO-SAC calculated σ-profiles for a) the anion and cation of the HBA [Ch]Cl salt, b) alcohols and glycols, c) acids, d) amines, e) carbohydrates and urea, and f) cosolvents.*

***Table 4.7.*** *Eight molecular descriptors derived from $S_{\sigma\text{-profiles}}$ used in this work and their corresponding charge densities and polarity regions.*

| Molecular descriptor | Screening charge density range (e/A) | Region |
|---|---|---|
| $S_1$ | $-0.030 < \sigma < -0.022$ | **strong HBD region** |
| $S_2$ | $-0.022 < \sigma < -0.014$ | |
| $S_3$ | $-0.014 < \sigma < -0.006$ | **weak HBD region** |
| $S_4$ | $-0.006 < \sigma < 0.000$ | **non-polar region** |
| $S_5$ | $0.000 < \sigma < +0.006$ | |
| $S_6$ | $+0.006 < \sigma < +0.014$ | **weak HBA region** |
| $S_7$ | $+0.014 < \sigma < +0.022$ | **strong HBA region** |
| $S_8$ | $+0.022 < \sigma < +0.030$ | |

The conversion of $\sigma$-profiles into eight $S_{\sigma\text{-profiles}}$ descriptors offers essential insights into the atomistic properties of each compound and their influence on governing intermolecular interactions by analyzing peaks in specific molecular descriptors. For instance, the peaks observed in the [$S_4$] and [$S_5$] zone (non-polar region) can be attributed to the non-polar alkyl groups present within the molecules, such as -$CH_3$, -$CH_2$ and -CH. Figure 4.17 (b) demonstrates that longer molecular chain lengths result in higher peak elevations in the non-polar region (e.g., triethylene glycol > 1,4 butanediol > ethylene glycol). The peaks observed within the [$S_1$-$S_3$] zone mainly correspond to the positively charged $H^{\delta+}$ part of the molecules, which induce a shift toward the negative pole of the field. Conversely, within the [$S_6$-$S_8$] zone, the peaks are primarily associated with the electronegative regions of $O^{\delta-}$, $N^{\delta-}$or $S^{\delta-}$ found in the O-H, N-H and S=O groups, or to the anion $[Cl]^-$, which exhibits a stronger screening charge density in [$S_7$] zone, as illustrated in Figure 4.17 (a). The calculated areas below the $S_{\sigma\text{-profiles}}$, providing the [$S_1$-$S_8$] descriptors for the compounds investigated are listed in Table 4.8.

***Table 4.8.*** *Calculated molecular descriptors for database compounds.*

| # | Element | $S_1$ | $S_2$ | $S_3$ | $S_4$ | $S_5$ | $S_6$ | $S_7$ | $S_8$ |
|---|---|---|---|---|---|---|---|---|---|
| 1 | **[Ch]+** | 0 | 0.01312 | 0.20541 | 0.05415 | 0.00771 | 0.01444 | 0.00900 | 0 |
| 2 | **[Cl]-** | 0 | 0 | 0 | 0 | 0 | 0 | 0.10562 | 0 |
| 3 | **PH** | 0 | 0.01216 | 0.04317 | 0.06867 | 0.08714 | 0.04321 | 0.00639 | 0 |
| 4 | **GL** | 0 | 0.01587 | 0.05448 | 0.07956 | 0.02631 | 0.03927 | 0.03054 | 0 |
| 5 | **EG** | 0 | 0.01192 | 0.03488 | 0.07491 | 0.02049 | 0.02708 | 0.02275 | 0 |
| 6 | **TGE** | 0 | 0.01570 | 0.05789 | 0.20460 | 0.03551 | 0.03411 | 0.05554 | 0 |
| 7 | **UR** | 0 | 0.02596 | 0.04423 | 0.02580 | 0.02552 | 0.02613 | 0.03211 | 0 |
| 8 | **AO** | 0.00557 | 0.03218 | 0.03311 | 0.02188 | 0.03068 | 0.07935 | 0.00806 | 0 |
| 9 | **LevA** | 0.00372 | 0.01097 | 0.08594 | 0.08181 | 0.02441 | 0.06248 | 0.03180 | 0 |
| 10 | **GLA** | 0.00200 | 0.02327 | 0.08491 | 0.07629 | 0.02671 | 0.07711 | 0.03332 | 0 |
| 11 | **MA** | 0.00177 | 0.02776 | 0.05414 | 0.03775 | 0.03341 | 0.07616 | 0.01704 | 0 |
| 12 | **LA** | 0.00041 | 0.02047 | 0.04232 | 0.06983 | 0.03490 | 0.04545 | 0.02273 | 0 |
| 13 | **p-cresol** | 0 | 0.01231 | 0.03789 | 0.09531 | 0.10338 | 0.04149 | 0.00711 | 0 |
| 14 | **1,4-BT** | 0 | 0.01001 | 0.01627 | 0.14666 | 0.03940 | 0.02180 | 0.02399 | 0 |
| 15 | **MEA** | 0 | 0.00753 | 0.04404 | 0.07809 | 0.02814 | 0.02050 | 0.02314 | 0.0026 |
| 16 | **DEA** | 0 | 0.01512 | 0.04989 | 0.12950 | 0.04184 | 0.03085 | 0.03646 | 0.0014 |
| 17 | **MDA** | 0 | 0.01572 | 0.03349 | 0.16378 | 0.05826 | 0.02845 | 0.03435 | 0 |
| 18 | **D-GLU** | 0 | 0.02463 | 0.09704 | 0.08970 | 0.04728 | 0.08621 | 0.03401 | 0 |
| 19 | **D-FT** | 0 | 0.02422 | 0.08896 | 0.09188 | 0.04251 | 0.07761 | 0.03473 | 0 |
| 20 | **PA** | 0.00043 | 0.01162 | 0.03252 | 0.08665 | 0.03534 | 0.03739 | 0.01596 | 0 |
| 21 | **H20** | 0 | 0.01009 | 0.02731 | 0.00690 | 0.00894 | 0.01866 | 0.01477 | 0 |
| 22 | **MeOH** | 0 | 0.00814 | 0.01536 | 0.06314 | 0.01745 | 0.01369 | 0.01598 | 0 |
| 23 | **DMSO** | 0 | 0.00019 | 0.07541 | 0.08251 | 0.01924 | 0.00852 | 0.02963 | 0.0065 |
| 24 | **IPA** | 0 | 0.00693 | 0.01299 | 0.10624 | 0.05798 | 0.01209 | 0.01625 | 0 |

### 4.2.3 ANN Model: Design and Evaluation

The ANN design was conducted using the Neural Network Toolbox of MATLAB R2023a software, employing the Bayesian regularization algorithm (Foresee & Hagan, 1997) as the training function for the ANN. The choice of this algorithm was motivated by its ability to effectively handle overfitting and improve generalization performance by adjusting the complexity of the neural network during training based on Bayesian principles (Panigrahi et al., 2018) .The eight $S_{\sigma\text{-profiles}}$ and the temperature descriptor in K ($T$) were employed as ANN input to predict the $\log_{10}$ viscosity (η) of the DESs (here denoted as $log\,(\eta)$ and their mixtures as an output response. The reason behind

calculating the logarithm instead of the direct property is to homogenize the weight when computing the errors of low viscosity compared to high viscosity data values. The predictive correlation is expressed as:

$$log\ (\eta)\ = f\ (\ S_1^{DES},\ S_2^{DES}, \ldots,\ S_8^{DES}, T) \tag{4.8}$$

The typical process of constructing a neural network for a specific task involves the optimization of the network structure. Therefore, to propose an effective design of the ANN model, this investigation has explored several network configurations, including single and double hidden layers with varying neuron quantities, in a similar manner as done by other authors (Matsukawa et al., 2021). Using the equations 3.42 - 3.44 from Section 3.2.1 and employing the hyperbolic tangent (tanh) as the activation function, the output neurons in the hidden layers 1 ($H_n^{(1)}$) and 2 ($H_n^{(2)}$) are expressed as follows:

$$H_n^{(1)}\ = \tanh\left(\sum_{j=1}^{9} W_{n,j}^{(1)}\,.u_j\ +\ b_n^{(1)}\right) \tag{4.9}$$

$$H_n^{(2)}\ = \tanh\left(\sum_{j=1}^{M} W_{n,j}^{(2)}\,.H_n^{(1)}\ +\ b_n^{(2)}\right) \tag{4.10}$$

In these equations, the subscripts *n* and *j* denote the neuron and the input indices, respectively, while the superscripts (1) and (2) refer to the first and second hidden layer. *W* and *b* denote the weights and bias terms. The term $u_j$ in Eq. 4.9 represents the external inputs, encompassing the eight $S_{\sigma\text{-profiles}}$ and the temperature. Finally, the output response

($log\ \eta$) of the ANN model, using the linear transfer function (purelin) for activation, is expressed by Eq. 4.11, where the superscripts *OL* refer to the output layer, and the input to the output layer can be $H_n^{(1)}$ or $H_n^{(2)}$, depending on whether the ANN configuration includes a single or double hidden layer.

$$log\ \eta = \sum_{j=1}^{M} W_{n,j}^{(OL)} . H_n^{(1\ or\ 2)} + b_n^{(OL)} \tag{4.11}$$

To evaluate and assure the prediction power of the designed ANN, the database consisting of 1891 data points was split into two primary sets, a training set containing 80% of the data and a testing set containing 20%. Within the testing dataset, approximately 9% was designated for internal testing during the ANN's development, denoted as the "testing set". In contrast, around 11% formed the "external testing set", which remained completely untouched during the development process of the ANN. The selection of the external testing set employed the "ordered response" method (Boublia et al., 2023; Gramatica et al., 2016), where the log (η) values of all DESs were sorted from lowest to highest, and then one out of every nine data points was selected for external testing set. Subsequently, the remaining data was randomly divided into training and testing sets for the ANN's development. This meticulous approach not only enhances the credibility of the model's performance evaluation, but also underscores its ability to generalize effectively to unseen data.

Furthermore, a comprehensive statistical analysis was conducted, considering classical metrics, such as the coefficient of determination ($R^2$) to assess the linear correlation between the calculated, the experimental data root-mean-square error (*RMSE*)

to measure the data dispersion around the zero deviation, and the average absolute relative deviation (*AARD*) to evaluate the relative absolute deviation from the experimental data (Zendehboudi et al., 2019). These metrics were determined using the following equations:

$$R^2 = 1 - \frac{\sum_{i=1}^{N}\left(log\,\eta_{exp,i} - log\,\eta_{calc,i}\right)^2}{\sum_{i=1}^{N}\left(log\,\eta_{exp,i} - \overline{log\,\eta}\right)^2} \tag{4.12}$$

$$RMSE = \sqrt{\frac{1}{N}\sum_{i=1}^{N}\left(log\,\eta_{calc,i} - log\,\eta_{exp,i}\right)^2} \tag{4.13}$$

$$AARD\ (\%) = \frac{100}{N}\sum_{i=1}^{N}\left|\frac{log\,\eta_{calc,i} - log\,\eta_{exp,i}}{log\,\eta_{exp,i}}\right| \tag{4.14}$$

In these equations, $log\,\eta_{calc}$, $log\,\eta_{exp}$ and $\overline{log\,\eta}$ represent the calculated, the experimental and the average value of the logarithm of DESs viscosities, respectively, $i$ represent the specific data point considered, and $N$ indicates the total number of data points.

Furthermore, to define the range of molecules in which the model prediction may be considered reliable, an Applicability Domain (AD) analysis was carried out. The AD of the developed ANN model was analyzed by means of the William plot (Gramatica, 2007), which is constructed by plotting the standardized residual ($SDR_i$) against the leverage value ($h_i$) of each data point $i$, with AD boundaries defined as horizontal boundaries (-3 < SDR < +3) and vertical boundaries (0 < $h_i$ < h*), where $h^*$ denotes the critical leverage value. The points located outside the AD boundaries are treated as outliers, and their presence is attributed to variations in the chemical structure compared

to the selected data points of the structural centroid used in the training set (Gramatica, 2007). The $h_i$ and $h^*$ (Tropsha et al., 2003), and the $SDR_i$ are expressed as follows:

$$h_i = v_i(V^T V)^{-1} \times v_i^T \tag{4.15}$$

$$h^* = \frac{3(d^* + 1)}{p} \tag{4.16}$$

$$SDR_i = \frac{log\,\eta_{calc,i} - log\,\eta_{exp,i}}{\sqrt{\frac{\sum_{i=1}^{N}\left(log\,\eta_{calc,i} - log\,\eta_{exp,i}\right)^2}{N}}}\ , \tag{4.17}$$

being $d^*$ the number of inputs within the ANN model, which is 9 in this study, $v_i$ a matrix with dimensions of $1 \times d^*$, and $V$ a matrix with dimensions $p \times d^*$, where $p$ indicates the number of experimental data points in training. The superscript $T$ denotes the transpose of the matrices. Lastly, the coverage of the AD in a William plot can be characterized by Eq. 4.18, where $N_{inside}$ represents the total number of data points within the boundaries of the AD, while $N$ denotes the entire number of data points (including both the training and testing set).

$$AD_{coverage}\ (\%) = \frac{N_{inside}}{N} \times 100 \tag{4.18}$$

*Optimization of the ANN Structure*

The performance of an ANN model is significantly influenced by the number of neurons in the hidden layer, which exerts a considerable impact on the complexity and accuracy of the resulting models (Shahbaz et al., 2012). Insufficient neurons in the hidden layer can generate an under-fitted model, resulting in lower accuracy in the training and testing data. Conversely, an excessive number of neurons may lead to overfitting, wherein the model achieves high training accuracy but poorer performance on testing data. Therefore, selecting the appropriate number of neurons in the hidden layer is pivotal for an optimal ANN model performance. As a first attempt, several network structures with a single hidden layer were examined, each one employing various neurons ranging from 1 to 25. Figure 4.18 illustrates the influence of varying the number of neurons in the first hidden layer on the RMSE values. Notably, the figure shows that the ANN model with 24 neurons achieved the most favorable performance in predicting the viscosity logarithm of DES, with an RMSE value of 0.01954.

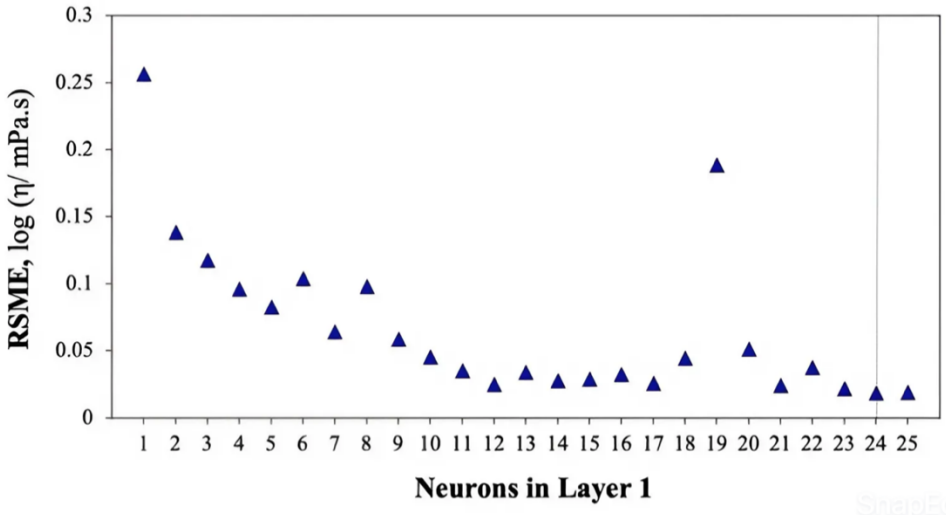


***Figure 4.18.*** *Effect of the number of neurons on the RMSE for predicting the viscosity of DES using the Bayesian regularization algorithm for training ANNs with one hidden layer.*

Previous literature have shown that highly non-linear relationships tend to be more accurately modeled using ANNs with two or more hidden layers (Asensio-Delgado et al., 2022; Boublia et al., 2022; Lemaoui et al., 2022). Based on this information, an extensive analysis was performed, exploring the impact of adding a second hidden layer to the ANN. For that purpose, two layers of ANNs were designed, spanning from 1 to 25 neurons in each layer, and the performance of each network was assessed in terms of RMSE and complexity of the model. Figure 4.18 shows the RMSE results from examining 625 two-hidden layer configurations. Among these configurations, the ANN featuring 19 neurons in the first hidden layer and 16 neurons in the second hidden layer has been selected as the optimal compromise between accuracy and architecture complexity, as it is the simplest model that achieves one of the lowest RSME, obtaining a value of 0.01424 in predicting the logarithm of DES viscosity in the total training and testing set. This RMSE is approximately 27% lower than the RMSE obtained by a model with a single hidden layer consisting of 24 neurons (0.01954).

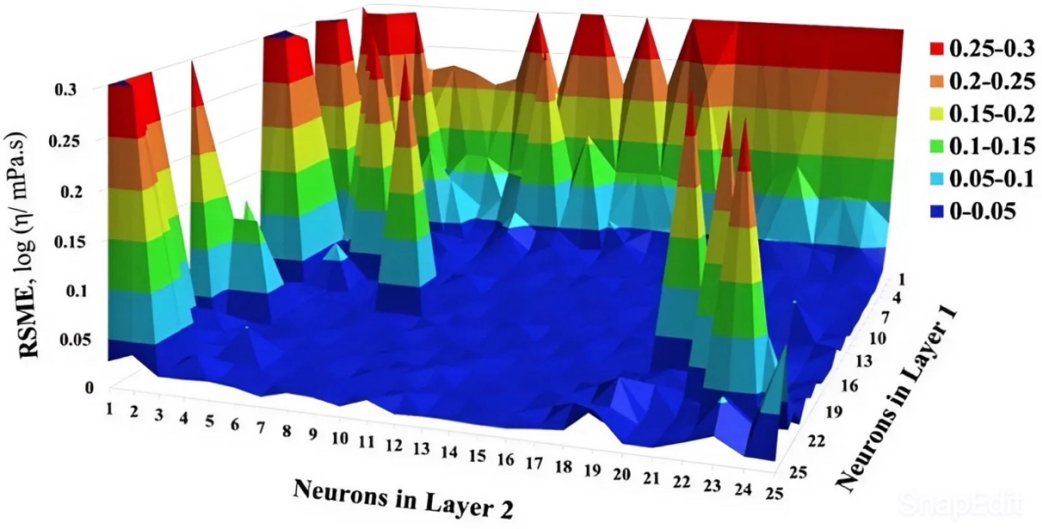


***Figure 4.19.*** *Effect of the number of neurons on the RMSE for predicting the viscosity of DES using the Bayesian regularization algorithm for training ANNs with two hidden layers.*

Hence, it has been determined that the most effective architecture for predicting the provided dataset is 9-19-16-1. The schematic diagram of the optimal ANN is displayed in Figure 4.20, and the weights and biases of each neuron are reported in Table 4. 9.

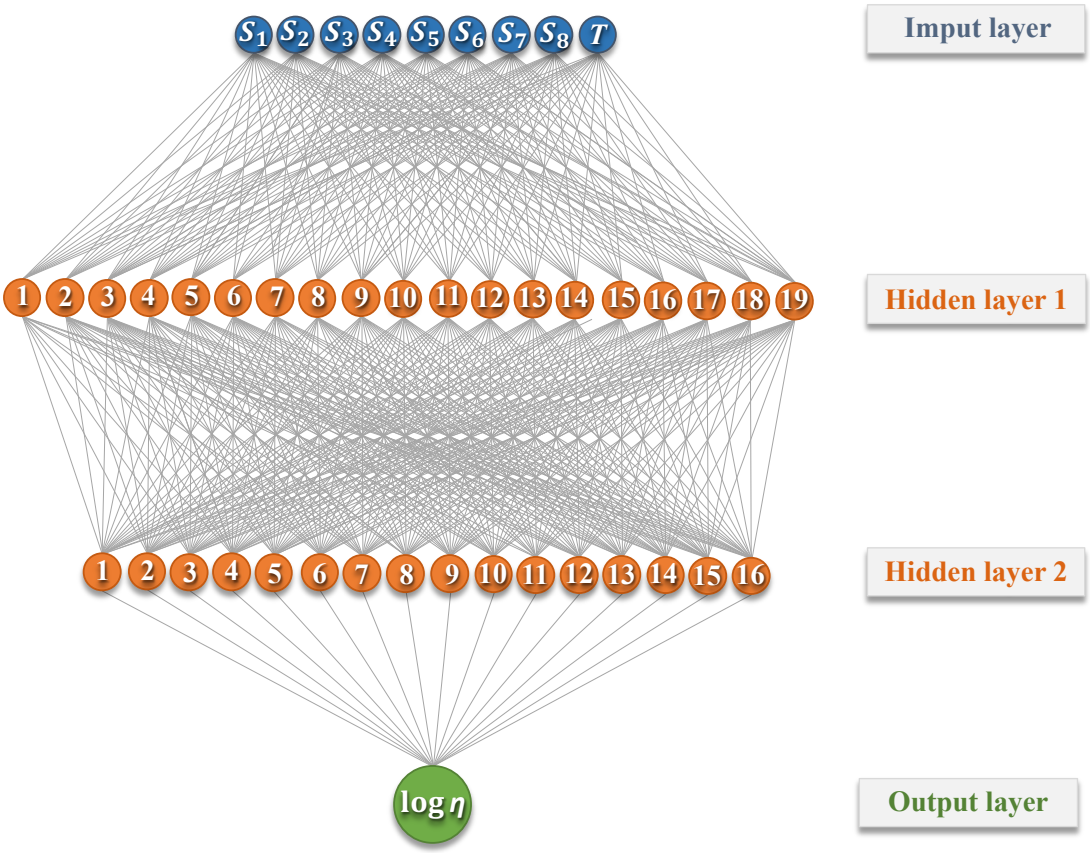


***Figure 4.20.*** *Schematic diagram of the optimal ANN model with a (9-19-16-1) configuration.*

Additionally, the developed ANN has been integrated into an open source and user-friendly Excel spreadsheet, which is freely available in a published contribution (Alencar et al., 2024). Figure 4.21 shows the prediction of the viscosity of DES 6.1, as detailed in Table 4.6.

***Table 4.9.*** *ANN weights and biases for the links between the neurons in the first hidden layer, the second hidden layer and the output layer.*

**Hidden Layer 1**

| | $H_1^{(1)}$ | $H_2^{(1)}$ | $H_3^{(1)}$ | $H_4^{(1)}$ | $H_5^{(1)}$ | $H_6^{(1)}$ | $H_7^{(1)}$ | $H_8^{(1)}$ | $H_9^{(1)}$ | $H_{10}^{(1)}$ | $H_{11}^{(1)}$ | $H_{12}^{(1)}$ | $H_{13}^{(1)}$ | $H_{14}^{(1)}$ | $H_{15}^{(1)}$ | $H_{16}^{(1)}$ | $H_{17}^{(1)}$ | $H_{18}^{(1)}$ | $H_{19}^{(1)}$ |
|---|---|---|---|---|---|---|---|---|---|---|---|---|---|---|---|---|---|---|---|
| $S_1$ | 1.327 | -1.502 | -0.125 | -1.190 | 2.992 | 0.368 | 2.864 | -0.434 | 1.295 | -0.395 | -0.096 | -2.750 | -0.037 | 2.058 | -3.617 | 4.144 | 0.013 | 0.478 | -3.192 |
| $S_2$ | -62.253 | -58.220 | 57.293 | -39.040 | -88.611 | 53.525 | -69.615 | 67.183 | 20.004 | -0.241 | -87.743 | -54.656 | -4.806 | 56.855 | -87.698 | 42.931 | -75.854 | 42.205 | -10.219 |
| $S_3$ | 0.370 | 7.029 | -23.738 | 8.669 | -9.216 | -9.417 | 6.213 | -7.536 | -1.511 | 2.477 | 9.747 | 9.098 | -16.243 | 5.497 | -1.968 | 7.428 | -11.221 | 12.150 | 5.663 |
| $S_4$ | 6.741 | -13.016 | -9.958 | 4.182 | -0.936 | -0.175 | -7.289 | -5.661 | -13.034 | 12.213 | -6.211 | 14.816 | 13.197 | 5.372 | 2.758 | 3.581 | -7.976 | -8.701 | -0.246 |
| $S_5$ | -1.953 | 0.593 | 19.359 | -3.629 | 9.456 | 26.766 | -24.688 | -10.403 | 5.166 | 18.046 | -10.036 | -8.570 | -20.847 | -18.329 | -21.224 | -18.277 | -12.572 | 17.331 | -0.769 |
| $S_6$ | 27.362 | -5.813 | -19.632 | -26.129 | 37.129 | -35.001 | -16.639 | -33.546 | 11.175 | 42.120 | -11.256 | 35.809 | -10.769 | 37.674 | -4.219 | -48.155 | 25.650 | -32.875 | 27.553 |
| $S_7$ | 6.275 | -26.557 | -26.239 | 12.444 | -7.650 | -13.096 | -5.803 | -14.187 | -9.975 | 2.430 | -22.883 | 24.811 | -29.605 | -9.496 | -20.212 | -10.038 | -15.756 | 21.635 | 2.015 |
| $S_8$ | -103.375 | 229.005 | -6.776 | 290.065 | 153.598 | 214.473 | 56.499 | -61.365 | 100.754 | -53.050 | -150.728 | 131.905 | 212.786 | 176.655 | -168.59 | 248.797 | -40.981 | -55.651 | 210.813 |
| $T$ | 0.001 | 0.002 | 0.002 | 0.003 | -0.009 | -0.040 | 0.000 | -0.009 | 0.005 | 0.011 | 0.006 | 0.001 | 0.003 | -0.003 | 0.008 | -0.003 | 0.004 | 0.000 | -0.019 |
| $b^{(1)}$ | -10.558 | 0.308 | 1.927 | -1.078 | 7.368 | -3.780 | 4.711 | 4.397 | -1.760 | -7.079 | 1.396 | -6.426 | 2.937 | 1.023 | -2.851 | 4.793 | 2.189 | 0.077 | -0.191 |

**Hidden Layer 2**

| | $H_1^{(2)}$ | $H_2^{(2)}$ | $H_3^{(2)}$ | $H_4^{(2)}$ | $H_5^{(2)}$ | $H_6^{(2)}$ | $H_7^{(2)}$ | $H_8^{(2)}$ | $H_9^{(2)}$ | $H_{10}^{(2)}$ | $H_{11}^{(2)}$ | $H_{12}^{(2)}$ | $H_{13}^{(2)}$ | $H_{14}^{(2)}$ | $H_{15}^{(2)}$ | $H_{16}^{(2)}$ |
|---|---|---|---|---|---|---|---|---|---|---|---|---|---|---|---|---|
| $H_1^{(1)}$ | 3.327 | -1.032 | -1.545 | 0.455 | -0.747 | 2.419 | 1.190 | -0.118 | -2.198 | 0.703 | -1.396 | 0.532 | 2.754 | -0.496 | -0.825 | 0.488 |
| $H_2^{(1)}$ | 2.649 | -1.348 | 4.574 | 0.084 | -3.591 | -0.947 | 1.161 | -0.110 | 11.800 | -0.031 | 0.136 | -0.315 | -2.780 | -0.115 | -2.533 | 2.238 |
| $H_3^{(1)}$ | 0.228 | 0.693 | -2.437 | 0.888 | 3.427 | 0.133 | -0.656 | -0.048 | -8.711 | -0.903 | 2.246 | -1.032 | -0.579 | -1.697 | 0.531 | 1.038 |
| $H_4^{(1)}$ | 9.132 | 3.022 | -0.324 | 0.997 | 1.752 | 3.308 | 1.384 | 2.255 | 1.200 | -1.210 | 1.767 | -1.430 | 0.187 | 0.566 | 3.845 | 1.019 |
| $H_5^{(1)}$ | 3.958 | -0.245 | 0.131 | 0.079 | 2.313 | 0.485 | 1.088 | -0.031 | 0.079 | 1.169 | 0.083 | 1.969 | -0.083 | 0.770 | 0.493 | 2.821 |
| $H_6^{(1)}$ | 3.465 | -0.816 | -0.682 | -0.035 | -0.415 | 2.382 | 1.491 | -0.018 | -2.489 | 0.848 | -1.410 | 0.615 | 2.519 | -1.238 | -0.945 | 0.918 |
| $H_7^{(1)}$ | -0.230 | -0.790 | -3.250 | 0.375 | 2.430 | 0.183 | 1.236 | -0.400 | -6.514 | -0.314 | -0.008 | -0.224 | -3.304 | 0.041 | -0.549 | -0.581 |
| $H_8^{(1)}$ | 3.122 | 0.513 | -0.160 | 0.438 | -2.353 | -0.759 | -0.355 | 0.188 | 1.730 | -1.265 | 1.841 | -0.351 | -2.093 | -0.466 | -0.740 | 0.565 |
| $H_9^{(1)}$ | 0.376 | 1.484 | 0.480 | 2.623 | -3.537 | 0.952 | 1.227 | 1.639 | 1.644 | 1.055 | 1.408 | 4.836 | -1.591 | 0.808 | 1.692 | 1.266 |
| $H_{10}^{(1)}$ | -0.621 | 0.418 | 0.547 | -1.107 | -0.259 | -0.838 | -0.727 | 0.103 | 3.095 | -1.360 | 1.345 | -0.932 | -0.231 | -0.638 | -0.237 | -0.038 |
| $H_{11}^{(1)}$ | -0.123 | -0.561 | -0.689 | 2.041 | -5.918 | -2.487 | -1.966 | 1.249 | -7.018 | -1.644 | -1.430 | -1.842 | -0.007 | 3.259 | -4.846 | 7.196 |
| $H_{12}^{(1)}$ | 2.281 | 0.875 | 2.689 | 1.024 | 3.768 | -0.655 | -0.145 | -0.313 | -0.203 | 0.218 | 5.572 | 2.065 | -3.186 | 1.444 | 0.450 | -0.121 |
| $H_{13}^{(1)}$ | 1.113 | -0.545 | -2.526 | -1.240 | -7.050 | -1.268 | -0.271 | 0.067 | -1.875 | -1.442 | -1.127 | -1.459 | 1.978 | -2.358 | -0.190 | -1.375 |
| $H_{14}^{(1)}$ | 2.658 | 0.123 | -2.344 | -0.730 | -9.504 | 1.113 | 1.105 | 0.397 | -2.568 | 1.307 | -6.161 | 1.070 | 1.760 | 0.130 | 0.056 | 4.620 |
| $H_{15}^{(1)}$ | 0.407 | 0.301 | -2.368 | 0.223 | -2.353 | 1.319 | 0.131 | -0.142 | -1.510 | 1.121 | -2.059 | 0.590 | -1.157 | -0.258 | 1.231 | -1.059 |
| $H_{16}^{(1)}$ | -7.144 | 0.938 | 2.521 | 1.340 | 0.934 | -2.284 | -3.379 | -0.018 | 3.440 | -1.976 | 3.276 | -3.173 | -0.337 | -2.621 | -1.076 | -1.215 |
| $H_{17}^{(1)}$ | -0.995 | 0.058 | 4.051 | -1.078 | 5.454 | 0.164 | 0.375 | -0.043 | 5.885 | 1.867 | 1.970 | 4.911 | 0.096 | 0.318 | 1.331 | -3.668 |
| $H_{18}^{(1)}$ | 0.890 | -0.721 | -2.816 | 1.490 | 6.191 | 3.827 | 1.500 | -0.020 | -7.496 | 1.364 | 3.937 | 2.614 | 1.936 | 1.350 | -0.604 | -1.318 |
| $H_{19}^{(1)}$ | 5.870 | 0.717 | -4.700 | 0.012 | -1.473 | -1.248 | -0.794 | 0.571 | -6.705 | -0.399 | -0.620 | -0.627 | 0.474 | 2.472 | 0.431 | 2.020 |
| $b^{(2)}$ | -4.524 | 1.912 | 2.152 | -0.861 | 1.177 | -2.385 | -1.032 | 0.106 | 3.086 | 0.023 | 2.097 | 0.226 | -3.663 | 1.798 | 2.078 | -2.213 |

**Output Layer**

$$log\,\eta = 0.2440\left(H_1^{(2)}\right) - 4.8844\left(H_2^{(2)}\right) - 5.8474\left(H_3^{(2)}\right) - 2.6789\left(H_4^{(2)}\right) + 12.6615\left(H_5^{(2)}\right) + 3.2011\left(H_6^{(2)}\right) + 2.0377\left(H_7^{(2)}\right) - 3.8898\left(H_8^{(2)}\right) + 1.7997\left(H_9^{(2)}\right) - 7.2019\left(H_{10}^{(2)}\right) - 6.9226\left(H_{11}^{(2)}\right) + 5.0880\left(H_{12}^{(2)}\right) - 4.7702\left(H_{13}^{(2)}\right) + 1.6620\left(H_{14}^{(2)}\right) - 2.2138\left(H_{15}^{(2)}\right) + 3.3922\left(H_{16}^{(2)}\right) - 4.1363$$

| Inputs | | | | | | | |
|---|---|---|---|---|---|---|---|
| HBA | Choline Chloride | | | | | | |
| HBD | Glycerol | | | | | | |
| co-solvent | Water | | | | | | |
| $x_{HBA}$ | 0.2 | | | | | | |
| $x_{HBD}$ | 0.4 | | | | | | |
| $x_{co\text{-}solv} = 1 - x_{DES}$ | 0.4 | | | | | | |
| Temperature (K) | 303.15 | | | | | | |
| Calculated molecular descriptors | | | | | | | |
| $S_1$ | $S_2$ | $S_3$ | $S_4$ | $S_5$ | $S_6$ | $S_7$ | $S_8$ |
| 0 | 0.0130059 | 0.0737982 | 0.0454151 | 0.0156431 | 0.0260593 | 0.0410487 | 0 |
| Prediction result | LOG η | | | | η (mPa.s) | | |
| | 1.6999 | | | | 50.1041 | | |

***Figure 4.21**. Image of the Excel Spreadsheet available in for the prediction of viscosity of the DES 6.1 (as detailed in Table 4.6) available in (Alencar et al., 2024).*

*Statistical Analyses*

Following the determination of the optimal ANN configuration, the performance of the developed model in predicting the training and test sets was analyzed by the assessment of various statistical parameters. A detailed summary is provided in Table 4.10.

***Table 4.10.** Summary of the statistical parameters for the performance evaluation of the developed ANN Model.*

| Metric | Training | Testing | External testing | Total |
|---|---|---|---|---|
| $R^2$ | 0.99989 | 0.99723 | 0.99809 | 0.9995 |
| *RSME (log η)* | 0.008271 | 0.037594 | 0.035381 | 0.017887 |
| *AARD (%)* | 1.6288 | 1.4729 | 1.5225 | 1.6031 |
| $AD_{coverage}$ *(%)* | 94.3122 | 92.8571 | 94.7867 | 94.1667 |
| *Data points* | 1512 | 168 | 211 | 1891 |

The ANN model exhibits high statistical performances, achieving an $R^2$ value of 0.99989 and an *AARD* of 1.6288% for the training set, 0.99723 and 1.4729% for the testing set, and 0.99809 and 1.5225% for the external testing set. Furthermore, the *RMSE* values for predicting *log η* were also quite low, standing at 0.008271, 0.037594 and 0.035381 for the training, testing and external testing sets, respectively, providing further evidence of the ANN model reliability.

Figure 4.22 displays scatter plots of experimental and predicted DESs *log η* values, demonstrating the excellent model fit and absence of overfitting, with most points closely aligned along the y = x diagonal.

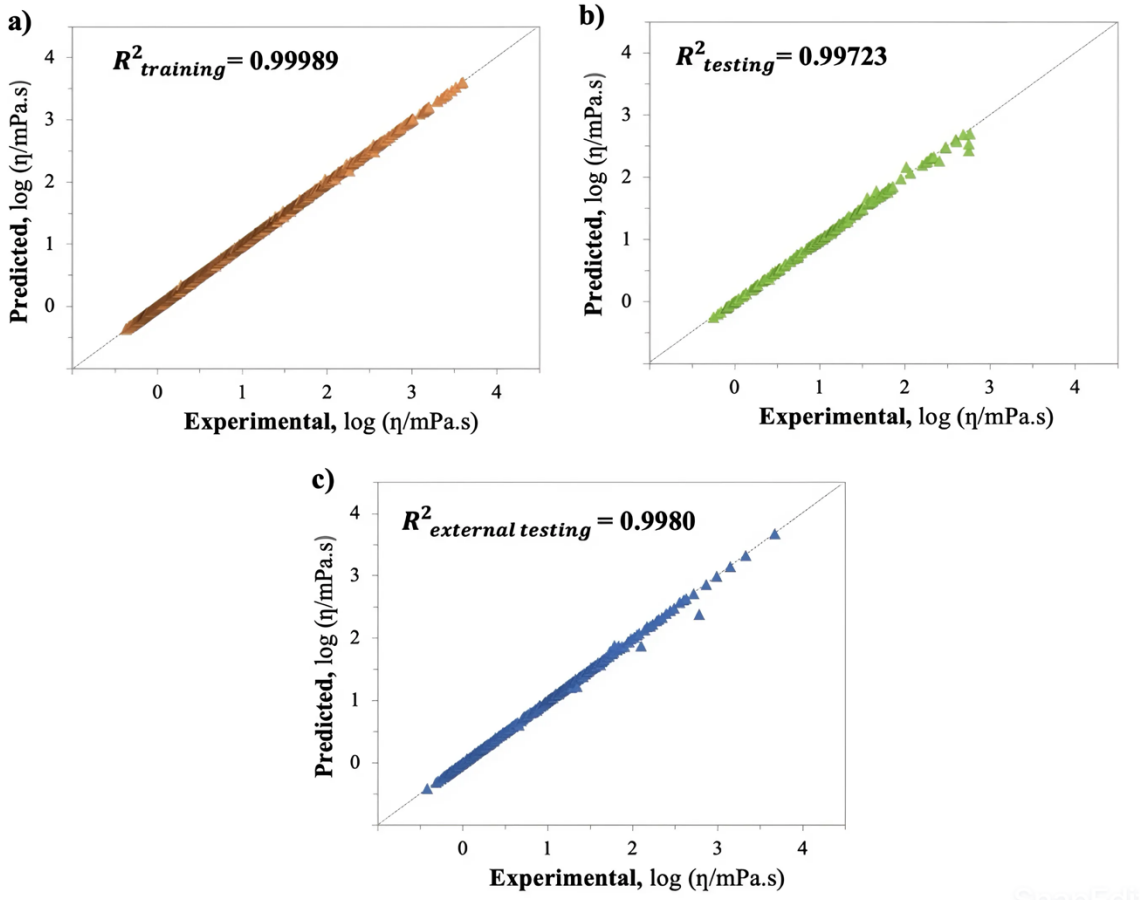


***Figure 4.22.*** *Parity graph comparing experimental and predicted DESs log η values from the ANN model, with corresponding $R^2$ values from a) training, b) testing and c) external testing.*

The residual plot was also employed to analyze the model's accuracy for further evaluation. As illustrated in Figure 4.23, the proposed model exhibited exceptional performance in predicting the *log η* of DESs, with 99.15 % of residuals concentrated within the ±0.05 range.

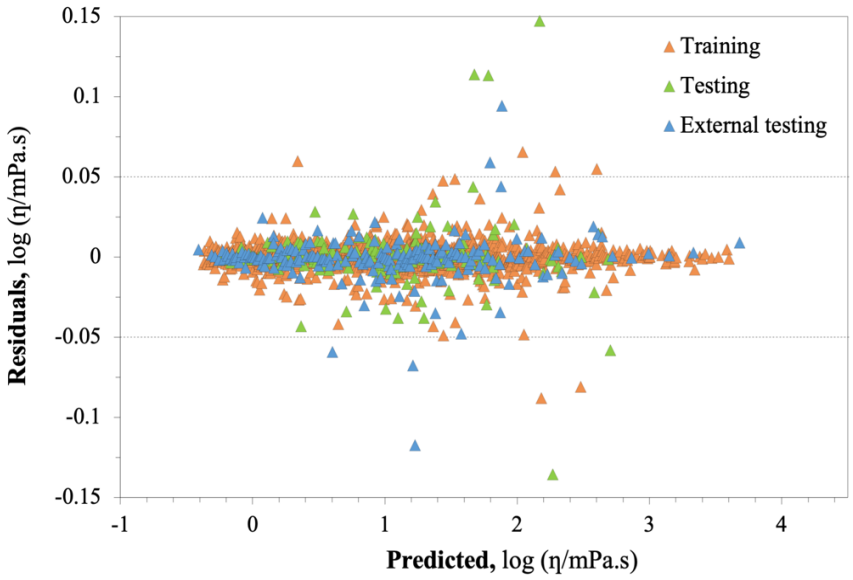


***Figure 4.23.*** *The residual deviation between the experimental and predicted DESs log η values for training, testing and external testing sets.*

Furthermore, an *y*-scrambling approach was applied to ensure that the obtained ANN was not correlated by chance. Firstly, the dataset was modified by randomly arranging the *log η* responses. Then, another ANN model with the same hypertuned parameters (i.e. the same network architecture) was created for the randomly reordered responses, and the *y*-scrambling regression coefficient ($R^2_{\text{scramble}}$) value of the new model was calculated. This procedure was performed 100 times to generate new randomly reordered responses and ANN models. The mean value of $R^2_{\text{scramble}}$ was found to be

0.2086, which suggests that there is no significant correlation due to random chance in the regression, reinforcing the validity of the ANN.

In order to further ensure the robustness of the selected descriptors and their insensitivity to changes in the input dataset, a cross-validation test based on the leave-one-system-out technique (Lemaoui et al., 2021) was conducted. Aiming to assess the predictivity of a thermophysical property, the cross-validation is performed for systems rather than individual data points or random sets of points, in a similar manner as done for QSAR models in a recent contribution, where this validation was done by anions (Liu et al., 2023). Thus, this technique is computed here by excluding one DES from the training set and determining the model's internal fit assessed by the coefficient of determination calculated for the DES "predicted as new" by the developed model. The process is then repeated multiple times until all the DESs shown in Table 4.6 are held-out once from the training set, and an average of the internal fits is computed as the $Q^2$ cross-validation coefficient. The mean value of $Q^2$ was found to be 0.9044, which reflects the robustness of the model.

Considering all error analyses, the developed ANN, based on COSMO-SAC $\sigma$-profiles of the compounds and the experimental data temperature, exhibits a strong capacity to accurately describe DESs and DESs + cosolvent viscosities with very modest deviations.

*Applicability Domain*

The scope and reliability of the developed ANN model can be further assessed using the Applicability Domain (AD) analysis. Evaluating the AD holds significant

importance, especially for molecular-based ANNs, as it quantitatively defines the range of molecules and conditions where the prediction can be performed accurately (Lemaoui et al., 2021; Lemaoui et al., 2023; Tropsha et al., 2003). The AD of the developed ANN model was assessed using the William plot, shown in Figure 4.24, where the AD boundaries are defined by the vertical dashed line ($0 < h_i < h^*$) and the horizontal dashed lines ($-3 < SDR < +3$) (Tropsha et al., 2003).

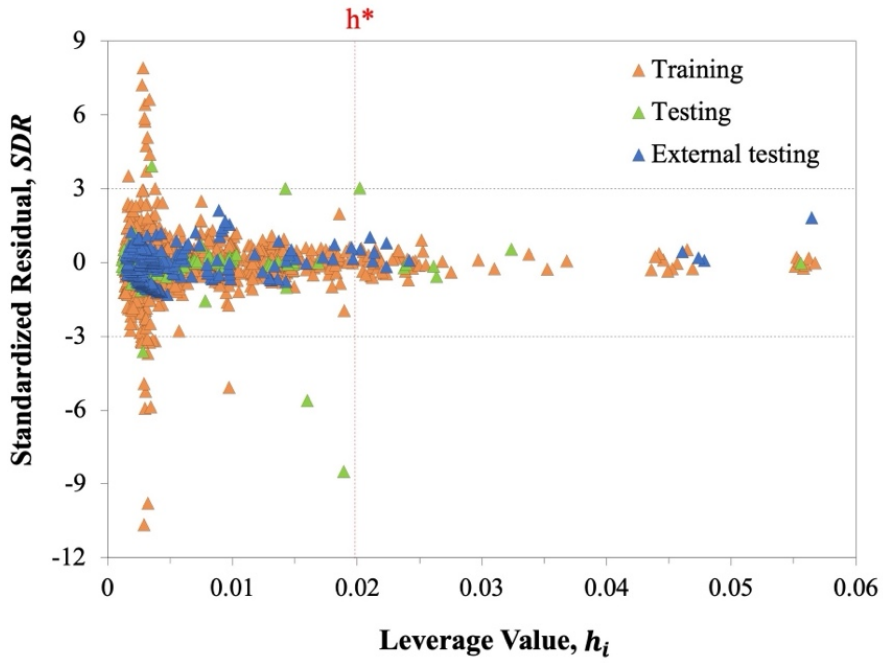


***Figure 4.24.*** *William plot for the log η of the total set of DESs.*

The analysis reveals that most of the DESs data employed in the development of the ANN model and the external testing are within the AD boundaries, with an $AD_{coverage}$ of 94.167% across the entire dataset. However, the predictions in training, testing and external testing of some few data points at exceptional temperature values are considered structural outliers due to their leverage values surpassing $h^*$ or SDRs exceeding the standard limit of $\pm 3$. Nevertheless, these outliers constitute a minor fraction, accounting

for less than 6% of the total data points. Hence, the database used in this study does not contain a substantial number of outliers and the developed ANN model is properly accurate within its domain of applicability, indicating the robustness and reliability of the proposed ANN model due to its large AD and structural coverage.

*Molecular Descriptor Importance*

To assess the significance of the individual input variables within the molecular-based ANN model and their influence on the viscosity of the DESs, a relative contribution analysis has been performed. This analysis was conducted employing the Partial Derivatives (PaD) method, identified as the most effective approach for studying the relative contributions of input parameters to the ANN's output (Gevrey et al., 2003). The PaD method involves computing the partial derivatives of the output over the input variables (Asensio-Delgado et al., 2022). The results of the relative contribution of the molecular descriptors inputs related to the discretization of the $\sigma$-profiles are illustrated in Figure 4.25.

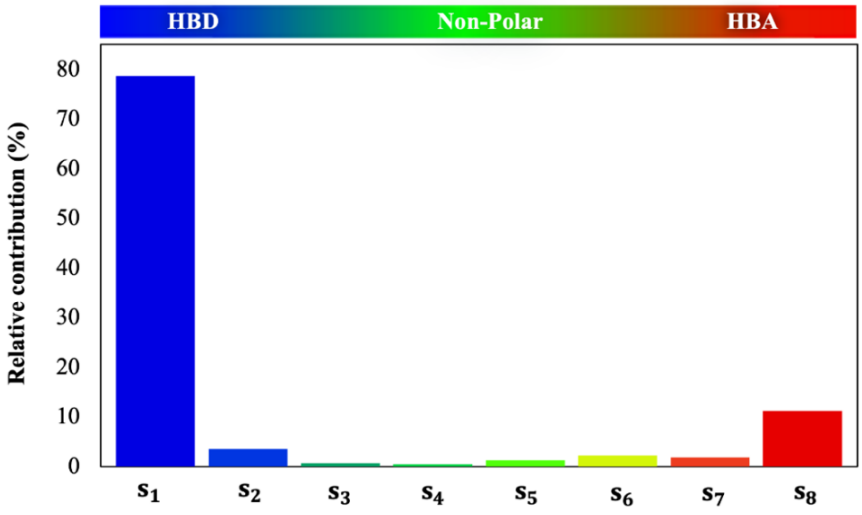


***Figure 4.25.*** *Relative contributions of the $S_{1\text{-}8}$ molecular descriptors inputs to the log η of the DESs for the optimized ANN (9-19-16-1) calculated with the PaD method.*

As it can be observed, the regions with strong hydrogen bonding areas exhibit the most significant contributions to the log $\eta$ of the DESs, as the strongest HBD region [$S_1$] presents a relative contribution of 78.71% and the strongest HBA region [$S_8$] of 11.23%. From a chemical perspective, the viscosity of DESs primarily depends on the strength of hydrogen bonds, as the extensive network of these bonds limits the mobility of free species within the DESs, leading to a viscosity increase (Mbous et al., 2017; Zhang et al., 2012). As an example, the viscosity of [Ch]Cl-based DESs is significantly higher when using a diacid, like oxalic acid, as the HBD, compared to a monoacid, like levulinic acid, due to the formation of additional hydrogen bonds (Florindo et al., 2014). Figure 4.26 provides a visual representation of the direct influence of all input variables on the output, illustrating the relationship between derivatives of the log η with respect to each input variable and their corresponding input.

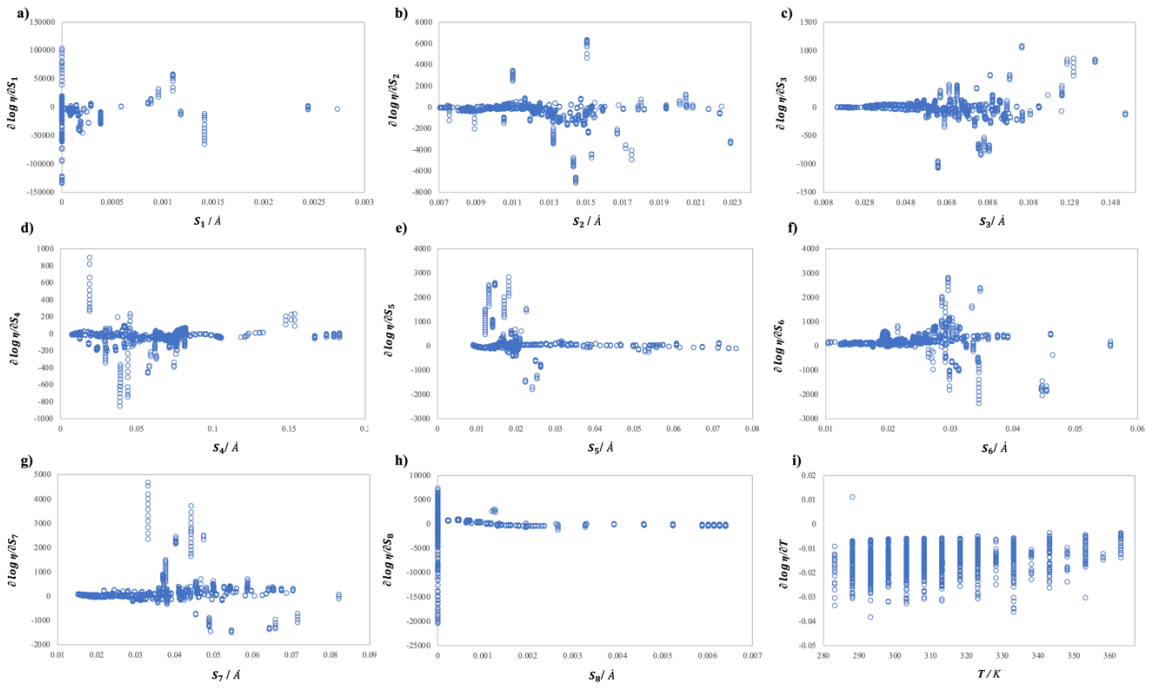


***Figure 4.26.*** *Partial derivatives of the log η with respect to each input variable represented against its corresponding input variable.*

Figure 4.27 also shows a visual representation of the direct influence of all input variables on the output, depicting the relationship between these derivatives and the resulting log $\eta$ of the DESs.

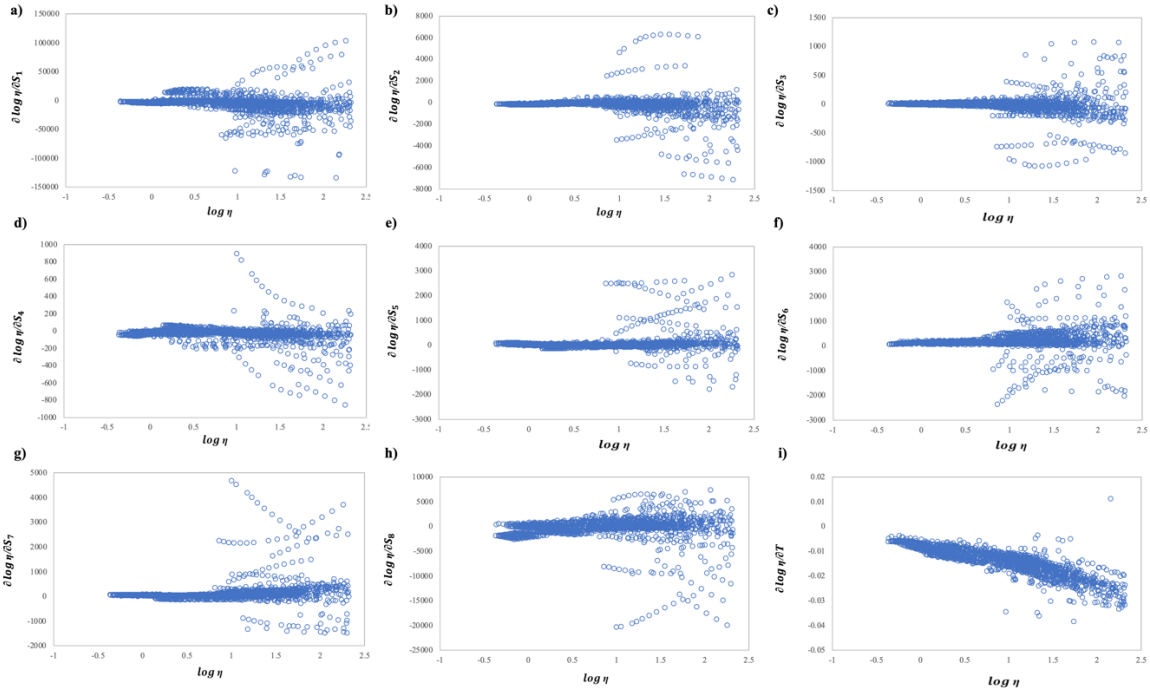


***Figure 4.27.*** *Partial derivatives of the log η with respect to each input variable represented against the log η.*

Both Figures 4.26 and 4.27 demonstrate the sensitivity of the output (log η) to each input variable, where higher values of the partial derivatives indicate greater sensitivity. This means that small changes in an input variable with a high partial derivative value significantly impact the output. Specifically, in Figure 4.26(a) and Figure 4.27(a), it can be observed that the [$S_1$] descriptor has the highest partial derivative values, indicating that this descriptor most significantly affects the viscosity of DESs in this ANN. Overall, the relative contributions mentioned above provide valuable insights

related to the impact of hydrogen bonding on viscosity, facilitating an ad-hoc selection of promising DESs for specific applications.

*Predictive Capabilities*

As previously stated, the purpose of this study is to develop a versatile tool able to accurately estimate an important property, such as the viscosity, in a wide range of conditions. Consequently, it is crucial to evaluate the predictive capabilities of the model presented. Hence, the developed ANN is here applied to predict the viscosities of some DESs in specific conditions not included in the experimental dataset. This includes scenarios featuring different combinations of HBDs and cosolvents, which were outside the scope of both the training and testing procedures. In particular, these data encompass a new HBD, 2,3 butanediol, through the prediction of DESs based in [Ch]Cl : 2,3-butanediol at different ratios (Deng et al., 2020), as well as ethanol as a new cosolvent, through mixtures of [Ch]Cl : EG (1:2) at various ratios (Haghbakhsh et al., 2021a), extending the model's predictive capacity beyond its original scope. The $\sigma$-profile of these new compounds are shown in Figure 4.28.

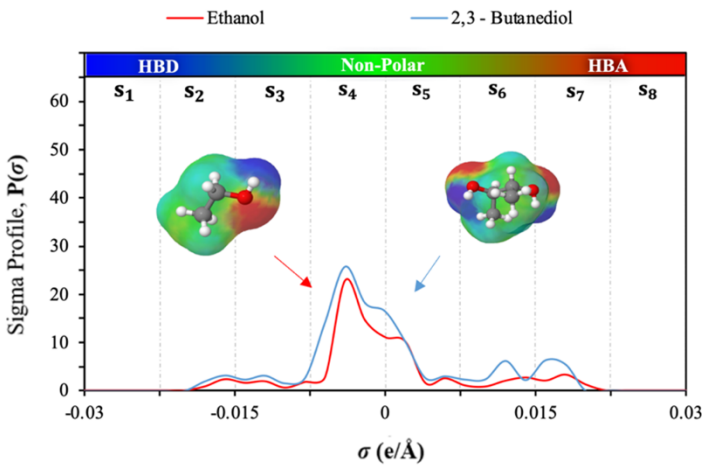


***Figure 4.28.*** *COSMO-SAC calculated σ-profiles for the new cosolvent (Ethanol) and the new HBD (2,3-butanediol), with their 3D geometrically optimized COSMO-SAC surfaces.*

The calculated areas below the $S_{\sigma\text{-profiles}}$, providing the [$S_1$-$S_8$] descriptors for these two compounds are listed in Table 4.11.

***Table 4.11.*** *Calculated molecular descriptor for compounds used in extrapolation tests.*

| Element | $S_1$ | $S_2$ | $S_3$ | $S_4$ | $S_5$ | $S_6$ | $S_7$ | $S_8$ |
|---|---|---|---|---|---|---|---|---|
| **Ethanol** | 0 | 0.00785 | 0.01276 | 0.08856 | 0.03699 | 0.01283 | 0.01575 | 0 |
| **2,3 Butanediol** | 0 | 0.01246 | 0.03107 | 0.11845 | 0.04512 | 0.02689 | 0.02570 | 0 |

The comparison between the experimental data and the extrapolated predictions of DES viscosities for the first test, using ethanol as a new cosolvent, with the proposed ANN is depicted in Figure 4.29.

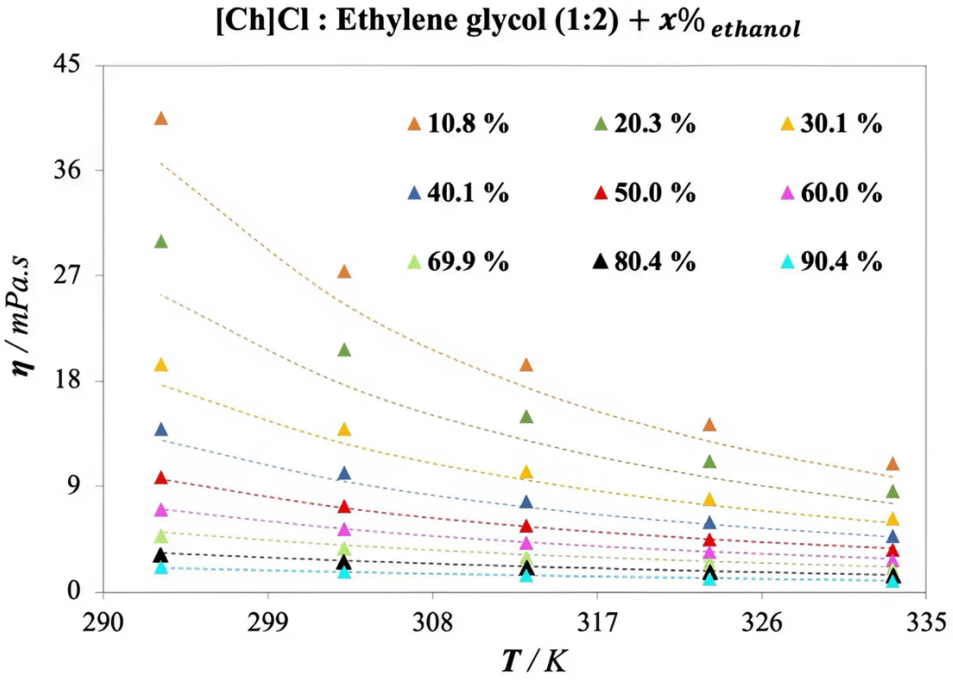


***Figure 4.29.*** *Viscosity predictions in the presence of a new cosolvents: Viscosity experimental data (Haghbakhsh et al., 2021a) (symbols) and predictions calculated (dashed lines) by the proposed optimized ANN model (9-19-16-1) for [Ch]Cl- EG (1:2) + Ethanol at different proportions.*

The high accuracy achieved by the network to predict the viscosity of [Ch]Cl:EG (1:2) in solution with ethanol is demonstrated through the low AARD of 6.19% encountered across a wide range of ethanol proportions, spanning from 10% to 90% of the molar fraction. It is important to remark that no degeneracy is observed when increasing the amount of cosolvent in the solution.

The second test explores the addition of 2,3-butanediol as a new HBD combined with [Ch]Cl at different ratios. The predictions show reasonable agreement with the available experimental data, as illustrated in Figure 4.30. While the results offer and acceptable AARD of 18.91%, the major deviations are caused by the inclusion of a proportion with a bigger amount of 2,3-butanediol (1:4) and grow at lower temperatures. On the other hand, the results for the [Ch]Cl:2,3-butanediol (1:3) are excellent in the whole range of temperatures.

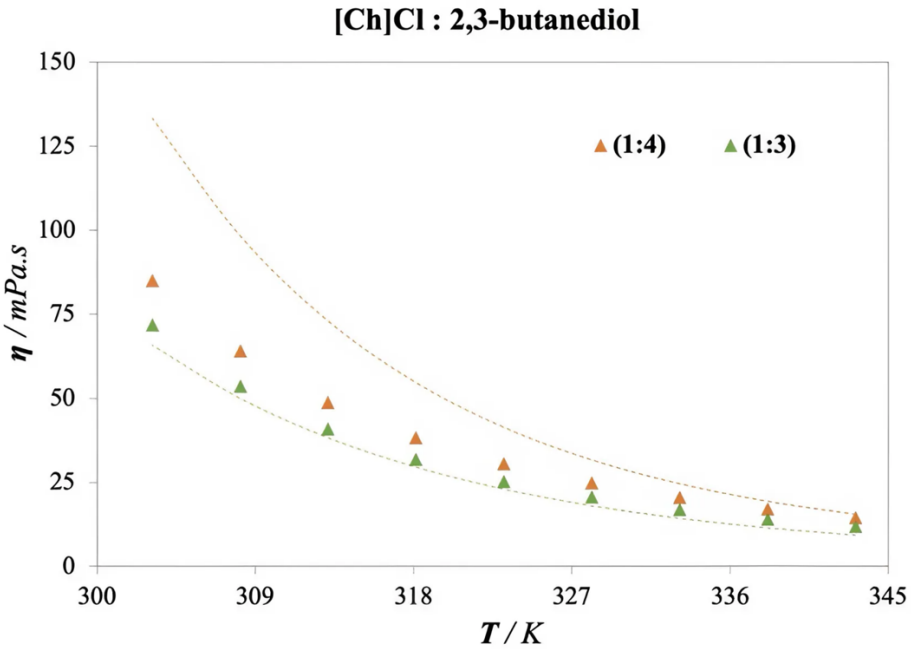


***Figure 4.30.*** *Viscosity predictions in the presence of a new HBD (2,3-butanediol): Viscosity experimental data (Deng et al., 2020) (symbols) and predictions calculated (dashed lines) by the proposed optimized ANN model (9-19-16-1) for [Ch]Cl- 2,3-butanediol at different proportions.*

Finally, the extrapolation capacity of the ANN is further stressed by predicting a range of extremely high viscosities, omitted from the dataset due to values exceeding 4000 mPa·s (Florindo et al., 2014), for the DES [Ch]Cl: OA (1:1). The results are plotted in Figure 4.31. Remarkably, the ANN predicts the viscosity of [Ch]Cl: OA (1:1) with an AARD of 8.57%, covering a wide range of viscosity values from 5000 to 16000 mPa·s, highlighting the capacity to estimate values where measurements are difficult due to the inherent complexities of a highly viscous flow.

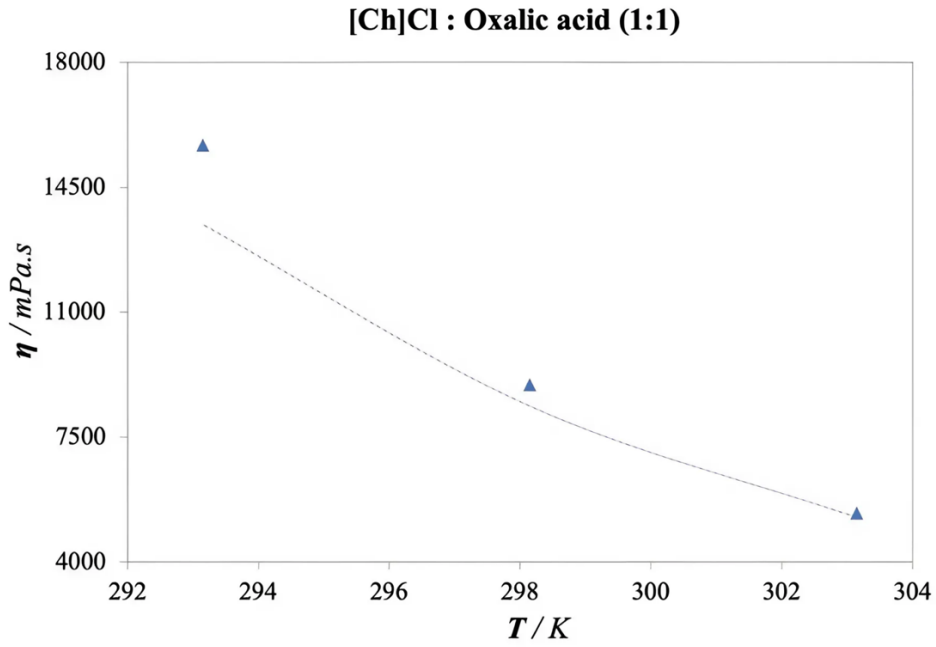


***Figure 4.31.*** *Extrapolation capability of the ANN for data outside the fitting viscosity range. Viscosity experimental data (Florindo et al., 2014) (symbols) and predictions calculated (dashed lines) by the proposed optimized ANN model (9-19-16-1) for [Ch]Cl:OA (1.1) at low temperatures.*

Additionally, all these new experimental data are tested for their AD, yielding a 95.45% of $AD_{coverage}$, implying that most of them fall within the model's applicability domain. The William plot of these data is shown in Figure 4.32. Particularly, the data for [ChCl] : OA (1:1) at the lowest temperatures fall outside the AD of the model. Therefore,

the developed model can be considered reliable, except for these specific data points, for which viscosity predictions should be treated with caution.

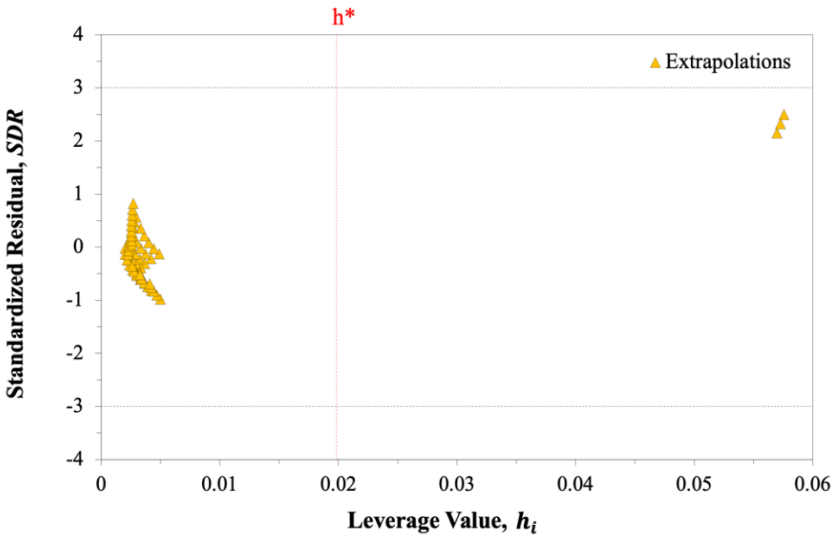


***Figure 4.32.*** *William plot for the log η of the extrapolations set of DESs.*

## 4.3 Key Findings of the Chapter

This chapter develops a framework to describe the impact of cosolvents on the thermophysical properties of [Ch]Cl-based DESs. The soft-SAFT EoS, combined with FVT, effectively characterizes density, isentropic compressibility, speed of sound, vapor-liquid phase equilibria and viscosity for various DESs and their mixtures with cosolvents. This model provides a robust and transferable parametrization, accurately predicting the behavior of DESs across different HBDs, ratios and temperatures. Additionally, an ANN model using COSMO-SAC-based σ-profiles and temperature inputs was developed to estimate viscosity of [Ch]Cl-based DESs, using a database of 1891experimental viscosity measurements. The ANN achieved high accuracy, demonstrating excellent performance metrics and predicting viscosity for various [Ch]Cl-based DESs, including new HBDs

and cosolvents not included in the training dataset. This ANN model facilitates efficient property prediction, significantly accelerating research and industrial application of DESs. Together, these methods provide a comprehensive and reliable approach for understanding and predicting the properties of DESs, aiding in their development and practical application.

# 5

# Gas Separation Technological Applications using DESs

*This chapter delves into the selective recovery of Greenhouse Gases (GHGs) using Deep Eutectic Solvents (DESs). The investigation encompasses two primary areas: the separation of commercial refrigerant blends and the recovery of ammonia from a mixture containing carbon dioxide from melamine streams. The solubility of a range of GHGs in DESs is examined using the soft-SAFT EoS, which includes determining enthalpy and entropy of dissolution, Henry's constants, as well as ideal and competitive selectivity of the DES in GHG blends.*

Currently, global warming represents one of the most pressing topics in modern science, exerting far-reaching impacts across virtually all areas of society and serving as an incentive for public policies, regulations, and studies (Hoesung, 2023). The advance of this phenomenon can be attributed mainly to the anthropogenic emission of greenhouse gases (GHGs), whose atmospheric concentration has increased in recent years (*The NOAA Annual Grenhouse Gas Index (AGGI)*). Historically, the most common GHGs have been carbon dioxide ($CO_2$), nitrous oxide, methane, and fluorinated gases (F-gases) ("Inventory of U.S. greenhouse gas emissions and sinks: 1990-2018," 2020).

In this context, the exploration and application of DESs in gas capture and separation technologies have attracted considerable attention, as highlighted in Section 2.2. These solvents offer the capacity for selective extraction and separation of various compounds, providing a sustainable and efficient alternative to traditional solvents. Particularly, the ability of DESs to facilitate the capture of gases, particularly $CO_2$ and other greenhouse gases, underscores their potential in addressing environmental challenges and promoting cleaner industrial practices.

As shown in Section 2.3.1, previous studies have highlighted the remarkable predictive capability of soft-SAFT EoS in characterizing the solubility of GHGs in DESs. Therefore, this section delves into describing, via soft-SAFT EoS, two specific applications of DESs in gas separation and capture, highlighting their efficacy and versatility in this pivotal domain.

## 5.1 Recovery of Commercial Refrigerants Blends

### 5.1.1 The Case Problem

F-gases are mainly employed in the refrigeration industry and are emitted at much lower rates than other GHGs. As of 2019, these compounds accounted for approximately 2.3% of the total GHG emissions globally (IPCC, 2024). However, their high global warming potentials (GWPs), usually thousands of times the value of $CO_2$, dramatically raises their impact, leading to further regulations to lessen global warming effects. The Kigali Amendment to the Montreal Protocol ("Amendment to the Montreal protocol on substances that deplete the ozone layer," 2016) established the future of usage of F-gases, aiming to significantly decrease global hydrofluorocarbon (HFC) emissions to 0.9-1 Gt of $CO_2$ equivalent per year by 2050, along with a reduction in the surface warming to 0.04°C by 2100, which presents an uninspiring contrast to current projections of 1.9-3.6 Gt of $CO_2$ equivalent per year and surface warming of 0.14-0.31°C, respectively (Velders et al., 2022). In this context, there are several challenges to address. For example, it is essential to determine the source of emissions and analyze the appropriate methods for reducing them from specific sources (Sovacool et al., 2021). Indeed, F-gases, especially HFCs, have been characterized by a remarkable increase in their emissions over time ("Fluorinated greenhouse gases," 2019; Velders et al., 2022). Thus, treating these substances represents one of the most challenging tasks in modern chemical engineering.

Destruction of F-gases is the most direct approach to remove these compounds. However, it still copes with difficulties such as high energy demands, hazardous decomposition products under non-optimal conditions, and lack of technological availability in every country (Castro et al., 2021; Sheldon & Crimmin, 2022). A circular

economy framework around F-gases may circumvent this issue, reducing the requirement to produce new F-gases (Castro et al., 2021). Regardless of the approach, an efficient and highly selective recovery of F-gases from end-of-life equipment is crucial for adhering to mid and long-term phase-out regulations. However, using F-gases under highly non-ideal conditions, such as in azeotropic blends (Morrison & McLinden, 1993), limits the alternatives for performing the separation process.

Among techniques involved in recovering F-gases, absorption into ionic liquids (ILs) and deep eutectic solvents (DESs) has raised as a promising alternative, as elucidated in Section 2.2.2. The application of ILs to the absorption process is widely spread in the literature (Asensio-Delgado et al., 2021; Han & Row, 2010; Lei et al., 2014; Vega et al., 2010), while DESs have been studied in a more limited way, with a significant increase over past years (Castro et al., 2020; Codera et al., 2023; Demirbek et al., 2024; Jovell et al., 2020). Some advantages have been attributed to DESs over ILs, namely lower toxicity, viscosity, and corrosivity, better degradability and lower production cost (Prabhune & Dey, 2023).

Merging a remarkable predictive capability with a lower computational cost, previous studies have highlighted the accuracy and predictive power of the soft-SAFT EoS variant (Blas & Vega, 1997) in characterizing the thermodynamic behavior of F-gases (Albà et al., 2021; Albà et al., 2023; Alkhatib et al., 2022), including the modelling of their solubility in DESs (Demirbek et al., 2024; Jovell et al., 2020).

Thus, this section is devoted to verifying the potential absorption of four common F-gases (R-125, R-134a, R-32, and R143a) using specific low-cost, non-toxic, and environmentally friendly DESs. For this purpose, solubility description via soft-SAFT EoS of these F-gases in DESs composed of tetramethylammonium chloride (TMAC) and [Ch]Cl as HBA, and ethylene glycol, glycerol and lactic acid as HBD. Figure 5.1

illustrates the molecular structures of all compounds studied in this section. The thermophysical model is then used to describe various properties, including the density and viscosity of pure DESs, the enthalpy and entropy of dissolution, Henry's constants, and ideal selectivity. Additionally, the study assesses the competitive selectivity among gases in multi-component mixtures based on commercial refrigerant blends and DESs. From this information, a rational analysis is provided to determine the best DES for recovering a specific component in a given commercial blend, facilitating the pre-design of a gas separation unit for industrial applications.

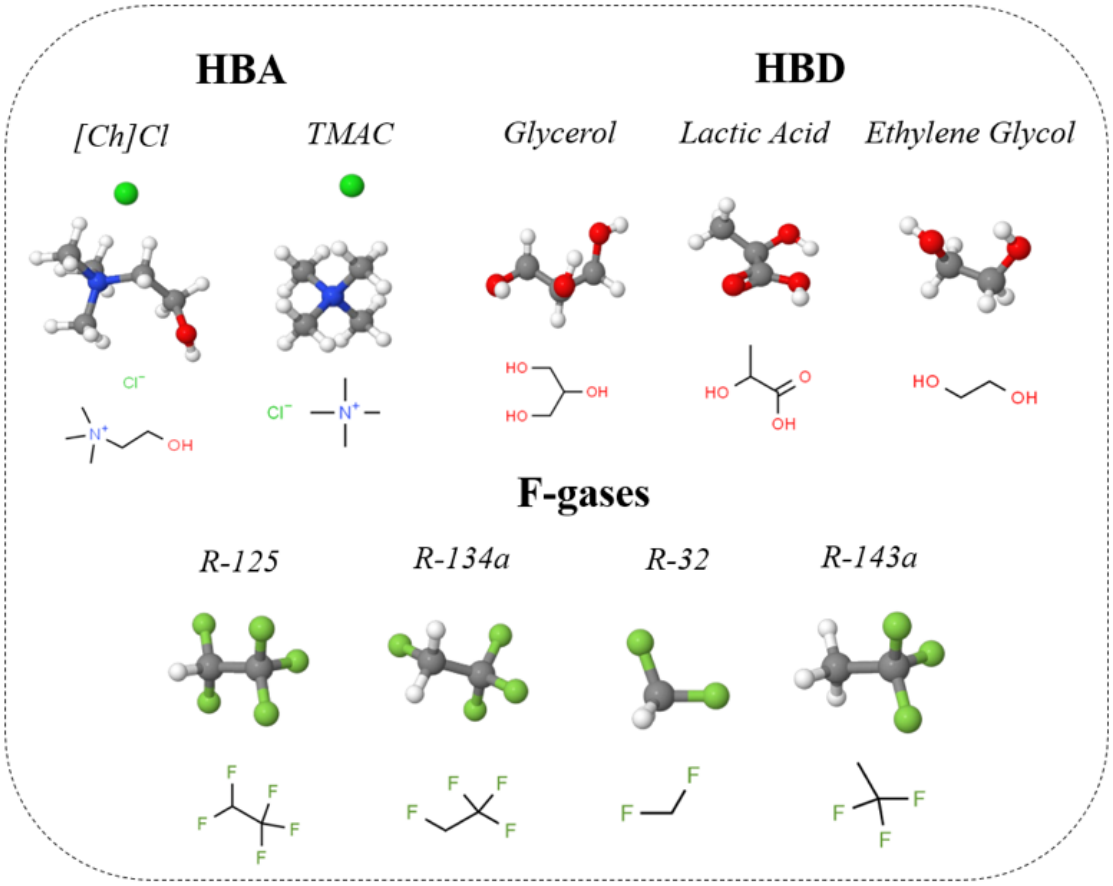


***Figure 5.1.*** *Chemical structures of the compounds studied in this section.*

### 5.1.2 Molecular Models

From a computational perspective, two HBAs ([Ch]Cl and TMAC) and three HBDs (ethylene glycol – EG, glycerol – GL, and lactic acid – LA), forming a total of five combinations (excluding the TMAC and LA combination), were studied in detail.

As concluded in Chapter 4, modelling DESs using the individual-component approach provides a more reliable representation of their behavior. Therefore, in this section, DESs are modeled as mixtures of two independent species using this approach. The models for [Ch]Cl, GL, EG, and water were described in Chapter 4, and their soft-SAFT parameters are presented in Table 4.2. TMAC is modeled similarly to [Ch]Cl, as an associating compound with two association sites each—one positive and one negative—to simulate the cation-anion interaction. LA is modeled with two association sites, one positive and one negative, to mimic the hydroxyl groups present in these molecules, following the same approach used for GL and EG. The F-gases R-125, R-134a, R-143a, and R-32 are described as homonuclear chains with two association sites each—one positive and one negative—to simulate the dipole moment caused by the molecule's electronegativity. This model has demonstrated superior performance in describing interactions with ILs and DESs. (Demirbek et al., 2024; Jovell et al., 2020).

The complete set of parameters for the new compounds explored in this section of the thesis is derived from previous works (Albà et al., 2020; Asensio-Delgado et al., 2020; Lloret et al., 2017; Vilaseca et al., 2010) and is presented in Table 5.1

***Table 5.1.*** *Molecular weight and soft-SAFT molecular parameters optimized for the species that form DESs, and F-gases studied in this section.*

| Compound | $M_w$ (g/mol) | $m$ | $\sigma$ (Å) | $\varepsilon/k_B$ (K) | $\varepsilon^{HB}/k_B$ (K) | $k^{HB}$ (Å$^3$) | Reference |
|---|---|---|---|---|---|---|---|
| TMAC | 109.6 | 3.818 | 3.413 | 360.8 | 3384 | 2100 | Lloret et al. (2017) |
| LA | 90.08 | 1.812 | 4.059 | 433.1 | 1510 | 3200 | Lloret et al. (2017) |
| R-125 | 120.02 | 1.392 | 4.242 | 148.8 | 1685 | 24050 | Asensio-Delgado et al. (2020) |
| R-134a | 102.03 | 1.392 | 4.166 | 166.6 | 1862 | 24050 | Albà et al. (2020) |
| R-143a | 84.04 | 1.392 | 4.103 | 149.0 | 1717 | 24050 | Vilaseca et al. (2010) |
| R-32 | 52.00 | 1.321 | 3.529 | 144.4 | 1708 | 24050 | Asensio-Delgado et al. (2020) |

### 5.1.3 Solvents Thermophysical Characterization

Before examining the solubility of F-gases, the performance of the soft-SAFT EoS in calculating the density and dynamic viscosity (using the FVT approach) of the DESs was assessed. Utilizing the pure-component parameters detailed in Table 4.2 of Chapter 4 and Table 5.1 of this chapter, the density-temperature diagram for the five studied DESs was predicted and is presented in Figure 5.2.

As observed, soft-SAFT predictions are highly accurate when compared to the experimental data, with an %AAD of 1.12%, 1.51%, 1.52%, 1.16% and 1.13% for [Ch]Cl:GL (1:3) + 10wt% water, TMAC:GL (1:3), [Ch]Cl:LA (1:3), [Ch]Cl:EG (1:3), and TMAC:EG (1:3), respectively. To achieve these low values of %AAD for [Ch]Cl: LA (1:3) and TMAC-based DESs, a binary parameter $\eta$ = 0.978 was introduced for [Ch]Cl:LA (1:3) and $\eta$ = 1.023 for both TMAC-based DESs. Still, this minor correction, with a temperature-independent common coefficient, ensures quantitative agreement across both TMAC-based DESs.

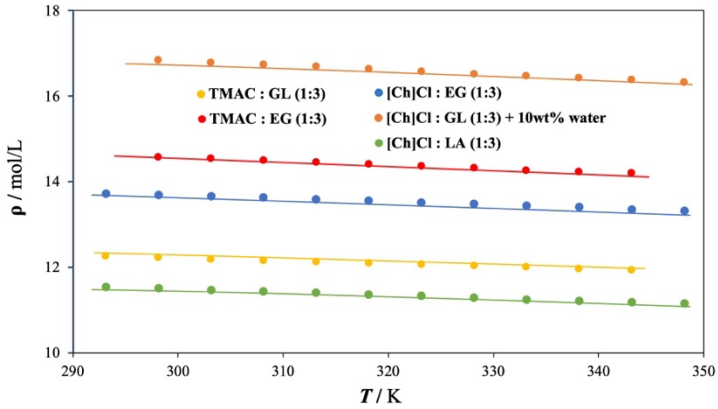


***Figure 5.2.*** *Density (ρ) – temperature (T) diagram, at atmospheric pressure, for the DESs: TMAC:EG (1:3), TMAC:GL (1:3), [Ch]Cl:LA (1:3), [Ch]Cl:GL (1:3) + 10%wt water and [Ch]Cl:EG (1:3). Symbols correspond to experimental data (Codera et al., 2023; D. Clijnk, 2024; Tavares Duarte de Alencar, 2024) and lines to soft-SAFT modelling (with parameters from Table 4.2 and 5.1).*

The experimental viscosity data of the studied DES have also been theoretically modeled using FVT coupled with soft-SAFT, applying the spider-web methodology (Cané et al., 2017) to fit the FVT parameters for the compounds forming the examined DESs using mixture data. The density values required to use FVT were calculated through the soft-SAFT EoS utilizing parameters outlined in Table 4.2 of Chapter 4 and Table 5.1 of this chapter. The optimized parameters for [Ch]Cl, GL, water, and EG are already presented in Table 4.3 of Chapter 4, and the optimized parameters for the other compounds explored in this section are included in Table 5.2.

***Table 5.2.*** *FVT viscosity parameters optimized for DESs forming molecules.*

| Compound | $\alpha$ ($J\,m^3\,mol^{-1}\,kg^{-1}$) | $B \cdot 10^2$ | $L_v \cdot 10^2$ (Å) |
|---|---|---|---|
| LA | 525.20 | 0.0858 | 1.5284 |
| TMAC | 379.55 | 0.7920 | 0.0042 |

The performance of the model to describe the DESs viscosities is displayed in Figure 5.3.

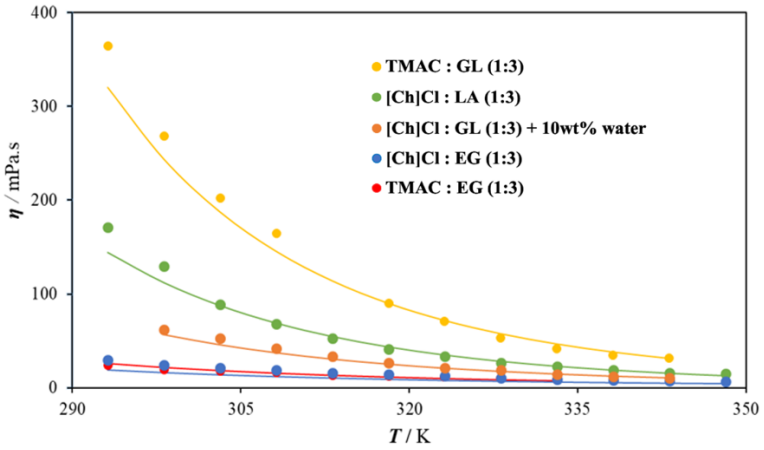


***Figure 5.3.*** *Viscosity (η) – temperature (T) diagram, at atmospheric pressure for the DESs: TMAC:EG (1:3), TMAC:GL (1:3), [Ch]Cl:LA (1:3), [Ch]Cl:GL (1:3) + 10%wt water and [Ch]Cl:EG (1:3). Symbols correspond to experimental data (Codera et al., 2023; D. Clijnk, 2024; Tavares Duarte de Alencar, 2024), while the lines to FVT soft-coupled to SAFT calculations.*

At standard ambient temperature (298.15 K), noticeable differences in viscosity among DESs were observed. Notably, the DES composed of TMAC:GL (1:3) exhibited the highest viscosity, surpassing 250 mPa·s. This rise in viscosity is attributed to the higher number of hydroxyl groups of GL compared to the TMAC:EG (1:3) DES, facilitating enhanced hydrogen bonding interactions with TMAC and, consequently, leading to higher viscosity levels. About the soft-SAFT + FVT predictions, an excellent agreement between the model and the viscosity data has been found (lines of Figure 5.3), with an AAD% of 8.46%. The major deviations correspond to the lowest temperatures, where the uncertainty of the viscosity measurements is higher. Otherwise, the description of aqueous DES is remarkable, reconfirming the high versatility of the approach in achieving a reliable description of this property at different conditions.

### 5.1.4 Solubility in [Ch]Cl and TMAC Based-DESs

Once the density and viscosity of the investigated DESs has been described, their capacity to absorb the most common refrigeration F-gases (R-32, R-134a, R-143a, and R-125) is studied. In Figure 5.4, the vapor-liquid equilibria for the DESs with F-gases at 300.15K are plotted.

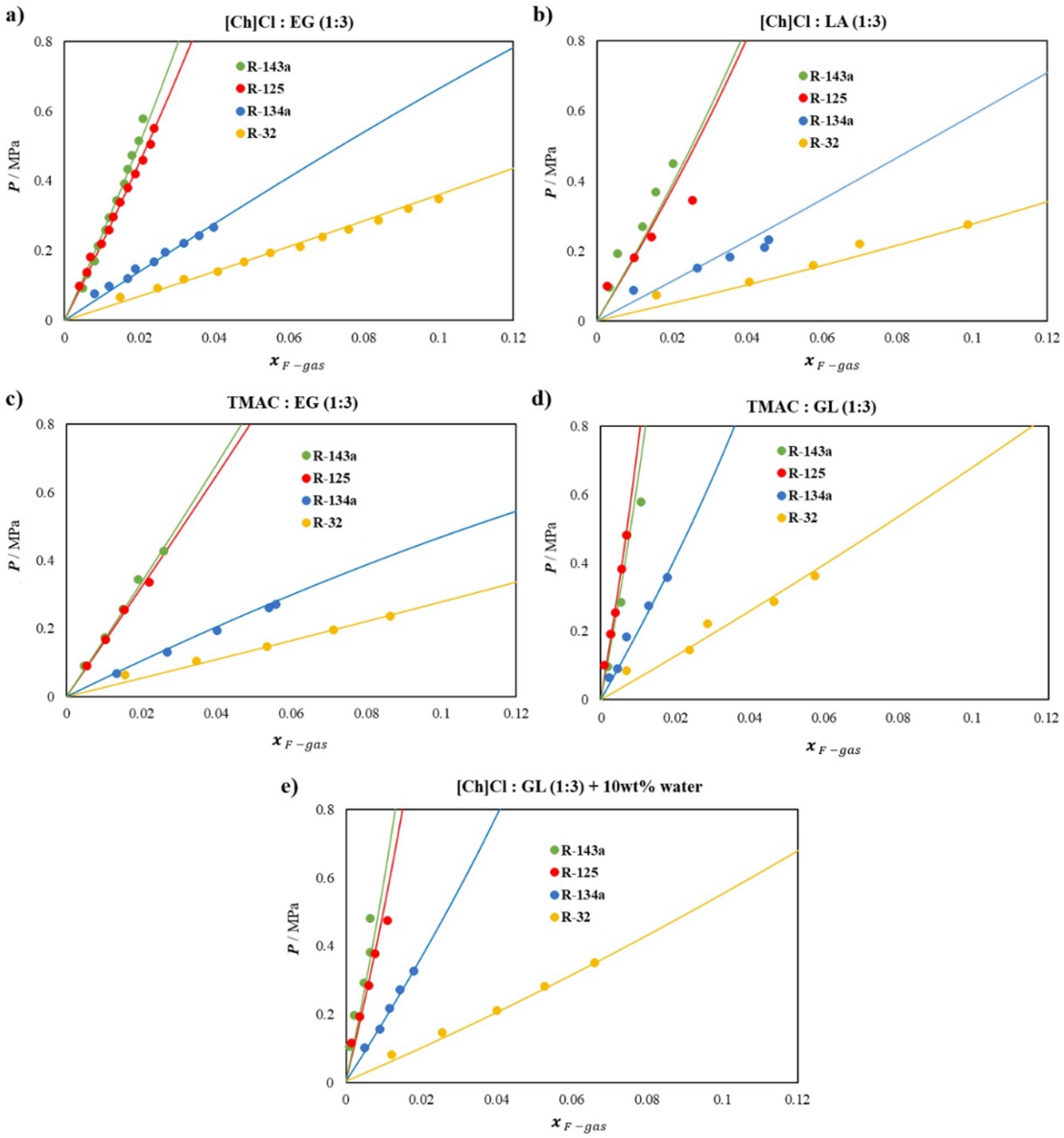


***Figure 5.4.*** *Vapor-liquid equilibria for the DESs with F-gases at 300.15 K. Symbols correspond to experimental data (Codera et al., 2023; D. Clijnk, 2024; Tavares Duarte de Alencar, 2024), while the lines to soft-SAFT predictions.*

A comprehensive analysis of the results demonstrated a relatively low solubility of F-gases for all DESs investigated here, which can be attributed to the absence of fluorine atoms in their chemical structure. Previous works (Castro et al., 2020; Jovell et al., 2020) have suggested that fluorine atoms in DESs can enhance the F-gases solubility by forming hydrogen bonds (H-F-H), at the price of a more complex synthesis and higher environmental impact. In the DESs under investigation in this section, it appears that the primary influence lies on a weak physical absorption dominated by entropic effects, where the volume of the F-gas molecule plays a key role. Indeed, R-32, the smallest F-gas among those studied, being the only single-carbon compound (with two fluorine atoms), exhibits the highest solubility. Concerning the two-carbon refrigerants, it may be noted that the amount of fluorine atoms in F-gases do not consistently correlate with enhanced solubility. For instance, while R-134a, containing four fluorine atoms, ranks as the second compound with the highest solubility, R-125 (with five fluorine atoms) and R-143a (with three fluorine atoms) exhibit similar and lower solubility levels compared to other F-gases. In this case, two different effects play a role. On one hand, R-125 has a low solubility due to the presence of five fluorine atoms, forming a relatively stable structure of a certain size and leaving low allocation for strong interactions with the DESs. Conversely, the asymmetric R-143a, with three fluorine atoms at the same molecule end, exhibits a high dipole moment (Fouad & Vega, 2018), but lacks the previously mentioned H-F-H structure, resulting in a lower solubility. In any case, this variation in solubility among these F-gases presents an advantage for their separation. Specifically, it suggests that R-125 and R-143a could potentially be readily separated from mixtures of F-gases containing R-134a and R-32.

Although the qualitative outcomes among all DESs are somewhat similar, it is notable that TMAC:EG (1:3) exhibits a slightly higher absorption capacity, closely

followed by [Ch]Cl:LA (1:3), and then by [Ch]Cl:EG (1:3), [Ch]Cl:GL (1:3) + 10wt% of water, and finally TMAC:GL (1:3). The latter seems to be clearly related to its higher viscosity, possibly affecting mass transfer. In any case, no substantial differences are appreciated among all DESs, suggesting that the influence of the DESs structure on the solubilities of the F-gases appears to be modest. However, it is important to remember that the choice of the best solvent will be determined by selectivity and not by solubility.

The thermodynamic model, also shown in Figure 5.4, provides a good agreement with the experimental data. The molecular parameters provided in Table 4.2 (from Chapter 4) and 5.1 are used here to deal with multicomponent calculations, where each combination between DES and F-gas is treated as a ternary mixture, except for the corresponding F-gas with the DES [Ch]Cl:GL (1:3) + 10wt% water, which is treated as a quaternary mixture. Subsequently, the model must account for all possible interactions among the three or four compounds involved. On one side, cross-association interactions between sites are explicitly considered by using the combining rules shown in Eqs. 3.23 and 3.24, with only positive-negative interactions being allowed. On the other side, given the very different structure of the molecules involved, it is necessary to apply a correction in the crossed dispersion by means of the energy binary parameter, $\xi_{ij}$ (see Eq. 3.22). No further size corrections are necessary for the Berthelot combining rule (see Eq. 3.21) with $\eta = 1$ for all binary combinations, with the exception of the TMAC:HBDs and [Ch]Cl:LA DESs (as explained in Section 5.1.3), having a constant value of $\eta = 1.023$ for TMAC and $\eta = 0.980$ for [Ch]Cl, respectively. All these equations are detailed in Section 3.1.2. A summary of the necessary $\xi_{ij}$ values to quantitatively describe the F-gases solubility in DESs is provided in Table 5.3

***Table 5.3.*** *soft-SAFT energy binary interaction parameter ($\xi_{ij}$) adjusted in this work.*

| Compound *i* | Compound *j* | $\xi_{ij}$ |
|---|---|---|
| [Ch]Cl | R-143a | 1.13738 |
| [Ch]Cl | R-125 | 1.21031 |
| [Ch]Cl | R-134a | 1.14499 |
| [Ch]Cl | R-32 | 1.29977 |
| TMAC | R-143a | 1.04771 |
| TMAC | R-125 | 1.12775 |
| TMAC | R-134a | 1.05766 |
| TMAC | R-32 | 1.29998 |
| EG | $F-gases$ | 1.10080 |
| LA | $F-gases$ | 1.17705 |
| GL | $F-gases$ | 1.05315 |
| [Ch]Cl | Water | 1.04500 |
| R-134a | Water | 0.85000 |
| R-143a | Water | 0.85000 |

Some remarkable trends emerge from analyzing the values of these parameters and their relevance to the interactions within the mixture. Notably, most cases exhibit an energy binary parameter $\xi_{ij}$ greater than one, specifically in adjusting the interactions involving the DESs forming molecules and F-gases. These results suggest that the classical Lorentz-Berthelot combining rules underestimate the solubility of the F-gases in the DESs, indicating potential missing interactions within the model for the investigated mixtures. Interestingly, a consistent $\xi_{ij}$ value is observed across interactions between each HBD and the four F-gases, suggesting that the parameter can be transferred among F-gases if no experimental data are available. For the case of the quaternary mixture containing water, one parameter between [Ch]Cl and water was transferred from Chapter 4 ($\xi$=1.0450). In contrast, the parameter for interactions between R-134a or R-143a with water was optimized here and fixed at $\xi$=0.8500. Overall, the soft-SAFT calculations effectively describe the solubility of each F-gas in the examined DESs, showing good agreement with experimental data as depicted by the lines in Figure 5.3. The individual deviation values are available in Table 5.4.

***Table 5.4.*** *Absolute averaged deviations (AAD) of the soft-SAFT predictions for Vapor-liquid equilibria of DESs with F-gases at 300.15 K.*

| DES | *AAD (%)* | | | |
|---|---|---|---|---|
| | **R- 143a** | **R-125** | **R-134a** | **R-32** |
| **TMAC : GL (1:3)** | 11.55 | 7.32 | 10.15 | 10.64 |
| **[Ch]Cl : GL (1:3) + 10wt% water** | 12.57 | 7.61 | 4.24 | 2.98 |
| **[Ch]Cl : EG (1:3)** | 4.27 | 3.87 | 3.23 | 3.00 |
| **[Ch]Cl : LA (1:3)** | 13.51 | 10.15 | 5.35 | 11.02 |
| **TMAC : EG (1:3)** | 5.42 | 2.41 | 3.61 | 2.83 |

### 5.1.5 Enthalpy and Entropy of Dissolution

The absorption of F-gases into the DESs does involve examining additional thermodynamic metrics, apart from solubility, such as the absorption enthalpy and entropy. These metrics provide insights into the strength of the interactions and the degree of order when a gas is dissolved into the solvent, respectively (Cadena et al., 2004). Their values under different constant compositions can be determined utilizing data derived from the soft-SAFT EoS, according to the following equations:

$$\Delta H_{dis} = -RT^2 \left(\frac{d \ln P_i}{dT}\right)_{x_i} \tag{5.1}$$

$$\Delta S_{dis} = -RT \left(\frac{d \ln P_i}{dT}\right)_{x_i}, \tag{5.2}$$

where $\Delta H_{dis}$ is the molar enthalpy of dissolution $\Delta S_{dis}$ is the molar entropy of dissolution; $R$ is the universal gas constant (8.3145 J.mol$^{-1}$.K$^{-1}$); $P_i$ is the partial pressure of the dissolved gas $i$; $T$ is overall system temperature and $x_i$ is the mole fraction of the dissolved gas $i$ in the DESs, which is fixed at 0.0001 (a very low gas concentration). The results for of each F-gas within the respective DESs are provided in Table 5.5.

***Table 5.5.*** *Calculated enthalpy and entropy of dissolution for F-gases in DESs from 298.15 to 333.15 K at $x_i$ = 0.0001.*

| DES | $\Delta H_{dis}$/kJ. mol$^{-1}$ | | | | $\Delta S_{dis}$/J. K$^{-1}$. mol$^{-1}$ | | | |
|---|---|---|---|---|---|---|---|---|
| | **R- 143a** | **R-125** | **R-134a** | **R-32** | **R- 143a** | **R-125** | **R-134a** | **R-32** |
| **TMAC:GL (1:3)** | -8.00 | -7.55 | -11.35 | -14.15 | -25.36 | -23.92 | -35.96 | -44.84 |
| **[Ch]Cl:GL (1:3)+10wt% $H_2O$** | -30.01 | -30.58 | -34.90 | -37.33 | -95.06 | -96.89 | -110.5 | -118.2 |
| **[Ch]Cl:EG (1:3)** | -11.28 | -11.60 | -17.28 | -21.51 | -35.74 | -36.74 | -54.76 | -68.16 |
| **[Ch]Cl:LA (1:3)** | -24.51 | -24.60 | -32.85 | -37.13 | -77.65 | -77.94 | -104.0 | -117.6 |
| **TMAC:EG (1:3)** | -11.06 | -11.17 | -17.13 | -21.60 | -35.05 | -35.38 | -54.26 | -68.44 |

As can be seen in Table 5.5, R-32 exhibits higher negative values of $\Delta H_{dis}$ among the F-gases, which implies that all investigated DESs have a higher affinity for R-32 than for the other F-gases studied. Regarding the results of $\Delta S_{dis}$, negative values are found in all cases, stemming from the gas's condensation. The decrease in entropy caused by this phase transition is not compensated by the entropy generated from the disruption of the F-gases into the organized structure of the DESs.

### 5.1.6 Selectivity and Absorption Calculations

The ability of an absorbent to selectively capture a specific F-gas from a blend mixture is crucial for tailoring gas recycling and separation processes. Thus, the ideal selectivity of each F-gas within the respective DESs is used to pre-screen their efficiency in separating binary F-gases mixtures. The ideal selectivity at infinite dilution, denoted as $\alpha$, relates the amount of the F-gas dissolved in the DES at an isotherm set and is expressed as the ratio of Henry's law constants between the two pure F-gases (Llovell et al., 2015). Following this, the soft-SAFT EoS is employed to predict pressure data as solubility approaches zero for each isotherm and compound. These predictions enable the

computation of the ideal selectivity for two specific refrigerants *i* and *j* in terms of the effective Henry's law constants, as follows:

$$\alpha_{i/j}{}^{T} = \frac{k_{H,eff}^{j}{}^{T}}{k_{H,eff}^{i}{}^{T}} = \frac{\lim_{x_j \to 0}\left(\frac{P}{x_j}\right)^{T}}{\lim_{x_i \to 0}\left(\frac{P}{x_i}\right)^{T}} \quad , \tag{5.3}$$

where $k_{H,eff}^{i}$ signifies effective Henry´s law constant (Sander et al., 2022) for gas *i* at temperature *T*, while $x_i$ denotes the mole fraction of compound *i* in the liquid. Lastly, $\alpha_{i/j}$ represents the ideal selectivity at infinite dilution of the compound *j* with respect to the compound *i*. The ideal selectivity obtained for a temperature of 300.15 K is plotted in Figure 5.5, where the effective Henry´s law constants are visually illustrated in the same figure and listed in Table 5.6.

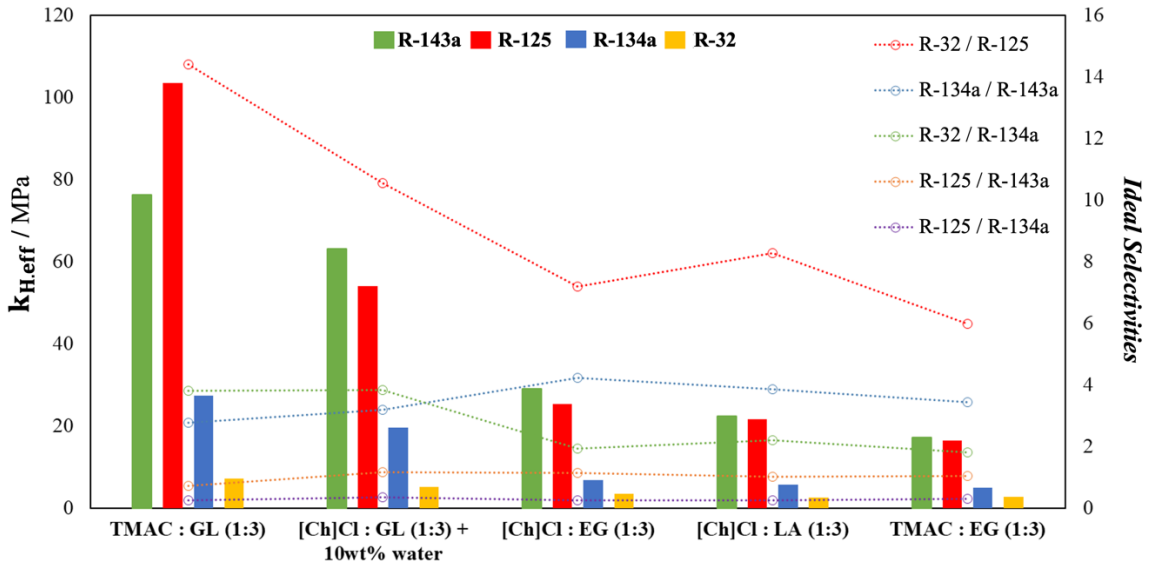


***Figure 5.5.*** *Calculated effective Henry's constants ($k_{H,eff}$) for F-gases (bars graph, left axis) and ideal selectivity ($\alpha_{i/j}$, symbols and lines, right axis) in TMAC:GL (1:3), [Ch]Cl:GL (1:3) + 10%wt water, [Ch]Cl:EG (1:3), [Ch]Cl:LA (1:3) and TMAC:EG (1:3) at 300.15 K.*

***Table 5.6.*** *Effective Henry's law constants determined for the absorption of F-gases at 300.15 K in the selected DESs (MPa).*

| DES | *Effective Henry's law constants* | | | |
|---|---|---|---|---|
| | **R- 143a** | **R-125** | **R-134a** | **R-32** |
| **TMAC : GL (1:3)** | 76.294 | 103.48 | 27.492 | 7.1837 |
| **[Ch]Cl : GL (1:3) + 10wt% water** | 63.148 | 54.029 | 19.668 | 5.1196 |
| **[Ch]Cl : EG (1:3)** | 29.047 | 25.482 | 6.8669 | 3.5361 |
| **[Ch]Cl : LA (1:3)** | 22.391 | 21.744 | 5.7818 | 2.6267 |
| **TMAC : EG (1:3)** | 17.242 | 16.423 | 4.9858 | 2.7452 |

The values of effective Henry´s constants are directly linked to the results observed for the solubility experimental data (Figure 5.4). TMAC:EG (1:3) shows the lowest $k_H$, indicating a higher absorption capacity, followed by [Ch]Cl:LA (1:3), [Ch]Cl:EG (1:3), [Ch]Cl:GL (1:3) + 10wt% of water, and finally TMAC:GL (1:3), which exhibits the highest $k_{H,eff}$ for all F-gases. Additionally, it is evident that, for all DESs, R-32 has the lowest $k_{H,eff}$, followed by R-134a, while higher $k_{H,eff}$ values are consistently observed for R-125 and R-143a across all DESs (Demirbek et al., 2024).

Concerning the ideal selectivity, Figure 5.5 illustrates the selectivity for the binary mixtures R-32/R-125, R-134a/R-143a, R-32/R-134a, R-125/R-143a and R-125/R-134a at 300.15 K. Despite lower absorption capacities compared to fluorinated DESs (Castro et al., 2020; Demirbek et al., 2024), the DESs investigated in this study exhibit excellent selectivities for certain F-gas mixtures. The highest values (ranging between 5.98 and 14.4) are obtained for the R-32/R-125 mixtures with the studied DESs, with TMAC:GL (1:3) having the best selectivity, indicating its preference for R-32 in this mixture. For the R-134a/R-143a mixture, the selectivity ranges between 2.78 and 3.46, with [Ch]Cl:EG (1:3) yielding the highest value. Unfortunately, none of the DESs considered in this work seems appropriate to separate R-125 from R-143, as it was previously inferred from the solubility figures.

The ideal selectivity calculated from effective Henry´s coefficients is an approximation based on the infinite dilution behavior of pure compounds (i.e., F-gases in this study), which does not consider the competition between the gases and is solely used to provide a first qualitative approximation on the separation capacity for each DESs. Based on this preliminary information, a more accurate assessment of the gas separation efficiency needs to be performed by studying the competitive selectivity to recover the compounds from multicomponent commercial refrigeration blends, including R410A (with 70.583 mol% R-32 and 29.417 mol% R-125), R407F (with 48.299 mol% R-32, 20.129 mol% R-125, and 31.571 mol% R-134a), and R404A (with 35.7821 mol% R-125, 60.392 mol% R-143a, and 3.826 mol% R-134a).

In this case, the values of competitive selectivities (*S*) calculated for these gas mixtures are obtained throughout Eq. 5.4.

$$S_{i/j} = \frac{y_j/x_j}{y_i/x_i} \tag{5.4}$$

where *x* is the mole fraction of each component in the liquid phase, and *y* is the mole fraction of each component in the gas phase. However, the intrinsic nature of Eq. (5.4) is originally thought for a binary comparison and needs to be adapted for ternary gas mixtures (R407F and R404A). In that case, we have opted to define the selectivity of one gas over the other two by considering the non-desired gases as a single entity "$GAS_m$", where the $x_{GAS_m}$ is the sum of their liquid mole fractions, and $y_{GAS_m}$ represents the sum of their vapor mole fractions. For instance, in a mixture comprising three gases ($GAS_1$, $GAS_2$, and $GAS_3$), the equation to determine the selectivity (*S*) of $GAS_1$ over the other two gases would be as follows:

$$x_{GASm} = x_{GAS_2} + x_{GAS_3} \tag{5.5}$$

$$y_{GASm} = y_{GAS_2} + y_{GAS_3} \tag{5.6}$$

$$S_{GAS_1/\,GAS_m} = \frac{y_{GASm}/x_{GAS_m}}{y_{GAS_1}/x_{GAS_1}} \tag{5.7}$$

The equilibrium compositions in Eqs. 5.4 and 5.7 are obtained from liquid-vapor flash calculations using soft-SAFT EoS, which are computed by an iterative process that involves solving a flash model into the Rachford-Rice equation (Mejía et al., 2021). This calculation considers an initial global composition with a DES mole fraction of 0.7 ($z_{DES} = 0.7$) and 0.3 for the corresponding F-gas blend ($z_{F-gas} = 0.3$), the latter with the commercial proportions previously stated, at the desired operating pressure and 300.15 K, as illustrated in Figure 5.6.

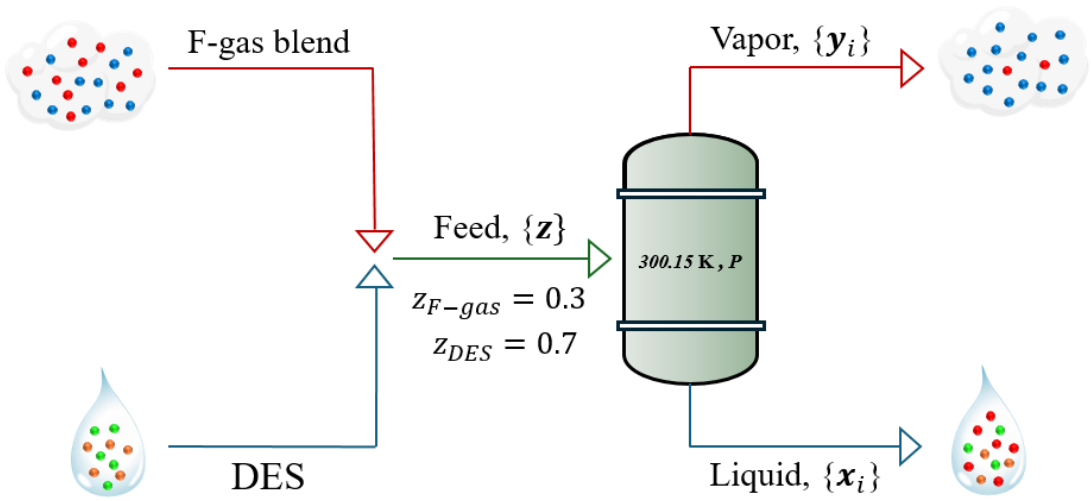


***Figure 5.6.*** *Illustration of liquid-vapor flash calculations via soft-SAFT EoS depicting the separation performance of commercial refrigerant blends at 300.15 K and various pressures (1, 5, and 10 bar).*

The separation performance of three commercial refrigerant blends at 300.15 K and different pressures is shown in Figure 5.7. In general terms, the predicted competitive selectivity aligns with the ideal selectivity at infinite dilution from Figure 5.5, particularly at low pressure, where ideal conditions apply. However, on the one hand, while lower pressures enhance separation performance, as shown in Figure 5.7, this comes at the cost of reduced sorption capacity, evident in Figure 5.4, and consequently lower recovery. On the other hand, high-pressure conditions do not seem to be attractive, as they lead to decreased separation performance for specific DESs. Therefore, according to our analysis, operating under moderate pressure conditions is advisable for an efficient separation of F-gases.

An analysis of Figure 5.7 also reveals that a high separation efficiency can be achieved to separate R410A compounds, with TMAC:GL (1:3) and [Ch]Cl:GL (1:3) + 10wt% standing out, as seen in Figure 5.7 (a), while the latter has a higher competitive selectivity to separate R-32 from the blend R407F (i.e. so when adding R-134a, forming a ternary system), as shown in Figure 5.7 (b). Finally, no significant differences are appreciated when extracting R-134a from R404A blend (in the presence of R-125 and R-143a), with a slightly better performance of [Ch]Cl:EG (1:3) and [Ch]Cl:LA (1:3) over the rest (see Figure 5.7 (c)).

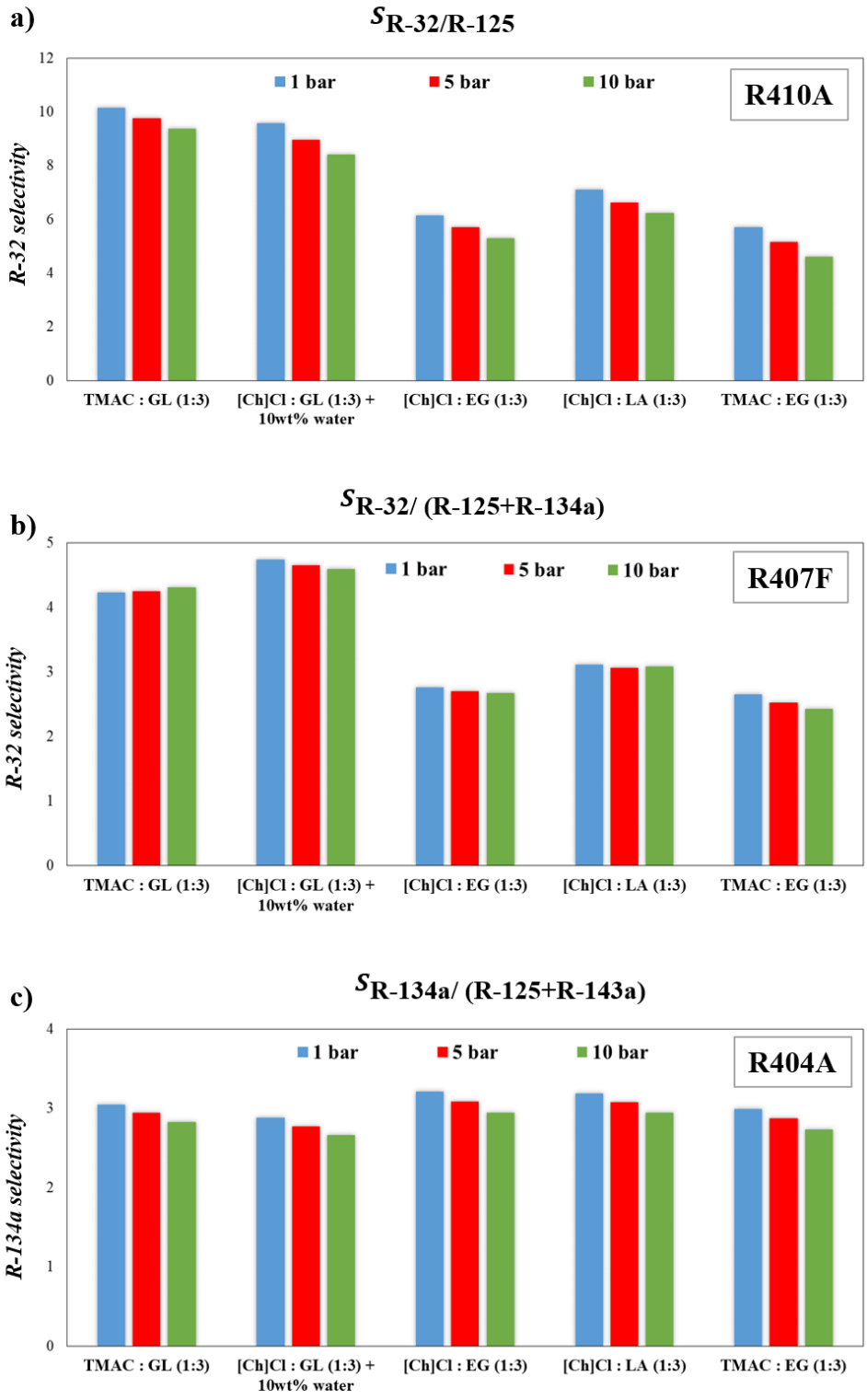


***Figure 5.7.*** *Competitive selectivity of refrigerant blends in DESs at 300.15 K and different pressures, for a mixture with a global composition of* $z_{DES} = 0.7$ *and* $z_{F-gas\ blend} = 0.3$ *modeled using soft-SAFT EoS for* ***a)*** *R32 recovery from R410A blend,* ***b)*** *R32 recovery from R407F blend and* ***c)*** *R134a recovery from R404A blend.*

## 5.2 Separation of $NH_3/CO_2$ from Melamine Streams

### 5.2.1 The Case Problem

Several industrial chemical processes produce tail gases containing environmentally harmful components, such as carbon dioxide ($CO_2$) and ammonia ($NH_3$). Emitting these industrial tail gases directly into the atmosphere leads to significant pollution and environmental damage. $CO_2$ can originate from various energy sources such as natural gas, shale gas, biogas, syngas, and more (George et al., 2016; Huang et al., 2014). $NH_3$ can be found in gaseous mixtures in various situations, including ammonia synthesis, refrigerating circuits, and water treatment (Appl, 2011). In particular, gaseous mixtures containing both $NH_3$ and $CO_2$ are found in melamine tail gas, where the separation of these compounds has become an urgent issue (Duan et al., 2022; Liu et al., 2021; Makhloufi et al., 2013).

Melamine ($C_3H_6N_6$) is a vital industrial raw material extensively utilized in manufacturing thermal insulation materials, adhesives, and fiber materials (Liao et al., 2021). Typically, the production of one ton of melamine through the decomposition and condensation of urea results in approximately 2.2 tons of tail gas, containing about 70% $NH_3$ and 29% $CO_2$ (Zeng et al., 2020). Annually, the global production of melamine exceeds 1.59 million tons, leading to substantial exhaust gas emissions (Xue et al., 2022). This not only contributes to greenhouse gas emissions but also represents a significant waste of valuable resources, as $NH_3$ is an important chemical material used as a versatile agent in preparing many fine chemicals (Deng et al., 2021; Ndegwa et al., 2008). Therefore, efficient separation and recovery of these gases can mitigate environmental impacts, enhance resource efficiency, and contribute to sustainable industrial practices.

According to literature reports, two primary methods have been developed for the simultaneous separation of $NH_3$ and $CO_2$ from gas mixtures. The first method involves co-producing urea or ammonium bicarbonate (Xiang et al., 2012; Zhuang et al., 2012). However, maintaining material balance in the co-production system is challenging, and excess ammonia cannot be effectively utilized (Xue et al., 2022). The second method is water scrubbing, which, while effective in separating $NH_3$ and $CO_2$, suffers from high utility consumption, making it an energy-intensive and costly process (Duan et al., 2022).

An effective alternative method for $NH_3$ recovery from tail gas streams in melamine production involves absorption into ionic liquids (ILs), particularly imidazolium-based ILs, which have proven to be cost-efficient compared to traditional water scrubbing techniques (Duan et al., 2022; Liu et al., 2021). Additionally, the viability of IL-based $NH_3$ recovery from melamine tail gas has been validated through the construction of the first industrial test pilot plant worldwide run by the Institute of Process Engineering Chinese Academy of Sciences, with a capacity of 50 $Nm^3h^{-1}$ of IL-based $NH_3$ recovery, with 3500 hours of stable operation (Zeng et al., 2020). Nonetheless, as previously discussed, DESs present a promising avenue for gas capture, offering notable advantages over ILs including lower toxicity, reduced corrosivity, enhanced degradability, and decreased production costs (Prabhune & Dey, 2023). Section 2.2 underscores the extensive adoption of DESs in the literature for capturing $CO_2$ (García et al., 2015; Oke, 2024; Warrag et al., 2017; Zhang et al., 2018; Zhang, Y. et al., 2024) and $NH_3$ (Chen et al., 2020; Shao et al., 2024; Zhang, J. et al., 2024; Zhong et al., 2019).

In this section, we analyze the solubility of $CO_2$ and $NH_3$ in three different [Ch]Cl-based DESs formed with EG, UR, and GL. The ideal selectivity of $NH_3$ versus $CO_2$ in these DESs is examined, along with the prediction of absorption isotherms, enthalpy and entropy of dissolution and Henry's constants. Furthermore, the study predicts the

competitive selectivity of $NH_3$ versus $CO_2$ in multi-component mixtures based on melamine tail gas and DESs. From these analyses, a rational determination is made to identify the most suitable DES for efficient $NH_3$ recovery and from melamine tail gas, while capturing the $CO_2$ at the same time, supporting the initial design phase of an industrial gas separation unit.

### 5.2.2 Molecular Models

The DESs [Ch]Cl: EG (1:2), [Ch]Cl: GL (1:2) and [Ch]Cl:UR (1:2) were modeled using the individual-component approach, as described in Chapter 4. In this manner, each individual component is characterized by a separate set of parameters. The models for [Ch]Cl, GL, EG, and UR were already explained in Chapter 4, and their soft-SAFT parameters are presented in Table 4.2. Additionally, to address the solubility of $CO_2$ and $NH_3$ in the DESs, a suitable model for these gases is necessary. A schematic picture of the models proposed is given in Figure 5.8.

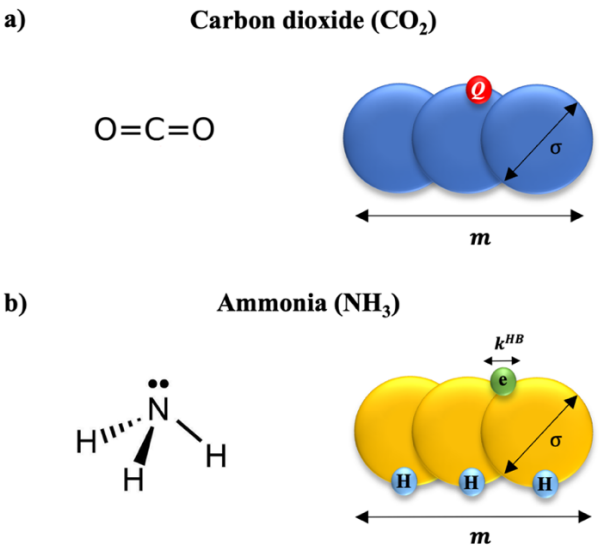


***Figure 5.8.*** *Image of the chemical structure for (a) carbon dioxide ($CO_2$) and (b) ammonia ($NH_3$), and sketch of the molecular model used to describe each compound within the soft-SAFT approach.*

$CO_2$ is modeled as a Lennard-Jones (LJ) non-associating chain, but explicitly incorporating quadrupolar interactions through the incorporation of the polar term. This requires not only the usual three soft-SAFT molecular parameters employed in non-associating systems, but also the value for the quadrupole moment contribution, $Q$, and the fraction of chain segments containing the quadrupole, $x_p$. For $CO_2$, $x_p$ was fixed at 1/3, representing that only one third of the molecule is affected by the quadrupolar interactions (Figure 5.8a). The effective quadrupole moment for $CO_2$ ($Q$ = 4.40.10$^{-40}$ C.m$^{-2}$), derived from fitting, was consistent with experimental values. The final set of molecular parameters for $CO_2$ was taken from Dias et al. (2006).

Following Llovell et al. (2012), $NH_3$ is modeled with four associating sites to capture the hydrogen bonding interactions that define its fluid-phase behavior. Three H-type sites represent the hydrogen atoms, and one e-type site represents the lone pair of electrons (as depicted in Figure 5.8b). Only e−H associating interactions are allowed. To develop a suitable parameter set for the $NH_3$ molecular model, the soft-SAFT parameters are adjusted to match vapor−liquid equilibrium data. Llovell et al. (2012) had already adjusted $NH_3$ parameters, but they were not able to accurately describe the experimental data of the liquid phase at low temperatures, specifically between 275 and 375 K (see the right side of Figure 5.9), with an %AAD of 7.03%. This temperature range is crucial for the current study on the absorption of $NH_3$ from tail gas in melamine production with DESs. Consequently, new soft-SAFT parameters for $NH_3$ have been generated to achieve a better fit in the vapor-liquid equilibrium diagram of ammonia (%AAD of 1.02% in the 275-375 K range). The updated molecular parameters for $NH_3$ and its previously calculated parameters, along with those for $CO_2$, are provided in Table 5.7.

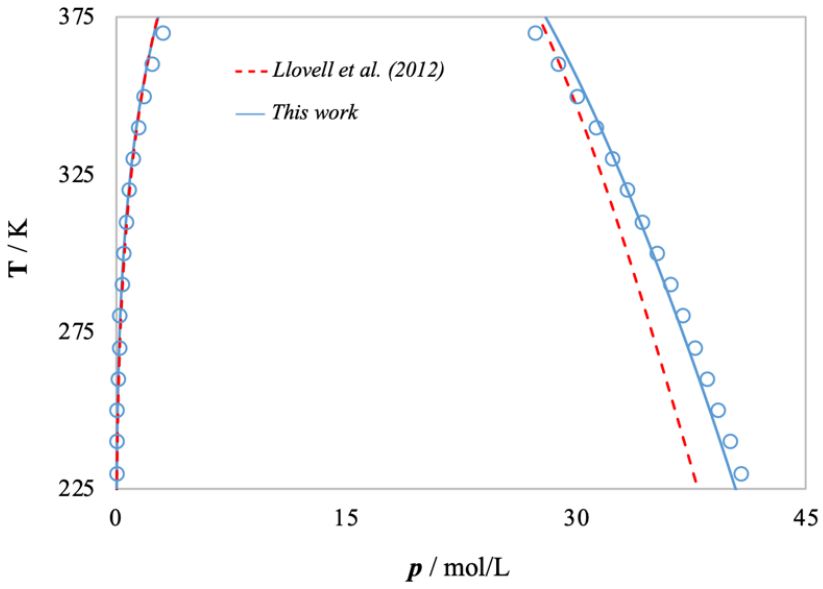


***Figure 5.9.*** *Vapor-liquid equilibrium diagram of ammonia. The experimental data (circles) are taken from (NIST). The lines represent the soft-SAFT calculations, with dashed lines from Llovell et al. (2012) and solid lines from this work.*

***Table 5.7.*** *soft-SAFT molecular parameters optimized for the gases studied in this section.*

| Compound | $M_w$ (g/mol) | $m$ | $\sigma$ (Å) | $\varepsilon/k_B$ (K) | $\varepsilon^{HB}/k_B$ (K) | $k^{HB}$ (Å$^3$) | Reference |
|---|---|---|---|---|---|---|---|
| $CO_2$* | 44.01 | 1.571 | 3.184 | 160.2 | - | - | Dias et al. (2006) |
| $NH_3$ | 17.04 | 1.418 | 2.974 | 280.5 | 483.0 | 2160.5 | Llovell et al. (2012) |
| $NH_3$ | 17.04 | 1.873 | 2.679 | 236.5 | 1136 | 1498.0 | This work |

* Additional molecular parameters for the polar contribution: Q = 4.40.10$^{-40}$ C.m$^{-2}$, $x_p$ = 1/3.

### 5.2.3 Solubility of $CO_2$ in [Ch]Cl Based-DESs

In order to have a robust and consistent molecular model, it is important to account for the binary interactions between all components in the system. Consequently, and before proceeding to evaluate the solubility of $CO_2$ in the selected DESs, the binary system $CO_2$-EG, for which experimental data were available (Gui et al., 2011), has been first examined. Results concerning the soft-SAFT description of the VLE for the mixture

between EG and $CO_2$ at different temperatures are depicted in Figure 5.10 and compared to experimental data (Gui et al., 2011).

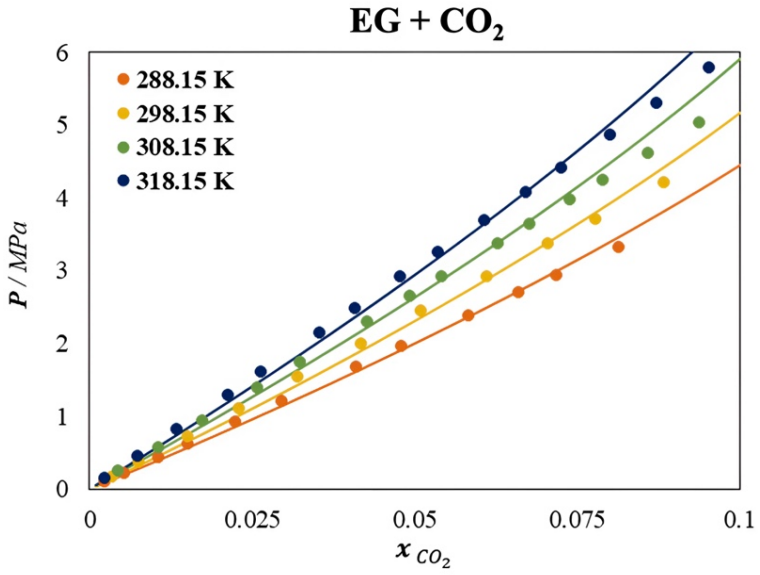


***Figure 5.10.*** *Solubility of $CO_2$ in EG at different temperatures. Symbols represent experimental data from Gui et al. (2011), and lines soft-SAFT calculations.*

As can be seen, an excellent agreement was achieved (%AAD of 3.06%) by fitting a constant binary parameter $\xi$=0.886. This parameter was fitted to data at 298.15 K and used to predict the other three isotherms at 288.15, 308.15, and 318.15 K, ensuring that it can be temperature-independent.

The next step consists in the description of the $CO_2$ solubility in the selected DES (using EG, GL and UR as HBDs), considering them as ternary mixtures. Although soft-SAFT can qualitatively describe the behavior of the DES, as previously shown in Chapter 4, achieving quantitative agreement with the available data of the ternary systems is crucial to properly assess the validity of these DESs for separation purposes. Consequently, it is necessary to account for all the binary interactions between the three components involved (HBA-HBD, HBA-$CO_2$ and HBD-$CO_2$).

The HBA-HBD interactions are always set to unity, as the DESs have already been described without involving additional binary parameters, as shown in Chapter 4. Concerning the HBD-$CO_2$, the $\xi$ value corresponding to the interaction between EG and $CO_2$ has been determined in Figure 5.10. This $\xi_{EG\text{-}CO2}$ value has been then applied to address the $CO_2$-EG interaction in the ternary mixture of [Ch]Cl:EG (1:2) + $CO_2$, while the $\xi$ parameter describing the interaction between [Ch]Cl and $CO_2$, has been fitted to the ternary data. Subsequently, the $\xi_{[Ch]Cl-CO_2}$ value has been transferred to the other two [Ch]Cl-based DESs. Additionally, the $\xi_{HBD-CO_2}$ values, corresponding to UR and GL with $CO_2$, have been fitted to the corresponding ternary data. In both cases, the intermediate temperature isotherm is used to obtain optimal $\xi$ values, while the other two isotherms were predicted. A summary of the necessary $\xi$ values to quantitatively describe the $CO_2$ solubility in DESs is provided in Table 5.8.

***Table 5.8.*** *soft-SAFT energy binary interaction parameter ($\xi_{ij}$) adjusted in this work.*

| **Compound *i*** | **Compound *j*** | $\xi_{ij}$ |
|---|---|---|
| [Ch]Cl | $CO_2$ | 1.100 |
| EG | $CO_2$ | 0.886 |
| GL | $CO_2$ | 1.018 |
| UR | $CO_2$ | 1.095 |

No further adjustments are necessary for the Berthelot combining rule with $\eta$=1, which is consistently applied across all binary combinations, except for [Ch]Cl: UR (1:2), where a constant $\eta$ value of 0.9 between UR and $CO_2$ is necessary. This variation may potentially be attributed to findings from Crespo et al. (2019), which suggested that different types of hydrogen bonds may form in the [Ch]Cl:UR (1:2) mixture, beyond what simplified models can accurately capture. In our approach, we simplify these interactions

to two association sites each for [Ch]Cl and UR, in order to preserve transferable soft-SAFT parameters, possibly underestimating certain interactions.

Figure 5.11 presents the results for the [Ch]Cl-based DESs with EG, UR, and GL in a (1:2) ratio. Overall, this approach yields excellent predictions of $CO_2$ solubility across various isotherms for the DESs, with an %AAD of 6.02%, 3.24% and 5.17% for [Ch]Cl: EG (1:2), [Ch]Cl: GL (1:2) and [Ch]Cl: UR (1:2), respectively. This underscores the accuracy of the straightforward, yet reliable molecular models proposed with soft-SAFT.

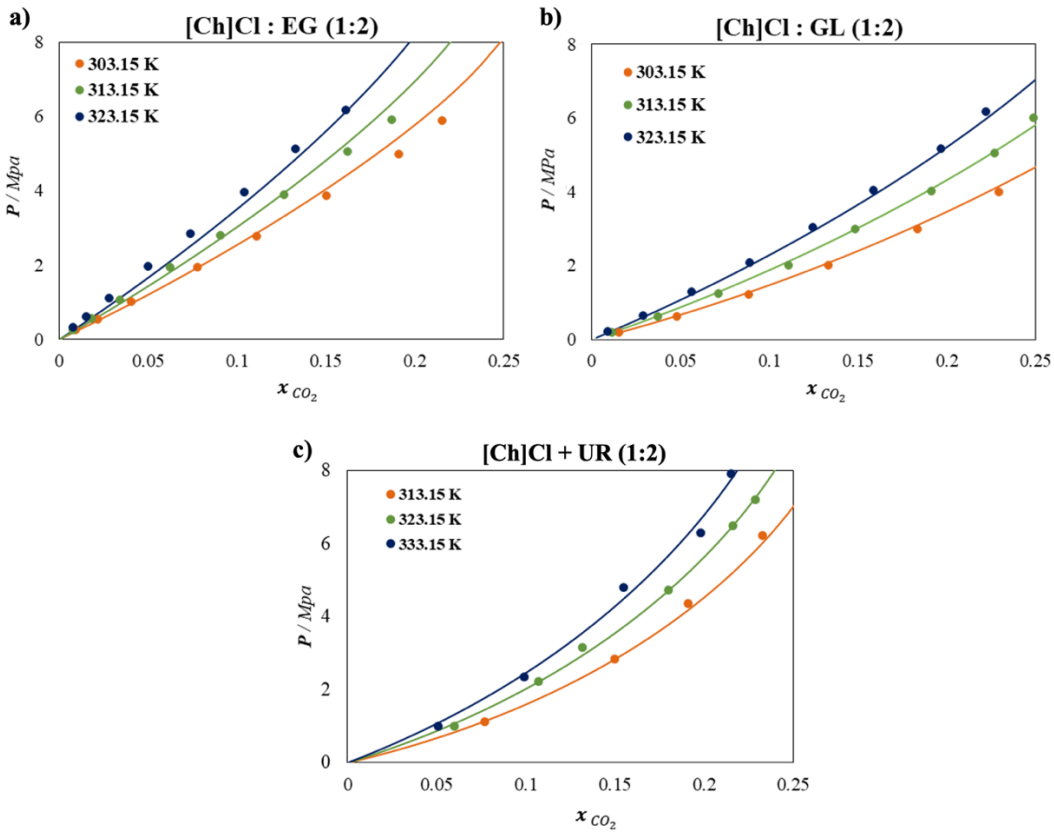


***Figure 5.11.*** *Solubility of $CO_2$ at different temperatures in a) [Ch]Cl:EG (1:2) DES, b) [Ch]Cl:GL (1:2) DES and c) [Ch]Cl:UR (1:2) DES. Symbols represent experimental data (Leron & Li, 2013a, b; Li et al., 2008), and lines soft-SAFT calculations.*

### 5.2.4 Solubility of $NH_3$ in [Ch]Cl Based-DESs

In an analogous manner as done for the solubility of $CO_2$, the solubility of $NH_3$ in DESs must be first characterized by accurately describing the binary interactions. For this reason, the mixture EG-$NH_3$ for which experimental data were available (Zhou et al., 2014), has been evaluated with soft-SAFT. The results of the soft-SAFT description of the VLE for the EG-$NH_3$ mixture at various temperatures are presented in Figure 5.12.

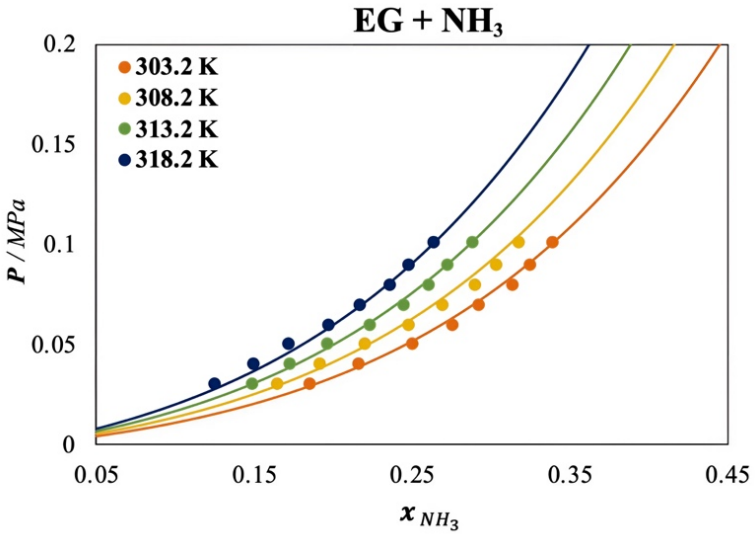


***Figure 5.12.*** *Solubility of $NH_3$ in EG at different temperatures. Symbols represent experimental data from Zhou et al. (2014), and lines soft-SAFT calculations.*

While $CO_2$ was modeled as a non-associating (but polar) compound, the associating nature of ammonia, represented by 4 sites in soft-SAFT, allows to optimize the cross-association interactions between $NH_3$ and the DESs components, given their substantial influence on thermophysical property predictions in such mixtures (Llovell et al., 2012). To optimize these interactions, suitable values for cross-association parameters were determined within a logical range based on the physical interpretation of chemical

reactions. A high cross-association energy is expected, indicating strong interactions, closer to those of a covalent bond. Specifically, a cross-association energy of 3093K between EG and $NH_3$ was found suitable. Additionally, the size binary interaction parameter $\eta = 0.9$ was also fitted to better capture the behavior of the system in the whole range of compositions. The fitting was done to an intermediate temperature of 313.2 K and then used to predict, in a transferable manner, the solubility at other temperatures. As can be seen in Figure 5.12, these adjustments resulted in good agreement between experimental data (Zhou et al., 2014) and calculations using the soft-SAFT model, with an %AAD of 2.01%.

The subsequent step involves detailing the solubility of $NH_3$ within the selected DESs, treating them as a ternary mixture. Once again, the DES [Ch]Cl:EG is taken as the reference system to estimate all necessary binary interactions and cross associating parameters with $NH_3$. While no binary parameters are required for the HBA:HBD interaction, a $\eta$ value of 0.9 was set to describe the interaction between EG and $NH_3$ (taken from the optimization shown in Figure 5.12), accompanied by a cross-association energy between them of 3093 K. The remaining interaction between the salt ([Ch]Cl) and $NH_3$ was fitted to adjust the ternary mixture of [Ch]Cl: EG (1:2) + $NH_3$, obtaining $\xi_{[Ch]Cl-NH_3}$= 0.9 and $\eta_{[Ch]Cl-NH_3}$= 1.03 across all isotherms. These parameters were subsequently transferred to $NH_3$ mixtures for the other two [Ch]Cl-based DESs with GL and UR. The remaining $\eta_{HBD-NH_3}$ values were optimized to a constant value of 0.97 for GL and UR using the intermediate temperature isotherm, with predictions extended to the other two isotherms. Finally, cross-association energy parameters were also determined between $NH_3$ and the other HBDs, resulting in values of 3418K for GL and 2665K for UR, indicating strong interactions of covalent bonds. A summary of the necessary $\eta$ values for quantitatively describing $NH_3$ solubility in DESs is provided in Table 5.9.

***Table 5.9.*** *soft-SAFT size parameters ($\eta_{ij}$) adjusted in this work.*

| Compound *i* | Compound *j* | $\eta_{ij}$ |
|---|---|---|
| [Ch]Cl | $NH_3$ | 1.03 |
| EG | $NH_3$ | 0.90 |
| GL | $NH_3$ | 0.97 |
| UR | $NH_3$ | 0.97 |

The outcomes for the [Ch]Cl-based with EG, GL and UR in a (1:2) ratio are illustrated in Figure 5.13.

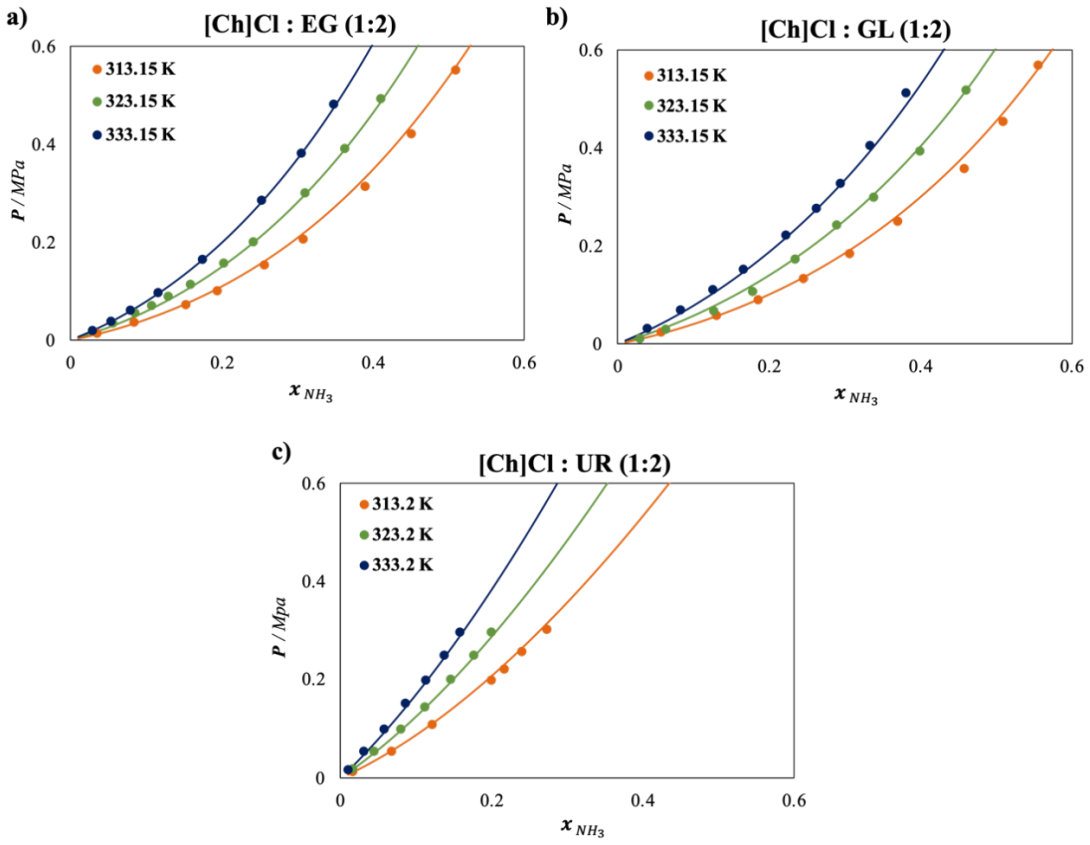


***Figure 5.13.*** *Solubility of $NH_3$ at different temperatures in a) [Ch]Cl:EG (1:2) DES, b) [Ch]Cl:GL (1:2) DES and c) [Ch]Cl:UR (1:2) DES. Symbols represent experimental data (Duan et al., 2019; Zhong et al., 2019), and lines soft-SAFT calculations.*

In summary, this approach yielded an accurate description of $NH_3$ solubility across various isotherms for the studied DESs, with %AAD of 4.45%, 6.94% and 3.01% for [Ch]Cl: EG (1:2), [Ch]Cl: GL (1:2) and [Ch]Cl: UR (1:2), respectively.

### 5.2.5 Enthalpy and Entropy of Dissolution

Using the expression described in Eq. 5.1 and 5.2, the enthalpy and entropy of absorption for $CO_2$ and $NH_3$ solubility were calculated. The mole fraction $x_i$ of $CO_2$ and $NH_3$ in the DESs was fixed at 0.01 (a low gas concentration). The results for each gas within the respective DESs are provided in Table 5.10.

***Table 5.10.*** *Calculated Enthalpy and Entropy of Dissolution for $CO_2$ and $NH_3$ in DESs from 303.15 to 333.15 K at a DES Liquid Phase Molar Composition of 0.01.*

| DES | $\Delta H_{dis}$/kJ. mol$^{-1}$ | | $\Delta S_{dis}$/J. K$^{-1}$. mol$^{-1}$ | |
|---|---|---|---|---|
| | **$CO_2$** | **$NH_3$** | **$CO_2$** | **$NH_3$** |
| **[Ch]Cl : EG (1:2)** | -12.97 | -29.56 | -40.82 | -93.06 |
| **[Ch]Cl : GL (1:2)** | -18.34 | -31.51 | -57.69 | -99.16 |
| **[Ch]Cl : UR (1:2)** | -23.10 | -33.74 | -72.65 | -106.15 |

As shown in Table 5.10, $\Delta H_{dis}$ is more negative for $NH_3$ compared to $CO_2$, indicating that all examined DESs exhibit a stronger preference for $NH_3$ over $CO_2$. In terms of $\Delta S_{dis}$ results, negative values are universally observed, attributed to the gas condensing, being also more negative for $NH_3$ than for $CO_2$, indicating that all examined DESs exhibit a stronger preference for $NH_3$ over $CO_2$. The reduction in entropy due to this phase transition is not compensated by the entropy generated from the disruption of $CO_2$ or $NH_3$ into the ordered structure of the DESs.

### 5.2.6 Selectivity and Absorption Calculations

From the slope of the absorption isotherms from Figures 5.11 and 5.13, the effective Henry's coefficients ($k^i_{H,eff}$) of $CO_2$ and $NH_3$ have been calculated in the three

DESs. The $k^{i}_{H,eff}$ values for the DESs at different temperatures are reported in Table 5.11.

***Table 5.11.*** *Effective Henry's law constants determined for the absorption of $CO_2$ and $NH_3$ at different temperatures in the selected DESs (MPa).*

| DES | $CO_2$ Absorption | | | | $NH_3$ Absorption | | |
|---|---|---|---|---|---|---|---|
| | 303.15 K | 313.15 K | 323.15 K | 333.15 K | 313.15 K | 323.15 K | 333.15 K |
| [Ch]Cl : EG (1:2) | 24.279 | 28.985 | 33.628 | - | 0.3759 | 0.5208 | 0.7013 |
| [Ch]Cl : GL (1:2) | 13.857 | 17.840 | 21.800 | - | 0.3668 | 0.5215 | 0.7128 |
| [Ch]Cl : UR (1:2) | - | 13.995 | 17.965 | 21.973 | 0.8101 | 1.1748 | 1.6193 |

The effective Henry's constants are directly linked to the solubility measurements depicted in those Figures. In general, all DESs exhibit larger values of effective Henry´s constants (i.e., lower affinity) for $CO_2$ than for $NH_3$. The values of $CO_2$ absorption are in agreement with those reported in the literature for ammonium salt-based DESs (Lloret et al., 2017; Ojeda & Llovell, 2018). As illustrated in Figure 5.14 (blue bars graph, left axis), [Ch]Cl:UR (1:2) shows the lowest $k_{H,eff}$ for $CO_2$, indicating a higher absorption capacity, followed by [Ch]Cl:GL (1:2) and [Ch]Cl:EG (1:2). On the other hand, [Ch]Cl:UR shows the highest $k_{H,eff}$ for $NH_3$, indicating a lower absorption capacity, and the other DESs exhibit lower similar values of $k_{H,eff}$ for $NH_3$, as can be seen in Figure 5.14 (orange bars graph, left axis).

Once all gases Henry's law constants in the different DESs are estimated, the ideal gas selectivity can be easily calculated for all the DES using the Eq. 5.3. The ideal selectivity for the binary mixtures of $NH_3/CO_2$ obtained at 323.15 K is also plotted in Figure 5.14 (symbols and lines, right axis).

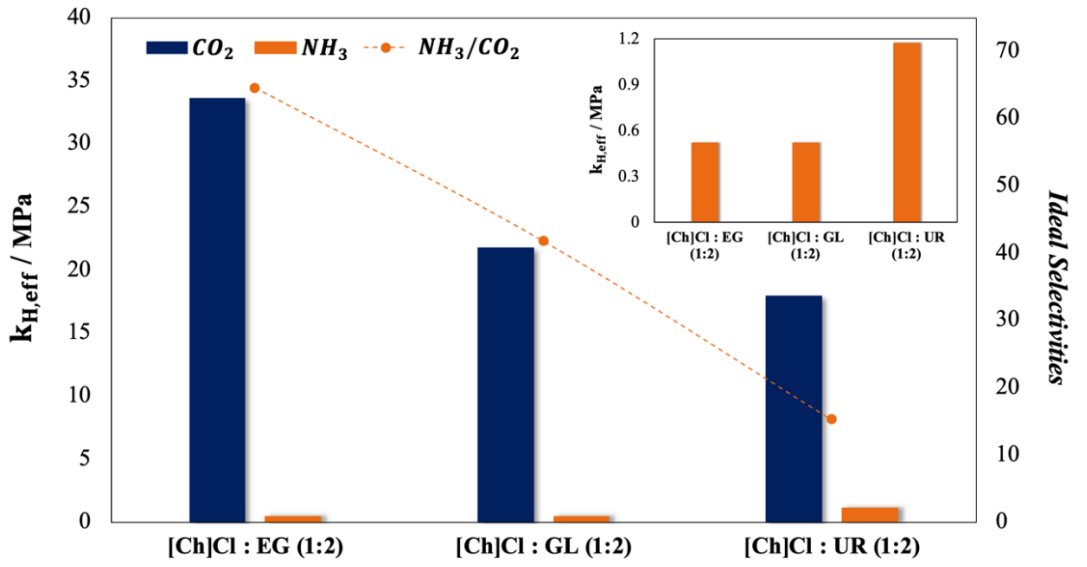


***Figure 5.14.*** *Calculated effective Henry's constants ($k_{H,eff}$) for $CO_2$ and $NH_3$ (bars graph, left axis) and ideal selectivity ($\alpha_{NH_3/CO_2}$, symbols and lines, right axis) in [Ch]Cl:EG (1:2), [Ch]Cl:GL (1:2) and [Ch]Cl:UR (1:2) at 323.15 K.*

The highest value of $\alpha_{NH_3/CO_2}$ (64.57) among the investigated DESs for the binary mixtures is obtained with [Ch]:EG (1:2), indicating the best selectivity and preference for $NH_3$ in this mixture. Based on these preliminary results, [Ch]Cl:EG is preselected as the most suitable DES for $NH_3$-$CO_2$ separation.

The next step is to investigate the influence of the molar ratio of this DES on the selectivity of $NH_3$ over $CO_2$. For this, the solubility of both gases in the DES [Ch]Cl:EG was calculated at different ratios, including a lower ratio (1:1.7) and a higher ratio (1:2.5) of EG relative to [Ch]Cl compared to the [Ch]Cl:EG (1:2). The results of these solubility predictions are shown in Figure 5.15.

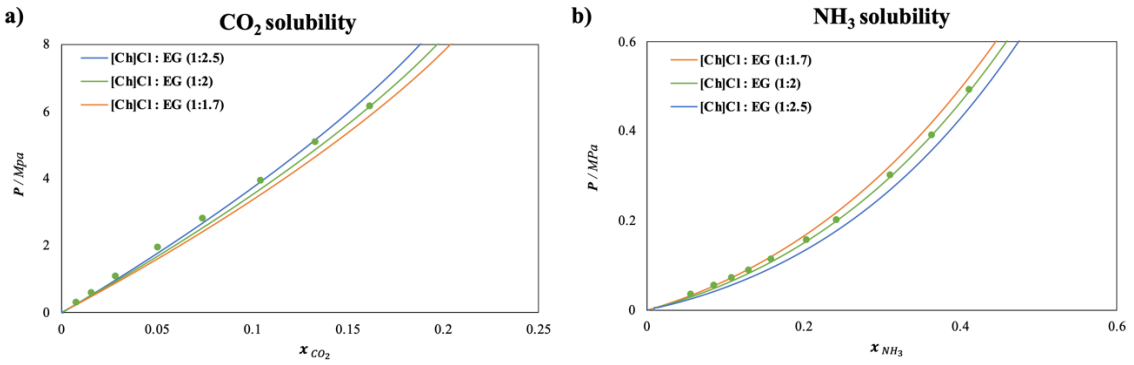


***Figure 5.15.*** *Solubility of a) $CO_2$ and b) $NH_3$ in the DESs [Ch]Cl:EG at different ratios at 323.15 K. Symbols represent experimental data (Duan et al., 2019; Leron & Li, 2013a) and lines soft-SAFT predictions.*

From the slope of the absorption isotherms shown in Figure 5.15, the $k^{i}_{H,eff}$ of $CO_2$ and $NH_3$, as well as the ideal $\alpha_{NH_3/CO_2}$, were calculated for the three DESs. Table 5.12 presents the $k^{i}_{H,eff}$ values for the three DESs, while Figure 5.16 illustrates these values (bar graph on the left axis), and the ideal selectivity of $NH_3$ over $CO_2$ (symbols and lines on the right axis).

***Table 5.12.*** *Effective Henry's law constants determined for the absorption of $CO_2$ and $NH_3$ at 323.15K in the DES [Ch]Cl : EG at different ratios (MPa).*

| DES | $CO_2$ absorption | $NH_3$ absorption |
|---|---|---|
| [Ch]Cl : EG (1:2.5) | 35.652 | 0.4334 |
| [Ch]Cl : EG (1:2) | 33.628 | 0.5208 |
| [Ch]Cl : EG (1:1.7) | 32.115 | 0.575 |

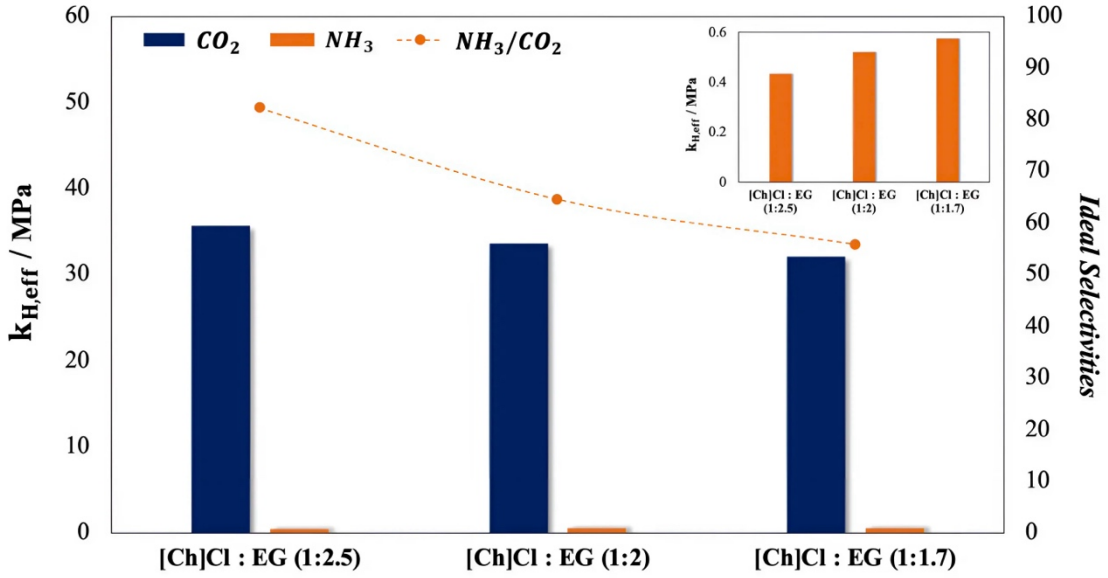


***Figure 5.16.*** *Calculated effective Henry's constants ($k_{H,eff}$) for $CO_2$ and $NH_3$ (bars graph, left axis) and ideal selectivity ($\alpha_{i/j}$, symbols and lines, right axis) in the DESs [Ch]Cl:EG at different ratios at 323.15 K.*

The results reveal that increasing the molar ratio of [Ch]Cl:EG from 1:2 to 1:2.5 decreases the $CO_2$ absorption capacity, as evidenced by the increase in $k^i_{H,eff}$ from 33.628 to 35.652. Conversely, this change increases the $NH_3$ absorption capacity, indicated by the decrease in the corresponding $k^i_{H,eff}$ from 0.5208 to 0.4334. When the molar ratio is decreased from 1:2 to 1:1.7, the opposite effect occurs. Thus, increasing the molar ratio from 1:2 to 1:2.5 results in an approximately 27% increase in the ideal $\alpha_{NH_3/CO_2}$, from 64.57 to 82.25.

As discussed in Section 5.1.6, the ideal selectivity calculated from effective Henry's coefficients is an approximation based on the infinite dilution behavior of pure compounds ($CO_2$ and $NH_3$ in this study). This method does not account for the competition between gases, providing only a preliminary indication of each DES's separation capacity. To accurately assess gas separation efficiency, competitive selectivity is evaluated here to simulate the recovery of $NH_3$ from melamine tail gas.

According to Duan et al. (2022), a melamine tail gas produced in China contains 7.6% $N_2$, 0.4% $H_2O$, 55% $NH_3$, and 37% $CO_2$ in mole fraction. For this analysis, we simplify this residual mixture to 60% $NH_3$ and 40% $CO_2$ in mole fraction.

The competitive selectivity is determined using Eq. 5.4, where the equilibrium compositions are derived from liquid-vapor flash calculations employing the soft-SAFT EoS. This involve an iterative process that solves a flash model based on the Rachford-Rice equation (Mejía et al., 2021). The calculation assumes an initial global composition with a DES mole fraction of 0.7 ($z_{DES} = 0.7$) and 0.3 for the melamine tail gas blend ($z_{NH_3+CO_2} = 0.3$), consisting of 60% $NH_3$ and 40% $CO_2$ in mole fractions, as previously specified, at different pressures and 323.15 K, as depicted in Figure 5.16.

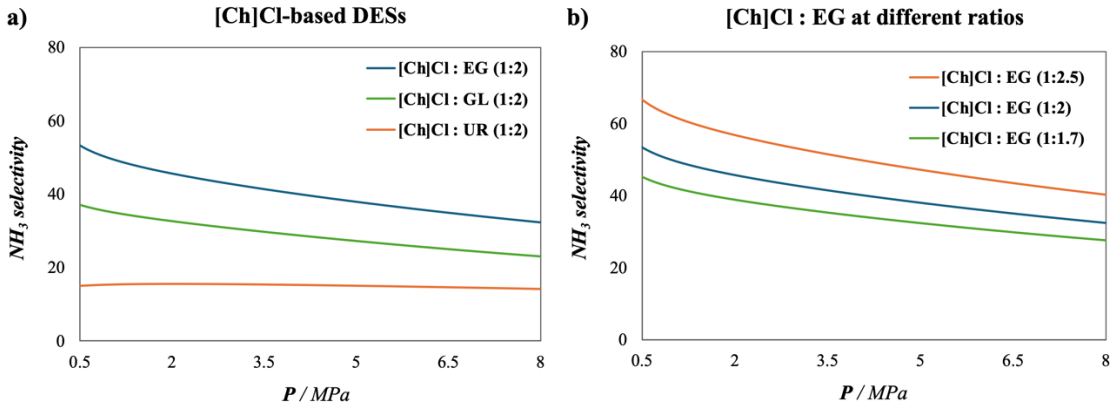


***Figure 5.17.*** *Competitive selectivity of $NH_3/CO_2$ in a) [Ch]Cl-based DESs and b) [Ch]Cl-EG at different ratios, at 323.15 K and different pressures. The mixture has a global composition of $z_{DES} = 0.7$ and $z_{CO_2 \text{ and } NH_3 \text{ blend}} = 0.3$ modeled using soft-SAFT EoS, which the $CO_2$ and $NH_3$ blend contains 60% $NH_3$ and 40% $CO_2$ in mole fraction.*

In general, the predicted competitive selectivity aligns closely with the ideal selectivity at infinite dilution, as seen when comparing Figures 5.14 and 5.16. This correlation is especially evident at low pressures, where ideal conditions are predominant. However, lower pressures, while enhancing separation performance, come at the expense of reduced sorption capacity, as indicated in Figure 5.11 and 5.13, leading to lower $NH_3$

recovery. Conversely, high-pressure conditions do not yield favorable outcomes, as they decrease the $NH_3$-$CO_2$ separation efficiency for [Ch]Cl-based DESs. Therefore, based on this analysis, operating under moderate pressure conditions is recommended for efficient $NH_3$-$CO_2$ separation. Figure 5.16 analysis also reveals significant potential for achieving high separation efficiency in $NH_3$-$CO_2$ separation. Among the studied DESs, [Ch]Cl:EG (1:2.5) stands out as the best choice for $NH_3$ capture from melamine tail gas streams.

## 5.3 Key Findings of the Chapter

This chapter focuses on the selective recovery of greenhouse gases (GHGs) using DESs. The research includes the separation of commercial refrigerant blends and the recovery of ammonia from carbon dioxide mixtures in melamine streams. Using the soft-SAFT EoS, the solubility of various GHGs in DESs was examined, determining key properties such as enthalpy and entropy of dissolution, Henry's constants, and ideal and competitive selectivity.

Among the DESs studied for refrigerants blends, TMAC:EG (1:3) exhibited a higher affinity for the studied F-gases, presenting a slightly higher absorption capacity. Despite having a relatively low absorption, the DESs investigated exhibited promising selectivity for separating F-gas mixtures, particularly those containing R-32, suggesting potential applications in separating commercial blends like R410A and R410F. Additionally, the solubility of $CO_2$ and $NH_3$ in [Ch]Cl-based DESs (with EG, UR, and GL as HBDs) was described. [Ch]Cl:UR demonstrated a higher $CO_2$ absorption capacity, while [Ch]:EG showed a higher $NH_3$ absorption capacity. For the recovery of $NH_3$ from $CO_2$ mixtures in melamine streams, [Ch]Cl: EG (1:2.5) emerged as the most effective

DES among those studied. These findings underscore the potential of DESs in advancing sustainable gas separation technologies.

# 6

# Conclusions and Future Works

*Based on the objectives of this doctoral thesis, which explores the physicochemical properties of DESs using a variety of computational tools, with a particular focus on their applications in GHG capture and separation, the encountered key findings and future lines of work are discussed.*

## 6.1 Conclusions

This thesis's primary goal was to explore the physicochemical properties of DESs using a range of computational tools, focusing particularly on their applications in GHG capture and separation. This approach utilized advanced techniques such as, quantum-based charge distribution analysis through COSMO-SAC, the soft-SAFT EoS and molecular-based ANNs to (i) develop a consistent framework to describe the impact of cosolvents in the key thermophysical properties of the DESs and (ii) assess their effectiveness in separating commercial refrigerant blends and separating ammonia from $CO_2$ during the melamine production process.

The main conclusions drawn from the analysis of the results obtained in this work are highlighted below:

1. Two molecular models for several [Ch]Cl-Based DESs have been built within the soft-SAFT framework employing a simple and a more realistic approach.
   (a) The simplest model, considering the DESs as pseudo-pure compounds, demonstrated excellent agreement with experimental density data for both pure DESs and aqueous solutions, but its transferability is limited.
   (b) The second, more realistic model treated DESs as mixtures of independent species, accurately describing density, isentropic compressibility, speed of sound, and viscosity of pure DESs. It effectively accounted for the influence of adding alcohols or water as solvents on DESs density and viscosity, and reasonably predicted vapor-liquid equilibria and activity coefficients in aqueous DES mixtures.
   (c) This methodology allows the screening of the thermophysical properties of DESs, whose knowledge is essential pre-requisite for process design.

2. An ANN model was developed to estimate the viscosity of Choline-Chloride based DESs and their mixtures with cosolvents using COSMO-SAC-based $\sigma$-profiles and temperature as parameter inputs.
   (a) The $\sigma$-profiles of the 24 compounds that form the DESs investigated, including amines, glycols, and carboxylic acids as HBDs, were obtained through COSMO-SAC methodology, each divided into eight descriptors.
   (b) The training dataset included 48 DES based on [Ch]Cl with 1891 data points, encompassing 18 different HBDs and mixtures of DESs with water, methanol, isopropanol and dimethyl sulfoxide.
   (c) The best performance in predicting the $log\ \eta$ of DESs was found to be 9-19-16-1 architecture, achieving an RMSE value of 0.01424, with high $R^2$ values of 0.99989, 0.99723, and 0.99809 in training, internal testing and external testing, respectively.
   (d) The relative contributions of input variables to DESs viscosity in the molecular-based ANN model were evaluated using the Partial Derivatives method, revealing the substantial impact of hydrogen bonding regions on the the $log\ \eta$ of DESs.
   (e) The developed ANN showed a remarkable extrapolation capacity, as it was capable to predict the viscosity of systems including solvents (ethanol) and HBD (2,3-butanediol) not considered in the training, as well as extrapolating to viscosity values outside the fitting range.
3. A comprehensive study was conducted to model the solubility of four common F-gases (R-125, R-134a, R-32, and R143a) in three [Ch]Cl-based DESs and two TMAC-based DESs. The study was carried out at 300.15 K and low pressure using the soft-SAFT EoS.

(a) The soft-SAFT calculations effectively described the solubility of each F-gas in the examined DESs, demonstrating good agreement with experimental data. Energy and size binary parameters were specifically tuned between the DESs components and the F-gases to achieve this accuracy.

(b) The soft-SAFT EoS was employed to determine key properties such as enthalpy and entropy of dissolution, Henry's constants, and ideal selectivity.

(c) Among the DESs studied, TMAC:EG (1:3) showed a higher affinity for the studied F-gases, presenting a slightly higher absorption capacity.

(d) Competitive selectivity among gases in multi-component systems based on commercial refrigerant blends and DESs was evaluated at 300.15 K and various pressures using soft-SAFT EoS.

(e) Despite having a relatively low absorption, the DESs investigated exhibited promising selectivity for separating F-gas mixtures, particularly those containing R-32, thereby suggesting potential applications in separating commercial blends like R410A and R407F.

4. A comprehensive study was conducted to model the solubility of $CO_2$ and $NH_3$ in three [Ch]Cl-based DESs with EG, UR, and GL as HBDs using the soft-SAFT EoS.

(a) The soft-SAFT calculations effectively described the isotherms of $CO_2$ and $NH_3$ in the three DESs over the temperature range of 303.15 to 333.14 K, showing excellent agreement with experimental data. Temperature-independent binary parameters for energy and size were meticulously adjusted between the DESs components and gases to achieve this level of accuracy.

(b) The soft-SAFT EoS was used to calculate essential properties including enthalpy and entropy of dissolution, Henry's constants, and ideal selectivity.

(c) Among the investigated DESs, [Ch]Cl:UR demonstrated a higher $CO_2$ absorption capacity, while [Ch]:EG showed a higher $NH_3$ absorption capacity at 323.12 K using soft-SAFT EoS.

(d) Competitive selectivity between $NH_3$ and $CO_2$ in multi-component mixtures-based melamine tail gas (60% $NH_3$ and 40% $CO_2$ in mole fraction) and DESs was evaluated at 323.15 K and different pressures.

(e) For the separation of $NH_3$ from $CO_2$ mixtures in melamine streams, [Ch]Cl: EG (1:2.5) emerged as the most effective DES among those studies.

## 6.1 Final Remarks and Future Works

This thesis has been devoted to combine different computational tools, taking advantage of the different strengths that they offer, to add more insight into the characterization of DESs and, particularly, in Choline Chloride-based solvents, given its low cost and synthesis. While the work presented here has successfully addressed with the description of key physicochemical properties and has provided a suitable platform for engineering applications in the field of gas treatment, this is only a first step that should be completed with further studies, in order to achieve a new industrial efficient technology. Consequently, a set of further strategies to continue this research are given below:

1. **Process simulation, integrating the soft-SAFT model to design a gas recovery pre-unit:** Based on the results obtained in Chapter 5, a process simulation using

Aspen software could be carried out optimize the two gas recovery processes using DESs proposed in this thesis, focusing on enhancing energy efficiency, and addressing an adequate technoeconomic assessment. For this purpose, the soft-SAFT thermodynamic model could be integrated into ASPEN, although it would also be possible to carry out the simulation using COSMO-SAC.

2. Performing a **Life Cycle Analysis (LCA)** of the simulated recovery processes. In order to ensure the sustainability of the proposed units, it would be necessary to carry out a cradle-to-grave LCA to check the environmental impact of the DES production, electricity and energy process consumption, and final disposal to fully demonstrate that this circular economy approach is suitable and superior to current strategies.

3. **ANN for Predicting Additional Properties**: Given the powerful performance of ANNs based on COSMO-SAC descriptors, it would be possible to develop additional ANN models to predict properties beyond viscosity, such as the toxicity or other environmental properties, that cannot be obtained with an equation of state, enabling comprehensive assessment and optimization of DES formulations.

4. **Refinement of the coarse-grained DESs models**: As mentioned along the dissertation, a balance between model complexity and accuracy was seek. This is the main reason while the number of hydrogen bonding interactions has been kept limited to a restricted number of association sites. In some cases, such as for instance, [Ch]Cl : Urea, the number of possible interactions is known to be higher, limiting the accuracy of the predictions. In this regard, molecular simulations can

be used as an additional tool to gain insight on these interactions, as well as the behavior in the presence of water and cosolvents, and additional sites may be added to better capture the physicochemical properties.

5. **Extension of the screening to other DESs with a different HBA**: As far as [Ch]Cl-based DESs are a very attractive option due to their availability and easy synthesis, the methodology presented in this work is applicable to other DESs. In this regard, the potential of natural deep eutectic solvents (NADES) based on betaine, menthol, and other natural products, could enhance the sustainability of these processes.

# A

## Papers published in indexed journals and contributions to scientific meetings

## A.1 Papers published during the development of this thesis

1. **Alencar, L. V. T. D.**, Rodriguez-Reartes, S. B., Tavares, F. W., & Llovell, F. (2024). A consistent framework to characterize the impact of co-solvents in the key process thermophysical properties of choline chloride-based DESs. *Journal of Industrial and Engineering Chemistry*, 132, 279-290. https://doi.org/10.1016/j.jiec.2023.11.021.

2. **Alencar, L. V. T. D.**, Rodríguez-Reartes, S. B., Tavares, F. W., & Llovell, F. (2024). Assessing Viscosity in Sustainable Deep Eutectic Solvents and Cosolvent Mixtures: An Artificial Neural Network-Based Molecular Approach. *ACS Sustainable Chemistry & Engineering*, 12(21), 7987-8000. https://doi.org/10.1021/acssuschemeng.3c07219.

3. **Alencar, L. V. T. D.**, G.B., Bastían; Rodríguez Reartes, Sabrina Belén; Quinteros-Lama, Héctor; Garrido, José Matías; Codera, Victoria; Pou, Josep Oriol; Tavares, F. W; Gonzalez-Olmos, Rafael; Llovell, F. (2024). Thermophysical Characterization of Sustainable Pathways for F-Gas Separation Utilizing Deep Eutectic Solvents. *Submitted to Journal of Industrial and Engineering Chemistry.*

4. **Alencar, L. V. T. D.**, Rodriguez-Reartes, S. B., Tavares, F. W., & Llovell, F. Assessing $CO_2$–$NH_3$ Separation with Choline Chloride-Based Deep Eutectic Solvents Using the Soft-SAFT Equation of State. (In preparation).

5. G.B., Bastían, **Alencar, L. V. T. D.,** Llovell, F., Quinteros-Lama, Héctor, Garrido, José Matías. Modelling of a dual solvent-based separation process for the treatment of refrigerant blends. (In preparation).

## A.2 Contributions to scientific meetings

1. Jovell, D., Demirbek, M.G., **Alencar, L.V. T. D**., Alkhatib, I.I.I., Vega, L.F., & Llovell, F. (2022, September 7-9). Thermophysical Characterization of Deep Eutectic Solvents for Practical Applications in Greenhouse Gas Capture and Separation [Oral Presentation]. The 27th Thermodynamics Conference, Bath, United Kingdom.

2. **Alencar, L. V. T. D.**, Rodriguez-Reartes, S. B., Tavares, F. W., & Llovell, F., (2022, October 24-27). Accurate description of the effect of water in the thermophysical properties of Choline Chloride Based Deep Eutectic Solvents with the soft-SAFT EoS [Poster Presentation]. XII Iberoamerican Conference on Phase Equilibria and Fluid Properties for Process Design, Campinas, São Paulo, Brazil.

3. **Alencar, L. V. T. D.**, Rodriguez-Reartes, S. B., González-Olmos R., Llovell F. (2023, March 21-23). Understanding the potential of DES for GHG capture and separation: from thermodynamics to process design [Oral Presentation]. 2nd Greenering International Conference, Valladolid, Spain.

4. **Alencar, L. V. T. D.**, Rodriguez-Reartes, S. B., Tavares, F. W., & Llovell, F., (2023, May 21-25). Describing the effect of some cosolvents in the thermophysical properties of Choline Chloride Based Deep Eutectic Solvents for gas [Poster Presentation]. 16th Internacional Conference on Properties and Phase Equilibria for Product and Process Design, La Pineda, Tarragona, Spain.

5. **Alencar, L. V. T. D.**, Rodriguez-Reartes, S. B., Tavares, F. W., & Llovell, F., (2023, May 30 - June 1). Predicting the thermophysical properties of Choline Chloride based Deep Eutectic Solvents through soft-SAFT EoS and machine learning [Poster Presentation]. 15th Mediterranean Congress of Chemical Engineering, Barcelona, Spain.

6. **Alencar, L. V. T. D.**, Rodriguez-Reartes, S. B., Tavares, F. W., & Llovell, F., (2023, May 30 - June 1). Accurate Description of the Thermophysical Properties of Choline Chloride-Based Deep Eutectic Solvents and Their Aqueous Mixtures using soft-SAFT EoS [Oral Presentation]. 3rd International Meeting on Deep Eutectic Systems, Lisbon, Portugal.

7. **Alencar, L. V. T. D.**, Rodriguez-Reartes, S. B., Tavares, F. W., & Llovell, F., (2024, May 5-7). Viscosity Prediction of DESs and Their Cosolvents Mixtures: A Molecular-Based Artificial Neural Network Approach [Poster Presentation]. XII Congresso Brasileiro de Termodinâmica Aplicada, Curitiba, Paraná, Brazil.

8. **Alencar, L. V. T. D.**, Rodriguez-Reartes, S. B., Tavares, F. W., & Llovell, F., (2024, May 5-7). A consistent framework to characterize the impact of co-solvents in the key process thermophysical properties of choline chloride-based DESs [Poster Presentation]. XII Congresso Brasileiro de Termodinâmica Aplicada, Curitiba, Paraná, Brazil.

9. **Alencar, L. V. T. D.**, Rodriguez-Reartes, S. B., Tavares, F. W., & Llovell, F., (2024, June 9-12). Integrating Theoretical Approaches for Profiling the Thermophysical Behavior of DESs in Greenhouse Gas Treatments [Oral Presentation]. 33rd European Symposium on Applied Thermodynamics**,** Edinburgh, United Kingdom.

10. **Alencar, L. V. T. D.**, Rodriguez-Reartes, S. B., Tavares, F. W., & Llovell, F., (2024, June 23-28). Combining Theoretical Tools to Characterize the Thermophysical Profile of Deep Eutectic Solvents for $CO_2$ and F-Gas Capture Applications [Oral Presentation]. 22nd symposium on thermophysical properties**,** Boulder, United States.

**References**


Abaid, A. C. (2022). *Integration of Artificial Neural Networks and First Principles Modelling* Norwegian University of Science and Technology]. https://hdl.handle.net/11250/3009527

Abbott, A. P., Boothby, D., Capper, G., Davies, D. L., & Rasheed, R. K. (2004). Deep Eutectic Solvents Formed between Choline Chloride and Carboxylic Acids: Versatile Alternatives to Ionic Liquids. *Journal of the American Chemical Society*, *126*(29), 9142-9147. https://doi.org/10.1021/ja048266j

Abbott, A. P., Capper, G., Davies, D. L., Rasheed, R. K., & Tambyrajah, V. (2003). Novel solvent properties of choline chloride/urea mixtures [10.1039/B210714G]. *Chemical Communications*(1), 70-71. https://doi.org/10.1039/B210714G

Abdel Jabbar, N. M., & Mjalli, F. S. (2019). Ultrasonic study of binary aqueous mixtures of three common eutectic solvents. *Physics and Chemistry of Liquids*, *57*(1), 1-18. https://doi.org/10.1080/00319104.2017.1385075

Abo-Hamad, A., Hayyan, M., AlSaadi, M. A., & Hashim, M. A. (2015). Potential applications of deep eutectic solvents in nanotechnology. *Chemical Engineering Journal*, *273*, 551-567. https://doi.org/10.1016/j.cej.2015.03.091

Aboshatta, M., & Magueijo, V. (2021). A Comprehensive Study of CO2 Absorption and Desorption by Choline-Chloride/Levulinic-Acid-Based Deep Eutectic Solvents. *Molecules*, *26*(18), 5595. https://doi.org/10.3390/molecules26185595

Abranches, D. O., Larriba, M., Silva, L. P., Melle-Franco, M., Palomar, J. F., Pinho, S. P., & Coutinho, J. A. P. (2019). Using COSMO-RS to design choline chloride pharmaceutical eutectic solvents. *Fluid Phase Equilibria*, *497*, 71-78. https://doi.org/10.1016/j.fluid.2019.06.005

Adeyemi, I., Abu-Zahra, M. R. M., & Alnashef, I. (2017a). Experimental Study of the Solubility of CO2 in Novel Amine Based Deep Eutectic Solvents. *Energy Procedia*, *105*, 1394-1400. https://doi.org/10.1016/j.egypro.2017.03.519

Adeyemi, I., Abu-Zahra, M. R. M., & Alnashef, I. (2017b). Novel Green Solvents for CO2 Capture. *Energy Procedia*, *114*, 2552-2560. https://doi.org/10.1016/j.egypro.2017.03.1413

Adeyemi, I., Abu-Zahra, M. R. M., & AlNashef, I. M. (2018). Physicochemical properties of alkanolamine-choline chloride deep eutectic solvents: Measurements, group

contribution and artificial intelligence prediction techniques. *Journal of Molecular Liquids*, *256*, 581-590. https://doi.org/10.1016/j.molliq.2018.02.085

Ainai, Y., Taniguchi, A., Kuramochi, T., Yokoyama, C., & Kodama, D. (2024). Density, viscosity, and CO2 solubility of deep eutectic solvents comprising tetrabutylammonium or phosphonium bromide and ethylene glycol. *Fluid Phase Equilibria*, *584*, 114122. https://doi.org/10.1016/j.fluid.2024.114122

Aissaoui, T., AlNashef, I. M., Qureshi, U. A., & Benguerba, Y. (2017). Potential applications of deep eutectic solvents in natural gas sweetening for CO2 capture. *Reviews in Chemical Engineering*, *33*(6), 523-550. https://doi.org/10.1515/revce-2016-0013

Alam, M. A., Deng, L., Ngatcha, A. D. P., Fouegue, A. D. T., Wu, J., Zhang, S., Zhao, A., Xiong, W., & Xu, J. (2023). Biodiesel production from microalgal biomass by Lewis acidic deep eutectic solvent catalysed direct transesterification. *Industrial Crops and Products*, *206*, 117725. https://doi.org/10.1016/j.indcrop.2023.117725

Alam, M. A., Muhammad, G., Khan, M. N., Mofijur, M., Lv, Y., Xiong, W., & Xu, J. (2021). Choline chloride-based deep eutectic solvents as green extractants for the isolation of phenolic compounds from biomass. *Journal of Cleaner Production*, *309*, 127445. https://doi.org/10.1016/j.jclepro.2021.127445

Albà, C. G., Alkhatib, I. I. I., Llovell, F., & Vega, L. F. (2021). Assessment of Low Global Warming Potential Refrigerants for Drop-In Replacement by Connecting their Molecular Features to Their Performance. *ACS Sustainable Chemistry & Engineering*, *9*(50), 17034-17048. https://doi.org/10.1021/acssuschemeng.1c05985

Albà, C. G., Alkhatib, I. I. I., Llovell, F., & Vega, L. F. (2023). Hunting sustainable refrigerants fulfilling technical, environmental, safety and economic requirements. *Renewable and Sustainable Energy Reviews*, *188*, 113806. https://doi.org/10.1016/j.rser.2023.113806

Albà, C. G., Vega, L. F., & Llovell, F. (2020). A consistent thermodynamic molecular model of n-hydrofluoroolefins and blends for refrigeration applications. *International Journal of Refrigeration*, *113*, 145-155. https://doi.org/10.1016/j.ijrefrig.2020.01.008

Alcalde, R., Atilhan, M., & Aparicio, S. (2018). On the properties of (choline chloride + lactic acid) deep eutectic solvent with methanol mixtures. *Journal of Molecular Liquids*, *272*, 815-820. https://doi.org/10.1016/j.molliq.2018.10.052

Alcalde, R., Gutiérrez, A., Atilhan, M., & Aparicio, S. (2019). An experimental and theoretical investigation of the physicochemical properties on choline chloride – Lactic acid based natural deep eutectic solvent (NADES). *Journal of Molecular Liquids*, *290*, 110916. https://doi.org/10.1016/j.molliq.2019.110916

Alencar, L. V. T. D., Rodríguez-Reartes, S. B., Tavares, F. W., & Llovell, F. (2024). Assessing Viscosity in Sustainable Deep Eutectic Solvents and Cosolvent Mixtures: An Artificial Neural Network-Based Molecular Approach. *ACS Sustainable Chemistry & Engineering*. https://doi.org/10.1021/acssuschemeng.3c07219

Alhadid, A., Mokrushina, L., & Minceva, M. (2019). Modeling of Solid–Liquid Equilibria in Deep Eutectic Solvents: A Parameter Study. *Molecules*, *24*(12). https://doi.org/10.3390/molecules24122334

Alkhatib, I., Bahamon, D., Llovell, F., Abu-Zahra, M. R. M., & Vega, L. F. (2020). Perspectives and guidelines on thermodynamic modelling of deep eutectic solvents. *Journal of Molecular Liquids*, *298*, 112183. https://doi.org/10.1016/j.molliq.2019.112183

Alkhatib, I. I. I., Albà, C. G., Darwish, A. S., Llovell, F., & Vega, L. F. (2022). Searching for Sustainable Refrigerants by Bridging Molecular Modeling with Machine Learning. *Industrial & Engineering Chemistry Research*, *61*(21), 7414-7429. https://doi.org/10.1021/acs.iecr.2c00719

Alkhatib, I. I. I., Ferreira, M. L., Alba, C. G., Bahamon, D., Llovell, F., Pereiro, A. B., Araújo, J. M. M., Abu-Zahra, M. R. M., & Vega, L. F. (2020a). Screening of Ionic Liquids and Deep Eutectic Solvents for Physical CO2 Absorption by Soft-SAFT Using Key Performance Indicators. *Journal of Chemical & Engineering Data*, *65*(12), 5844-5861. https://doi.org/10.1021/acs.jced.0c00750

Alkhatib, I. I. I., Pereira, L. M. C., Torne, J., & Vega, L. F. (2020b). Polar soft-SAFT: theory and comparison with molecular simulations and experimental data of pure polar fluids [https://doi.org/10.1039/D0CP00846J]. *Physical Chemistry Chemical Physics*, *22*(23), 13171-13191. 10.1039/D0CP00846J

Allal, A., Boned, C., & Baylaucq, A. (2001a). Free-volume viscosity model for fluids in the dense and gaseous states. *Phys Rev E Stat Nonlin Soft Matter Phys*, *64*(1 Pt 1), 011203. https://doi.org/10.1103/PhysRevE.64.011203

Allal, A., Moha-ouchane, M., & Boned, C. (2001b). A New Free Volume Model for Dynamic Viscosity and Density of Dense Fluids Versus Pressure and Temperature.

*Physics and Chemistry of Liquids*, *39*(1), 1-30. https://doi.org/10.1080/00319100108030323

Altamash, T., Nasser, M. S., Elhamarnah, Y., Magzoub, M., Ullah, R., Anaya, B., Aparicio, S., & Atilhan, M. (2017). Gas Solubility and Rheological Behavior of Natural Deep Eutectic Solvents (NADES) via Combined Experimental and Molecular Simulation Techniques. *ChemistrySelect*, *2*(24), 7278-7295. https://doi.org/10.1002/slct.201701223

Amendment to the Montreal protocol on substances that deplete the ozone layer. (2016). In *European Parliament and Council*.

Andreu, J. S., & Vega, L. F. (2007). Capturing the Solubility Behavior of CO2 in Ionic Liquids by a Simple Model. *The Journal of Physical Chemistry C*, *111*(43), 16028-16034. https://doi.org/10.1021/jp074353x

Appl, M. (2011). Ammonia, 2. Production Processes. In *Ullmann's Encyclopedia of Industrial Chemistry*. https://doi.org/10.1002/14356007.o02_o11

Aravena, C., Lee, D., Park, J., & Yoo, Y. (2022). Characteristics of Deep eutectic solvents for CO2 capture with Hydro effects for improvement of mass transfer. *Journal of Industrial and Engineering Chemistry*, *111*, 337-345. https://doi.org/10.1016/j.jiec.2022.04.015

Aroso, I. M., Paiva, A., Reis, R. L., & Duarte, A. R. C. (2017). Natural deep eutectic solvents from choline chloride and betaine – Physicochemical properties. *Journal of Molecular Liquids*, *241*, 654-661. https://doi.org/10.1016/j.molliq.2017.06.051

Asensio-Delgado, S., Jovell, D., Zarca, G., Urtiaga, A., & Llovell, F. (2020). Thermodynamic and process modeling of the recovery of R410A compounds with ionic liquids. *International Journal of Refrigeration*, *118*, 365-375. https://doi.org/10.1016/j.ijrefrig.2020.04.013

Asensio-Delgado, S., Pardo, F., Zarca, G., & Urtiaga, A. (2021). Absorption separation of fluorinated refrigerant gases with ionic liquids: Equilibrium, mass transport, and process design. *Separation and Purification Technology*, *276*, 119363. https://doi.org/10.1016/j.seppur.2021.119363

Asensio-Delgado, S., Pardo, F., Zarca, G., & Urtiaga, A. (2022). Machine learning for predicting the solubility of high-GWP fluorinated refrigerants in ionic liquids. *Journal of Molecular Liquids*, *367*, 120472. https://doi.org/10.1016/j.molliq.2022.120472

Awaja, N. E., Almustafa, G., Darwish, A. S., Lemaoui, T., Benguerba, Y., Banat, F., Arafat, H. A., & AlNashef, I. (2023). Molecular-based artificial neural networks for selecting deep eutectic solvents for the removal of contaminants from aqueous media. *Chemical Engineering Journal*, *476*, 146429. https://doi.org/10.1016/j.cej.2023.146429

Bagh, F. S. G., Shahbaz, K., Mjalli, F. S., AlNashef, I. M., & Hashim, M. A. (2013). Electrical conductivity of ammonium and phosphonium based deep eutectic solvents: Measurements and artificial intelligence-based prediction. *Fluid Phase Equilibria*, *356*, 30-37. https://doi.org/10.1016/j.fluid.2013.07.012

Basheer, I. A., & Hajmeer, M. (2000). Artificial neural networks: fundamentals, computing, design, and application. *Journal of Microbiological Methods*, *43*(1), 3-31. https://doi.org/10.1016/S0167-7012(00)00201-3

Baz, J., Held, C., Pleiss, J., & Hansen, N. (2019). Thermophysical properties of glyceline–water mixtures investigated by molecular modelling [10.1039/C9CP00036D]. *Physical Chemistry Chemical Physics*, *21*(12), 6467-6476. https://doi.org/10.1039/C9CP00036D

Benguerba, Y., Alnashef, I. M., Erto, A., Balsamo, M., & Ernst, B. (2019). A quantitative prediction of the viscosity of amine based DESs using Sσ-profile molecular descriptors. *Journal of Molecular Structure*, *1184*, 357-363. https://doi.org/10.1016/j.molstruc.2019.02.052

Blas, F. J., & Vega, L. F. (1997). Thermodynamic behaviour of homonuclear and heteronuclear Lennard-Jones chains with association sites from simulation and theory. *Molecular Physics*, *92*(1), 135-150. https://doi.org/10.1080/002689797170707

Boublia, A., Lemaoui, T., Abu Hatab, F., Darwish, A. S., Banat, F., Benguerba, Y., & AlNashef, I. M. (2022). Molecular-based artificial neural network for predicting the electrical conductivity of deep eutectic solvents. *Journal of Molecular Liquids*, *366*, 120225. https://doi.org/10.1016/j.molliq.2022.120225

Boublia, A., Lemaoui, T., AlYammahi, J., Darwish, A. S., Ahmad, A., Alam, M., Banat, F., Benguerba, Y., & AlNashef, I. M. (2023). Multitask Neural Network for Mapping the Glass Transition and Melting Temperature Space of Homo- and Co-Polyhydroxyalkanoates Using σProfiles Molecular Inputs. *ACS Sustainable Chemistry & Engineering*, *11*(1), 208-227. https://doi.org/10.1021/acssuschemeng.2c05225

Cadena, C., Anthony, J. L., Shah, J. K., Morrow, T. I., Brennecke, J. F., & Maginn, E. J. (2004). Why Is CO2 So Soluble in Imidazolium-Based Ionic Liquids? *Journal of the American Chemical Society*, *126*(16), 5300-5308. https://doi.org/10.1021/ja039615x

Cané, E., Llovell, F., & Vega, L. F. (2017). Accurate viscosity predictions of linear polymers from n-alkanes data. *Journal of Molecular Liquids*, *243*, 115-123. https://doi.org/10.1016/j.molliq.2017.08.033

Carranza-Abaid, A., Svendsen, H. F., & Jakobsen, J. P. (2020). Surrogate modelling of VLE: Integrating machine learning with thermodynamic constraints. *Chemical Engineering Science: X*, *8*, 100080. https://doi.org/10.1016/j.cesx.2020.100080

Carriazo, D., Serrano, M. C., Gutiérrez, M. C., Ferrer, M. L., & del Monte, F. (2012). Deep-eutectic solvents playing multiple roles in the synthesis of polymers and related materials [10.1039/C2CS15353J]. *Chemical Society Reviews*, *41*(14), 4996-5014. https://doi.org/10.1039/C2CS15353J

Castro, P. J., Aráujo, J. M. M., Martinho, G., & Pereiro, A. B. (2021). Waste Management Strategies to Mitigate the Effects of Fluorinated Greenhouse Gases on Climate Change. *Applied Sciences*, *11*(10), 4367. https://doi.org/10.3390/app11104367

Castro, P. J., Redondo, A. E., Sosa, J. E., Zakrzewska, M. E., Nunes, A. V. M., Araújo, J. M. M., & Pereiro, A. B. (2020). Absorption of Fluorinated Greenhouse Gases in Deep Eutectic Solvents. *Industrial & Engineering Chemistry Research*, *59*(29), 13246-13259. https://doi.org/10.1021/acs.iecr.0c01893

Chapman, W. G., Gubbins, K. E., Jackson, G., & Radosz, M. (1989). SAFT: Equation-of-state solution model for associating fluids. *Fluid Phase Equilibria*, *52*, 31-38. https://doi.org/10.1016/0378-3812(89)80308-5

Chapman, W. G., Gubbins, K. E., Jackson, G., & Radosz, M. (1990). New reference equation of state for associating liquids. *Industrial & Engineering Chemistry Research*, *29*(8), 1709-1721. https://doi.org/10.1021/ie00104a021

Chemspider. (2022). *The free chemical database*

Chen, Y., Han, X., Liu, Z., Yu, D., Guo, W., & Mu, T. (2020). Capture of Toxic Gases by Deep Eutectic Solvents. *ACS Sustainable Chemistry & Engineering*, *8*(14), 5410-5430. https://doi.org/10.1021/acssuschemeng.0c01493

Chen, Y., & Mu, T. (2021). Revisiting greenness of ionic liquids and deep eutectic solvents. *Green Chemical Engineering*. https://doi.org/10.1016/j.gce.2021.01.004

Chung, T. H., Ajlan, M., Lee, L. L., & Starling, K. E. (1988). Generalized multiparameter correlation for nonpolar and polar fluid transport properties. *Industrial & Engineering Chemistry Research*, *27*(4), 671-679. https://doi.org/10.1021/ie00076a024

*Climate Change 2023 Synthesis Report: Summary for Policymakers*. (2024). https://www.ipcc.ch/report/ar6/syr/downloads/report/IPCC_AR6_SYR_SPM.pdf

Codera, V., Clijnk, D., Pou, J. O., Fernandez-Garcia, J., Llovell, F., & Gonzalez-Olmos, R. (2023). Process design for the recovery of waste refrigerants using deep eutectic solvents. *Journal of Environmental Chemical Engineering*, *11*(3), 110255. https://doi.org/10.1016/j.jece.2023.110255

Coutinho, J. A. P., Andersen, S. I., & Stenby, E. H. J. F. P. E. (1995). Evaluation of activity coefficient models in prediction of alkane solid-liquid equilibria. *103*, 23-39. https://doi.org/10.1016/0378-3812(94)02600-6

Crespo, E. A., Silva, L. P., Lloret, J. O., Carvalho, P. J., Vega, L. F., Llovell, F., & Coutinho, J. A. P. (2019). A methodology to parameterize SAFT-type equations of state for solid precursors of deep eutectic solvents: the example of cholinium chloride. *Physical Chemistry Chemical Physics*, *21*(27), 15046-15061. https://doi.org/10.1039/C9CP02548K

Crespo, E. A., Silva, L. P., Martins, M. A. R., Fernandez, L., Ortega, J., Ferreira, O., Sadowski, G., Held, C., Pinho, S. P., & Coutinho, J. A. P. (2017). Characterization and Modeling of the Liquid Phase of Deep Eutectic Solvents Based on Fatty Acids/Alcohols and Choline Chloride. *Industrial & Engineering Chemistry Research*, *56*(42), 12192-12202. https://doi-org.sabidi.urv.cat/10.1021/acs.iecr.7b02382

Cui, Y., Li, C., Yin, J., Li, S., Jia, Y., & Bao, M. (2017). Design, synthesis and properties of acidic deep eutectic solvents based on choline chloride. *Journal of Molecular Liquids*, *236*, 338-343. https://doi.org/10.1016/j.molliq.2017.04.052

D. Clijnk, V. C., J.O. Pou, J. Fernandez-Garcia, R. Gonzalez-Olmos. (2024). Enhancing Circular Economy of Waste Refrigerants Management using Deep Eutectic Solvents. *Sustainable Materials and Technologies*, *39*. Under review

Dai, Y., Verpoorte, R., & Choi, Y. H. (2014). Natural deep eutectic solvents providing enhanced stability of natural colorants from safflower (Carthamus tinctorius). *Food Chemistry*, *159*, 116-121. https://doi.org/10.1016/j.foodchem.2014.02.155

Dai, Y., Witkamp, G.-J., Verpoorte, R., & Choi, Y. H. (2015). Tailoring properties of natural deep eutectic solvents with water to facilitate their applications. *Food Chemistry*, *187*, 14-19. https://doi.org/10.1016/j.foodchem.2015.03.123

de Andrade, D. C., Monteiro, S. A., & Merib, J. (2022). A review on recent applications of deep eutectic solvents in microextraction techniques for the analysis of biological matrices. *Advances in Sample Preparation*, *1*, 100007. https://doi.org/10.1016/j.sampre.2022.100007

Demirbek, M. G., Rodriguez Reartes, S. B., & Llovell, F. (2024). Thermodynamic Analysis of the Absorption of Common Refrigerants in Fluorinated Deep Eutectic Solvents. *Fluid Phase Equilibria*, *581*, 114077. https://doi.org/10.1016/j.fluid.2024.114077

Deng, D., Deng, X., Duan, X., & Gong, L. (2021). Protic guanidine isothiocyanate plus acetamide deep eutectic solvents with low viscosity for efficient NH3 capture and NH3/CO2 separation. *Journal of Molecular Liquids*, *324*, 114719. https://doi.org/10.1016/j.molliq.2020.114719

Deng, X., Duan, X., Gong, L., & Deng, D. (2020). Ammonia Solubility, Density, and Viscosity of Choline Chloride–Dihydric Alcohol Deep Eutectic Solvents. *Journal of Chemical & Engineering Data*, *65*(10), 4845-4854. https://doi.org/10.1021/acs.jced.0c00386

Dias, A. M. A., Carrier, H., Daridon, J. L., Pàmies, J. C., Vega, L. F., Coutinho, J. A. P., & Marrucho, I. M. (2006). Vapor−Liquid Equilibrium of Carbon Dioxide−Perfluoroalkane Mixtures: Experimental Data and SAFT Modeling. *Industrial & Engineering Chemistry Research*, *45*(7), 2341-2350. 10.1021/ie051017z

Dietz, C. H. J. T., Erve, A., Kroon, M. C., van Sint Annaland, M., Gallucci, F., & Held, C. (2019). Thermodynamic properties of hydrophobic deep eutectic solvents and solubility of water and HMF in them: Measurements and PC-SAFT modeling. *Fluid Phase Equilibria*, *489*, 75-82. https://doi.org/10.1016/j.fluid.2019.02.010

Doherty, B., & Acevedo, O. (2018). OPLS Force Field for Choline Chloride-Based Deep Eutectic Solvents. *The Journal of Physical Chemistry B*, *122*(43), 9982-9993. https://doi.org/10.1021/acs.jpcb.8b06647

Doolittle, A. K. (1951). Studies in Newtonian Flow. II. The Dependence of the Viscosity of Liquids on Free-Space. *Journal of Applied Physics*, *22*(12), 1471-1475. https://doi.org/10.1063/1.1699894

Duan, X., Gao, B., Zhang, C., & Deng, D. (2019). Solubility and thermodynamic properties of NH3 in choline chloride-based deep eutectic solvents. *The Journal of Chemical Thermodynamics*, *133*, 79-84. https://doi.org/10.1016/j.jct.2019.01.031

Duan, Y., Zhan, G., Chang, F., Shi, S., Zeng, S., Dong, H., Abildskov, J., Kjøbsted Huusom, J., & Zhang, X. (2022). Process simulation and evaluation for NH3/CO2 separation from melamine tail gas with protic ionic liquids. *Separation and Purification Technology*, *288*, 120680. https://doi.org/10.1016/j.seppur.2022.120680

Dyre, J. C. (2018). Perspective: Excess-entropy scaling. *The Journal of Chemical Physics*, *149*(21). https://doi.org/10.1063/1.5055064

El Achkar, T., Fourmentin, S., & Greige-Gerges, H. (2019). Deep eutectic solvents: An overview on their interactions with water and biochemical compounds. *Journal of Molecular Liquids*, *288*, 111028. https://doi.org/10.1016/j.molliq.2019.111028

Emami, S., & Shayanfar, A. (2020). Deep eutectic solvents for pharmaceutical formulation and drug delivery applications. *Pharm Dev Technol*, *25*(7), 779-796. https://doi.org/10.1080/10837450.2020.1735414

Farooq, M. Q., Abbasi, N. M., & Anderson, J. L. (2020). Deep eutectic solvents in separations: Methods of preparation, polarity, and applications in extractions and capillary electrochromatography. *Journal of Chromatography A*, *1633*, 461613. https://doi.org/10.1016/j.chroma.2020.461613

Fernandez, L., Silva, L. P., Martins, M. A. R., Ferreira, O., Ortega, J., Pinho, S. P., & Coutinho, J. A. P. (2017). Indirect assessment of the fusion properties of choline chloride from solid-liquid equilibria data. *Fluid Phase Equilibria*, *448*, 9-14. https://doi.org/10.1016/j.fluid.2017.03.015

Ferrarini, F., Flôres, G. B., Muniz, A. R., & de Soares, R. P. (2018). An open and extensible sigma-profile database for COSMO-based models [https://doi.org/10.1002/aic.16194]. *AIChE Journal*, *64*(9), 3443-3455. https://doi.org/10.1002/aic.16194

Ferreira, C., & Sarraguça, M. (2024). A Comprehensive Review on Deep Eutectic Solvents and Its Use to Extract Bioactive Compounds of Pharmaceutical Interest. *Pharmaceuticals*, *17*(1), 124. https://doi.org/10.3390/ph17010124

Florindo, C., Branco, L. C., & Marrucho, I. M. (2019). Quest for Green-Solvent Design: From Hydrophilic to Hydrophobic (Deep) Eutectic Solvents. *ChemSusChem*, *12*(8), 1549-1559. https://doi.org/10.1002/cssc.201900147

Florindo, C., Oliveira, F. S., Rebelo, L. P. N., Fernandes, A. M., & Marrucho, I. M. (2014). Insights into the Synthesis and Properties of Deep Eutectic Solvents Based on Cholinium Chloride and Carboxylic Acids. *ACS Sustainable Chemistry & Engineering*, *2*(10), 2416-2425. https://doi.org/10.1021/sc500439w

Florindo, C., Oliveira, M. M., Branco, L. C., & Marrucho, I. M. (2017). Carbohydrates-based deep eutectic solvents: Thermophysical properties and rice straw dissolution. *Journal of Molecular Liquids*, *247*, 441-447. https://doi.org/10.1016/j.molliq.2017.09.026

Fluorinated greenhouse gases. (2019). In *European Commission Climate Action*.

Foresee, F. D., & Hagan, M. T. (1997, 12-12 June 1997). Gauss-Newton approximation to Bayesian learning. Proceedings of International Conference on Neural Networks (ICNN'97),

Fouad, W. A., & Vega, L. F. (2018). Next generation of low global warming potential refrigerants: Thermodynamic properties molecular modeling. *64*(1), 250-262. https://doi.org/10.1002/aic.15859

Francisco, M., van den Bruinhorst, A., & Kroon, M. C. (2013a). Low-transition-temperature mixtures (LTTMs): a new generation of designer solvents. *Angew Chem Int Ed Engl*, *52*(11), 3074-3085. https://doi.org/10.1002/anie.201207548

Francisco, M., van den Bruinhorst, A., Zubeir, L. F., Peters, C. J., & Kroon, M. C. (2013b). A new low transition temperature mixture (LTTM) formed by choline chloride+lactic acid: Characterization as solvent for CO2 capture. *Fluid Phase Equilibria*, *340*, 77-84. https://doi.org/10.1016/j.fluid.2012.12.001

Frenkel, D., & Smit, B. (2002). Chapter 1 - Introduction. In D. Frenkel & B. Smit (Eds.), *Understanding Molecular Simulation (Second Edition)* (pp. 1-6). Academic Press. https://doi.org/10.1016/B978-012267351-1/50003-1

Fu, H., Hou, Y., Sang, H., Mu, T., Lin, X., Peng, Z., Li, P., & Liu, J. (2021). Carbon dioxide capture by new DBU-based DES: The relationship between ionicity and absorptive capacity. *AIChE Journal*, *67*(7), e17244. https://doi.org/10.1002/aic.17244

Gabriele, F., Chiarini, M., Germani, R., Tiecco, M., & Spreti, N. (2019). Effect of water addition on choline chloride/glycol deep eutectic solvents: Characterization of

their structural and physicochemical properties. *Journal of Molecular Liquids*, *291*, 111301. https://doi.org/10.1016/j.molliq.2019.111301

Gajardo-Parra, N. F., Cotroneo-Figueroa, V. P., Aravena, P., Vesovic, V., & Canales, R. I. (2020). Viscosity of Choline Chloride-Based Deep Eutectic Solvents: Experiments and Modeling. *Journal of Chemical & Engineering Data*, *65*(11), 5581-5592. https://doi.org/10.1021/acs.jced.0c00715

Gamsjäger, H., Lorimer, J. W., Scharlin, P., & Shaw, D. G. (2008). Glossary of terms related to solubility (IUPAC Recommendations 2008). *Pure and Applied Chemistry*, *80*(2), 233-276. https://doi.org/10.1351/pac2008800202333

García, G., Aparicio, S., Ullah, R., & Atilhan, M. (2015). Deep Eutectic Solvents: Physicochemical Properties and Gas Separation Applications. *Energy & Fuels*, *29*(4), 2616-2644. https://doi.org/10.1021/ef5028873

García-Argüelles, S., Ferrer, M. L., Iglesias, M., Del Monte, F., & Gutiérrez, M. C. (2017). Study of Superbase-Based Deep Eutectic Solvents as the Catalyst in the Chemical Fixation of CO2 into Cyclic Carbonates under Mild Conditions. *Materials*, *10*(7), 759. https://www.mdpi.com/1996-1944/10/7/759

Gavarić, A., Pastor, K., Nastić, N., Vidović, S., Živanović, N., Simin, N., Duarte, A. R. C., & Vladić, J. (2023). Recovery of Polyphenols from Rosehip Seed Waste Using Natural Deep Eutectic Solvents and Ultrasonic Waves Simultaneously. *Foods*, *12*(19), 3655. https://www.mdpi.com/2304-8158/12/19/3655

George, G., Bhoria, N., AlHallaq, S., Abdala, A., & Mittal, V. (2016). Polymer membranes for acid gas removal from natural gas. *Separation and Purification Technology*, *158*, 333-356. https://doi.org/10.1016/j.seppur.2015.12.033

Gevrey, M., Dimopoulos, I., & Lek, S. (2003). Review and comparison of methods to study the contribution of variables in artificial neural network models. *Ecological Modelling*, *160*(3), 249-264. https://doi.org/10.1016/S0304-3800(02)00257-0

Gil-Villegas, A., Galindo, A., Whitehead, P. J., Mills, S. J., Jackson, G., & Burgess, A. N. (1997). Statistical associating fluid theory for chain molecules with attractive potentials of variable range. *The Journal of Chemical Physics*, *106*(10), 4168-4186. https://doi.org/10.1063/1.473101

Gotor-Fernández, V., & Paul, C. E. (2019). Deep eutectic solvents for redox biocatalysis. *Journal of Biotechnology*, *293*, 24-35. https://doi.org/10.1016/j.jbiotec.2018.12.018

Gramatica, P. (2007). Principles of QSAR models validation: internal and external. *26*(5), 694-701. https://doi.org/10.1002/qsar.200610151

Gramatica, P., Cassani, S., & Sangion, A. (2016). Aquatic ecotoxicity of personal care products: QSAR models and ranking for prioritization and safer alternatives' design [10.1039/C5GC02818C]. *Green Chemistry*, *18*(16), 4393-4406. https://doi.org/10.1039/C5GC02818C

Gross, J., & Sadowski, G. (2001). Perturbed-Chain SAFT: An Equation of State Based on a Perturbation Theory for Chain Molecules. *Industrial & Engineering Chemistry Research*, *40*(4), 1244-1260. https://doi.org/10.1021/ie0003887

Gubbins, K. E., & Twu, C. H. (1978). Thermodynamics of polyatomic fluid mixtures—I theory. *Chemical Engineering Science*, *33*(7), 863-878. https://doi.org/10.1016/0009-2509(78)85176-8

Gui, X., Tang, Z., & Fei, W. (2011). Solubility of CO2 in Alcohols, Glycols, Ethers, and Ketones at High Pressures from (288.15 to 318.15) K. *Journal of Chemical & Engineering Data*, *56*(5), 2420-2429. https://doi.org/10.1021/je101344v

Guo, W., Hou, Y., Ren, S., Tian, S., & Wu, W. (2013). Formation of Deep Eutectic Solvents by Phenols and Choline Chloride and Their Physical Properties. *Journal of Chemical & Engineering Data*, *58*(4), 866-872. https://doi.org/10.1021/je300997v

Haghbakhsh, R., Duarte, A. R. C., & Raeissi, S. (2021a). Viscosity Investigations on the Binary Systems of (1 ChCl:2 Ethylene Glycol) DES and Methanol or Ethanol. *Molecules*, *26*(18).

Haghbakhsh, R., Duarte, A. R. C., & Raeissi, S. (2021b). Viscosity Investigations on the Binary Systems of (1 ChCl:2 Ethylene Glycol) DES and Methanol or Ethanol. *26*(18), 5513. https://doi.org/10.3390/molecules26185513

Haghbakhsh, R., Duarte, A. R. C., & Raeissi, S. (2022). Aqueous mixture viscosities of phenolic deep eutectic solvents. *Fluid Phase Equilibria*, *553*, 113290. https://doi.org/10.1016/j.fluid.2021.113290

Haghbakhsh, R., & Raeissi, S. (2018a). Densities and volumetric properties of (choline chloride + urea) deep eutectic solvent and methanol mixtures in the temperature range of 293.15–323.15 K. *The Journal of Chemical Thermodynamics*, *124*, 10-20. https://doi.org/10.1016/j.jct.2018.04.010

Haghbakhsh, R., & Raeissi, S. (2018b). Investigation of solutions of ethyl alcohol and the deep eutectic solvent of Reline for their volumetric properties. *Fluid Phase Equilibria*, *472*, 39-47. https://doi.org/10.1016/j.fluid.2018.05.008

Haghbakhsh, R., & Raeissi, S. (2020). A study of non-ideal mixtures of ethanol and the (1 choline chloride +2 ethylene glycol) deep eutectic solvent for their volumetric behaviour. *The Journal of Chemical Thermodynamics*, *150*, 106219. https://doi.org/10.1016/j.jct.2020.106219

Haghbakhsh, R., Raeissi, S., & Duarte, A. R. C. (2021c). Group contribution and atomic contribution models for the prediction of various physical properties of deep eutectic solvents. *Scientific Reports*, *11*(1), 6684. https://doi.org/10.1038/s41598-021-85824-z

Hamidian, A. H., Esfandeh, S., Zhang, Y., & Yang, M. (2019). Simulation and optimization of nanomaterials application for heavy metal removal from aqueous solutions. *Inorganic and Nano-Metal Chemistry*, *49*(7), 217-230. https://doi.org/10.1080/24701556.2019.1653321

Hammond, O. S., Bowron, D. T., & Edler, K. J. (2017). The Effect of Water upon Deep Eutectic Solvent Nanostructure: An Unusual Transition from Ionic Mixture to Aqueous Solution. *Angewandte Chemie International Edition*, *56*(33), 9782-9785. https://doi.org/10.1002/anie.201702486

Han, D., & Row, K. H. (2010). Recent Applications of Ionic Liquids in Separation Technology. *Molecules*, *15*(4), 2405-2426. https://doi.org/10.3390/molecules15042405

Hansen, B. B., Spittle, S., Chen, B., Poe, D., Zhang, Y., Klein, J. M., Horton, A., Adhikari, L., Zelovich, T., Doherty, B. W., Gurkan, B., Maginn, E. J., Ragauskas, A., Dadmun, M., Zawodzinski, T. A., Baker, G. A., Tuckerman, M. E., Savinell, R. F., & Sangoro, J. R. (2021). Deep Eutectic Solvents: A Review of Fundamentals and Applications. *Chem Rev*, *121*(3), 1232-1285. https://doi.org/10.1021/acs.chemrev.0c00385

Harifi-Mood, A. R., & Sarafrazi, M. (2023). CO2 solubility in terpenoid-based hydrophobic deep eutectic solvents: An experimental and theoretical study. *Journal of Environmental Chemical Engineering*, *11*(1), 109177. https://doi.org/10.1016/j.jece.2022.109177

Harifi-Mood, A. R., & Sadrzadeh, S. (2018). Dimethyl sulfoxide/deep eutectic solvents mixtures as media in the reaction of 1-fluoro-2,4-dinitrobenzene with piperidine:

A solvent effect study. *Journal of Physical Organic Chemistry*, *31*(4), n/a. https://doi.org/10.1002/poc.3787

Harris, R. C. (2009). *Physical Properties of Alcohol Based Deep Eutectic Solvents* [Ph.d. Thesis University of Leicester]. https://leicester.figshare.com/articles/thesis/Physical_Properties_of_Alcohol_Based_Deep_Eutectic_Solvents_/10087709

Harrison, B. K., & Seaton, W. H. (1988). Solution to missing group problem for estimation of ideal gas heat capacities. *Industrial & Engineering Chemistry Research*, *27*(8), 1536-1540. https://doi.org/10.1021/ie00080a031

Haykin, S. (2009). *Neural Networks and Learning Machines* (Third ed.). Pearson Education.

Held, C., Neuhaus, T., & Sadowski, G. (2010). Compatible solutes: Thermodynamic properties and biological impact of ectoines and prolines. *Biophysical Chemistry*, *152*(1), 28-39. https://doi.org/10.1016/j.bpc.2010.07.003

Hoesung, L. (2023). *IPCC, 2023: Climate Change 2023: Synthesis Report. Contribution of Working Groups I, II and III to the Sixth Assessment Report of the Intergovernmental Panel on Climate Change* https://doi.org/10.59327/IPCC/AR6-9789291691647

Hu, L., Chen, L., Fang, Y., Wang, A., Chen, C., & Yan, Z. (2018). Facile synthesis of zeolitic imidazolate framework-8 (ZIF-8) by forming imidazole-based deep eutectic solvent. *Microporous and Mesoporous Materials*, *268*, 207-215. https://doi.org/10.1016/j.micromeso.2018.04.039

Huang, K., Zhang, X.-M., Xu, Y., Wu, Y.-T., Hu, X.-B., & Xu, Y. (2014). Protic ionic liquids for the selective absorption of H2S from CO2: Thermodynamic analysis. *AIChE Journal*, *60*(12), 4232-4240. https://doi.org/10.1002/aic.14634

Huang, S. H., & Radosz, M. (1990). Equation of state for small, large, polydisperse, and associating molecules. *Industrial & Engineering Chemistry Research*, *29*(11), 2284-2294. https://doi.org/10.1021/ie00107a014

Inventory of U.S. greenhouse gas emissions and sinks: 1990-2018. (2020). In *EPA: United States Environmental Protection Agency*.

IPCC. (2024). *Climate Change 2022: Mitigation of Climate Change* https://www.ipcc.ch/report/ar6/wg3/

Jiang, B., Ma, J., Yang, N., Huang, Z., Zhang, N., Tantai, X., Sun, Y., & Zhang, L. (2019). Superbase/Acylamido-Based Deep Eutectic Solvents for Multiple-Site Efficient

CO2 Absorption. *Energy & Fuels*, *33*(8), 7569-7577. https://doi.org/10.1021/acs.energyfuels.9b01361

Jiang, W.-J., Zhong, F.-Y., Liu, Y., & Huang, K. (2019). Effective and Reversible Capture of NH3 by Ethylamine Hydrochloride Plus Glycerol Deep Eutectic Solvents. *ACS Sustainable Chemistry & Engineering*, *7*(12), 10552-10560. https://doi.org/10.1021/acssuschemeng.9b01102

Jog, P. K., Sauer, S. G., Blaesing, J., & Chapman, W. G. (2001). Application of Dipolar Chain Theory to the Phase Behavior of Polar Fluids and Mixtures. *Industrial & Engineering Chemistry Research*, *40*(21), 4641-4648. https://doi.org/10.1021/ie010264+

Johnson, J., Mueller, E. A., & Gubbins, K. E. (1994). Equation of State for Lennard-Jones Chains. *The Journal of Physical Chemistry*, *98*(25), 6413-6419. https://doi.org/10.1021/j100076a028

Johnson, J. K., Zollweg, J. A., & Gubbins, K. E. (1993). The Lennard-Jones equation of state revisited. *Molecular Physics*, *78*(3), 591-618. https://doi.org/10.1080/00268979300100411

Jovell, D., B. Gómez, S., Zakrzewska, M. E., Nunes, A. V. M., Araújo, J. M. M., Pereiro, A. B., & Llovell, F. (2020). Insight on the Solubility of R134a in Fluorinated Ionic Liquids and Deep Eutectic Solvents. *Journal of Chemical & Engineering Data*, *65*(10), 4956-4969. https://doi.org/10.1021/acs.jced.0c00588

Juneidi, I., Hayyan, M., & Hashim, M. A. (2015). Evaluation of toxicity and biodegradability for cholinium-based deep eutectic solvents [https://doi.org/10.1039/C5RA12425E]. *RSC Advances*, *5*(102), 83636-83647. 10.1039/C5RA12425E

Juneidi, I., Hayyan, M., & Mohd Ali, O. (2016). Toxicity profile of choline chloride-based deep eutectic solvents for fungi and Cyprinus carpio fish. *Environ Sci Pollut Res Int*, *23*(8), 7648-7659. https://doi.org/10.1016/j.foodchem.2015.03.12310.1007/s11356-015-6003-4

Kalman, B. L., & Kwasny, S. C. (1992, 7-11 June 1992). Why tanh: choosing a sigmoidal function. [Proceedings 1992] IJCNN International Joint Conference on Neural Networks,

Khandelwal, M., & Singh, T. N. (2009). Prediction of blast-induced ground vibration using artificial neural network. *International Journal of Rock Mechanics and Mining Sciences*, *46*(7), 1214-1222. https://doi.org/10.1016/j.ijrmms.2009.03.004

Kim, K.-S., & Park, B. H. (2018). Volumetric properties of solutions of choline chloride + glycerol deep eutectic solvent with water, methanol, ethanol, or iso-propanol. *Journal of Molecular Liquids*, *254*, 272-279. https://doi.org/10.1016/j.molliq.2018.01.087

Klamt, A., & Schüürmann, G. (1993). COSMO: a new approach to dielectric screening in solvents with explicit expressions for the screening energy and its gradient [10.1039/P29930000799]. *Journal of the Chemical Society, Perkin Transactions 2*(5), 799-805. https://doi.org/10.1039/P29930000799

Kontogeorgis, G. M., & Folas, G. K. (2010). Activity Coefficient Models Part 2: Local Composition Models, from Wilson and NRTL to UNIQUAC and UNIFAC. In *Thermodynamic Models for Industrial Applications* (pp. 109-157). https://doi.org/10.1002/9780470747537.ch5

Lapeña, D., Lomba, L., Artal, M., Lafuente, C., & Giner, B. (2019). Thermophysical characterization of the deep eutectic solvent choline chloride:ethylene glycol and one of its mixtures with water. *Fluid Phase Equilibria*, *492*, 1-9. https://doi.org/10.1016/j.fluid.2019.03.018

Lawrence, S., Giles, C. L., & Tsoi, A. C. (1997). *Lessons in Neural Network Training: Overfitting May be Harder than Expected* http://www.aaai.org/Library/AAAI/1997/aaai97-084.php

Lei, Z., Dai, C., Zhu, J., & Chen, B. (2014). Extractive distillation with ionic liquids: A review. *AIChE Journal*, *60*(9), 3312-3329. https://doi.org/10.1002/aic.14537

Lemaoui, T., Abu Hatab, F., Darwish, A. S., Attoui, A., Hammoudi, N. E. H., Almustafa, G., Benaicha, M., Benguerba, Y., & Alnashef, I. M. (2021). Molecular-Based Guide to Predict the pH of Eutectic Solvents: Promoting an Efficient Design Approach for New Green Solvents. *ACS Sustainable Chemistry & Engineering*, *9*(17), 5783-5808. https://doi.org/10.1021/acssuschemeng.0c07367

Lemaoui, T., Boublia, A., Darwish, A. S., Alam, M., Park, S., Jeon, B.-H., Banat, F., Benguerba, Y., & AlNashef, I. M. (2022). Predicting the Surface Tension of Deep Eutectic Solvents Using Artificial Neural Networks. *ACS Omega*, *7*(36), 32194-32207. https://doi.org/10.1021/acsomega.2c03458

Lemaoui, T., Darwish, A. S., Almustafa, G., Boublia, A., Sarika, P. R., Jabbar, N. A., Ibrahim, T., Nancarrow, P., Yadav, K. K., Fallatah, A. M., Abbas, M., Algethami, J. S., Benguerba, Y., Jeon, B.-H., Banat, F., & AlNashef, I. M. (2023). Machine learning approach to map the thermal conductivity of over 2,000 neoteric solvents

for green energy storage applications. *Energy Storage Materials*, *59*, 102795. https://doi.org/10.1016/j.ensm.2023.102795

Lemaoui, T., Darwish, A. S., Hammoudi, N. E. H., Abu Hatab, F., Attoui, A., Alnashef, I. M., & Benguerba, Y. (2020a). Prediction of Electrical Conductivity of Deep Eutectic Solvents Using COSMO-RS Sigma Profiles as Molecular Descriptors: A Quantitative Structure–Property Relationship Study. *Industrial & Engineering Chemistry Research*, *59*(29), 13343-13354. https://doi.org/10.1021/acs.iecr.0c02542

Lemaoui, T., Hammoudi, N. E. H., Alnashef, I. M., Balsamo, M., Erto, A., Ernst, B., & Benguerba, Y. (2020b). Quantitative structure properties relationship for deep eutectic solvents using Sσ-profile as molecular descriptors. *Journal of Molecular Liquids*, *309*, 113165. https://doi.org/10.1016/j.molliq.2020.113165

Lepre, L. F., Andre, D., Denis-Quanquin, S., Gautier, A., Pádua, A. A. H., & Costa Gomes, M. (2019a). Ionic Liquids Can Enable the Recycling of Fluorinated Greenhouse Gases. *ACS Sustainable Chemistry & Engineering*, *7*(19), 16900-16906. https://doi.org/10.1021/acssuschemeng.9b04214

Lepre, L. F., Pison, L., Otero, I., Gautier, A., Dévemy, J., Husson, P., Pádua, A. A. H., & Costa Gomes, M. (2019b). Using hydrogenated and perfluorinated gases to probe the interactions and structure of fluorinated ionic liquids [10.1039/C9CP00593E]. *Physical Chemistry Chemical Physics*, *21*(17), 8865-8873. https://doi.org/10.1039/C9CP00593E

Leron, R. B., & Li, M.-H. (2013a). Solubility of carbon dioxide in a choline chloride–ethylene glycol based deep eutectic solvent. *Thermochimica Acta*, *551*, 14-19. https://doi.org/10.1016/j.tca.2012.09.041

Leron, R. B., & Li, M.-H. (2013b). Solubility of carbon dioxide in a eutectic mixture of choline chloride and glycerol at moderate pressures. *The Journal of Chemical Thermodynamics*, *57*, 131-136. https://doi.org/10.1016/j.jct.2012.08.025

Li, J.-E., Chien, S.-C., & Hsieh, C.-M. (2024). Modeling solid solute solubility in supercritical carbon dioxide by machine learning algorithms using molecular sigma profiles. *Journal of Molecular Liquids*, *395*, 123884. https://doi.org/10.1016/j.molliq.2023.123884

Li, K., Zong, K., Zhou, Z., & Deng, D. (2021). Highly efficient absorption and separation of NH3 by simple lithium deep eutectic solvents. *Separation and Purification Technology*, *279*, 119763. https://doi.org/10.1016/j.seppur.2021.119763

Li, M., Zhu, C., Fu, T., Gao, X., & Ma, Y. (2022). Effect of water on amine-based deep eutectic solvents (choline chloride + monoethanolamine): Structure and physicochemical properties. *Journal of Environmental Chemical Engineering*, *10*(1), 106952. https://doi.org/10.1016/j.jece.2021.106952

Li, N., Wang, Y., Xu, K., Huang, Y., Wen, Q., & Ding, X. (2016). Development of green betaine-based deep eutectic solvent aqueous two-phase system for the extraction of protein. *Talanta*, *152*, 23-32. https://doi.org/10.1016/j.talanta.2016.01.042

Li, X., Hou, M., Han, B., Wang, X., & Zou, L. (2008). Solubility of CO2 in a Choline Chloride + Urea Eutectic Mixture. *Journal of Chemical & Engineering Data*, *53*(2), 548-550. https://doi.org/10.1021/je700638u

Li, Z., Wang, L., Li, C., Cui, Y., Li, S., Yang, G., & Shen, Y. (2019). Absorption of Carbon Dioxide Using Ethanolamine-Based Deep Eutectic Solvents. *ACS Sustainable Chemistry & Engineering*, *7*(12), 10403-10414. https://doi.org/10.1021/acssuschemeng.9b00555

Li, Z.-L., Zhong, F.-Y., Huang, J.-Y., Peng, H.-L., & Huang, K. (2020). Sugar-based natural deep eutectic solvents as potential absorbents for NH3 capture at elevated temperatures and reduced pressures. *Journal of Molecular Liquids*, *317*, 113992. https://doi.org/10.1016/j.molliq.2020.113992

Liao, X., Chen, C., Shi, P., & Yue, L. (2021). Determination of melamine in milk based on β-cyclodextrin modified carbon nanoparticles via host-guest recognition. *Food Chem*, *338*, 127769. https://doi.org/10.1016/j.foodchem.2020.127769

Lin, S.-T., & Sandler, S. I. (2002). A Priori Phase Equilibrium Prediction from a Segment Contribution Solvation Model. *Industrial & Engineering Chemistry Research*, *41*(5), 899-913. https://doi.org/10.1021/ie001047w

Liu, X., Chen, Y., Zeng, S., Zhang, X., Liang, X., Gani, R., & Kontogeorgis, G. M. (2021). Separation of NH3/CO2 from melamine tail gas with ionic liquid: Process evaluation and thermodynamic properties modelling. *Separation and Purification Technology*, *274*, 119007. https://doi.org/10.1016/j.seppur.2021.119007

Liu, X., Gao, B., Jiang, Y., Ai, N., & Deng, D. (2017). Solubilities and Thermodynamic Properties of Carbon Dioxide in Guaiacol-Based Deep Eutectic Solvents. *Journal of Chemical & Engineering Data*, *62*(4), 1448-1455. https://doi.org/10.1021/acs.jced.6b01013

Liu, X., Yu, M., Jia, Q., Yan, F., Zhou, Y.-N., & Wang, Q. (2023). Leave-one-ion-out cross-validation for assisting in developing robust QSPR models of ionic liquids.

*Journal of Molecular Liquids*, *388*, 122711. https://doi.org/10.1016/j.molliq.2023.122711

Lloret, J. O., Vega, L. F., & Llovell, F. (2017). Accurate description of thermophysical properties of Tetraalkylammonium Chloride Deep Eutectic Solvents with the soft-SAFT equation of state. *Fluid Phase Equilibria*, *448*, 81-93. https://doi.org/10.1016/j.fluid.2017.04.013

Llovell, F., Marcos, R. M., MacDowell, N., & Vega, L. F. (2012). Modeling the Absorption of Weak Electrolytes and Acid Gases with Ionic Liquids Using the Soft-SAFT Approach. *The Journal of Physical Chemistry B*, *116*(26), 7709-7718. https://doi.org/10.1021/jp303344f

Llovell, F., Marcos, R. M., & Vega, L. F. (2013a). Free-Volume Theory Coupled with Soft-SAFT for Viscosity Calculations: Comparison with Molecular Simulation and Experimental Data. *The journal of physical chemistry. B*, *117*. https://doi.org/10.1021/jp401307t

Llovell, F., Marcos, R. M., & Vega, L. F. (2013b). Transport properties of mixtures by the soft-SAFT + free-volume theory: application to mixtures of n-alkanes and hydrofluorocarbons. *J Phys Chem B*, *117*(17), 5195-5205. https://doi.org/10.1021/jp401754r

Llovell, F., Marcos, R. M., & Vega, L. F. (2013c). Transport Properties of Mixtures by the Soft-SAFT + Free-Volume Theory: Application to Mixtures of n-Alkanes and Hydrofluorocarbons. *The Journal of Physical Chemistry B*, *117*(17), 5195-5205. https://doi.org/10.1021/jp401754r

Llovell, F., Oliveira, M. B., Coutinho, J. A. P., & Vega, L. F. (2015). Solubility of greenhouse and acid gases on the [C4mim][MeSO4] ionic liquid for gas separation and CO2 conversion. *Catalysis Today*, *255*, 87-96. https://doi.org/10.1016/j.cattod.2014.12.049

Llovell, F., & Vega, L. F. (2014). Assessing Ionic Liquids Experimental Data Using Molecular Modeling: [Cnmim][BF4] Case Study. *Journal of Chemical & Engineering Data*, *59*(10), 3220-3231. https://doi.org/10.1021/je5002472

Llovell, F., Vilaseca, O., Jung, N., & Vega, L. F. (2013d). Water+1-alkanol systems: Modeling the phase, interface and viscosity properties. *Fluid Phase Equilibria*, *360*, 367-378. https://doi.org/10.1016/j.fluid.2013.10.002

Luckas, M., Lucas, K., Deiters, U., & Gubbins, K. E. (1986). Integrals over pair- and triplet-correlation functions for the Lennard-Jones (12–6)-fluid. *Molecular Physics*, *57*(2), 241-253. https://doi.org/10.1080/00268978600100191

Lymperiadis, A., Adjiman, C. S., Galindo, A., & Jackson, G. (2007). A group contribution method for associating chain molecules based on the statistical associating fluid theory (SAFT-γ). *The Journal of Chemical Physics*, *127*(23), 234903. https://doi.org/10.1063/1.2813894

Ma, C., Laaksonen, A., Liu, C., Lu, X., & Ji, X. (2018). The peculiar effect of water on ionic liquids and deep eutectic solvents. *Chem Soc Rev*, *47*(23), 8685-8720. https://doi.org/10.1039/c8cs00325d

Ma, C., Liu, C., Lu, X., & Ji, X. (2018). Techno-economic analysis and performance comparison of aqueous deep eutectic solvent and other physical absorbents for biogas upgrading. *Applied Energy*, *225*, 437-447. https://doi.org/10.1016/j.apenergy.2018.04.112

Ma, Y., Zhang, J., Huang, K., & Jiang, L. (2021). Highly efficient and selective separation of ammonia by deep eutectic solvents through cooperative acid-base and strong hydrogen-bond interaction. *Journal of Molecular Liquids*, *337*, 116463. https://doi.org/10.1016/j.molliq.2021.116463

Makhloufi, C., Roizard, D., & Favre, E. (2013). Reverse selective NH3/CO2 permeation in fluorinated polymers using membrane gas separation. *Journal of Membrane Science*, *441*, 63-72. https://doi.org/10.1016/j.memsci.2013.03.048

Marchel, M., Cieśliński, H., & Boczkaj, G. (2022). Thermal Instability of Choline Chloride-Based Deep Eutectic Solvents and Its Influence on Their Toxicity─Important Limitations of DESs as Sustainable Materials. *Industrial & Engineering Chemistry Research*, *61*(30), 11288-11300. https://doi.org/10.1021/acs.iecr.2c01898

Marcus, Y. (2018). Gas solubilities in deep eutectic solvents. *Monatshefte für Chemie - Chemical Monthly*, *149*(2), 211-217. https://doi.org/10.1007/s00706-017-2031-8

Martins, M. A. R., Pinho, S. P., & Coutinho, J. A. P. (2019). Insights into the Nature of Eutectic and Deep Eutectic Mixtures. *Journal of Solution Chemistry*, *48*(7), 962-982. https://doi.org/10.1007/s10953-018-0793-1

Matsukawa, H., Kitahara, M., & Otake, K. (2021). Estimation of pure component parameters of PC-SAFT EoS by an artificial neural network based on a group

contribution method. *Fluid Phase Equilibria*, *548*, 113179. https://doi.org/10.1016/j.fluid.2021.113179

Mbous, Y. P., Hayyan, M., Hayyan, A., Wong, W. F., Hashim, M. A., & Looi, C. Y. (2017). Applications of deep eutectic solvents in biotechnology and bioengineering—Promises and challenges. *Biotechnology Advances*, *35*(2), 105-134. https://doi.org/10.1016/j.biotechadv.2016.11.006

Mejía, A., Müller, E. A., & Chaparro Maldonado, G. (2021). SGTPy: A Python Code for Calculating the Interfacial Properties of Fluids Based on the Square Gradient Theory Using the SAFT-VR Mie Equation of State. *Journal of Chemical Information and Modeling*, *61*(3), 1244-1250. https://doi.org/10.1021/acs.jcim.0c01324

Mirza, N. R., Nicholas, N. J., Wu, Y., Kentish, S., & Stevens, G. W. (2015). Estimation of Normal Boiling Temperatures, Critical Properties, and Acentric Factors of Deep Eutectic Solvents. *Journal of Chemical & Engineering Data*, *60*(6), 1844-1854. https://doi.org/10.1021/acs.jced.5b00046

Mjalli, F. S., & Naser, J. (2015). Viscosity model for choline chloride-based deep eutectic solvents [https://doi.org/10.1002/apj.1873]. *Asia-Pacific Journal of Chemical Engineering*, *10*(2), 273-281. https://doi.org/10.1002/apj.1873

Moghimi, M., & Roosta, A. (2019). Physical properties of aqueous mixtures of (choline chloride + glucose) deep eutectic solvents. *The Journal of Chemical Thermodynamics*, *129*, 159-165. https://doi.org/10.1016/j.jct.2018.09.029

Morrison, G., & McLinden, M. O. (1993). Azeotropy in refrigerant mixtures: Azéotropie dans les mélanges de frigorigènes. *International Journal of Refrigeration*, *16*(2), 129-138. https://doi.org/10.1016/0140-7007(93)90069-K

NASA. (2024). *Vital signs of the global temperature*. Retrieved July 1 from https://climate.nasa.gov/vital-signs/global-temperature/?intent=111

Ndegwa, P. M., Hristov, A. N., Arogo, J., & Sheffield, R. E. (2008). A review of ammonia emission mitigation techniques for concentrated animal feeding operations. *Biosystems Engineering*, *100*(4), 453-469. https://doi.org/10.1016/j.biosystemseng.2008.05.010

Neufeld, P. D., Janzen, A. R., & Aziz, R. A. (1972). Empirical Equations to Calculate 16 of the Transport Collision Integrals Ω(l, s)* for the Lennard-Jones (12–6) Potential. *The Journal of Chemical Physics*, *57*(3), 1100-1102. 10.1063/1.1678363

NIST. *Chemistry Webbook* (https://webbook.nist.gov/chemistry/

*The NOAA Annual Grenhouse Gas Index (AGGI)*. Retrieved Mar. 05 from https://gml.noaa.gov/aggi/aggi.html

Ojeda, R. M., & Llovell, F. (2018). Soft-SAFT Transferable Molecular Models for the Description of Gas Solubility in Eutectic Ammonium Salt-Based Solvents. *Journal of Chemical & Engineering Data*, *63*(7), 2599-2612. https://doi.org/10.1021/acs.jced.7b01103

Oke, E. A. (2024). Sustainable advancements in hazardous gases capture: Harnessing the potential of deep eutectic solvents. *Sustainable Chemistry for the Environment*, *6*, 100083. https://doi.org/10.1016/j.scenv.2024.100083

Oliveira, M. B., Crespo, E. A., Llovell, F., Vega, L. F., & Coutinho, J. A. P. (2016). Modeling the vapor–liquid equilibria and water activity coefficients of alternative refrigerant-absorbent ionic liquid–water pairs for absorption systems. *Fluid Phase Equilibria*, *426*, 100-109. https://doi.org/10.1016/j.fluid.2016.02.017

Paiva, A., Craveiro, R., Aroso, I., Martins, M., Reis, R. L., & Duarte, A. R. C. (2014). Natural Deep Eutectic Solvents – Solvents for the 21st Century. *ACS Sustainable Chemistry & Engineering*, *2*(5), 1063-1071. https://doi.org/10.1021/sc500096j

Palomar, J., Torrecilla, J. S., Lemus, J., Ferro, V. R., & Rodríguez, F. (2010). A COSMO-RS based guide to analyze/quantify the polarity of ionic liquids and their mixtures with organic cosolvents [10.1039/B920651P]. *Physical Chemistry Chemical Physics*, *12*(8), 1991-2000. https://doi.org/10.1039/B920651P

Pàmies, J. C. (2003). *Bulk and Interfacial properties of chain fluids: a molecular modelling approach* [Ph.D. Thesis, Universitat Rovira i Virgili]. Spain.

Panigrahi, B. K., Hoda, M. N., Sharma, V., & Goel, S. (2018). *Nature Inspired Computing*. https://doi.org/10.1007/978-981-10-6747-1

Papaioannou, V., Lafitte, T., Avendaño, C., Adjiman, C. S., Jackson, G., Müller, E. A., & Galindo, A. (2014). Group contribution methodology based on the statistical associating fluid theory for heteronuclear molecules formed from Mie segments. *The Journal of Chemical Physics*, *140*(5). https://doi.org/10.1063/1.4851455

Pavlić, B., Mrkonjić, Ž., Teslić, N., Kljakić, A. C., Pojić, M., Mandić, A., Stupar, A., Santos, F., Duarte, A. R. C., & Mišan, A. (2022). Natural Deep Eutectic Solvent (NADES) Extraction Improves Polyphenol Yield and Antioxidant Activity of Wild Thyme (Thymus serpyllum L.) Extracts. *Molecules*, *27*(5), 1508. https://doi.org/10.3390/molecules27051508

Pedrosa, N., Pàmies, J. C., Coutinho, J. A. P., Marrucho, I. M., & Vega, L. F. (2005). Phase Equilibria of Ethylene Glycol Oligomers and Their Mixtures. *Industrial & Engineering Chemistry Research*, *44*(17), 7027-7037. https://doi.org/10.1021/ie050361t

Peng, D.-Y., & Robinson, D. B. (1976). A New Two-Constant Equation of State. *Industrial & Engineering Chemistry Fundamentals*, *15*(1), 59-64. https://doi.org/10.1021/i160057a011

Peng, Y., Goff, K. D., dos Ramos, M. C., & McCabe, C. (2009). Developing a predictive group-contribution-based SAFT-VR equation of state. *Fluid Phase Equilibria*, *277*(2), 131-144. https://doi.org/10.1016/j.fluid.2008.11.008

Peng, Y., Lu, X., Liu, B., & Zhu, J. (2017). Separation of azeotropic mixtures (ethanol and water) enhanced by deep eutectic solvents. *Fluid Phase Equilibria*, *448*, 128-134. https://doi.org/10.1016/j.fluid.2017.03.010

Pereira, P. F., & Andrade, C. T. (2017). Optimized pH-responsive film based on a eutectic mixture-plasticized chitosan. *Carbohydrate Polymers*, *165*, 238-246. https://doi.org/10.1016/j.carbpol.2017.02.047

Pereiro, A. B., Llovell, F., Araújo, J. M. M., Santos, A. S. S., Rebelo, L. P. N., Piñeiro, M. M., & Vega, L. F. (2017). Thermophysical Characterization of Ionic Liquids Based on the Perfluorobutanesulfonate Anion: Experimental and Soft-SAFT Modeling Results. *18*(15), 2012-2023. https://doi.org/10.1002/cphc.201700327

Pfohl, O., & Brunner, G. (1998). 2. Use of BACK To Modify SAFT in Order To Enable Density and Phase Equilibrium Calculations Connected to Gas-Extraction Processes. *Industrial & Engineering Chemistry Research*, *37*(8), 2966-2976. https://doi.org/10.1021/ie9705259

Prabhune, A., & Dey, R. (2023). Green and sustainable solvents of the future: Deep eutectic solvents. *Journal of Molecular Liquids*, *379*, 121676. https://doi.org/10.1016/j.molliq.2023.121676

Qin, R., Wang, Z., Wei, C., Zhou, F., Tian, Y., Chen, Y., & Mu, T. (2024). Quantification of alkalinity of deep eutectic solvents based on (H−) and NMR. *Physical Chemistry Chemical Physics*, *26*(8), 7042-7048. https://doi.org/10.1039/D3CP05590F

Quiñones-Cisneros, S. E., Zéberg-Mikkelsen, C. K., & Stenby, E. H. (2000). The friction theory (f-theory) for viscosity modeling. *Fluid Phase Equilibria*, *169*(2), 249-276. https://doi.org/10.1016/S0378-3812(00)00310-1

Radošević, K., Cvjetko Bubalo, M., Gaurina Srček, V., Grgas, D., Landeka Dragičević, T., & Radojčić Redovniković, I. (2015). Evaluation of toxicity and biodegradability of choline chloride based deep eutectic solvents. *Ecotoxicology and Environmental Safety*, *112*, 46-53. https://doi.org/10.1016/j.ecoenv.2014.09.034

Renon, H., & Prausnitz, J. M. (1968). Local compositions in thermodynamic excess functions for liquid mixtures. *AIChE Journal*, *14*(1), 135-144. https://doi.org/10.1002/aic.690140124

Reyes-Téllez, E. D., Parrales, A., Ramírez-Ramos, G. E., Hernández, J. A., Urquiza, G., Heredia, M. I., & Sierra, F. Z. (2020). Analysis of transfer functions and normalizations in an ANN model that predicts the transport of energy in a parabolic trough solar collector. *Desalination and Water Treatment*, *200*, 23-41. https://doi.org/10.5004/dwt.2020.26063

Rodriguez, N. R., Ferre Guell, J., & Kroon, M. C. (2016). Glycerol-Based Deep Eutectic Solvents as Extractants for the Separation of MEK and Ethanol via Liquid–Liquid Extraction. *Journal of Chemical & Engineering Data*, *61*(2), 865-872. https://doi.org/10.1021/acs.jced.5b00717

Rodríguez, N. R., González, A. S. B., Tijssen, P. M. A., & Kroon, M. C. (2015). Low transition temperature mixtures (LTTMs) as novel entrainers in extractive distillation. *Fluid Phase Equilibria*, *385*, 72-78. https://doi.org/10.1016/j.fluid.2014.10.044

Roosta, A., Haghbakhsh, R., Rita C. Duarte, A., & Raeissi, S. (2023). Deep eutectic solvent viscosity prediction by hybrid machine learning and group contribution. *Journal of Molecular Liquids*, *388*, 122747. https://doi.org/10.1016/j.molliq.2023.122747

Rosenfeld, Y. (1977). Relation between the transport coefficients and the internal entropy of simple systems. *Physical Review A*, *15*(6), 2545-2549. https://doi.org/10.1103/PhysRevA.15.2545

Rowlinson, J. S. (1970). Molecular thermodynamics of fluid-phase equilibria: Prausnitz, J. M. Prentice-Hall: Englewood Cliffs, New Jersey. 1969. xi v + 523 pp Price: £7 5s. 0d. *The Journal of Chemical Thermodynamics*, *2*(1), 158-159. https://doi.org/10.1016/0021-9614(70)90078-9

Salehi, H. S., Ramdin, M., Moultos, O. A., & Vlugt, T. J. H. (2019). Computing solubility parameters of deep eutectic solvents from Molecular Dynamics simulations. *Fluid Phase Equilibria*, *497*, 10-18. https://doi.org/10.1016/j.fluid.2019.05.022

Sander, R., Acree, W. E., Visscher, A. D., Schwartz, S. E., & Wallington, T. J. (2022). Henry's law constants (IUPAC Recommendations 2021). *94*(1), 71-85. https://doi.org/doi:10.1515/pac-2020-0302

Santana-Mayor, Á., Rodríguez-Ramos, R., Herrera-Herrera, A. V., Socas-Rodríguez, B., & Rodríguez-Delgado, M. Á. (2021). Deep eutectic solvents. The new generation of green solvents in analytical chemistry. *TrAC Trends in Analytical Chemistry*, *134*, 116108. https://doi.org/10.1016/j.trac.2020.116108

Sarmad, S., Mikkola, J.-P., & Ji, X. (2017). Carbon Dioxide Capture with Ionic Liquids and Deep Eutectic Solvents: A New Generation of Sorbents [https://doi.org/10.1002/cssc.201600987]. *ChemSusChem*, *10*(2), 324-352. https://doi.org/10.1002/cssc.201600987

Sarmento, C., Duarte, A. R. C., & Rita Jesus, A. (2024). Can (Natural) deep eutectic systems increase the efficacy of ocular therapeutics? *European Journal of Pharmaceutics and Biopharmaceutics*, *198*, 114276. https://doi.org/10.1016/j.ejpb.2024.114276

Shah, D., & Mjalli, F. S. (2014). Effect of water on the thermo-physical properties of Reline: An experimental and molecular simulation based approach. *Phys Chem Chem Phys*, *16*(43), 23900-23907. https://doi.org/10.1039/c4cp02600d

Shahbaz, K., Baroutian, S., Mjalli, F. S., Hashim, M. A., & AlNashef, I. M. (2012). Densities of ammonium and phosphonium based deep eutectic solvents: Prediction using artificial intelligence and group contribution techniques. *Thermochimica Acta*, *527*, 59-66. https://doi.org/10.1016/j.tca.2011.10.010

Shao, P., Xiong, W., Chen, P., Liu, F., Chen, T., & Zhao, T. (2024). Halogen-free deep eutectic solvents with multiple active sites for efficient absorption of ammonia. *Separation and Purification Technology*, *330*, 125390. https://doi.org/10.1016/j.seppur.2023.125390

Sharma, B., Singh, N., Jain, T., Kushwaha, J. P., & Singh, P. (2018). Acetonitrile Dehydration via Extractive Distillation Using Low Transition Temperature Mixtures as Entrainers. *Journal of Chemical & Engineering Data*, *63*(8), 2921-2930. https://doi.org/10.1021/acs.jced.8b00228

Sharma, B., Singh, N., & Kushwaha, J. P. (2020). Natural Deep Eutectic Solvent-Mediated Extractive Distillation for Separation of Acetonitrile + Water Azeotropic Mixture. *Journal of Chemical & Engineering Data*, *65*(4), 1497-1505. https://doi.org/10.1021/acs.jced.9b00932

Sheldon, D. J., & Crimmin, M. R. (2022). Repurposing of F-gases: challenges and opportunities in fluorine chemistry [10.1039/D1CS01072G]. *Chemical Society Reviews*, *51*(12), 4977-4995. https://doi.org/10.1039/D1CS01072G

Shiflett, M. B., & Yokozeki, A. (2008). Binary Vapor–Liquid and Vapor–Liquid–Liquid Equilibria of Hydrofluorocarbons (HFC-125 and HFC-143a) and Hydrofluoroethers (HFE-125 and HFE-143a) with Ionic Liquid [emim][Tf2N]. *Journal of Chemical & Engineering Data*, *53*(2), 492-497. https://doi.org/10.1021/je700588d

Smith, E. L., Abbott, A. P., & Ryder, K. S. (2014). Deep Eutectic Solvents (DESs) and Their Applications. *Chemical Reviews*, *114*(21), 11060-11082. https://doi.org/10.1021/cr300162p

Soares, R. P., Flores, G. B., Xavier, V. B., Pelisser, E. N., Ferrarini, F., & Staudt, P. B. (2017). lvpp/sigma: LVPP sigma-profile database (18.07). *Zenodo*. https://doi.org/10.5281/zenodo.3613786

Sosa, A., Ortega, J., Fernández, L., & Palomar, J. (2020). Development of a method to model the mixing energy of solutions using COSMO molecular descriptors linked with a semi-empirical model using a combined ANN-QSPR methodology. *Chemical Engineering Science*, *224*, 115764. https://doi.org/10.1016/j.ces.2020.115764

Sovacool, B. K., Griffiths, S., Kim, J., & Bazilian, M. (2021). Climate change and industrial F-gases: A critical and systematic review of developments, sociotechnical systems and policy options for reducing synthetic greenhouse gas emissions. *Renewable and Sustainable Energy Reviews*, *141*, 110759. https://doi.org/10.1016/j.rser.2021.110759

Stell, G., Rasaiah, J. C., & Narang, H. (1972). Thermodynamic perturbation theory for simple polar fluids, I. *Molecular Physics*, *23*(2), 393-406. https://doi.org/10.1080/00268977200100381

Tavares Duarte de Alencar, L. V. G.-B., Bastían; Rodríguez Reartes, Sabrina Belén; Quinteros-Lama, Héctor; Garrido, José Matías; Codera, Victoria; Pou, Josep Oriol; Tavares, Frederico; Gonzalez-Olmos, Rafael; Llovell, Fèlix. (2024).

Thermophysical Characterization of Sustainable Pathways for F-Gas Separation Utilizing Deep Eutectic Solvents. *ACS Sustainable Chemistry & Engineering*. . Under Review

Tomé, L. I. N., Baião, V., da Silva, W., & Brett, C. M. A. (2018). Deep eutectic solvents for the production and application of new materials. *Applied Materials Today*, *10*, 30-50. https://doi.org/10.1016/j.apmt.2017.11.005

Torrecilla, J. S., Palomar, J., Lemus, J., & Rodríguez, F. (2010). A quantum-chemical-based guide to analyze/quantify the cytotoxicity of ionic liquids [10.1039/B919806G]. *Green Chemistry*, *12*(1), 123-134. https://doi.org/10.1039/B919806G

Tropsha, A., Gramatica, P., & Gombar, V. K. (2003). The Importance of Being Earnest: Validation is the Absolute Essential for Successful Application and Interpretation of QSPR Models. *22*(1), 69-77. https://doi.org/10.1002/qsar.200390007

Twu, C. H., & Gubbins, K. E. (1978). Thermodynamics of polyatomic fluid mixtures—II: Polar, quadrupolar and octopolar molecules. *Chemical Engineering Science*, *33*(7), 879-887. https://doi.org/10.1016/0009-2509(78)85177-X

Valente, S., Oliveira, F., Ferreira, I. J., Paiva, A., Sobral, R. G., Diniz, M. S., Gaudêncio, S. P., & Duarte, A. R. C. (2023). Hydrophobic DES Based on Menthol and Natural Organic Acids for Use in Antifouling Marine Coatings. *ACS Sustainable Chemistry & Engineering*, *11*(27), 9989-10000. https://doi.org/10.1021/acssuschemeng.3c01120

Vega, L. F., & Llovell, F. (2016). Review and new insights into the application of molecular-based equations of state to water and aqueous solutions. *Fluid Phase Equilibria*, *416*, 150-173. https://doi.org/10.1016/j.fluid.2016.01.024

Vega, L. F., Llovell, F., & Blas, F. J. (2009). Capturing the Solubility Minima of n-Alkanes in Water by Soft-SAFT. *The Journal of Physical Chemistry B*, *113*(21), 7621-7630. https://doi.org/10.1021/jp9018876

Vega, L. F., Vilaseca, O., Llovell, F., & Andreu, J. S. (2010). Modeling ionic liquids and the solubility of gases in them: Recent advances and perspectives. *Fluid Phase Equilibria*, *294*(1), 15-30. https://doi.org/10.1016/j.fluid.2010.02.006

Velders, G. J. M., Daniel, J. S., Montzka, S. A., Vimont, I., Rigby, M., Krummel, P. B., Muhle, J., O'Doherty, S., Prinn, R. G., Weiss, R. F., & Young, D. (2022). Projections of hydrofluorocarbon (HFC) emissions and the resulting global warming based on recent trends in observed abundances and current policies.

*Atmos. Chem. Phys.*, *22*(9), 6087-6101. https://doi.org/10.5194/acp-22-6087-2022

Velez, C., & Acevedo, O. (2022). Simulation of deep eutectic solvents: Progress to promises. *WIREs Computational Molecular Science*, *12*(4), e1598. https://doi.org/10.1002/wcms.1598

Vilaseca, O., Llovell, F., Yustos, J., Marcos, R. M., & Vega, L. F. (2010). Phase equilibria, surface tensions and heat capacities of hydrofluorocarbons and their mixtures including the critical region. *The Journal of Supercritical Fluids*, *55*(2), 755-768. https://doi.org/10.1016/j.supflu.2010.10.015

Vilková, M., Płotka-Wasylka, J., & Andruch, V. (2020). The role of water in deep eutectic solvent-base extraction. *Journal of Molecular Liquids*, *304*, 112747. https://doi.org/10.1016/j.molliq.2020.112747

Vladić, J., Jakovljević Kovač, M., Pavić, V., Jokić, S., Simić, S., Paiva, A., Jerković, I., & Duarte, A. R. (2023a). Towards a Greener Approach for Biomass Valorization: Integration of Supercritical Fluid and Deep Eutectic Solvents. *Antibiotics*, *12*(6), 1031. https://doi.org/10.3390/antibiotics12061031

Vladić, J., Kovačević, S., Aladić, K., Jokić, S., Radman, S., Podunavac-Kuzmanović, S., Duarte, A. R. C., & Jerković, I. (2023b). Innovative Strategy for Aroma Stabilization Using Green Solvents: Supercritical CO2 Extracts of Satureja montana Dispersed in Deep Eutectic Solvents. *Biomolecules*, *13*(7), 1126. https://doi.org/10.3390/biom13071126

Vladić, J., Kovačević, S., Aladić, K., Rebocho, S., Jokić, S., Podunavac-Kuzmanović, S., Duarte, A. R. C., & Jerković, I. (2024). Novel Insights Into the Recovery and Stabilization of Rosmarinus officinalis Volatile Aroma Compounds Using Green Solvents. *Food and Bioprocess Technology*, *17*(5), 1215-1230. https://doi.org/10.1007/s11947-023-03188-w

Vladić, J., Kovačević, S., Rebocho, S., Paiva, A., Jokić, S., Duarte, A. R., & Jerković, I. (2023c). A new green approach for Lavandula stoechas aroma recovery and stabilization coupling supercritical CO2 and natural deep eutectic solvents. *Scientific Reports*, *13*(1), 12443. https://doi.org/10.1038/s41598-023-39516-5

Wagle, D. V., Adhikari, L., & Baker, G. A. (2017). Computational perspectives on structure, dynamics, gas sorption, and bio-interactions in deep eutectic solvents. *Fluid Phase Equilibria*, *448*, 50-58. https://doi.org/10.1016/j.fluid.2017.04.018

Wang, J., Song, Z., Chen, L., Xu, T., Deng, L., & Qi, Z. (2021). Prediction of CO2 solubility in deep eutectic solvents using random forest model based on COSMO-RS-derived descriptors. *Green Chemical Engineering*, *2*(4), 431-440. https://doi.org/10.1016/j.gce.2021.08.002

Wang, J., Zhang, S., Ma, Z., & Yan, L. (2021). Deep eutectic solvents eutectogels: progress and challenges. *Green Chemical Engineering*, *2*(4), 359-367. https://doi.org/10.1016/j.gce.2021.06.001

Wang, Q., Wen, H., Wang, Y., Li, Z., Hao, J., Wei, L., Zhai, S., Xiao, Z., & An, Q. (2024). Pyridine derivatives as hydrogen bond acceptors to prepare deep eutectic solvents for ammonia storage. *International Journal of Hydrogen Energy*, *50*, 1489-1501. https://doi.org/10.1016/j.ijhydene.2023.10.017

Wang, Y., Ma, C., Liu, C., Lu, X., Feng, X., & Ji, X. (2020). Thermodynamic Study of Choline Chloride-Based Deep Eutectic Solvents with Water and Methanol. *Journal of Chemical & Engineering Data*, *65*(5), 2446-2457. https://doi.org/10.1021/acs.jced.9b01113

Warrag, S. E. E., Peters, C. J., & Kroon, M. C. (2017). Deep eutectic solvents for highly efficient separations in oil and gas industries. *Current Opinion in Green and Sustainable Chemistry*, *5*, 55-60. https://doi.org/10.1016/j.cogsc.2017.03.013

Wen, Q., Chen, J.-X., Tang, Y.-L., Wang, J., & Yang, Z. (2015). Assessing the toxicity and biodegradability of deep eutectic solvents. *Chemosphere*, *132*, 63-69. https://doi.org/10.1016/j.chemosphere.2015.02.061

Wertheim, M. S. (1984a). Fluids with highly directional attractive forces. I. Statistical thermodynamics. *Journal of Statistical Physics*, *35*(1), 19-34. https://doi.org/10.1007/BF01017362

Wertheim, M. S. (1984b). Fluids with highly directional attractive forces. II. Thermodynamic perturbation theory and integral equations. *Journal of Statistical Physics*, *35*(1), 35-47. https://doi.org/10.1007/BF01017363

Wertheim, M. S. (1986a). Fluids with highly directional attractive forces. III. Multiple attraction sites. *Journal of Statistical Physics*, *42*(3), 459-476. https://doi.org/10.1007/BF01127721

Wertheim, M. S. (1986b). Fluids with highly directional attractive forces. IV. Equilibrium polymerization. *Journal of Statistical Physics*, *42*(3), 477-492. https://doi.org/10.1007/BF01127722

Xiang, X., Guo, L., Wu, X., Ma, X., & Xia, Y. (2012). Urea formation from carbon dioxide and ammonia at atmospheric pressure. *Environmental Chemistry Letters*, *10*(3), 295-300. https://doi.org/10.1007/s10311-012-0366-2

Xie, Y., Dong, H., Zhang, S., Lu, X., & Ji, X. (2014). Effect of Water on the Density, Viscosity, and CO2 Solubility in Choline Chloride/Urea. *Journal of Chemical & Engineering Data*, *59*(11), 3344-3352. https://doi.org/10.1021/je500320c

Xu, K., Wang, Y., Ding, X., Huang, Y., Li, N., & Wen, Q. (2016). Magnetic solid-phase extraction of protein with deep eutectic solvent immobilized magnetic graphene oxide nanoparticles. *Talanta*, *148*, 153-162. https://doi.org/10.1016/j.talanta.2015.10.079

Xu, P., Zheng, G.-W., Zong, M.-H., Li, N., & Lou, W.-Y. (2017). Recent progress on deep eutectic solvents in biocatalysis. *Bioresources and Bioprocessing*, *4*(1), 34. https://doi.org/10.1186/s40643-017-0165-5

Xue, X., Zhang, Q., Liu, Y., Guo, Q., Jiao, W., & Zhang, C. (2022). Selective absorption process intensification of ammonia from melamine exhaust gas using a counter airflow shear-rotating packed bed. *Journal of Environmental Chemical Engineering*, *10*(6), 108760. https://doi.org/10.1016/j.jece.2022.108760

Yadav, A., Kar, J. R., Verma, M., Naqvi, S., & Pandey, S. (2015). Densities of aqueous mixtures of (choline chloride+ethylene glycol) and (choline chloride+malonic acid) deep eutectic solvents in temperature range 283.15–363.15K. *Thermochimica Acta*, *600*, 95-101. https://doi.org/10.1016/j.tca.2014.11.028

Yadav, A., & Pandey, S. (2014). Densities and Viscosities of (Choline Chloride + Urea) Deep Eutectic Solvent and Its Aqueous Mixtures in the Temperature Range 293.15 K to 363.15 K. *Journal of Chemical & Engineering Data*, *59*(7), 2221-2229. https://doi.org/10.1021/je5001796

Yadav, A., Trivedi, S., Rai, R., & Pandey, S. (2014). Densities and dynamic viscosities of (choline chloride+glycerol) deep eutectic solvent and its aqueous mixtures in the temperature range (283.15–363.15)K. *Fluid Phase Equilibria*, *367*, 135-142. https://doi.org/10.1016/j.fluid.2014.01.028

Yates, A. A., Schlicker, S. A., & Suitor, C. W. (1998). Dietary Reference Intakes: the new basis for recommendations for calcium and related nutrients, B vitamins, and choline. *J Am Diet Assoc*, *98*(6), 699-706. https://doi.org/10.1016/s0002-8223(98)00160-6

Yokozeki, A., & Shiflett, M. B. (2010). Water Solubility in Ionic Liquids and Application to Absorption Cycles. *Industrial & Engineering Chemistry Research*, *49*(19), 9496-9503. https://doi.org/10.1021/ie1011432

Yu, D., Xue, Z., & Mu, T. (2022). Deep eutectic solvents as a green toolbox for synthesis. *Cell Reports Physical Science*, 100809. https://doi.org/10.1016/j.xcrp.2022.100809

Zendehboudi, A., Saidur, R., Mahbubul, I. M., & Hosseini, S. H. (2019). Data-driven methods for estimating the effective thermal conductivity of nanofluids: A comprehensive review. *International Journal of Heat and Mass Transfer*, *131*, 1211-1231. https://doi.org/10.1016/j.ijheatmasstransfer.2018.11.053

Zeng, S., Dong, H., Bai, Y., Zhang, X., & Zhang, S. (2020). New technology of ionic liquid-based NH3/CO2 separation from melamine tail gas. *Green Chemical Engineering*, *1*(1), 5. https://doi.org/10.1016/j.gce.2020.10.010

Zhang, J., Zheng, L., Fang, S., Zhang, H., Cai, Z., Huang, K., & Jiang, L. (2024). Efficient and reversible separation of NH3 by deep eutectic solvents with multiple active sites and low viscosities. *Chinese Journal of Chemical Engineering*, *67*, 97-105. https://doi.org/10.1016/j.cjche.2023.10.012

Zhang, Q., De Oliveira Vigier, K., Royer, S., & Jérôme, F. (2012). Deep eutectic solvents: syntheses, properties and applications [10.1039/C2CS35178A]. *Chemical Society Reviews*, *41*(21), 7108-7146. https://doi.org/10.1039/C2CS35178A

Zhang, W., Cheng, S., Zhai, X., Sun, J., Hu, X., Pei, H., & Chen, G. (2020). Green and Efficient Extraction of Polysaccharides From Poria cocos F.A. Wolf by Deep Eutectic Solvent. *Natural Product Communications*, *15*(2), 1934578X19900708. https://doi.org/10.1177/1934578X19900708

Zhang, Y., Ji, X., & Lu, X. (2018). Choline-based deep eutectic solvents for CO2 separation: Review and thermodynamic analysis. *Renewable and Sustainable Energy Reviews*, *97*, 436-455. https://doi.org/10.1016/j.rser.2018.08.007

Zhang, Y., Song, Y., Jin, H., Wu, T., Xiao, H., Xiang, Y., Yun, J., & Shao, L. (2023). Study on CO2 absorption by novel choline chloride-diethylenetriamine-water deep eutectic solvents in a rotor-stator reactor. *Chemical Engineering and Processing - Process Intensification*, *184*, 109299. https://doi.org/10.1016/j.cep.2023.109299

Zhang, Y., Zhu, C., Fu, T., Gao, X., & Ma, Y. (2022). CO2 absorption performance of ChCl-MEA deep eutectic solvent in microchannel. *Journal of Environmental*

*Chemical Engineering*, *10*(6), 108792. https://doi.org/10.1016/j.jece.2022.108792

Zhang, Y., Zhu, C., Fu, T., Gao, X., Ma, Y., & Li, H. Z. (2024). CO2 absorption and desorption performance by ChCl-MEA-PZ deep eutectic solvent aqueous solutions. *Separation and Purification Technology*, *330*, 125275. https://doi.org/10.1016/j.seppur.2023.125275

Zhao, R.-t., Pei, D., Yu, P.-l., Wei, J.-t., Wang, N.-l., Di, D.-L., & Liu, Y.-w. (2020). Aqueous two-phase systems based on deep eutectic solvents and their application in green separation processes. *Journal of Separation Science*, *43*(1), 348-359. https://doi.org/10.1002/jssc.201900991

Zhong, F.-Y., Huang, K., & Peng, H.-L. (2019). Solubilities of ammonia in choline chloride plus urea at (298.2–353.2) K and (0–300) kPa. *The Journal of Chemical Thermodynamics*, *129*, 5-11. https://doi.org/10.1016/j.jct.2018.09.020

Zhou, H., Zhang, S., Gao, F., Bai, X., & Sha, Z. (2014). Solubility of Ammonia in Ethylene Glycol Between 303 K and 323 K under Low Pressure from 0.030 to 0.101 MPa. *Chinese Journal of Chemical Engineering*, *22*(2), 181-186. https://doi.org/10.1016/S1004-9541(14)60022-7

Zhu, J., Yu, K., Zhu, Y., Zhu, R., Ye, F., Song, N., & Xu, Y. (2017). Physicochemical properties of deep eutectic solvents formed by choline chloride and phenolic compounds at T=(293.15 to 333.15)K: The influence of electronic effect of substitution group. *Journal of Molecular Liquids*, *232*, 182-187. https://doi.org/10.1016/j.molliq.2017.02.071

Zhuang, Q., Clements, B., & Li, Y. (2012). From ammonium bicarbonate fertilizer production process to power plant CO2 capture. *International Journal of Greenhouse Gas Control*, *10*, 56-63. https://doi.org/10.1016/j.ijggc.2012.05.019

Zubeir, L. F., Held, C., Sadowski, G., & Kroon, M. C. (2016). PC-SAFT Modeling of CO2 Solubilities in Deep Eutectic Solvents. *The Journal of Physical Chemistry B*, *120*(9), 2300-2310. https://doi.org/10.1021/acs.jpcb.5b07888

Zuo, Z., Cao, B., Wang, Y., Ma, C., Lu, X., & Ji, X. (2024). Thermodynamic study of choline chloride-based deep eutectic solvents with dimethyl sulfoxide and isopropanol. *Journal of Molecular Liquids*, *394*, 123731. https://doi.org/10.1016/j.molliq.2023.123731

Zuo, Z., Sun, Y., Lu, X., & Ji, X. (2021). Simultaneous representation of thermodynamic properties and viscosities of ILs/DESs+co-solvent systems by Eyring-NRTL

model. *Fluid Phase Equilibria*, *547*, 113176. https://doi.org/10.1016/j.fluid.2021.113176